The University of Oxford

Department of Chemistry

Structural and Dynamic Studies of Zr-Based Metal-Organic Frameworks toward External Stimuli

Tatchamapan Yoskamtorn

St Edmund Hall

Michaelmas 2021

A thesis submitted for the degree of

Doctor of Philosophy in Inorganic Chemistry

Declaration

I confirm that this thesis is a result of my original work except where specific reference is made. All the material from other sources has been properly and fully acknowledged.

Tatchamapan Yoskamtorn

1 March 2021

Dedication

To my parents and grand father

Abstract

Advanced studies of structures and dynamics of functional materials based on metal-organic frameworks (MOFs) showing exceptional stimuli-driven properties is of strong current interest for the design of next-generation smart materials, especially for sorption-based applications such as gas storage, energy storage, controlled drug delivery, and molecular sensing, to name but a few. State-of-the-art diffraction and spectroscopy in conjunction with theoretical calculations are one of the most powerful approaches to achieve these detailed analyses at a molecular level. This thesis aims to study mechanistic aspects of stimuli-responsive behaviours responsible for a distinctive stepwise ammonia (NH_3) adsorption in the defect-rich Zr-based metal-organic frameworks (MOFs), namely UiO-67 and its isostructural UiO-bpydc, both experimentally and computationally. In Chapter 3, high-resolution neutron and synchrotron diffractions along with Rietveld refinement and density functional theory (DFT) calculations have been used to characterise the binding domains and the interactions of NH_3/ND_3 with defect-rich UiO-67 and UiO-bpydc containing biphenyl dicarboxylate and bipyridine dicarboxylate linkers, respectively. The results establish that the dramatic alteration of stepwise adsorption processes is closely associated with hydrogen bonding network between NH_3/ND_3 and the frameworks at the disordered/defective trigonal and lozenge pore windows of the materials without significant change in pore volume and unit cell parameters. Specifically, UiO-bpydc is possible to make stronger and more extensive hydrogen bonding using pyridine sites of the linker than in UiO-67. These molecular controls lead to stimulus-tailoring properties such as gate-controlled porosity by dynamic linker flipping, disorder, and structural rigidity which are further confirmed by temperature-dependence of *in situ* structural analyses accompanied with guest-induced rotational motions of the organic linkers studied by

DFT in Chapter 4. To get deeper insights into the interesting NH_3-induced stepwise adsorption, the dynamic features of the MOF-NH_3 systems have been further investigated by using advanced inelastic neutron scattering (INS), quasi-elastic neutron scattering (QENS) in conjunction with theoretical calculations. Guest-induced linker stiffening reflected by the suppression of lattice motions of the host frameworks upon NH_3 adsorption is achieved, which exhibits greater effect in the UiO-bpydc case. More excitingly, analysis of INS difference spectra reveals heterogeneous dynamics of the trapped NH_3 depending on MOF functionality and gas loading. For the UiO-67, the well-ordered NH_3 molecules primarily adsorbed at μ_3-OH have more feasibility to undergo progressive interactions with the incoming NH_3 molecules, signifying its more accessible porous structure for NH_3 inclusion due to the lack of guest-stimulated pore blocking conversely observed in the UiO-bpydc. QENS study elucidates negligible mobility of NH_3 in both MOFs at the lowest dosage, indicative of the similar localised diffusion caused by strongly bound NH_3 at the μ_3-OH sites of the hosts. On the other hand, the NH_3 diffusivities in these frameworks become distinct at higher NH_3 uptake where the stepped adsorption occurs. This observation points toward the confined NH_3 molecules experiencing a diversity of either pore environments or host-guest interactions.

Acknowledgements

I am indebted to many people who have contributed to the existence of this thesis. I would first and foremost like to express my deep gratitude to my supervisor, Professor Edman Tsang for providing me an opportunity to work independently, sowing the seeds of the research, and giving me endless encouragement throughout my study. Without his constructive supervision, my research would have never been successfully completed.

It was my great honour to have worked with excellent and helpful postdoc researchers in Tsang group; Dr. Pu Zhao, Dr. Tugce Alvari, and Dr. Jianwei Zhang. Deep gratitude is given to my major collaborator, Dr. Pu Zhao, for kindly sharing her research expertise and thoughtful ideas over the years. My research skill has been much developed thanks to her advice. I would also like to thank Dr. Xin-Ping Wu from East China University of Science and Technology for his excellent collaboration in density functional theory calculations. Great acknowledgements are also given to Dr. David Fairen-Jimenez, Dr. Nakul Rampal and Rocio Bueno Perez for their collaborative work on molecular dynamics simulations.

My special thanks go to Dr. Fabio Orlandi, Dr. Pascal Manuel, Dr. Svemir Rudic, and Dr. Sanghamitra Mukhopadhyay for their generous help in planning and performing the neutron experiments together with their useful discussion on the results. Dr. Sarah Day and Dr. Chiu C. Tang are gratefully acknowledged for their assistance in the synchrotron measurements and the data interpretation. I would also like to thank Dr. James Taylor for his kind help in the ammonia sorption analyses.

My study was fully funded by the Development and Promotion for Science and Technology Talents Project (DPST scholarship), under the Royal Thai Government. I greatly acknowledge them for their long-term financial support since I was sixteen when my

enthusiasm in Chemistry began. I would also like to acknowledge the ISIS Neutron and Muon Source and the Diamond Light Source for access to beamline facilities.

Many thanks also to friends and colleagues in Tsang group in both past and present, especially Dr. Lin Ye, Dr. Benedict Lo, Kirsty Purchase, Yiyang Li, Guangchao Li, and Chris Fu for their generous supports and words of encouragement over the years. I would also like to thanks Department of Chemistry, The University of Oxford for providing high-standard research environment and facilities together with financial support to attend an international conference. My college, St Edmund Hall, is also acknowledged for making my DPhil life in Oxford absolutely valuable.

Naturally, the final and greatest thanks are given to my family: Mom, Dad, Grandpa, and Bro who always understand, support, and believe in me in any situations. Without these amazing people, this thesis would have never been successful this far. Thank you for everything.

Tatchamapan Yoskamtorn

1 March 2021

List of Abbreviations

Abbreviation	Definition
AA	Acetic acid
BA	Benzoic acid
bdc	*1,4*-benzenedicarboxylate
BET	Brunauer Emmett Teller
bpdc	biphenyl-*4,4′*-dicarboxylate
bpydc	*2,2′*-bipyridine-*5,5′*-dicarboxylate
btc	*1,3,5*-benzenetricarboxylate
CH_3COO	Acetate
CH_3COOH	Acetic acid
DFA	Difluoric acid
DFT	Density funcional theory
DMF	*N,N*-dimethylformamide
ELM	Elastic layer material
FA	Formic acid
FWHM	Full width at half maximum
GCMC	Grand canonical Monte Carlo
GGA	Generalized gradient approximation
GOF	Goodness-of-fit
HF	Hydrofluoric acid
ICP-MS	Inductively-coupled plasma mass spectroscopy
IFM	Interference microscopy

Abbreviation	Definition
INS	Inelastic neutron scattering
IP	In plane
IRM	Infrared microscopy
IRMOF	Isoreticular metal-organic framework
MD	Molecular dynamics
MOF	Metal-organic framework
MOPS	Microporous organically pillared layered silicates
ND_3	Fully-deuterated ammonia
NGA	Negative gas adsorption
NMR	Nuclear magnetic resonance
NPD	Neutron powder diffraction
NTE	Negative thermal expansion
NU	Northwestern University
OP	Out of plane
OPTZ	Phenothiazine-*5,5*-dioxide
PAW	Projector-augmented wave
PBE	Perdew-Burke-Ernzerhof
PCP	Porous coordination polymer
PFG-NMR	Pulsed-field gradient nuclear magnetic resonance
PH	Polyhedra
PSD	Pore size distribution
QENS	Quasielastic neutron scatterin
SBU	Secondary building unit

Abbreviation	**Definition**
SPC	Soft porous crystal
SXRD	Synchrotron X-ray diffraction
TFA	Trifluoroacetic acid
TGA	Thermogravimetric analysis
TOF	Time-of-flight
TPD	Temperature-programmed desorption
$TPDC^2$	*4,4′*-terphenyldicarboxylate
VASP	Vienna *ab-initio* simulation package
WPPF	Whole powder pattern fitting
XRD	X-ray diffraction
ZIF	Zeolitic imidazole framework

List of Figures and Tables

Chapter 1

Figure 1.1 | Comparison of the CO_2 adsorption isotherms of X-PCPs (X=I: red curve, Br: blue curve, Cl: black curve) measured at 194.7 K.....3

Figure 1.2 | Examples of the organic linkers used to construct Zr-based MOFs. 7

Figure 1.3 | Structural representation of the $[Zr_6O_4(OH)_4]^{12+}$ cluster (**a**), the $Zr_6O_4(OH)_4(COO)_{12}$ secondary building unit (SBU) (**b**) and its corresponding SBU with a polyhedral model (**c**).. 7

Figure 1. 4 | Crystallographic model and corresponding topological representative of perfect UiO-66 structure (**a**), UiO-66 with missing linker defects (**b**), UiO-66 with missing cluster defects (**c**) and UiO- 66 with both missing linker and cluster defects (**d**).. 8

Table 1.1 | Examples of the proposed terminating species in defective Zr-based MOFs prepared by adding various modulators during the synthesis. 10

Figure 1.5 | CO_2 adsorption isotherms measured at 298 K up to 1 bar (**a**), isosteric heat of CO_2 adsorption (**b**), CO_2 adsorption isotherms measured at 298 K up to 35 bar (**c**) and water adsorption isotherms measured at 298 K (**d**) for defect-free UiO-66... 12

Figure 1.6 | Various types of flexibility in MOFs. One class is characterised by the change in unit cell volume ($\Delta V \neq 0$; A, B and D) while in the other case the unit cell volume does not change ($\Delta V = 0$; C, D). 14

Figure 1.7 | Typical examples of "gate pressure" and "breathing" MOFs. 15

Figure 1.8 | Illustrations of mobile groups and partial crystal structures of several compounds……. 17

Table 1.2 | Details of activation energy, frequency, temperature, and mode of rotational motion. 17

Figure 1.9 | Examples of novel guest-induced responsive behaviours of flexible PCPs...19

Figure 1.10 | Theoretical gas adsorption isotherms (left) and schematic evolution of energetic contributions and cartoons of structures (right) of **a**) rigid and open framework, **b**) a SPC in closed pore state that does not undergo adsorption-induced expansion, **c**) a SPC that undergoes expansion upon adsorption, and **d**) a SPC that undergoes successive contraction and expansion upon adsorption (breathing). 21

Figure 1.11 | *In situ* NPD patterns of on HKUST-1 upon D_2 loading collected at 5 K and the corresponding refined structures......26

Figure 1.12 | Illustration of the structural changes from the DUT-49*op* to DUT-49*cp* phase. 26

Figure 1.13 | The phonon mode in INS spectra of a Zr-based MOF, MIL-140A and the corresponding trampoline-like vibrational motions.....28

Figure 1.14 | Schematic illustration of the changes of the libration mode upon guest molecule adsorption in a phenylene-based MOF. 30

Chapter 2

Figure 2.1 | Illustration of a beam that satisfies the Bragg's law, where dhkl, ki and ks represent the inter-planar spacing, the incident vector and the scattered vector, respectively. 49

Figure 2.2 | Comparison of the X-ray and neutron atomic form factors for $^{12}_{6}C$ as a function of the momentum transfer $Q = 4\pi \sin\theta/\lambda$.....50

Figure 2.3 | Scattering triangles for elastic scattering (a) and inelastic scattering (b).....59

Figure 2.4 | Geometry of the neutron scattering experiment.....62

Figure 2.5 | Illustration of a very simple one-dimensional example of how a function, β(x), can be decomposed into the sum of an average pattern.....62

Table 2.1 | Neutron scattering lengths (b) and cross sections (σ) of the elements typically used to synthesise MOFs. 63

Figure 2.6 | Schematic illustration of the time-of-flight (TOF) instrumental configuration for NPD measurement. 66

Figure 2.7 | INS spectroscopy in comparison with optical (photon) spectroscopies.....69

Figure 2.8 | Schematic diagram of the TOSCA indirect geometry time-of-flight (TOF) spectrometer.....70

Figure 2.9 | Two types of diffusional motions of a particle (teal sphere) in a porous solid (grey sphere): **a**) translational diffusion and **b**) rotational diffusion such as a methyl ($-CH_3$) group. 72

Table 2.2 | Time scale, energy resolution and spectroscopic technique for QENS experiment. 73

Figure 2.10 | The broadenings (HWHM) of Lorentzian functions as a function of Q^2 fitted with different diffusion models.....77

Figure 2.11 | Elastic incoherent structure factor (EISF) as a function of Q simulated from the uniaxial jump rotation model with a constant radius of rotation $r = 2.0$ Å but various equivalent N sites.....78

Figure 2.12 | Schematic diagram of the neutron diffraction set up at WISH beamline, ISIS. 85

Chapter 3

Figure 3.1 | Visualisation of the UiO-67 type MOFs. 106

Table 3.1 | Sample information used in the *in situ* NPD experiments. 108

Figure 3.2 | NH_3 sorption isotherm of UiO-67. 110

Figure 3.3 | *In situ* NPD patterns of UiO-67 at various loadings of ND_3. 113

Table 3.2 | Crystallographic data and details of ND_3@UiO-67 samples at various ND_3 dosing. 115

Figure 3.4 | Fitted NPD data of UiO-67 as a function of ND_3 adsorption. 117

Figure 3.5 | ND_3 responsive behaviours of the defective UiO-67. 119

Figure 3.6 | Uptake data for NH_3 adsorption of MOF samples before and after the healing process. 122

Figure 3.7 | NH_3 sorption isotherm of UiO-bpydc. The isotherm was measured at 298 K and up to 1100 mbar of NH_3 pressure. 124

Figure 3.8 | *In situ* NPD patterns of UiO-bpydc at various loadings of ND_3. 126

Figure 3.9 | Fitted NPD data of UiO-bpydc as a function of ND_3 adsorption. 127

Table 3.3 | Crystallographic data and details of ND_3@UiO-bpydc samples at various ND_3 dosing. 128

Figure 3.10 | ND_3 responsive behaviours of the defective UiO-bpydc. 129

Figure 3.11 | Proposed NH_3 responsive behaviours of the defective UiO-67 type MOFs. 132

Figure 3.12 | Comparison of the UiO-67-NH_3 interactions by DFT calculations. 135

Figure 3.13 | Comparison of the UiO-bpydc-NH_3 interactions by DFT calculations. 135

Chapter 4

Figure 4.1 | Refined structures of UiO-67 (**a**) and UiO-bpydc (**b**) at different loadings of ND_3 at 300 K. 145

Figure 4.2 | *In situ* NPD patterns of UiO-67 at various loadings of ND_3 measured below 150 K and 300 K. 147

Figure 4.3 | *In situ* NPD patterns of UiO-bpydc at various loadings of ND_3 measured below 150 K and 300 K. 148

Figure 4.4 | Comparison of the NPD patterns of UiO-67 samples measured at different temperatures. 149

Table 4.1 | Summary of the dihedral angles between two aromatic rings of the linkers in UiO-67 and UiO-bpydc derived from Rietveld refinement of the NPD data. 150

Figure 4.5 | Fourier maps of ND_3 molecules inside UiO-67 with a loading of 4.63 mmol/g, measured at 300 Kand 7 K. 152

Figure 4.6 | Fourier maps of ND_3 molecules inside UiO-bpydc with a loading of 4.63 mmol/g, measured at 300 Kand 7 K. 152

Table 4.2 | Summary of the dihedral angles between two aromatic rings of the linkers of UiO-bpydc obtained from DFT calculations at 0 K. 153

Figure 4.7 | Proton-capped linker models used for estimating the rotational energy barriers (E_{rb}) of the NH_3-free and NH_3-loaded MOF samples. 155

Figure 4.8 | Energy as a function of the dihedral angles of the NH_3-free and NH_3-loaded MOF samples estimated from H_2bpdc (red) , H_2bpdc-1NH_3 (orange), H_2bpydc (blue), and H_2bpydc-1NH_3 (light blue) models. 155

Table 4.3 | Rotational energy barriers (E_{rb}) of the NH_3-free and NH_3-loaded MOF samples estimated from H_2bpdc, H_2bpdc-1NH_3, H_2bpydc, and H_2bpydc-1NH_3 models. 156

Chapter 5

Figure 5.1 | Proposed NH_3 responsive behaviours responsible of the UiO-67-type MOFs containing missing linker defects. 161

Table 5.1 | Sample information used in the *in situ* INS experiments. 164

Figure 5.2 | Comparison of experimental and DFT-calculated INS spectra of UiO-67, UiO-bpydc against solid CH_3COOH. 166

Table 5.2 | Calculated and experimental vibrational modes of UiO-67. 167

Table 5.3 | Calculated and experimental vibrational modes of UiO-bpydc.....170

Figure 5.3 | Schematic representation of UiO-67 and UiO-bpydc structures with missing linker defects.....173

Figure 5.4 | NH_3 uptake of UiO-67 and UiO-bpydc in INS experiments compared with its NH_3 sorption isotherm measured at 298 K. 176

Figure 5.5 | INS spectra collected below 10 K for UiO-67 as a function of NH_3 loadings with the range of neutron energy loss up to 2000 cm^{-1} (248 meV, **a**), 1000 cm^{-1} (124 meV, **b**), and 500 cm^{-1} (62 meV, **c**) and examples of deformational modes of UiO-67 most affected by the loading of NH_3, **d**).....178

Figure 5.6 | INS spectra collected below 10 K for defective UiO-bpydc as a function of NH_3 loadings with the range of neutron energy loss up to 2000 cm^{-1} (248 meV, **a**), 1000 cm^{-1} (124 meV, **b**), and 500 cm^{-1} (62 meV, **c**) and examples of deformational modes of UiO-bpydc most affected by the loading of NH_3, **d**). 179

Figure 5.7 | Comparison of the difference plots between UiO-67 (**a**) and UiO-bpydc (**b**) with increased NH_3 adsorption. 183

Figure 5.8 | Experimental (**a**) and simulated (**b**) INS spectra of UiO-67 and UiO-67_2.10NH_3 with the range of neutron energy loss up to 1000 cm^{-1} (124 meV). 185

Figure 5.9 | NH_3 uptake of UiO-67 (**a**) and UiO-bpydc (**b**) in QENS experiments compared with its NH_3 sorption isotherm measured at 298 K. 189

Table 5.4 | Sample information used in the *in situ* QENS experiments. 189

Figure 5.10 | Normalised QENS spectra measured for UiO-67 at 10 ± 2 K (grey triangle) and at 298 ± 2 K (red circle).. 190

Figure 5.11 | Surface plot of energy transfer versus ***Q*** values for unloaded UiO-67 collected at 10 ± 2 K (**a**) and 298 ± 2 K (**b**). 190

Figure 5.12 | Normalised QENS spectra measured for UiO-bpydc at 10 ± 2 K (grey triangle) and at 298 ± 2 K (red circle). 191

Figure 5.13 | Surface plot of energy transfer versus ***Q*** values for unloaded UiO-bpydc collected at 10 ± 2 K (**a**) and 298 ± 2 K (**b**).....191

Figure 5.14 | QENS spectra of defective UiO-67 as a function of NH_3 loading at ***Q*** = 0.27 $Å^{-1}$. Inset represents their associated simultaneous diffraction patterns. 192

Figure 5.15 | QENS spectra of defective UiO-bpydc as a function of NH_3 loading at ***Q*** = 0.27 $Å^{-1}$. Inset represents their simultaneous diffraction patterns. 192

Figure 5.16 | Subtracted QENS data of NH_3-adsorbed UiO-67 measured at 298 ± 2 K (**a, b,** and **c**) and the loading-dependent neutron diffraction pattern of UiO-67 from Chapter 3 (**d**). 193

Figure 5.17 | Subtracted QENS data of NH_3-adsorbed UiO-bpydc measured at 298 ± 2 K (**a, b,** and **c**) and the loading-dependent neutron diffraction pattern of UiO-bpydc from Chapter 3 (**d**).. 194

Figure 5.18 | The convolution fit of QENS spectrum of UiO-67 loaded with 4.11 mmol/g NH_3 at Q= 0.27 $Å^{-1}$.....196

Figure 5.19 | The convolution fit of QENS spectrum of UiO-67 loaded with 6.72 mmol/g NH_3 at Q= 0.27 $Å^{-1}$.....197

Figure 5.20 | The convolution fit of QENS spectrum of UiO-bpydc loaded with 4.04 mmol/g NH_3 at Q= 0.27 $Å^{-1}$.....197

Figure 5.21 | The convolution fit of QENS spectrum of UiO-bpydc loaded with 6.55 mmol/g NH_3 at Q= 0.27 $Å^{-1}$.....198

Figure 5.22 | Variations of the HWHM (**a, c**) and EISF (**b, d**) as a function of ***Q*** and NH_3 loading derived from QENS experiments at 298 ± 2 K.....198

Figure 5.23 | Solvent-excluded surface maps of defective MOF Models with 2x2x2 supercells used in the GCMC simulations.....202

Table 5.5 | Comparison of the experimental and simulated geometric properties of UiO-67-type MOFs with missing linker defects using He as a probe molecule.....204

Table 5.6 | Details of the MOF-NH_3 models used in the GCMC simulations.....204

Table 5.7 | Lennard Jones (LJ) parameters and charges for N_2 and NH_3.....205

Table 5.8 | Lennard Jones (LJ) parameters, charges and polarizabilities for the atoms in the framework.....205

Figure 5.24 | Comparison of experimental and simulated adsorption isotherms computed by GCMC.....206

Appendices

Figure A3.1 | Powder XRD patterns of UiO-67 (**a**) and UiO-bpydc (**b**) along with their corresponding diffraction patterns obtained from the literature. 219

Figure A3.2 | N_2 physisorption isotherms of activated samples at 77 K. 220

Table A3.1 | Corresponding missing linkers of the MOF samples derived from the elemental analyses and ICP-MS techniques.....220

Table A3.2 | Corresponding missing linkers of the MOF samples obtained from the TGA results. 221

Figure A3.3 | ^{1}H NMR spectra of aliquots from the UiO-67 (**a**) and UiO-67-healed (**b**) in 0.1 M NaOH in D_2O at 298 K.. 222

Figure A3.4 | ^{1}H NMR spectra of aliquots from the UiO-bpydc (**a**) and UiO-bpydc-healed (**b**) in 0.1 M NaOH in D_2O at 298 K. 223

Figure A3.5 | Powder XRD patterns of UiO-67 samples before and after the healing process. 224

Figure A3.6 | Powder XRD patterns of UiO-bpydc samples before and after the healing process. 224

Figure A3.7 | N_2 sorption profiles and pore size distribution of UiO-67 samples before and after the healing process. 225

Figure A3.8 | N_2 sorption profiles and pore size distribution of UiO-bpydc samples before and after the healing process.....225

Figure A3.9 | Stability tests of UiO-67 (**a**) and UiO-bpydc (**b**) for NH_3 uptake, measured by repeated gravimetric analysis.....226

Figure A3.10 | Powder XRD patterns of defective Zr-based MOFs before and after three cycles of NH_3 adsorption at 298 K and up to 600 mbar of NH_3 pressure, measured by gravimetric analysis.....227

Figure A3.11 | FT-IR spectra of the samples before and after NH_3 adsorption at room temperature. 227

Figure A3.12 | ND patterns of ND_3-free UiO-67 recorded at 300 K by using different detector banks. 228

Figure A3.13 | Refined lattice parameters of the NPD data of defective UiO-67 at different ND_3 loadings.....228

Table A3.3 | *R*-factors and *GOF* values of UiO-67 as a function of ND_3 loading obtained from Rietveld refinement of the associated NPD data recorded at 300 K...229

Table A3.4 | Summary of Rietveld refinement results of ND_3@UiO-67. 230

Table A3.5 | Structural data from the Rietveld refinement of UiO-67 sample loaded with 1.23 mmol/g ND_3 (9.65 ND_3 molecules per asymmetric unit). 231

Table A3.6 | Structural data from the Rietveld refinement of UiO-67 sample loaded with 4.63 mmol/g ND_3 (36.3 ND_3 molecules per asymmetric unit). 232

Table A3.7 | Structural data from the Rietveld refinement of UiO-67 sample loaded with 7.60 mmol/g ND_3 (59.6 ND_3 molecules per asymmetric unit). 233

Figure A3.14 | Normalised NH_3-TPD curves of defective MOF samples, measured with a heating rate of 10 °C/min. 235

Figure A3.15 | ND patterns of ND_3-free UiO-bpydc recorded at 300 K by using different detector banks. 235

Figure A3.16 | Refined lattice parameters of the NPD data of defective UiO-bpydc at different ND_3 loadings.. 236

Table A3.8 | *R*-factors and *GOF* values of UiO-bpydc as a function of ND_3 loading obtained from Rietveld refinement of the associated NPD data recorded at 300 K…236

Table A3.9 | Summary of the Rietveld refinement results of ND_3@UiO-bpydc samples. 238

Table A3.10 | Structural data from the Rietveld refinement of UiO-bpydc sample loaded with 4.15 mmol/g ND_3 (32.6 ND_3 molecules per asymmetric unit).....238

Table A3.11 | Structural data from the Rietveld refinement of UiO-bpydc sample loaded with 4.27 mmol/g ND_3 (33.6 ND_3 molecules per asymmetric unit).....239

Table A3.12 | Structural data from the Rietveld refinement of UiO-bpydc sample loaded with 6.06 mmol/g ND_3 (47.6 ND_3 molecules per asymmetric unit).....241

Table A3.13 | The guiding values of "strong", "moderate" and "weak" hydrogen bonds.[4] 242

Figure A3.17 | DFT Optimised structure of NH_3 dimer. The binding energy is 0.13 eV. The unit of the H bond length is in angstrom (Å).....243

Figure A3.18 | Synchrotron PXRD patterns of UiO-67 before and after NH_3 adsorption, measured at 298 K. 243

Figure A3.19 | Synchrotron PXRD patterns of UiO-67 before and after NH_3 adsorption, measured at 298 K. 244

Figure A3.20 | Synchrotron XRD patterns of the NH_3-loaded UiO-bpydc sample measured at different temperatures from 298 K to 773 K. 244

Figure A3.21 | Refined lattice parameters and their corresponding R_{wp} values of the NH_3-loaded UiO-bpydc sample obtained from the synchrotron XRD results.....245

Figure A3.22 | Synchrotron PXRD patterns and refined NH_3 positions in the channel of the UiO-bpydc structure. 245

Figure A3.23 | Scanning electron microscope (SEM) images of defective UiO-67 (**a**) and UiO-bpydc (**b**). Scale bar: 1 μm……..246

Figure A4.1 | *In situ* NPD patterns of UiO-67 before ND_3 loading measured at 7 K (blue line) and 300 K (red line).....247

Figure A4.2 | *In situ* NPD patterns of UiO-67 at ND_3 loading (*L*) of 1.23 mmol/g measured at 7 K (blue line) and 300 K (red line).....247

Figure A4.3 | *In situ* NPD patterns of UiO-67 at ND_3 loading (*L*) of 4.63 mmol/g measured at 7 K (blue line) and 300 K (red line).....248

Figure A4. 4 | *In situ* NPD patterns of UiO-67 at ND_3 loading (*L*) of 7.60 mmol/g measured at 150 K (blue line) and 300 K (red line).....248

Figure A4.5 | *In situ* NPD patterns of UiO-bpydc before ND_3 loading measured at 7 K (blue line) and 300 K (red line).....249

Figure A4.6 | *In situ* NPD patterns of UiO-bpydc at ND_3 loading (*L*) of 4.15 mmol/g measured at 7 K (blue line) and 300 K (red line). 249

Figure A4.7 | *In situ* NPD patterns of UiO-bpydc at ND_3 loading (*L*) of 4.27 mmol/g measured at 7 K (blue line) and 300 K (red line). 250

Figure A4.8 | *In situ* NPD patterns of UiO-bpydc at ND_3 loading (*L*) of 6.06 mmol/g measured at 7 K (blue line) and 300 K (red line). 250

Table A5.1 | Calculated and experimental vibrational modes of solid acetic acid (CH_3COOH).....252

Table A5.2 | Calculated and experimental vibrational modes of crystalline ammonia (NH_3) phase I from experimental data measured at 20 K. 252

Figure A5.1 | INS difference plots of UiO-67 with increased NH_3 adsorption. 254

Figure A5.2 | INS difference plots of UiO-bpydc with increased NH_3 adsorption. 254

Figure A5.3 | Experimental (**a**) and simulated (**b**) INS spectra of UiO-67 and UiO-67_2.10NH_3 with the range of neutron energy loss up to 2000 cm^{-1} (248 meV). 255

Figure A5.4 | QENS data of NH_3-adsorbed UiO-67 measured at 298 ± 2 K. 256

Figure A5.5 | QENS data of NH_3-adsorbed UiO-bpydc measured at 298 ± 2 K. 256

Table of Contents

DECLARATION ---------- **II**

DEDICATION ---------- **III**

ABSTRACT ---------- **IV**

ACKNOWLEDGEMENTS ---------- **VI**

LIST OF ABBREVIATIONS ---------- **VIII**

LIST OF FIGURES AND TABLES ---------- **XI**

TABLE OF CONTENTS ---------- **XXIV**

CHAPTER 1

INTRODUCTION ---------- **1**

1.1) MOTIVATION ---------- 1
1.2) BACKGROUND LITERATURE ---------- 5
1.2.1) Definition of MOFs ---------- *5*
1.2.2) Zr-based MOFs ---------- *6*
1.2.3) Defect engineering in MOFs ---------- *8*
1.2.4) Flexibility in MOFs ---------- *14*
1.2.5) Rotational dynamics in MOFs with flexible linkers ---------- *16*
1.2.6) Relationship of guest-induced structural dynamics and adsorption properties *20*
1.2.7) Advanced methods for studying structural and dynamic behaviours in MOFs *24*
1.2.8) Diffusion in MOFs ---------- *31*
1.3) AIMS AND OBJECTIVES ---------- 33
1.4) STRUCTURE OF THE THESIS ---------- 34
1.5) CHAPTER SUMMARY ---------- 36
1.6) REFERENCES ---------- 37

CHAPTER 2

EXPERIMENTAL AND THEORETICAL METHODOLOGIES ---------- **48**

2.1) BACKGROUND THEORIES ---------- 48
2.1.1) Powder diffraction ---------- *48*
2.1.2) Structure determination from powder diffraction data ---------- *52*
2.1.2.1) Rietveld method ---------- 52
2.1.2.2) Judging quality of Rietveld refinement ---------- 54
2.1.2.3) Le Bail extraction ---------- 57
2.1.3) Basic concepts of Neutron Scattering ---------- *58*
2.1.3.1) Elastic and inelastic scattering ---------- 60
2.1.3.2) Scattering cross section ---------- 61
2.1.3.3) Coherent and incoherent scattering ---------- 62
2.1.4) Neutron powder diffraction (NPD) ---------- *65*

2.1.5) Inelastic neutron scattering (INS) ----- *67*
2.1.5.1) INS experiments ----- 69
2.1.6) Quasielastic neutron scattering (QENS) ----- *72*
2.1.6.1) Fundamentals and type of information provided ----- 72
2.1.6.2) QENS experiments ----- 74
2.1.6.3) Information derived from QENS data ----- 75
2.2) EXPERIMENTAL PROCEDURES ----- 79
2.2.1) Chemicals ----- *79*
2.2.2) Sample preparation ----- *80*
2.2.3) Characterisation techniques ----- *81*
2.2.3.1) X-ray powder diffraction (XRD) ----- 81
2.2.3.2) Thermogravimetric analysis (TGA) ----- 81
2.2.3.3) Elemental analysis ----- 81
2.2.3.4) ^{1}H Nuclear magnetic resonance (NMR) of digested samples ----- 81
2.2.3.5) N_2 physisorption ----- 82
2.2.3.6) NH_3 temperature-programmed desorption (NH_3-TPD) ----- 82
2.2.3.7) Volumetric analysis of NH_3 sorption isotherms ----- 82
2.2.3.8) Gravimetric analysis of NH_3 sorption isotherms ----- 83
2.2.3.9) Synchrotron powder X-ray diffraction (SXRD): ----- 83
2.2.3.10) *In situ* synchrotron powder X-ray diffraction (*In situ* SXRD) for NH_3 desorption study: ----- 84
2.2.3.11) *In situ* neutron powder diffraction (*In situ* NPD) for ammonia adsorption analysis: ----- 84
2.2.4) Inelastic neutron scattering (INS) at TOSCA ----- *87*
2.2.5) Quasi-elastic neutron scattering (QENS) at OSIRIS ----- *89*
2.2.6) Data analysis ----- *90*
2.2.6.1) For XRD and NPD experiments ----- 90
2.2.6.2) For INS and QENS experiments ----- 93
2.3) THEORETICAL CALCULATIONS ----- 93
2.3.1) Density Functional Theory (DFT) calculations ----- *93*
2.3.1.1) Optimisation of NH_3-MOF structures ----- 93
2.3.1.2) Calculations of rotational energy barriers ----- 94
2.3.1.3) Calculations of vibrational (phonon) frequencies of NH_3-MOF structures 94
2.3.2) Grand cononical Monte Carlo (GCMC) simulations: ----- *95*
2.4) CHAPTER SUMMARY ----- 97
2.5) REFERENCES ----- 97

CHAPTER 3

RESPONSIVE BEHAVIOURS OF DEFECT-RICH ZR-BASED METAL-ORGANIC FRAMEWORKS TOWARD NH_3 ADSORPTION ----- 101

3.1) INTRODUCTION ----- 102
3.2) RESULTS AND DISCUSSION ----- 107
3.2.1) NH_3 adsorption in defective UiO-67 ----- *110*

3.2.2) Elucidation of ND_3 adsorption sites inside defective UiO-67 by in situ powder diffraction ---------- *112*
3.2.3) NH_3-induced linker flipping in defective UiO-bpydc ---------- *123*
3.2.4) Analyses of the MOF-NH_3 interactions by DFT calculations ---------- *134*
3.3) CHAPTER SUMMARY ---------- 137
3.4) REFERENCES ---------- 138

CHAPTER 4

TEMPERATURE-DEPENDENT RESPONSES OF DEFECT-RICH ZR-BASED METAL-ORGANIC FRAMEWORKS VIA NH_3 ADSORPTION ---------- 143

4.1) INTRODUCTION ---------- 144
4.2) RESULTS AND DISCUSSION ---------- 146
4.2.1) Structural Flexibility of Linker towards Temperature ---------- *146*
4.2.2) Rotational energy barriers of the NH_3-free and NH_3-loaded MOFs ---------- *155*
4.3) CHAPTER SUMMARY ---------- 157
4.4) REFERENCES ---------- 158

CHAPTER 5

DYNAMICS AND KINETICS OF NH_3 CONFINED IN DEFECTIVE ZR-BASED METAL-ORGANIC FRAMEWORKS ---------- 160

5.1) INTRODUCTION ---------- 161
5.2) RESULTS AND DISCUSSION ---------- 164
5.2.1.) Analysis of NH_3-MOF binding interactions via inelastic neutron scattering *164*
5.2.1.1) Analysis of the terminating species at defect sites of the hosts. ---------- 164
5.2.1.2) Dynamics of the MOF hosts upon the adsorption of NH_3 ---------- 175
5.2.1.3) Overall INS spectra of defective UiO-67 as a function of NH_3 loadings 177
5.2.1.4) Overall INS spectra of defective UiO-bpydc as a function of NH_3 loadings ---------- 180
5.2.1.5) Comparison of INS difference spectra of defective UiO-67 and UiO-bpydc upon NH_3 adsorption ---------- 182
5.2.2) Diffusion of adsorbed NH_3 inside the defective hosts ---------- *188*
5.2.2.1) Analysis of NH_3 diffusion by QENS ---------- 188
5.2.2.2) Analysis of stepwise adsorption in defective hosts by grand canonical Monte Carlo (GCMC) simulations ---------- 202
5.3) CHAPTER SUMMARY ---------- 208
5.4) REFERENCES ---------- 209

CHAPTER 6

CONCLUSION AND FUTURE PERSPECTIVES ---------- 213

6.1) CONCLUSION ---------- 213
6.2) FUTURE PERSPECTIVES ---------- 216
6.3) REFERENCE ---------- 217

APPENDICES

A) APPENDICES FOR CHAPTER 3 ---------- 218
B) APPENDICES FOR CHAPTER 4 ---------- 247
C) APPENDICES FOR CHAPTER 5 ---------- 252
D) REFERENCES ---------- 257

Chapter 1

Introduction

This thesis provides a brief introduction to the motivation, literature review related to this thesis, and structure of the thesis. Details of the basic theories, experimental procedures and relevant data analyses are presented in Chapter 2. There are three results and discussion chapters including Chapter 3, 4, and 5. Chapter 3 focuses on an understanding of the NH_3 loading dependent structural responses of defect-rich Zr-based metal-organic frameworks (MOFs), namely UiO-67 and UiO-bpydc at a molecular level. Effect of temperature on the responsive behaviours of the aforementioned MOF-NH_3 system is further explored in Chapter 4. The last result chapter (Chapter 5) reveals the comprehensive study of dynamic properties (vibrational and diffusive motions) of NH_3 molecules confined inside the pores of UiO-67 type MOFs. A summary of the overall results obtained throughout this thesis is given in Chapter 6 along with perspectives towards possible future directions of this research field.

1.1) Motivation

The development of smart materials for stimuli-responsive recognition, wherein a complex form in a manner that is sensitive to, or can be governed by, externally applied triggers such as light, temperature, pressure, magnetic or electric field has recently been receiving a lot of attention. Molecular engineering, biometric and design approaches offer an assortment of new chemistry and material design tools toward improving precision in tailoring properties. For example, understanding and controlling molecular motions of synthetic materials towards stimulus for their order-disorder transformation, reorientational and rotational motion associated with phase transitions may allow switching back and forth

between hard or soft state, a breakthrough that offers an innovative solution to a long-standing challenge with synthetic materials by giving them both strength and shape adaptability. [1-3]

Metal-organic frameworks (MOFs) [4] also known as porous coordination polymers (PCPs) [5] are highly topical classes of porous crystalline solids, consisting of metal ions/clusters, known as secondary building units (SBUs), coordinatively binding with organic ligands that typically form crystalline frameworks with long-range periodicity. They have attracted intense interest due to large surface area, designable porosity, functional diversity and structural flexibility, making them highly attractive for use in many applications. [6-8] The rational design of MOF materials for applications heavily relies on a thorough understanding of the host-guest interactions of the frameworks with exterior triggers. The nature of these interactions if controllable has been considered to primarily manipulate the MOF structural properties such as disorder, flexibility, compressibility as well as chemical reactivity. [3] Recently, different gas sorption phenomena in MOFs have been recognized for efficient gas separation application. [9-14] Sequential pore filling in non-uniform MOF pores has also been attributed for differential gas sorption phenomena. [9-10, 15] Flexible and dynamics motions of MOF linkers that undergo rotation or libration have been elucidated to play a dramatic role in guest-induced gate opening phenomena in many MOFs such as ZIF-8 [16], DUT-98 [17], and Cu-based PCPs [14].

The previously introduced structural transitions of MOFs, however, experience large volume change both in the nanospace and in the bulk solids challenging the practical use of these materials, especially in sorption-based applications. [18] This volume expansion in the adsorbent solid is disadvantageous as it may damage the storage tank, decompose the moldings, and also may result in slower diffusion of gases in the tank. Consequently, design

of new porous 'rigid' materials that can show guest adsorption and desorption with specific interaction(s) without significant volume change is highly desirable and technologically important. For example, Kitagawa and co-workers showed by SXRD and refinement of their crystalline MOFs and porous coordination polymer (PCP) that the polarised CH_2Br (also Cl and I) linker with CO_2 interaction can account for the additional CO_2 stepped uptake without significant structural or volume change (Figure 1.1)s. [18] Similarly, Bärwinkel and co-workers demonstrated that additional capacity of adsorption for CO_2 was realized by their crystalline microporous organically pillared layered silicates (MOPS) from their SXRD and refinement using the interaction of CO_2 with the organic cationic pillar based on electrostatic interactions without any framework and macroscopic pore volume changes. [19]

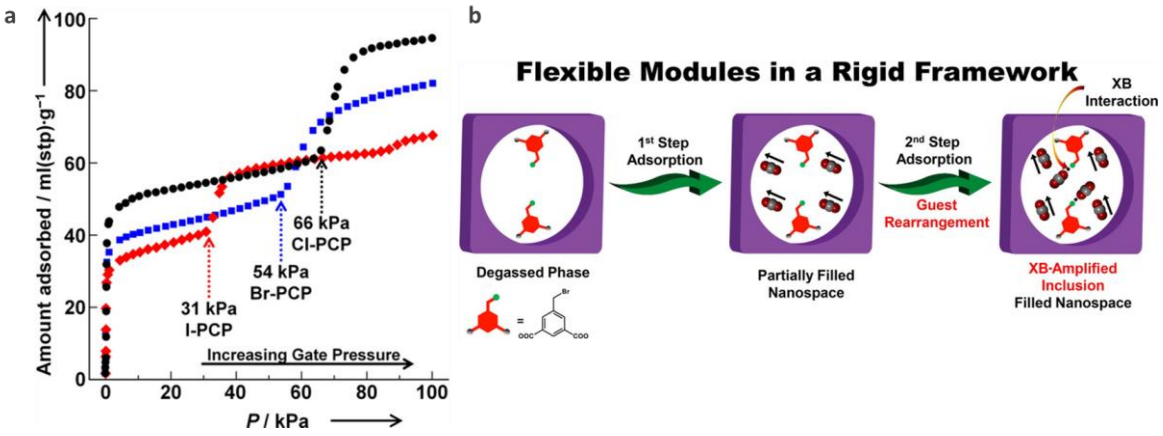

Figure 1.1 | Comparison of the CO_2 adsorption isotherms of X-PCPs (X=I: red curve, Br: blue curve, Cl: black curve) measured at 194.7 K (**a**) and the proposed mechanism of the two-step CO_2 adsorption in Br-PCP facilitated by cooperative XB interactions (**b**). Reprinted with permission from Ref [18].

In addition, studying the flexibility of MOF's organic linker by guest molecule stimulus at variable temperature may provide hints about their molecular interaction. To our understanding, flexible MOFs are characterised mainly by changes in the pore structure. For

example, the “flexibility” is well-known to occur in phenylene-based ligand systems. [14, 20-21] Gonzalez-Nelson *et al*. [2] have recently reviewed the studies of rotational barriers and dynamics of such ligand motives upon guest inclusion from the literature. However, these works were set in context to materials that exhibit large changes in unit cell and pore volume upon guest inclusion and other stimuli. The framework flexibility in the context of mainly ligand “flipping” but without significant pore volume alteration remains almost unexplored.

Apart from modification of flexibility in MOFs, incorporation of defects arising from either missing or dislocated atoms or ions can affect guest transport in the frameworks which is crucial for sorption- and catalysis-based applications. [22] For example, Zr-based MOF UiO-66 [23] which is well known for its robust yet defect-rich structure [24-25] was reported to show an exceptional CO_2 adsorption via modulation of missing linker defects. [26] An isostructural UiO-67 with biphenyl linkers also exhibited improved catalytic performances when defects were introduced to the framework. [27-28] These studies indicate that the defect engineering in the MOF materials can play a key role on the materials’ properties, possibly by either changing the characteristics of the pore structures of the framework or controlling the pore accessibility. Engineering chemical functionality into MOFs is a promising approach to finely tune host-guest interactions in the MOF pores. [3, 29] For instance, flexible gate-opening phenomena (i.e. transition between a closed and open structure) with improved framework stability towards external stimuli was reported, giving rise to a development of future smart materials for nanotechnology applications. [3, 14-19, 21, 30]

While several reports on the responsive adsorption properties of MOFs with non or less polar guests such as hydrogen (H_2), carbon dioxide (CO_2), and hydrocarbon have been

published, [9-11, 30-32] such adsorption studies in MOFs with more polar molecules such as water, alcohols, and NH_3, in which both host-guest and guest-guest interactions could play an important role on their sorption properties are rather scarce. [12, 17, 33-34] In addition, in-depth study on stimuli-induced structural responses of MOFs together with their sorption mechanisms at a molecular level is still in an early stage.

Recently, it is exciting to see that the combined used of advanced experimental techniques such as synchrotron powder x-ray diffraction (SXRD), single crystal diffraction, neutron powder diffraction (NPD), inelastic neutron scattering (INS), and quasielastic neutron scattering (QENS) in conjunction with theoretical calculations such as density functional theory (DFT) and molecular dynamics (MD) have made significant achievements in characterising guest-loaded MOF materials and their sorption mechanisms from both crystallographic and dynamic standpoints. [6, 35-36] These microscopic methods shed light on guest-induced structural and dynamic features of the MOF-guest systems such as preferable binding sites, nature of binding interactions, and diffusional motions of guests inside the frameworks. Therefore, a comprehensive understanding of the structural and dynamic properties of MOFs with guest molecules as external stimuli along with their sorption mechanisms will provide key insight into the design of future smart materials in which stimuli-induced responsive behaviours are precisely controlled.

1.2) Background literature

1.2.1) Definition of MOFs

MOFs [4] and also known as PCPs [5] are an emerging class of crystalline porous materials forming 1-, 2- or 3D extended networks. They are constructed by the

coordinative linkage between metal cations or clusters and organic ligands. [5] Their metal clusters are also known as secondary building units (SBUs). Their structural robustness which are able to withstand vigorous perturbation from external stimuli making them outstanding from traditional coordination polymers. One of the most distinctive characteristics of MOFs is their tunable functionalities leading to superior physical and chemical properties over traditional porous materials, such as zeolites, in various applications.

1.2.2) Zr-based MOFs

Zirconium-based MOFs (Zr-based MOFs) have emerged as a new subclass of highly tunable MOF materials that distinguished themselves with outstanding thermal and chemical stability. [23, 37] They are generally constructed from the highly connected Zr-oxo clusters and multitopic carboxylate linkers with a variety of symmetrical and geometrical features.

The first discovery of Zr-based MOFs including UiO-66, UiO-67, and UiO-68 (UiO stands for the University of Oslo) was reported in 2008 by Cavka *et al*. [23], making a remarkable step forward in MOF community. These MOFs exhibit unprecedented stability, especially hydrothermal stability exceeding most reported MOFs. They have a reticular formula of $Zr_6O_4(OH)_4(L)_6$, where *L* refers to *1,4*-benzenedicarboxylate (BDC^{2-}), *4,4′*-biphenyldicarboxylate ($BPDC^{2-}$), and *4,4′*-terphenyldicarboxylate ($TPDC^{2-}$) for UiO-66, UiO-67, and UiO-68, respectively (see Figure 1.2). Their crystallographic structure is created by coordinating each hexanuclear $[Zr_6O_4(OH)_4]^{12+}$ cluster with twelve organic linkers (Figure 1.3). By varying types of organic linkers to connect to the $[Zr_6O_4(OH)_4]^{12+}$ clusters, a large family of Zr-based MOFs featuring diverse geometries and symmetries have been achieved. [38-42]

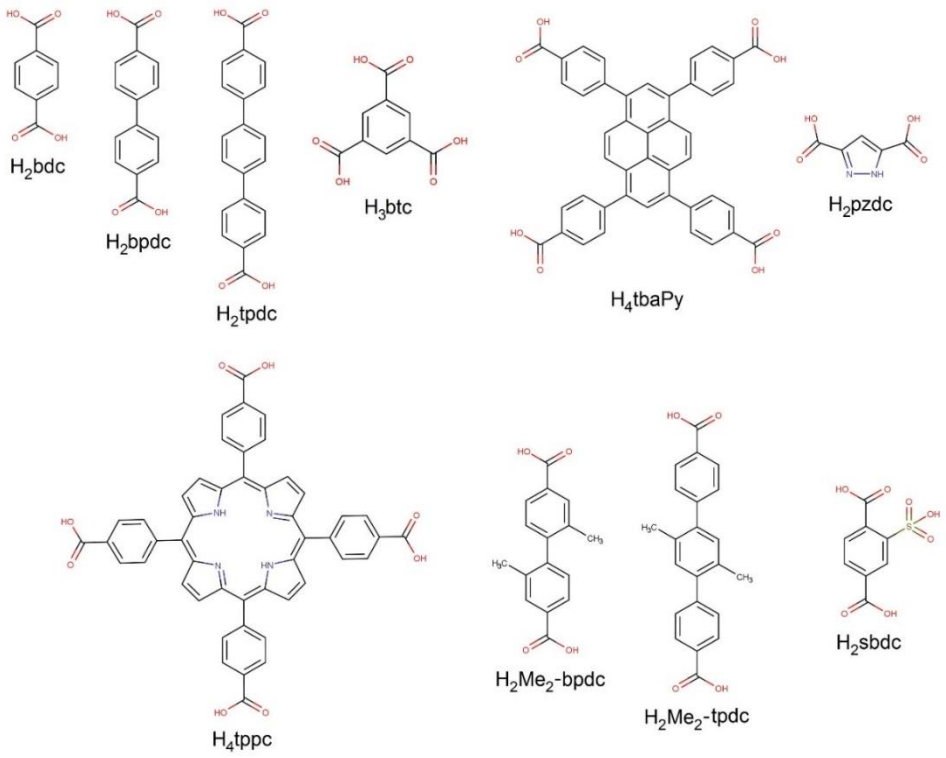

Figure 1.2 | Examples of the organic linkers used to construct Zr-based MOFs. [37]

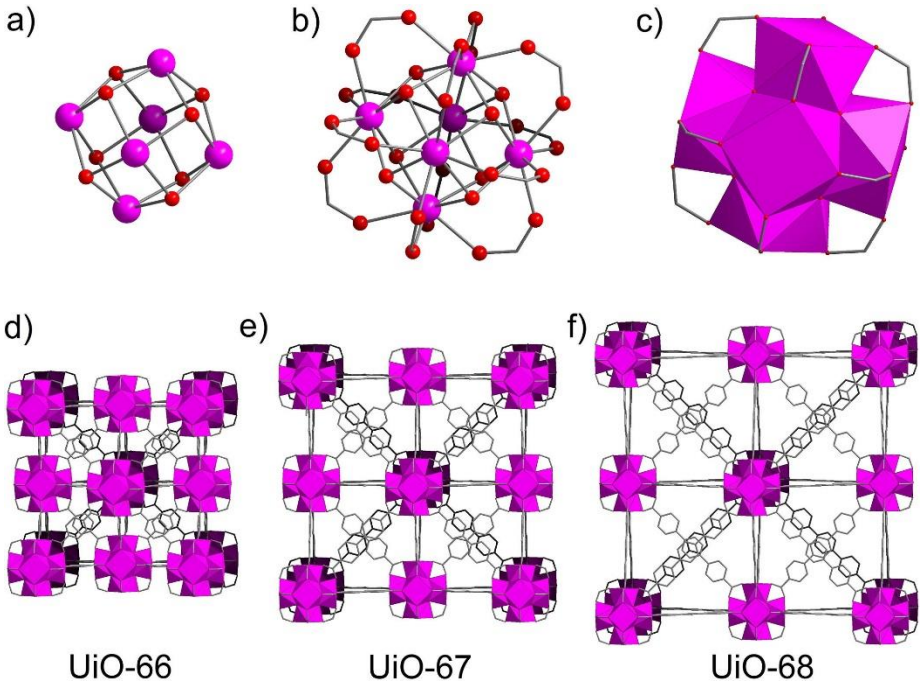

Figure 1.3 | Structural representation of the $[Zr_6O_4(OH)_4]^{12+}$ cluster (**a**), the $Zr_6O_4(OH)_4(COO)_{12}$ secondary building unit (SBU) (**b**) and its corresponding SBU with a

polyhedral model (**c**). Crystal structures of UiO-66 (**d**), UiO-67 (**e**) and UiO-68 (**f**) based on the coordinative linkage of $[Zr_6O_4(OH)_4]^{12+}$ clusters and BDC^{2-}, $BPDC^{2-}$ and $TPDC^{2-}$ linkers, respectively. Colour code: ZrO_8 polyhedra, pink; O, red; C, grey. H atoms are omitted for clarity.

1.2.3) Defect engineering in MOFs

Defect engineering in MOFs has attracted tremendous research attention in tuning their properties to specific functions and applications. Apart from attempts to manipulate their periodic bulk structure, tailoring defects in MOFs has offers exciting opportunities for modulating their porosity, catalytic active sites, electronic structures and surface properties, which are particular importance for separation, storage, catalysis, charge transport and stimuli responses. [22, 43-46]

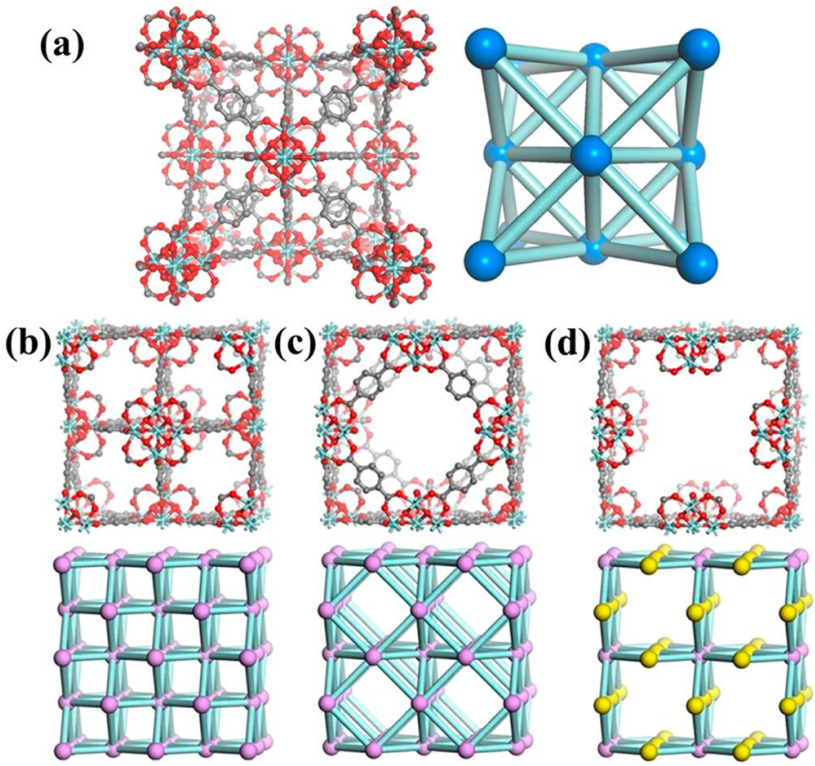

Figure 1.4 | Crystallographic models and corresponding topological representatives of perfect UiO-66 structure (**a**), UiO-66 with missing linker defects (**b**), UiO-66 with missing

cluster defects (**c**) and UiO- 66 with both missing linker and cluster defects (**d**). Reprinted with permission from ref [46].

Zr-based MOFs, especially UiO-66 type, is one of the most commonly studied MOFs owing to its high thermal and chemical stability [23] with remarkable catalytic performance strongly associated to the presence of defects [22, 45-46]. As mentioned in Section 1.2.2, UiO-66 is a prototype of UiO family with a reticular formula of $Zr_6O_4(OH)_4(BDC)_6$, where BDC refers to benzene-*1,4*-dicarboxylate. [23] Six coordinated Zr atoms are located at the vertices of octahedron with four μ_3-OH and four μ_3-O alternatively capping the eight faces to form the $Zr_6O_4(OH)_4$ cluster/node and each cluster is connected to twelve BDC linkers (12-connected nodes; fcu net) as shown in Figure 1.4a. [46] As a result of its high degree of linker connectivity, UiO-66 exhibits higher tolerance to linker missing than other MOFs. [26] The numbers of missing linkers can be as high as to 4.3 per Zr_6 cluster without causing collapse of the framework structures. [47] This feature makes Zr-based MOFs unique among MOF materials and is generating additional interest around them.

Two types of defects have been discovered in the Zr-based MOFs: missing linker defects and missing cluster defects which refer to the absence of a number of linkers and metal nodes from the perfect crystallographic structures, respectively (Figures 1.4b-1.4d). For the missing linker defects, assuming that one negatively charged BDC^{2-} linker is removed from each Zr_6 node, it will create two defect centres with four coordinatively unsaturated Zr sites.[26, 45, 48] These missing linker defects can be manipulated during or after synthesis by allowing less BDC linker to form a coordination bond to Zr_6 nodes or removing/exchanging some BDC linkers that are already attached to Zr_6 nodes. [24, 26, 48-52] In the case of missing cluster defects firstly reported by Cliffe *et al*. [25], the Zr_6 cluster

is entirely removed from the framework creating the *reo* and *scu* topologies as displayed in Figures 1.4c and 1.4d, respectively. [46]

Table 1.1 | Examples of the proposed terminating species in defective Zr-based MOFs prepared by adding various modulators during the synthesis.

Zr-based MOF	Modulator	Terminating species	Reference
UiO-66	HCl	OH^-/H_2O	[53]
UiO-66	AA	AA	[26]
UiO-66	TFA + HCl	TFA	[54]
UiO-66	HCl	Cl^-	[49]
UiO-66	HF	F^-	[55]
UiO-66	HCl; FA	Cl^-; FA	[56]
UiO-66	BA	BA	[57]
UiO-66/UiO-67	FA; AA; BA; TFA	FA; AA; DFA; TFA	[27]
UiO-66/UiO-67	HCl	OH^-/H_2O	[58]
MOF-808	FA	FA	[40]
NU-1000	BA	BA	[39]
DUT-51	BA	BA	[42]
DUT-53	AA	AA	[59]
DUT-84	AA	AA	[59]

There have been many methods to engineer defects in Zr-MOFs including adjusting the synthesis conditions (temperature, Zr/linker ratio and choice of Zr precursor), addition of modulators during synthesis, thermal activation/dehydration, linker modification and metal cation substitution. [52] Among them, incorporation of modulators has offered a precise control of defect density based on type of the modulator used and its concentration. [24, 26-27] The so called “Modulators” are defined as chemical species added during the synthesis of MOFs to compete with organic linkers to form coordination bond with Zr_6

clusters. [38] Examples of modulators having been reported are monocarboxylic acids, e.g. formic acid (FA), acetic acid (AA), difluoroacetic acid (DFA), trifluoroacetic acid (TFA), and benzoic acid(BA) and other acids such as hydrochloric acid (HCl) and hydrofluoric acid (HF). Similar to the organic linker, these modulators can act as terminal ligands to coordinate to Zr_6 clusters, and hence causing missing linker defects. Table 1.1 provides an overview of terminating species proposed on a basis of synthesis conditions and experimental observations. A promising study on using the modulator to finely tune degree of missing linker defects in UiO-66 was reported by Wu and co-workers. [26] The researchers employed acetic acid as the modulator and varied its concentrations during the synthesis and observed that the pore volume of the prepared frameworks was strongly dependent on the quantity of acetic acids used. The presence of missing linker defects and the possibility of acetate as the terminating species were also confirmed by using high-resolution neutron diffraction and inelastic neutron scattering, respectively.

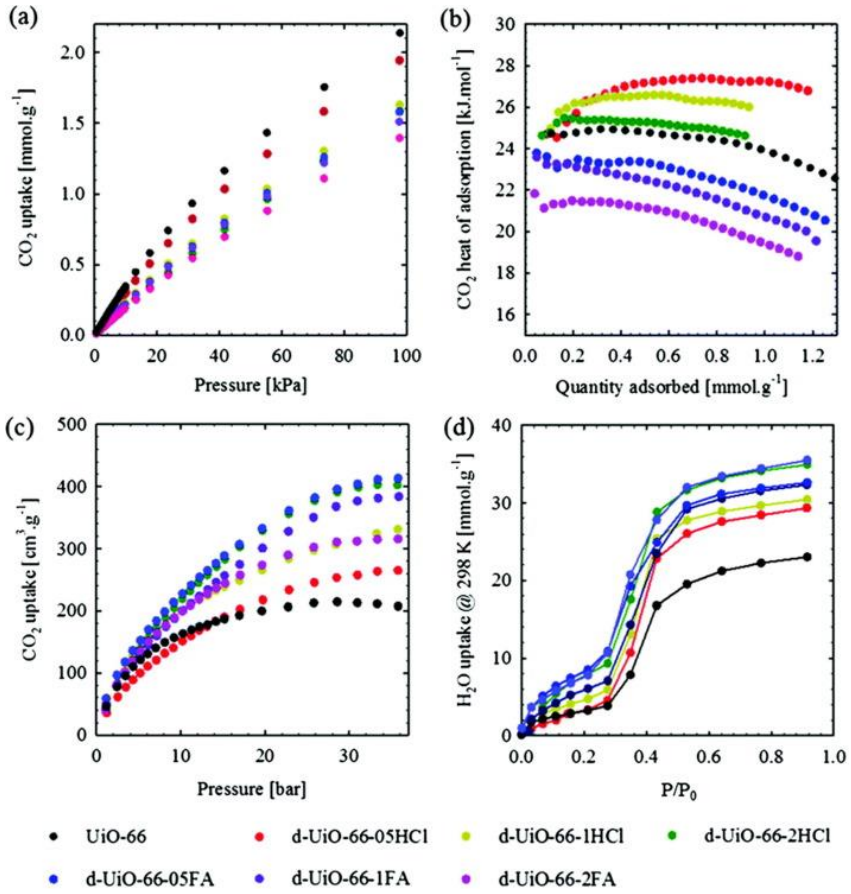

Figure 1.5 | CO_2 adsorption isotherms measured at 298 K up to 1 bar (**a**), isosteric heat of CO_2 adsorption (**b**), CO_2 adsorption isotherms measured at 298 K up to 35 bar (**c**) and water adsorption isotherms measured at 298 K (**d**) for defect-free UiO-66 (black), UiO-66 synthesised with addition of 0.5 mL (red), 1 mL (yellow) and 2 mL of HCl (green), UiO-66 synthesised with addition of 0.5 mL (blue), 1 mL (violet) and 2 mL of FA (purple). Reprinted with permission from ref [56].

The most prominent outcome arising from incorporation of defects in Zr-based MOFs is an increase in their pore volume and surface area. This result offers great opportunities to enhance adsorption ability in MOFs as higher amounts of gas molecules can occupy the pores. [26] In addition, defects can significantly affect a chemical environment inside the framework, and hence changing adsorption behaviours of the MOFs upon the guest inclusion. Liang and co-workers [56] demonstrated that defect engineering by using

HCl and FA as modulators could systematically control the CO_2 and H_2O adsorption behaviours of UiO-66. The uptake of CO_2 decreased as a function of defect density, indicating the weaker CO_2 affinity in the larger pore created by defects (Figure 1.5a). The CO_2 isosteric heats of adsorption (Qst), in turn, exhibited a different trend as OH > –Cl > perfect > –OOCH (Figure 1.5b). This observation was in excellent agreement with the binding energies of CO_2 adsorbed over the modulator-capped Zr-cluster models studied by DFT calculations. [60] Unlike the CO_2 adsorption, H_2O adsorption increased upon increasing of defect quantities regardless of types of the modulators used (Figure 1.5d), likely due to the removal of hydrophobic BDC linkers from the frameworks.

From the above literature, it is anticipated that defects in Zr-based MOFs can play a significant role on tailoring MOF properties for practical applications, especially gas separation, gas storage, and molecular sensing in which changes of pore size and pore structure are critical. How these defects and their spatial distribution in the MOF frameworks affect their sorption ability is one of the most exciting topics to intensively explore.

1.2.4) Flexibility in MOFs

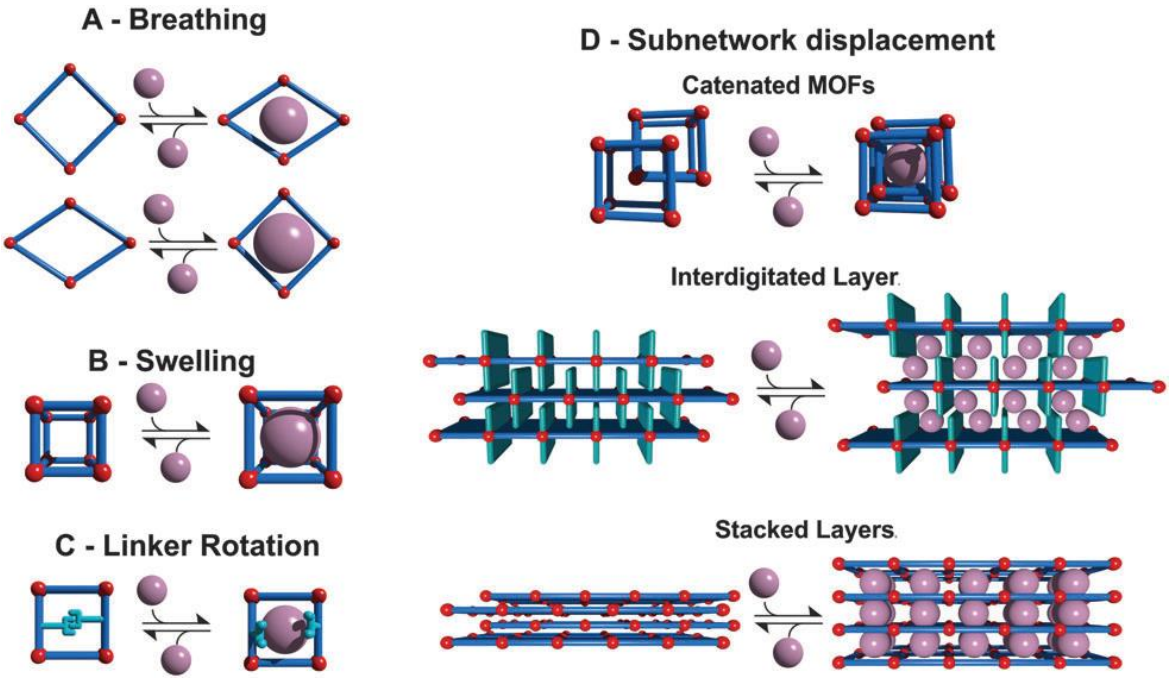

Figure 1.6 | Various types of flexibility in MOFs. One class is characterised by the change in unit cell volume ($\Delta V \neq 0$; A, B and D) while in the other case the unit cell volume does not change ($\Delta V = 0$; C, D), reproduced with permission from Ref [61].

One of the most unique features of MOFs beyond other porous solids, is structural flexibility as a response to external stimuli, such as guest molecules, electromagnetic irradiation, temperature or hydrostatic pressure. [3, 61-63] In general, the term "flexible MOFs" [61] or "soft porous crystals" (SPCs) [62] means a material can alter its form easily according to the situation without breaking. One widely accepted and up-to-date classification of flexibility in MOFs was presented by Bousquet *et al.* and Coudert *et al.* (Figure 1.6). [61, 64-65] There are four main types of flexibility: breathing, swelling, linker rotation, and subnetwork displacement. Breathing, swelling and subnetwork displacement generally undergo change in unit cell volume ($\Delta V \neq 0$), while such change in linker rotation is negligible and the crystal system remains unchanged during the structural

transformation. Framework flexibility or responsivity is usually triggered by external stimuli such as guest molecules, temperature, mechanical stress, light, etc. But sometimes it can take place without any external triggers or sorption involved.

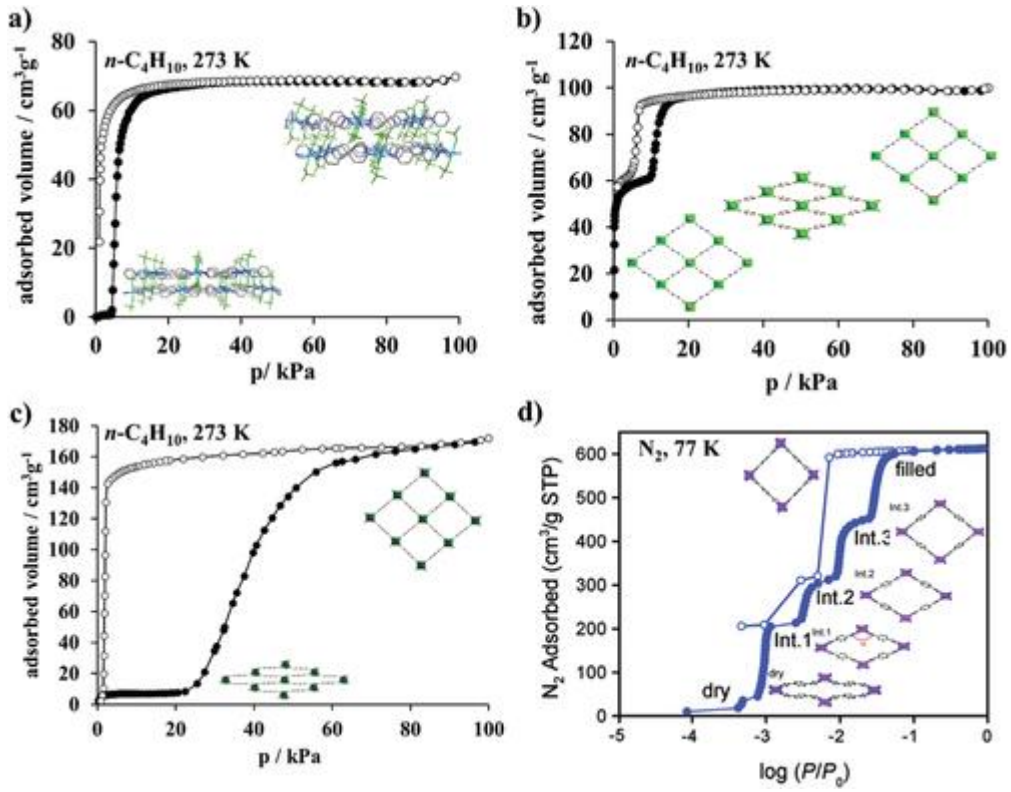

Figure 1.7 | Typical examples of "gate pressure" and "breathing" MOFs: **a**) physisorption of *n*-butane on ELM-11 at 273 K; **b**) physisorption of *n*-butane on MIL-53(Al) at 273 K; **c**) physisorption of *n*-butane on DUT-8(Ni) at 273 K; **d**) physisorption of nitrogen on Co(bdp) at 77 K (insets show structural evolution upon adsorption). **d**) Reproduced from ref [66].

Since MOFs was first discovered in the late 1990s, two research groups were independently reported MOFs exhibiting unusual hystereses in physisorption isotherms dissimilar to capillary condensation typically occurring in mesoporous solids. Li and Kaneko synthesised Cu-based coordination polymer with a composition of $Cu(bpy)_2(BF_4)_2$ (bpy: *4,4′*-bipyridine) and also known as ELM-11(ELM states for elastic layer material). [67] It was found that physisorption isotherms of ELM-11 in nitrogen (N_2, 77 K), argon (Ar,

87 K), and carbon dioxide (CO_2, 273 K) displayed "gate pressure" hysteresis. At the same time, Kitagawa and co-workers also reported similar phenomena in methanol sorption profiles of Cu(II)-based coordination polymer ($Cu_2(pzdc)_2(dpyg)$, where pzdc: pyrazine-2,3-dicarboxylate; dpyg: 1,2-di(4-pyridyl)-glycol). [68] Later, reversible contraction, further denotes as "breathing" was observed in CO_2 and H_2O adsorption of a 3D MOF framework, called MIL-53(Cr). [69] Physisorption isotherms and their associated phase transitions in MOFs MIL-53(Al), Co(bdp), ELM-11, and Dresden University of Technology (DUT)-8(Ni) are illustrated in Figure 1.7.

The flexibility in MOFs mentioned above, however, undergo breathing process which results in large volume change undesirable for the practical use of these materials, especially in sorption-based applications. [18] This volume expansion and contraction in the adsorbent solid may damage the storage tank, decompose the moldings, and also may result in slower diffusion of gases in the tank. As a consequence, design of new porous 'rigid' materials that can show guest adsorption and desorption with specific interaction(s) without significant volume change is highly desirable and technologically important. Recalling various types of MOF flexibility in Figure 1.6, it is obvious to see that the local flexibility generated by linker rotation could be the most promising choice to develop the responsive yet rigid materials.

1.2.5) Rotational dynamics in MOFs with flexible linkers

Design of novel MOF materials possessing flexibility while maintaining their pore volume is essentially attractive for their practical applications. To achieve this goal, molecular dynamics in MOFs caused by linker motions should be taken into account. These unique features largely depend on the nature of the organic linkers used to construct the

frameworks. Specifically, the organic linkers containing mobile fragments can create dynamic motions in their respective MOF framework via rotation or libration under particular conditions. Although the whole porous structure remains unchanged, the linker dynamics have a dramatic effect on controlling physical and chemical properties of the frameworks. [70] Thus, understanding and control of the dynamic phenomena in flexible MOFs is essential for development of future materials with desired dynamic properties.

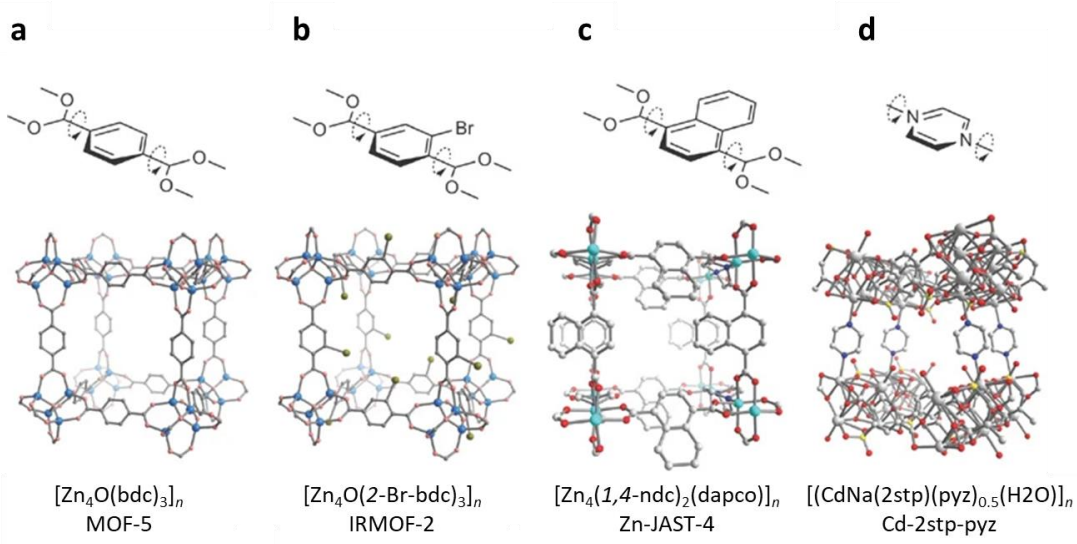

Figure 1.8 | a-d, Illustrations of mobile groups and partial crystal structures of several compounds, reproduced with permission from the work of Horike *et al*. [62]

Table 1.2 | Details of activation energy, frequency, temperature, and mode of rotational motion for the four compounds shown in Figure 1.8 and other reported MOFs.

	Activation energy (kcal mol^{-1})	**Frequency (MHz)**	**Temperature (K)**	**Rotational mode**
MOF-5 [68, 71]	11.3 ± 2, 14–16	0.001	300	π flip
IRMOF-2 [70]	7.3	-	-	-
Zn-JAST-4 [72]	12.7	50	223	4 sites flip

	Activation energy (kcal mol^{-1})	**Frequency (MHz)**	**Temperature (K)**	**Rotational mode**
Cd-2stp-pyz [72]	1.8	0.1	293	4 sites flip
MIL-53(Cr) [73]	41	1.26×10^5	333–453	π flip
MIL-53(Al) [74]	37 ± 1	0.6×10^4	359–492	π flip
UiO-66(Zr) [75]	30 ± 2	$0.5 \pm 0.8 \times 10^6$	213–403	π flip
DMOF [76]	32–36	$0.3–10 \times 10^5$	253–359	π flip
MFM-180 [77]	26, 28	1.6×10^5, 3×10^1	223–503	4-site flip
CdNa(2-stp)(pyz)$_{0.5}$(H_2O) [70]	7.7	2.40×10^0	193–293	4-site flip
Zn_2(1,4-ndc)$_2$(DABCO) [78]	53	-	193–293	4-site flip
UTSA-76 [79]	8.2	-	-	π flip

Examples of framework structures having dynamic linkers and corresponding activation energies are presented in Figure 1.8 and Table 1.2, respectively. For example, *2*-bromo-*1,4*-benzenedicarboxylate rings in the linker of IRMOF-2 can rotate freely in the square-grid porous lattice largely due to the well-ordered orientation of these molecular rotors in the framework (Figure 1.8b). [70] The estimated rotational energy barrier of 7.3 kcal mol^{-1} can be associated to the dipole moment of the rotating group. Using bulkier rotational group in Zn-JAST-4 led to a higher rotational energy barrier of 12.7 kcal mol^{-1} (Figure 1.8c). [72] Similar to MOFs with aromatic linkers, the dynamic behaviour from alkyl groups in the framework can also take place. For example, Cu-based PCP (MAF-2) consisting of pendent ethyl groups in the linkers underwent thermal linker flipping allowing effective pore opening for gas adsorption. [80]

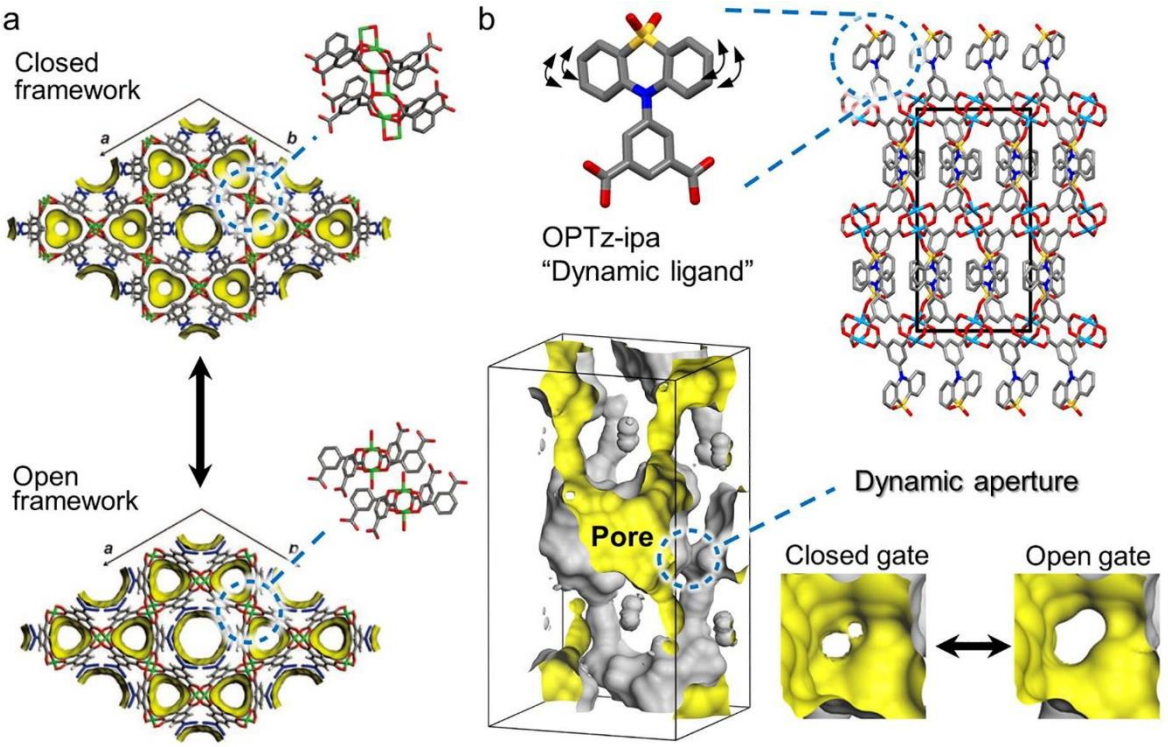

Figure 1.9 | Examples of novel guest-induced responsive behaviours of flexible PCPs. (**a**) Self-accelerating CO transport caused by the global structural change from closed to open framework, reprinted with permission from Sato *et al.* [81] (**b**) Diffusion-regulatory gate functionality due to the dynamic pore window, reprinted with permission from Gu *et al.* [14]

In some cases, although the lattice parameter of MOFs and PCPs is not affected by the linker dynamic motions, the pore structure does change significantly. For example, a Cu-based PCP with a *5*-azidoisophthalate linker was reported to show a self-accelerating adsorption process allowing excellent selective adsorption of carbon monoxide (CO) over N_2 (Figure 1.9a). [81] This unprecedented adsorption feature was induced by weak interactions between CO molecules and the Cu^{2+} sites in the framework causing a global structural change that consequently creates extra space for further uptake of CO. [81] Recently, Gu *et al*. designed a thermally responsive Cu-based PCP with a butterfly-type linker phenothiazine-*5,5*-dioxide (OPTZ) (Figure 1.9b). [14] This linker is located at the

channel wall that intercepts the guest diffusion path. A significant enlargement of the pore window diameter arising from thermal flipping of the OPTZ unit facilitates the adsorption of gas molecules at high temperatures but impedes them at low temperatures. By finely controlling the gas adsorption temperature, high separations of O_2/Ar and C_2H_4/C_2H_6 can be attained.

1.2.6) Relationship of guest-induced structural dynamics and adsorption properties

It is commonly known that adsorption behaviour is dominated by solid-fluid and fluid-fluid interactions. These interactions indeed depend on both the surface functionalities and pore structures of the host and types of the guest molecules. [3] Information on the pore properties such as specific surface area (SSA), pore size distribution (PSD), and pore geometry, can be achieved experimentally by characterisation of adsorption isotherms. To date, the adsorption isotherms defined by IUPAC are categorised into eight types based on specific host-guest interactions between the adsorbent and the adsorbate species. [82] Standard methods for assessment of SSA and PSD such as the Brunauer-Emmett-Teller (BET) and the Barrett-Joyner-Halenda (BJH) theories, respectively, assume a rigid adsorbent without guest-induced deformation. As a result, applying these methods to the non-rigid adsorbents, especially, flexible MOFs, may be insufficient to link their surface and pore features to the respective adsorption phenomena. The classification of isotherms in flexible MOFs (also known as SPCs) and the more realistic characterisation models are still under development.

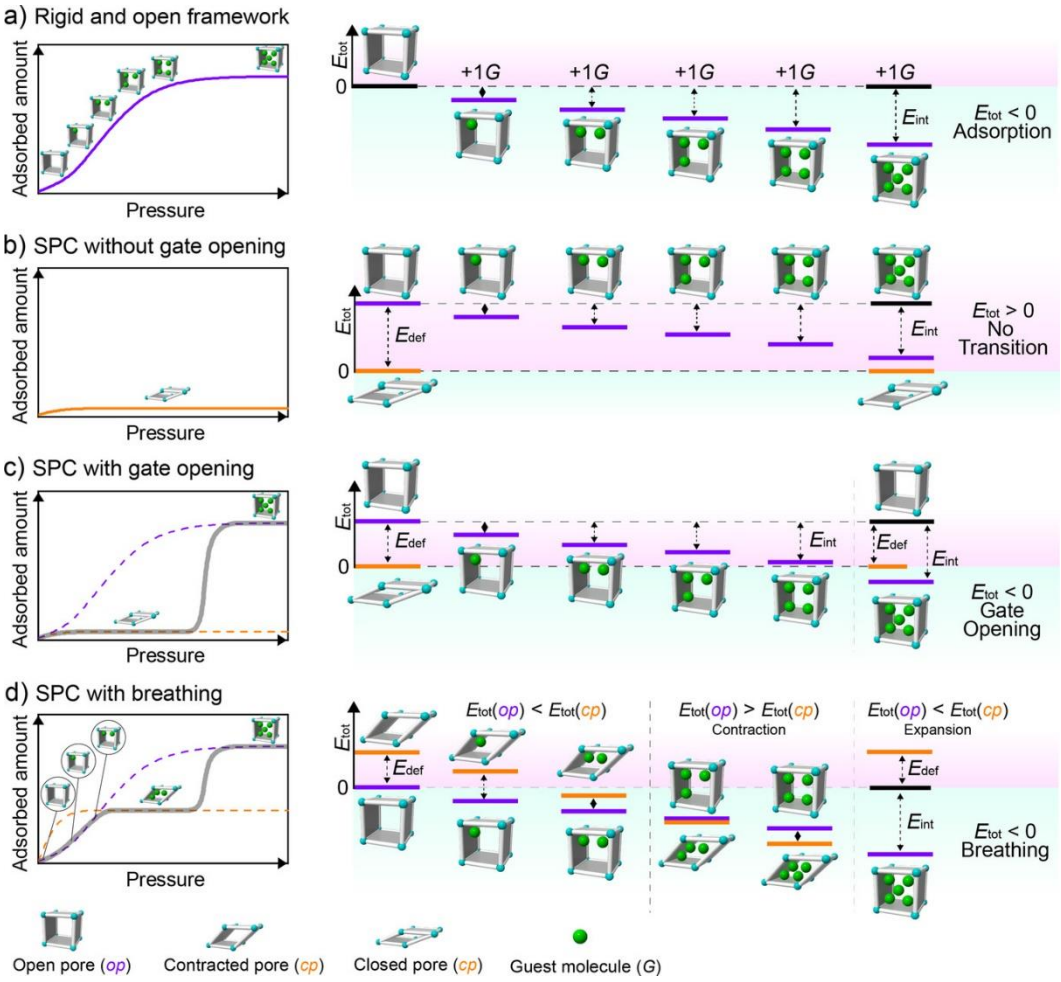

Figure 1.10 | Theoretical gas adsorption isotherms (left) and schematic evolution of energetic contributions and cartoons of structures (right) of **a**) rigid and open framework, **b**) a SPC in closed pore state that does not undergo adsorption-induced expansion, **c**) a SPC that undergoes expansion upon adsorption, and **d**) a SPC that undergoes successive contraction and expansion upon adsorption (breathing). Observable isotherms given as gray solid lines, reference isotherms of open pore (*op*), closed pore (*cp*), and contracted pore (*cp*) phases are shown as dashed lines. Increases in pressure and guest loading in adsorption isotherms are indicated with arrows; observable long-lived states are indicated as insets. Recreated with permission from Ref [3].

Based on types of guest-induced structural transitions classified by Krause *et al* [3], expansion (E-type) and contraction (C-type) isotherms are considered as fundamental adsorption behaviours for flexible MOFs or SPCs. Figure 1.10 illustrates the correlation between guest-responsive adsorption isotherms and energy diagrams for four different systems: a) a rigid and open-pore framework, b) a non-gate-opening SPC, c) a gate-opening SPC, and d) a breathing SPC. To undergo gate-opening (*go*) transition leading to an E-type isotherm, a deformation energy (E_{def}) of the SPC host, defined as the energy difference between *cp* and *op* structures without guest molecules and guest–guest and host–guest interactions, is required to switch the SPC structure from a closed pore (*cp*) to an open pore (*op*) form. Unless an interaction energy (E_{int}), representing the guest–host and guest–guest interactions, is larger than E_{def}, no phase transition occurs and the SPC possesses adsorption isotherm related to the *cp* form (Figure 1.10b). When the E_{int} exceed E_{def}, then a total energy (E_{tot}) of the system becomes negative causing a sudden increase in gas uptake with a sigmoidal isotherm (Figure 1.10c). On the other hand, a low pressure region of the SPC having a C-type isotherm is governed by the adsorption featuring the *op* phase (Figure 1.10d). This type of SPC undergoes structural contraction at intermediate pressures where $E_{int}(cp) - E_{int}(op) > E_{def}$ which are close to the intersection between the *op* and the *cp* isotherms. At this adsorption stage, the isotherm of the *cp* phase generally becomes a plateau as a result of the highly occupied pore. Upon an increasing pressure, a *cp*-*op* structural transformation can occur when a sum of E_{def} and $E_{int}(op)$ is less than $E_{int}(cp)$. This energy landscape analysis was adopted to investigate the role of the E_{def} on regulating guest-induced adsorption behaviours in a typical interpenetrated PCP, $[Zn_2(bdc)_2(bipy)]$ where bdc and bipy refer to *1,4*-benzenedicarbozylate and *4,4'*-bipyridine, respectively. [83] The results revealed that structural transformation of such flexible PCP from guest-free contracted phase

to guest-loaded open phase was achieved by systematic modulation of the E_{def} which strongly links to inter-framework interactions.

While the above guest-responsive behaviours of flexible MOFs generally undergo phase transitions propagating through the lattice of the materials, local dynamics in rigid frameworks can serve as another type of flexibility that can modulate the adsorption transitions without large change in pore volume as previously discussed in Section 1.2.5. For example, pyrazine, para-substituted phenylenes, and substituted naphthalenes-based linkers in MOFs showed remarkable thermally-induced rotation which can manipulate the dynamic pore accessibility and hence altering the adsorption properties toward guest molecules. [2] This strongly benefits the use of these materials in sorption-related applications where achieving dynamic behaviours without having major volume change is preferable. Thus, understanding how the linker dynamics influence guest diffusion and adsorption and *vice versa* is of increasing attraction.

One of the most well-known adsorption phenomena attributed to the interactions between a flexible linker and the guest molecules is the so-called "gate-opening effect". Such effect often occurs in the form of an inflection point, a step, or hysteresis in an adsorption isotherm, as a result of a structural transformation with a change in rotational dynamics of the linkers. [84] For instance, ZIF-8 containing a rotating imidazolate linker, was able to adsorb molecules seemingly larger than its pore window based on crystallographic data. This is arisen from the guest-induced librational motion of the imidazolate leading to enlargement of the pore opening and thus allowing the diffusion of large adsorbates through the pore. [85-87]

Another type of responsive adsorption transitions in flexible linker-incorporated MOFs can happen through the host-guest interactions in such a way that the conformation of the dynamic linker affords a better packing of the guest molecules or a more favourable adsorbate/adsorbent binding contacts. [18, 85, 88-89] This effect is particularly more pronounced in the case of small adsorbates at low temperature where their kinetic energy is suppressed. For example, ZIF-8 exhibits stepped gas adsorption for N_2, Ar, O_2 and CO at low temperature. This stepwise transition occurred when a more favourable packing arrangement of the adsorbates become possible at a particular conformation of the linkers and found to be governed by the polarizability and molecular size and shape of the guest molecules. [85, 88]

Based on these findings, it strikes the fact that linker dynamics can potentially modulate the guest-responsive properties of the MOFs which lead to interesting adsorption phenomena, depending on the specific interplay between the MOF porosity, flexibility, and the guest molecules.

1.2.7) Advanced methods for studying structural and dynamic behaviours in MOFs

Neutron powder diffraction (NPD) has made an excellent impact on elucidating structural properties of MOFs and preferred locations of guest molecules within the MOF cavities. [6, 36] Unlike commonly used x-ray and electron diffraction, the NPD can detect light elements and even distinguish isotopes of each element as a result of neutron scattering lengths and cross-sections randomly distributed over a periodic table. [90] For example, the coherent neutron scattering lengths of hydrogen (^{1}H) and deuterium (^{2}H or D) are −3.74 and

6.67 fm, respectively (see Table 2.1 in Chapter 2 for further details). [90] This unique feature makes the NPD very suitable for studying the light element-rich MOF-guest system. In addition, neutron spectroscopy including inelastic neutron scattering (INS) and quasielastic neutron scattering (QENS) is one of the most powerful methods to study dynamics of MOF-guest system in both molecular motion and diffusion aspects at a microscopic view. Compared to widely used infrared (IR) and Raman spectroscopic methods, the unique strengths of INS and QENS are the lack of selection rules, the excellent sensitivity to light elements, especially to hydrogen, and the ability to examine the full Brillouin zone. Details of the basic theories of such cutting-edge neutron techniques are given in Chapter 2. A comprehensive review of using these sophisticated techniques to analyse guest and substrate binding in MOFs was well written by Easun *et al*. [6] On the other hand, modern computational calculation including density functional theory (DFT) and molecular dynamics (MD) have become an invaluable tool to support and verify experimental observations. [35] A combination of these experimental and computational methods enables a thorough understanding of the guest–host responsive behaviours occurring in MOF frameworks. Thus, this section will primarily focus on recent studies involving using neutron diffraction and spectroscopy in conjunction with theoretical calculation for analysis of structural and dynamical responses of MOFs toward external stimuli, which initiate the motivation of this thesis.

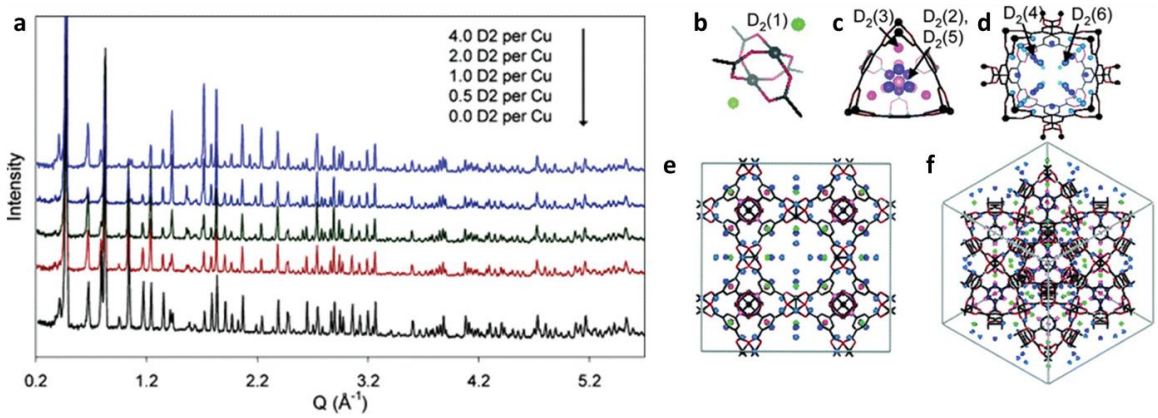

Figure 1.11 | *In situ* NPD patterns of HKUST-1 upon D_2 loading collected at 5 K (**a**) and the corresponding refined structures: D_2 sites in $Cu_3(BTC)_2$ at axial Cu site (**b**); view along [111] in the 5 Å small pore with 3.5 Å side windows (**c**); and view along [100] showing the 9 Å pore (**d**); D_2 in $Cu_3(BTC)_2$ shown along the [001] (**e**) and [111] (**f**) directions. Reproduced with permission from ref [91].

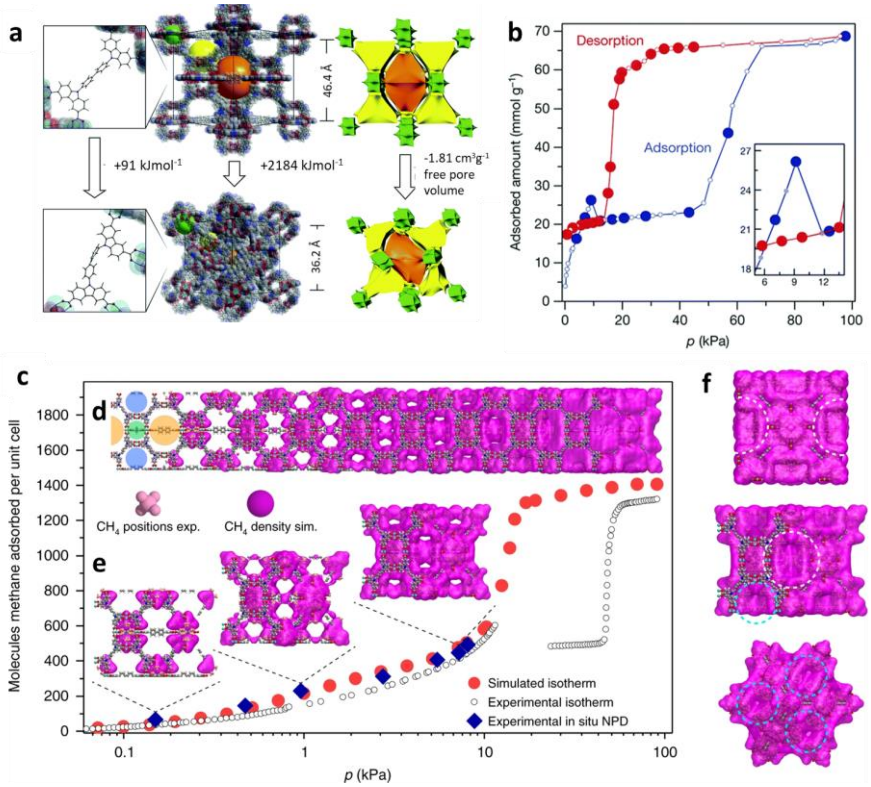

Figure 1.12 | (**a**) Illustration of the structural changes from the DUT-49*op* to DUT-49*cp* phase. (**b**) Methane (CH_4) adsorption and desorption isotherms at 111 K. **c**) Simulated (red

circles) and experimental (open symbols) CH_4 adsorption isotherm of DUT-49 at 111 K including points at which NPD patterns were recorded (blue diamonds). **d**) Structure of DUT-49 with increasing population of pores with CH_4 upon pressure increase, including on the left trimodal pore system: octahedral (oct, orange), tetrahedral (tet, blue), cuboctahedral (cub, green). Experimentally refined CH_4 positions in light pink, simulated CH_4 density in pink. **e**) Visualization of DUT-49 unit cell at selected loadings which correspond to experimentally investigated pressure. **f**) Illustration of CH_4-filled pores of DUT-49 unit cell in the region of negative thermal adsorption (NGA) viewed along (100) direction (top), (110) direction (middle), and (111) direction (bottom). Reproduced with permission from ref [10, 21]

In 2006, Peterson *et al*. were a pioneer group who employed *in situ* NPD to study the adsorption structures of a paddlewheel HKUST-1 ($Cu_3(BTC)_2$, where BTC= 1,3,5-benzenetricarboxylate) as a function of deuterium (D_2) dosing. [91] The obtained NPD patterns of HKUST-1 with different D_2 loadings are displayed in Figure 1.11. After analysing the NPD data by Rietveld refinement, nine crystallographically independent binding sites of D_2 were observed and the primary sites were located at the coordinatively unsaturated Cu(II) node. The D_2 adsorption inside this paddlewheel framework associated to a complex pore filling mechanism originated from the optimisation between D_2-D_2 and D_2-host interactions. Since then, similar methodology with and without the aid of computational modelling was rapidly extended to unveil the relationship of the structural features and the respective adsorption mechanism in other MOF-guest systems. [92-95] Recently, Krause *et al*. performed *in situ* NPD experiments in conjunction with grand canonical Monte Carlo (GCMC) simulations to analyse structural details of the mesoporous DUT-49 and its isostructural derivatives upon methane (CH_4) uptake. [21] They observed a

counterintuitive phenomenon, called "negative gas adsorption" (NGA) which was proposed to be due to the pore filling mechanism in these MOFs having trimodal pore structures (Figure 1.12). Indeed, the aforementioned studies emphasise a great impact of using the joint NPD and theoretical modelling to achieve structural details of precise locations of the trapping species in the MOF cavities allowing a clarification of the adsorption mechanism.

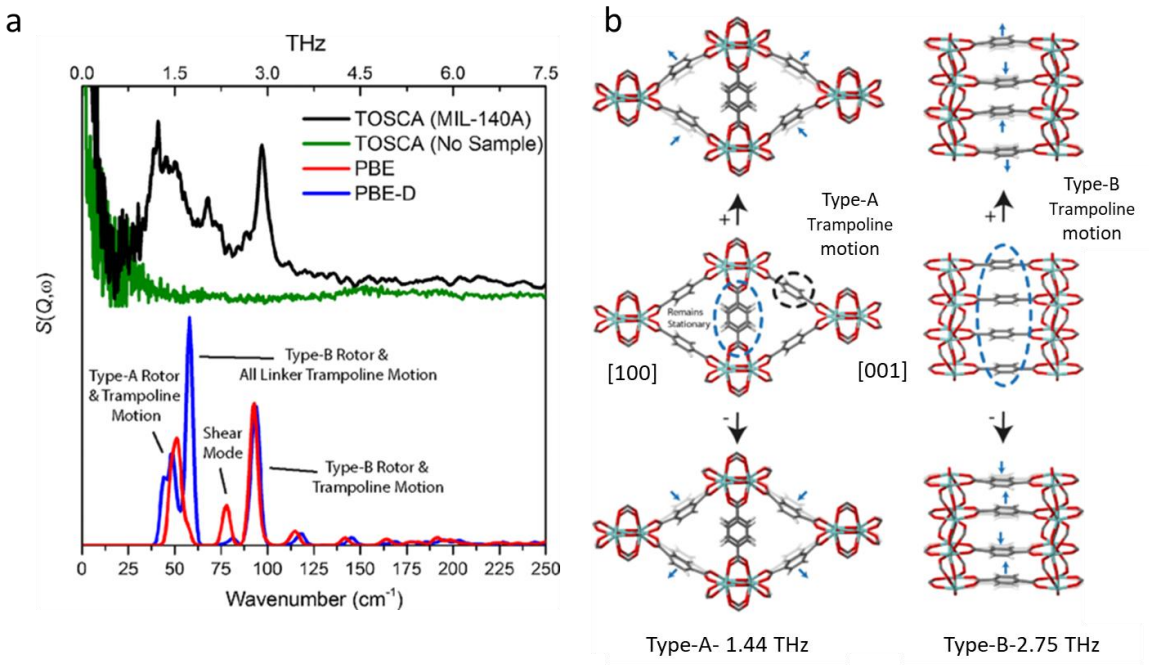

Figure 1.13 | The phonon mode in INS spectra of a Zr-based MOF, MIL-140A (**a**) and the corresponding trampoline-like vibrational motions (**b**). Figures adapted with permission from ref [96].

As previously stated, dynamical observation especially by using spectroscopic techniques is critical to establish the nature of host-guest interactions. In 2006, Zhou and Yildirim first performed INS experiments along with DFT calculations to analyse the lattice dynamics in a well-known MOF-5 ($Zn_4O(bdc)_3$, where bdc= *1,4*-benzenedicarboxylate). [97] With a good agreement between the experimental and theoretical INS spectra, many interesting vibrational modes such as the softest twisting of the organic linkers were

assigned. After that, an unusual quasi-free rotational motion for methyl (CH_3) groups in zeolitic imidazolate framework-8 (ZIF-8, $Zn(MeIM)_2$ where MeIM = *2*-methylimidazolate) by using QENS was discovered by Zhou *et al*. [98] An activation energy for the 3-fold rotation of each CH_3-group estimated by QENS was ~3 meV, suggesting a very low CH_3 rotational barrier of ~7 meV compared to most methylated solid-state compounds. Surprisingly, Fairen-Jimenez and co-workers revealed an unexpected adsorption behaviour in ZIF-8 with gas molecules larger than the pore window of the framework. [16] With a combination of experimental results and molecular simulations, they found that the ZIF-8 exhibited a gate-opening mechanism due to a swing effect of the imidazolate linkers induced by gas inclusion. This work highlighted an existence of structural flexibility in the ZIF-8 framework. Later, Ryder *et al*. observed similar gate-opening phenomena in a series of ZIF materials including ZIF-4 , ZIF-7, and ZIF-8 studied by combined use of INS, synchrotron far-infrared (IR) spectroscopy, and DFT [99] Pore breathing as another type of adsorption mechanisms and shear-induced destabilisation were also reported. Such dynamic behaviours were proposed to correlate to the collective vibrational modes at a low frequency region. The same group also extended their dynamic studies to Cu-based MOF (HKUST-1) [100] and Zr-based MOF (MIL-140A) [96] by using combined INS, synchrotron IR, and DFT. They observed a trampoline-like lattice vibration that linked to an interesting mechanical feature called negative thermal expansion (NTE) [101] (Figure 1.13). They also noted that the low-energy shearing modes found in MIL-140A could be a source of framework destabilisation. [96]

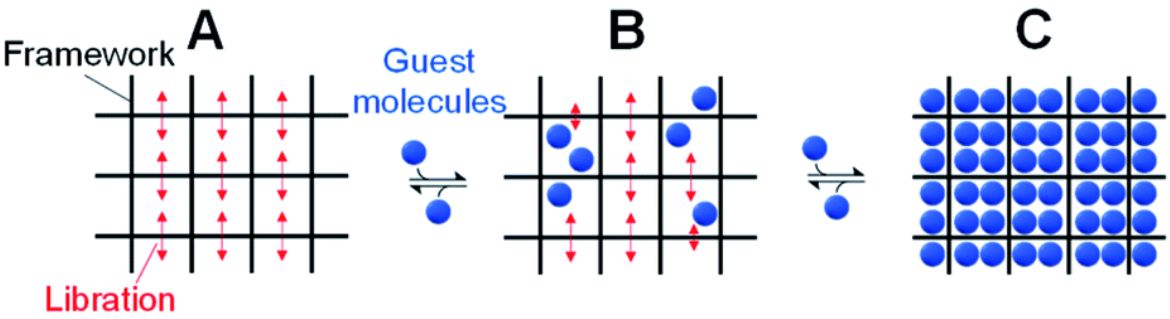

Figure 1.14 | Schematic illustration of the changes of the libration mode upon guest molecule adsorption in a phenylene-based MOF, reproduced with permission from Kusaka *et al*. [102]

The above discoveries encouraged further analysis of dynamical properties of MOFs toward external stimuli such as guest molecules, temperature, and pressure, etc. [9, 103-105] For example, Casco *et al*. performed INS experiments to detect gas-induced adsorption behaviours of ZIF-8 with N_2, Ar, O_2, and CO. [103] It was found that N_2 and CO having strong quadrupole moments were able to induce the linker swinging and the framework expansion of ZIF-8 possibly due to the quadrupole-dipole interaction. On the other hand, those symmetric molecules (Ar and O_2) only caused the framework swelling at relative high pressure without the linker rotation. Besides, Zhao and co-workers demonstrated a sequential pore filling in a non-uniform pore structure of ZIF-7 as an alternative adsorption mechanism by means of synchrotron XRD, QENS, and GCMC simulation. Such a distinct phenomenon could be explained by gas-induced gate opening between individual pores with different geometries. Recently, Kusaka and co-workers proposed the relationship of full-width at half-maximum (FWHM) of the Raman spectrum peaks and the corresponding libration modes of the phenylene-containing MOFs with confined guest molecules (Figure 1.14). [102] Without gas loading, the libration mode of the framework undergoes a uniform harmonic motion (scenario A in Figure 1.14). Once gas molecules start occupying the MOF

pores, the libration mode becomes heterogeneous due to a partial suppression of the linker motion, and hence causing an increased peak broadening (scenario B in Figure 1.14). Eventually, at the full gas dosage, the libration mode is totally inhibited together with an absence of the relevant Raman peak (scenario C in Figure 1.14). This work gives a strong evidence of using the spectroscopic technique to monitor how the rotational motions in flexible MOFs changes as a function of gas adsorption.

1.2.8) Diffusion in MOFs

Diffusive properties are essential functions of MOFs because they are required for most associated applications, such as gas storage, the separation of gases, sensors, and catalysis. In these applications, the interaction of guest molecules in the pores with the framework is crucial. Therefore, it is important to understand and quantify the transport of the guest molecules through their nanoscopic channels. In particular, the selectivity of the guest adsorption/separation is important, and is achieved by the differing transport rates of the chemical species through the pores. One use of such kinetic separations is practiced commercially for the N_2/O_2 separation from air using a pressure-swing adsorption process. [14]

Several techniques are available for the experimental quantification of guest mobility in MOFs and other porous materials, such as quasi-elastic neutron scattering (QENS) [106], pulsed-field gradient nuclear magnetic resonance (PFG-NMR) [107], interference microscopy (IFM), and infrared microscopy (IRM) [108-109]. Among these, QENS has proved to be a very powerful tool to give detailed molecular-level information on the diffusion of various guest molecules deep within nanoporous channels. [35, 110] For example, QENS was employed to investigate the loading effect of small molecules such as

H_2, NH_3, CO_2 and hydrocarbon on the self- and transport diffusivities of many MOFs [9, 106, 111-113] and zeolites [114-116]. Theoretical methodologies, in particular molecular simulations, are also valuable in interpreting QENS experiments and elucidating the diffusion mechanism at the microscopic scale, especially where multiple dynamical processes are coupled. [35, 111-112, 114-119]

In light of the above discoveries, the use of both neutron diffraction and spectroscopy in conjunction with theoretical calculations has shed light on the stimuli-responsive features of MOFs on both structural and dynamical aspects at a molecular level. Diffraction experiments give static crystallographic information, especially specific binding sites of guests confined in the MOF pores. On the other hand, spectroscopic observations provide insights into not only the dynamics of MOFs toward external triggers, but also the diffusive behaviours of the trapped molecules in the host frameworks, hence revealing nature of the host-guest interactions. Computational methodologies including DFT calculations and MD simulations are also the powerful tools to support the experimental data, specifically in terms of visualisation of molecular motions and diffusion in the pores. Overall, these studies explicitly instigate the motivation of this thesis. First, the structural responses of UiO-67-type MOFs toward NH_3 adsorption and temperature will be comprehensively analysed by NPD. Secondly, the loading-dependent dynamical motions of UiO-67-type MOFs in response to NH_3 adsorption will be investigated by using a combination of INS and DFT. Finally, the diffusivity and kinetics of the trapped NH_3 in these UiO-67-type pores will be preliminarily evaluated by QENS and GCMC approaches.

1.3) Aims and objectives

As discussed in the previous section of the introduction, the in-depth study of stimuli-induced responsive behaviours of MOFs along with their sorption mechanisms at a molecular level has been considered as a key area of research beneficial for a design of next-generation smart materials, especially for sorption-based applications such as gas storage, energy storage, controlled drug delivery, and molecular sensing. Therefore, this thesis aims to comprehensively investigate structural and dynamic properties of defect-rich Zr-based MOFs toward NH_3 adsorption and temperature by using state-of-the-art neutron diffraction and spectroscopy combined with theoretical calculations.

The first experimental chapter, Chapter 3, focuses on the study of structural responses of defect-rich Zr-based MOFs upon NH_3 adsorption as a fundamental linkage to their adsorption mechanisms. Defective UiO-67 and its bipyridine-functionalised isostructural UiO-bpydc have been rationally chosen to explore the effects of linker functionality, flexibility, and defects on the NH_3 adsorption profiles. By performing NPD experiments combined with Rietveld refinement and DFT calculations, the correlation between the preferred binding sites of the NH_3 molecules inside the MOF frameworks and their distinct stepwise NH_3 adsorption isotherms have been elucidated at a molecular level.

Chapter 4 also targets the responsive features of the defective UiO-67 and UiO-bpydc upon NH_3 inclusion but at different temperatures. Experimental methodologies similar to Chapter 3 have been applied to determine the NH_3-MOF adsorption structures at cryogenic and room temperatures, whilst DFT calculations have been used to estimate the rotational energy barriers of the studied MOF linkers. It is anticipated that the UiO-bpydc linker will interact with NH_3 molecules more strongly via hydrogen bonding. This host-

guest interaction will make the UiO-bpydc linker more rigid and hence suppressing the linker rotation at the elevated temperature.

Finally, the aim of Chapter 5 is to investigate both the dynamics of the defective UiO-67 and UiO-bpydc upon NH_3 adsorption and the diffusive motions of the trapped NH_3. Advanced neutron scattering experiments in conjunction with theoretical calculations have been carried out. Specifically, the combined use of INS and DFT methods has revealed the characteristic vibrational modes of the host frameworks and the adsorbed NH_3 which are strongly related to their host-guest binding interactions and adsorption behaviours. QENS studies accompanied by GCMC simulations have demonstrated the loading- and functionality-dependent diffusion of the NH_3 confined in the MOF frameworks.

1.4) Structure of the thesis

This thesis is divided into six chapters. In addition to a general introduction and literature review presented in this chapter, different components of my study on the structural and dynamic properties of Zr-based MOFs are given in the following chapters:

Chapter 2 is dedicated to the theoretical background of the major instrumental techniques used in this thesis and experimental procedures used for sample preparation and characterisation. Specific data analyses and collaborative computational calculations used throughout the thesis are also discussed.

Chapter 3 reveals the structural responses of defective UiO-67 and its derivatives upon the inclusion of NH_3 by using high-resolution *in situ* NPD in conjunction with Rietveld refinement and DFT calculations. The result demonstrates that different pore openings (windows) induced by missing linkers can introduce stepped and hysteresis NH_3 sorption in

UiO-type MOFs. H-bonding networks can be formed between the bipyridine linker in UiO-bpydc and the adsorbed NH_3, offering a steric hindrance to modify the NH_3 adsorption behaviour, disorder, and structural flexibility of the framework without large structural or pore volume change. This result highlights the importance of host-guest interactions on controlling the responsive behaviours of the MOFs with the trapped NH_3 molecules as external triggers.

Chapter 4 extends the use of *in situ* NPD, Rietveld refinement, and DFT calculations to elucidate the thermal-induced linker flipping of defected UiO-67 and UiO-bpydc with and without ND_3 loading. While dramatic alteration in the NPD patterns of the ND_3-trapped UiO-67 upon thermal stimulus is observed, the NPD patterns of the ND_3-trapped UiO-bpydc surprisingly remain unchanged. This result can be accounted for by the steric H-bonding networks between the bipyridine linkers and the adsorbed ND_3 in UiO-bpydc making the adsorption structures more rigid and hence suppressing the linker rotation over the studied temperature range. The results establish the importance of thermal linker flipping induced by the specific host-guest interactions on controlling the responsive adsorption behaviours in these MOFs, consistent with the diffraction study presented in Chapter 3.

Chapter 5 demonstrates the use of neutron spectroscopy techniques (INS and QENS) combined with theoretical calculations to preliminarily investigate the loading-dependent dynamics properties of the defective UiO-67 type MOFs with trapped NH_3 in a microscopic region. The first part focuses on identification of characteristic vibrational modes of both MOF linkers and adsorbed NH_3 molecules at various NH_3 dosing by INS and lattice dynamics DFT calculations, whereas the second part is concerned with the primary study of the diffusivity-loading relationship of the NH_3 confined in the MOF pores by using QENS and GCMC simulations. The correlation of the dynamical behaviours as a function of NH_3

adsorption highlights the importance of linker flexibility, pore structure (induced by defects), and specific host-guest interactions on controlling the responsive dynamic properties in the MOF materials. This Chapter also correlates the dynamic behaviours of the MOF linkers and the confined NH_3 to their respective structural responses studied by NPD in Chapter 3 and 4 and hence supporting the proposed unusual NH_3 adsorption mechanism by which stimuli-tailoring properties such as gate-controlled porosity can be modulated by dynamic linker flipping, disorder, and structural rigidity.

Finally, Chapter 6 summarises the key findings from the entire series of the studies together with a perspective for future study of this research field. Supplementary information consisting of additional characterisation results, details of the refined parameters of the studied MOF materials derived from Rietveld refinement and detailed description of the vibrational modes from vibrational frequency calculations by DFT are given in the Appendices section.

1.5) Chapter summary

This chapter has provided an overview of the introduction, motivation, background literature, as well as the structure of the thesis. For the background literature, it contains basic knowledge of MOFs and recent studies on how their functionality, porosity, and flexibility can be finely tuned to exhibit responsive behaviours toward external stimuli. The use of advanced *in situ* diffraction and spectroscopic techniques for monitoring stimuli-induced responsive behaviours in flexible MOFs at a molecular level has been also emphasised as a central focus of this thesis to develop a better understanding of structural and dynamic processes in these porous materials for future applications.

1.6) References

1. Budrikis, Z., Making the Switch. *Nature Reviews Materials* **2018,** *3* (6), 72-72.
2. Gonzalez-Nelson, A.; Coudert, F.-X.; van der Veen, M. A., Rotational Dynamics of Linkers in Metal–Organic Frameworks. *Nanomaterials* **2019,** *9* (3).
3. Krause, S.; Hosono, N.; Kitagawa, S., Chemistry of Soft Porous Crystals: Structural Dynamics and Gas Adsorption Properties. *Angewandte Chemie International Edition* **2020,** *59* (36), 15325-15341.
4. Zhou, H.-C.; Long, J. R.; Yaghi, O. M., Introduction to Metal–Organic Frameworks. *Chemical Reviews* **2012,** *112* (2), 673-674.
5. Kitagawa, S.; Kitaura, R.; Noro, S.-i., Functional Porous Coordination Polymers. *Angewandte Chemie International Edition* **2004,** *43* (18), 2334-2375.
6. Easun, T. L.; Moreau, F.; Yan, Y.; Yang, S.; Schröder, M., Structural and Dynamic Studies of Substrate Binding in Porous Metal–Organic Frameworks. *Chemical Society Reviews* **2017,** *46* (1), 239-274.
7. Karmakar, A.; Samanta, P.; Desai, A. V.; Ghosh, S. K., Guest-Responsive Metal–Organic Frameworks as Scaffolds for Separation and Sensing Applications. *Accounts of Chemical Research* **2017,** *50* (10), 2457-2469.
8. Wu, X.-P.; Gagliardi, L.; Truhlar, D. G., Cerium Metal–Organic Framework for Photocatalysis. *Journal of the American Chemical Society* **2018,** *140* (25), 7904-7912.
9. Zhao, P.; Fang, H.; Mukhopadhyay, S.; Li, A.; Rudić, S.; McPherson, I. J.; Tang, C. C.; Fairen-Jimenez, D.; Tsang, S. C. E.; Redfern, S. A. T., Structural Dynamics of a Metal–Organic Framework Induced by CO_2 Migration in Its Non-Uniform Porous Structure. *Nature Communications* **2019,** *10* (1), 999.
10. Krause, S.; Bon, V.; Senkovska, I.; Stoeck, U.; Wallacher, D.; Többens, D. M.; Zander, S.; Pillai, R. S.; Maurin, G.; Coudert, F.-X.; Kaskel, S., A Pressure-Amplifying Framework Material with Negative Gas Adsorption Transitions. *Nature* **2016,** *532*, 348.
11. Yang, S.; Lin, X.; Lewis, W.; Suyetin, M.; Bichoutskaia, E.; Parker, J. E.; Tang, C. C.; Allan, D. R.; Rizkallah, P. J.; Hubberstey, P.; Champness, N. R.; Mark Thomas, K.; Blake, A. J.; Schröder, M., A Partially Interpenetrated Metal–Organic Framework for Selective Hysteretic Sorption of Carbon Dioxide. *Nature Materials* **2012,** *11* (8), 710-716.
12. Zhang, S.-Y.; Jensen, S.; Tan, K.; Wojtas, L.; Roveto, M.; Cure, J.; Thonhauser, T.; Chabal, Y. J.; Zaworotko, M. J., Modulation of Water Vapor Sorption by a Fourth-Generation Metal–Organic Material with a Rigid Framework and Self-Switching Pores. *Journal of the American Chemical Society* **2018,** *140* (39), 12545-12552.
13. McDonald, T. M.; Mason, J. A.; Kong, X.; Bloch, E. D.; Gygi, D.; Dani, A.; Crocellà, V.; Giordanino, F.; Odoh, S. O.; Drisdell, W. S.; Vlaisavljevich, B.; Dzubak, A. L.; Poloni, R.; Schnell, S. K.; Planas, N.; Lee, K.; Pascal, T.; Wan, L. F.;

Prendergast, D.; Neaton, J. B.; Smit, B.; Kortright, J. B.; Gagliardi, L.; Bordiga, S.; Reimer, J. A.; Long, J. R., Cooperative Insertion of CO_2 in Diamine-Appended Metal-Organic Frameworks. *Nature* **2015,** *519* (7543), 303-308.

14. Gu, C.; Hosono, N.; Zheng, J.-J.; Sato, Y.; Kusaka, S.; Sakaki, S.; Kitagawa, S., Design and Control of Gas Diffusion Process in a Nanoporous Soft Crystal. *Science* **2019,** *363* (6425), 387.

15. Cho, H. S.; Yang, J.; Gong, X.; Zhang, Y.-B.; Momma, K.; Weckhuysen, B. M.; Deng, H.; Kang, J. K.; Yaghi, O. M.; Terasaki, O., Isotherms of Individual Pores by Gas Adsorption Crystallography. *Nature Chemistry* **2019,** *11* (6), 562-570.

16. Fairen-Jimenez, D.; Moggach, S. A.; Wharmby, M. T.; Wright, P. A.; Parsons, S.; Düren, T., Opening the Gate: Framework Flexibility in ZIF-8 Explored by Experiments and Simulations. *Journal of the American Chemical Society* **2011,** *133* (23), 8900-8902.

17. Krause, S.; Bon, V.; Stoeck, U.; Senkovska, I.; Többens, D. M.; Wallacher, D.; Kaskel, S., A Stimuli-Responsive Zirconium Metal–Organic Framework Based on Supermolecular Design. *Angewandte Chemie International Edition* **2017,** *56* (36), 10676-10680.

18. Kanoo, P.; Matsuda, R.; Sato, H.; Li, L.; Hosono, N.; Kitagawa, S., Pseudo-Gated Adsorption with Negligible Volume Change Evoked by Halogen-Bond Interaction in the Nanospace of MOFs. *Chemistry – A European Journal* **2020,** *26* (10), 2148-2153.

19. Bärwinkel, K.; Herling, M. M.; Rieß, M.; Sato, H.; Li, L.; Avadhut, Y. S.; Kemnitzer, T. W.; Kalo, H.; Senker, J.; Matsuda, R.; Kitagawa, S.; Breu, J., Constant Volume Gate-Opening by Freezing Rotational Dynamics in Microporous Organically Pillared Layered Silicates. *Journal of the American Chemical Society* **2017,** *139* (2), 904-909.

20. Jiang, X.; Duan, H.-B.; Khan, S. I.; Garcia-Garibay, M. A., Diffusion-Controlled Rotation of Triptycene in a Metal–Organic Framework (MOF) Sheds Light on the Viscosity of MOF-Confined Solvent. *ACS Central Science* **2016,** *2* (9), 608-613.

21. Krause, S.; Evans, J. D.; Bon, V.; Senkovska, I.; Iacomi, P.; Kolbe, F.; Ehrling, S.; Troschke, E.; Getzschmann, J.; Többens, D. M.; Franz, A.; Wallacher, D.; Yot, P. G.; Maurin, G.; Brunner, E.; Llewellyn, P. L.; Coudert, F.-X.; Kaskel, S., Towards General Network Architecture Design Criteria for Negative Gas Adsorption Transitions in Ultraporous Frameworks. *Nature Communications* **2019,** *10* (1), 3632.

22. Fang, Z.; Bueken, B.; De Vos, D. E.; Fischer, R. A., Defect-Engineered Metal–Organic Frameworks. *Angewandte Chemie International Edition* **2015,** *54* (25), 7234-7254.

23. Cavka, J. H.; Jakobsen, S.; Olsbye, U.; Guillou, N.; Lamberti, C.; Bordiga, S.; Lillerud, K. P., A New Zirconium Inorganic Building Brick Forming Metal Organic Frameworks with Exceptional Stability. *Journal of the American Chemical Society* **2008,** *130* (42), 13850-13851.

24. Shearer, G. C.; Chavan, S.; Bordiga, S.; Svelle, S.; Olsbye, U.; Lillerud, K. P., Defect Engineering: Tuning the Porosity and Composition of the Metal–Organic

Framework UiO-66 via Modulated Synthesis. *Chemistry of Materials* **2016,** *28* (11), 3749-3761.

25. Cliffe, M. J.; Wan, W.; Zou, X.; Chater, P. A.; Kleppe, A. K.; Tucker, M. G.; Wilhelm, H.; Funnell, N. P.; Coudert, F.-X.; Goodwin, A. L., Correlated Defect Nanoregions in a Metal–Organic Framework. *Nature Communications* **2014,** *5* (1), 4176.

26. Wu, H.; Chua, Y. S.; Krungleviciute, V.; Tyagi, M.; Chen, P.; Yildirim, T.; Zhou, W., Unusual and Highly Tunable Missing-Linker Defects in Zirconium Metal–Organic Framework UiO-66 and Their Important Effects on Gas Adsorption. *Journal of the American Chemical Society* **2013,** *135* (28), 10525-10532.

27. Gutov, O. V.; Hevia, M. G.; Escudero-Adán, E. C.; Shafir, A., Metal–Organic Framework (MOF) Defects under Control: Insights into the Missing Linker Sites and Their Implication in the Reactivity of Zirconium-Based Frameworks. *Inorganic Chemistry* **2015,** *54* (17), 8396-8400.

28. Gutterød, E. S.; Pulumati, S. H.; Kaur, G.; Lazzarini, A.; Solemsli, B. G.; Gunnæs, A. E.; Ahoba-Sam, C.; Kalyva, M. E.; Sannes, J. A.; Svelle, S.; Skúlason, E.; Nova, A.; Olsbye, U., Influence of Defects and H_2O on the Hydrogenation of CO_2 to Methanol over Pt Nanoparticles in UiO-67 Metal–Organic Framework. *Journal of the American Chemical Society* **2020,** *142* (40), 17105-17118.

29. Forgan, R. S.; Marshall, R. J.; Struckmann, M.; Bleine, A. B.; Long, D.-L.; Bernini, M. C.; Fairen-Jimenez, D., Structure-Directing Factors when Introducing Hydrogen Bond Functionality to Metal–Organic Frameworks. *CrystEngComm* **2015,** *17* (2), 299-306.

30. Yang, Q.-Y.; Lama, P.; Sen, S.; Lusi, M.; Chen, K.-J.; Gao, W.-Y.; Shivanna, M.; Pham, T.; Hosono, N.; Kusaka, S.; Perry Iv, J. J.; Ma, S.; Space, B.; Barbour, L. J.; Kitagawa, S.; Zaworotko, M. J., Reversible Switching between Highly Porous and Nonporous Phases of an Interpenetrated Diamondoid Coordination Network That Exhibits Gate-Opening at Methane Storage Pressures. *Angewandte Chemie International Edition* **2018,** *57* (20), 5684-5689.

31. Lama, P.; Barbour, L. J., Distinctive Three-Step Hysteretic Sorption of Ethane with *in situ* Crystallographic Visualization of the Pore Forms in a Soft Porous Crystal. *Journal of the American Chemical Society* **2018,** *140* (6), 2145-2150.

32. Sikiti, P.; Bezuidenhout, C. X.; van Heerden, D. P.; Barbour, L. J., Direct *in situ* Crystallographic Visualization of a Dual Mechanism for the Uptake of CO_2 Gas by a Flexible Metal–Organic Framework. *Inorganic Chemistry* **2019,** *58* (13), 8257-8262.

33. Rieth, A. J.; Dincă, M., Controlled Gas Uptake in Metal–Organic Frameworks with Record Ammonia Sorption. *Journal of the American Chemical Society* **2018,** *140* (9), 3461-3466.

34. Rieth, A. J.; Hunter, K. M.; Dincă, M.; Paesani, F., Hydrogen Bonding Structure of Confined Water Templated by a Metal-Organic Framework with Open Metal Sites. *Nature Communications* **2019,** *10* (1), 4771.

35. Armstrong, J.; O'Malley, A. J.; Ryder, M. R.; Butler, K. T., Understanding Dynamic Properties of Materials Using Neutron Spectroscopy and Atomistic Simulation. *Journal of Physics Communications* **2020,** *4* (7), 072001.

36. Bon, V.; Brunner, E.; Pöppl, A.; Kaskel, S., Unraveling Structure and Dynamics in Porous Frameworks via Advanced *in situ* Characterization Techniques. *Advanced Functional Materials* **2020,** *30* (41), 1907847.

37. Taddei, M., When Defects Turn into Virtues: The Curious Case of Zirconium-Based Metal-Organic Frameworks. *Coordination Chemistry Reviews* **2017,** *343*, 1-24.

38. Bai, Y.; Dou, Y.; Xie, L.-H.; Rutledge, W.; Li, J.-R.; Zhou, H.-C., Zr-Based Metal–Organic Frameworks: Design, Synthesis, Structure, and Applications. *Chemical Society Reviews* **2016,** *45* (8), 2327-2367.

39. Mondloch, J. E.; Bury, W.; Fairen-Jimenez, D.; Kwon, S.; DeMarco, E. J.; Weston, M. H.; Sarjeant, A. A.; Nguyen, S. T.; Stair, P. C.; Snurr, R. Q.; Farha, O. K.; Hupp, J. T., Vapor-Phase Metalation by Atomic Layer Deposition in a Metal–Organic Framework. *Journal of the American Chemical Society* **2013,** *135* (28), 10294-10297.

40. Furukawa, H.; Gándara, F.; Zhang, Y.-B.; Jiang, J.; Queen, W. L.; Hudson, M. R.; Yaghi, O. M., Water Adsorption in Porous Metal–Organic Frameworks and Related Materials. *Journal of the American Chemical Society* **2014,** *136* (11), 4369-4381.

41. Feng, D.; Gu, Z.-Y.; Li, J.-R.; Jiang, H.-L.; Wei, Z.; Zhou, H.-C., Zirconium-Metalloporphyrin PCN-222: Mesoporous Metal–Organic Frameworks with Ultrahigh Stability as Biomimetic Catalysts. *Angewandte Chemie International Edition* **2012,** *51* (41), 10307-10310.

42. Bon, V.; Senkovskyy, V.; Senkovska, I.; Kaskel, S., Zr(iv) and Hf(iv) Based Metal–Organic Frameworks with reo-Topology. *Chemical Communications* **2012,** *48* (67), 8407-8409.

43. Bennett, T. D.; Cheetham, A. K.; Fuchs, A. H.; Coudert, F.-X., Interplay Between Defects, Disorder and Flexibility in Metal-Organic Frameworks. *Nature Chemistry* **2017,** *9* (1), 11-16.

44. Lee, J.; Farha, O. K.; Roberts, J.; Scheidt, K. A.; Nguyen, S. T.; Hupp, J. T., Metal–Organic Framework Materials as Ctalysts. *Chemical Society Reviews* **2009,** *38* (5), 1450-1459.

45. Ling, S.; Slater, B., Dynamic Acidity in Defective UiO-66. *Chemical Science* **2016,** *7* (7), 4706-4712.

46. Liu, L.; Chen, Z.; Wang, J.; Zhang, D.; Zhu, Y.; Ling, S.; Huang, K.-W.; Belmabkhout, Y.; Adil, K.; Zhang, Y.; Slater, B.; Eddaoudi, M.; Han, Y., Imaging Defects and Their Evolution in a Metal–Organic Framework at Sub-Unit-Cell Resolution. *Nature Chemistry* **2019,** *11* (7), 622-628.

47. Bueken, B.; Van Velthoven, N.; Krajnc, A.; Smolders, S.; Taulelle, F.; Mellot-Draznieks, C.; Mali, G.; Bennett, T. D.; De Vos, D., Tackling the Defect Conundrum in UiO-66: A Mixed-Linker Approach to Engineering Missing Linker Defects. *Chemistry of Materials* **2017,** *29* (24), 10478-10486.

48. Trickett, C. A.; Gagnon, K. J.; Lee, S.; Gándara, F.; Bürgi, H.-B.; Yaghi, O. M., Definitive Molecular Level Characterization of Defects in UiO-66 Crystals. *Angewandte Chemie International Edition* **2015,** *54* (38), 11162-11167.

49. Shearer, G. C.; Chavan, S.; Ethiraj, J.; Vitillo, J. G.; Svelle, S.; Olsbye, U.; Lamberti, C.; Bordiga, S.; Lillerud, K. P., Tuned to Perfection: Ironing Out the Defects in Metal–Organic Framework UiO-66. *Chemistry of Materials* **2014,** *26* (14), 4068-4071.

50. Valenzano, L.; Civalleri, B.; Chavan, S.; Bordiga, S.; Nilsen, M. H.; Jakobsen, S.; Lillerud, K. P.; Lamberti, C., Disclosing the Complex Structure of UiO-66 Metal Organic Framework: A Synergic Combination of Experiment and Theory. *Chemistry of Materials* **2011,** *23* (7), 1700-1718.

51. Øien, S.; Wragg, D.; Reinsch, H.; Svelle, S.; Bordiga, S.; Lamberti, C.; Lillerud, K. P., Detailed Structure Analysis of Atomic Positions and Defects in Zirconium Metal–Organic Frameworks. *Crystal Growth & Design* **2014,** *14* (11), 5370-5372.

52. Feng, Y.; Chen, Q.; Jiang, M.; Yao, J., Tailoring the Properties of UiO-66 through Defect Engineering: A Review. *Industrial & Engineering Chemistry Research* **2019,** *58* (38), 17646-17659.

53. Katz, M. J.; Brown, Z. J.; Colón, Y. J.; Siu, P. W.; Scheidt, K. A.; Snurr, R. Q.; Hupp, J. T.; Farha, O. K., A Facile Synthesis of UiO-66, UiO-67 and Their Derivatives. *Chemical Communications* **2013,** *49* (82), 9449-9451.

54. Vermoortele, F.; Bueken, B.; Le Bars, G.; Van de Voorde, B.; Vandichel, M.; Houthoofd, K.; Vimont, A.; Daturi, M.; Waroquier, M.; Van Speybroeck, V.; Kirschhock, C.; De Vos, D. E., Synthesis Modulation as a Tool To Increase the Catalytic Activity of Metal–Organic Frameworks: The Unique Case of UiO-66(Zr). *Journal of the American Chemical Society* **2013,** *135* (31), 11465-11468.

55. Han, Y.; Liu, M.; Li, K.; Zuo, Y.; Wei, Y.; Xu, S.; Zhang, G.; Song, C.; Zhang, Z.; Guo, X., Facile Synthesis of Morphology and Size-Controlled Zirconium Metal-Organic Framework UiO-66: the Role of Hydrofluoric Acid in Crystallization. *CrystEngComm* **2015,** *17* (33), 6434-6440.

56. Liang, W.; Coghlan, C. J.; Ragon, F.; Rubio-Martinez, M.; D'Alessandro, D. M.; Babarao, R., Defect Engineering of UiO-66 for CO_2 and H_2O Uptake – a Combined Experimental and Simulation Study. *Dalton Transactions* **2016,** *45* (11), 4496-4500.

57. Wang, K.; Li, C.; Liang, Y.; Han, T.; Huang, H.; Yang, Q.; Liu, D.; Zhong, C., Rational Construction of Defects in a Metal–Organic Framework for Highly Efficient Adsorption and Separation of Dyes. *Chemical Engineering Journal* **2016,** *289*, 486-493.

58. Klet, R. C.; Liu, Y.; Wang, T. C.; Hupp, J. T.; Farha, O. K., Evaluation of Brønsted Acidity and Proton Topology in Zr- and Hf-Based Metal–Organic Frameworks Using Potentiometric Acid–Base Titration. *Journal of Materials Chemistry A* **2016,** *4* (4), 1479-1485.

59. Bon, V.; Senkovska, I.; Weiss, M. S.; Kaskel, S., Tailoring of Network Dimensionality and Porosity Adjustment in Zr- and Hf-Based MOFs. *CrystEngComm* **2013,** *15* (45), 9572-9577.

60. Ghosh, P.; Colón, Y. J.; Snurr, R. Q., Water Adsorption in UiO-66: the Importance of Defects. *Chemical Communications* **2014,** *50* (77), 11329-11331.

61. Schneemann, A.; Bon, V.; Schwedler, I.; Senkovska, I.; Kaskel, S.; Fischer, R. A., Flexible Metal–Organic Frameworks. *Chemical Society Reviews* **2014,** *43* (16), 6062-6096.

62. Horike, S.; Shimomura, S.; Kitagawa, S., Soft Porous Crystals. *Nature Chemistry* **2009,** *1* (9), 695-704.

63. Coudert, F.-X., Responsive Metal–Organic Frameworks and Framework Materials: Under Pressure, Taking the Heat, in the Spotlight, with Friends. *Chemistry of Materials* **2015,** *27* (6), 1905-1916.

64. Bousquet, D.; Coudert, F.-X.; Fossati, A. G. J.; Neimark, A. V.; Fuchs, A. H.; Boutin, A., Adsorption Induced Transitions in Soft Porous Crystals: an Osmotic Potential Approach to Multistability and IntermediateStructures. *The Journal of Chemical Physics* **2013,** *138* (17), 174706.

65. Coudert, F.-X.; Boutin, A.; Fuchs, A. H.; Neimark, A. V., Adsorption Deformation and Structural Transitions in Metal–Organic Frameworks: From the Unit Cell to the Crystal. *The Journal of Physical Chemistry Letters* **2013,** *4* (19), 3198-3205.

66. Salles, F.; Maurin, G.; Serre, C.; Llewellyn, P. L.; Knöfel, C.; Choi, H. J.; Filinchuk, Y.; Oliviero, L.; Vimont, A.; Long, J. R.; Férey, G., Multistep N_2 Breathing in the Metal−Organic Framework Co(*1,4*-benzenedipyrazolate). *Journal of the American Chemical Society* **2010,** *132* (39), 13782-13788.

67. Li, D.; Kaneko, K., Hydrogen Bond-Regulated Microporous Nature of Copper Complex-Assembled Microcrystals. *Chemical Physics Letters* **2001,** *335* (1), 50-56.

68. Kitaura, R.; Fujimoto, K.; Noro, S.-i.; Kondo, M.; Kitagawa, S., A Pillared-Layer Coordination Polymer Network Displaying Hysteretic Sorption: $[Cu_2(pzdc)_2(dpyg)]n$ (pzdc= Pyrazine-*2,3*-dicarboxylate; dpyg=*1,2*-Di(*4*-pyridyl)glycol). *Angewandte Chemie International Edition* **2002,** *41* (1), 133-135.

69. Serre, C.; Millange, F.; Thouvenot, C.; Noguès, M.; Marsolier, G.; Louër, D.; Férey, G., Very Large Breathing Effect in the First Nanoporous Chromium(III)-Based Solids: MIL-53 or $CrIII(OH)\cdot\{O_2C{-}C_6H_4{-}CO_2\}\cdot\{HO_2C{-}C_6H_4{-}CO_2H\}_x\cdot H_2O_y$. *Journal of the American Chemical Society* **2002,** *124* (45), 13519-13526.

70. Horike, S.; Matsuda, R.; Tanaka, D.; Matsubara, S.; Mizuno, M.; Endo, K.; Kitagawa, S., Dynamic Motion of Building Blocks in Porous Coordination Polymers. *Angewandte Chemie International Edition* **2006,** *45* (43), 7226-7230.

71. Gonzalez, J.; Nandini Devi, R.; Tunstall, D. P.; Cox, P. A.; Wright, P. A., Deuterium NMR Studies of Framework and Guest Mobility in the Metal–Organic Framework Compound MOF-5, $Zn_4O(O_2CC_6H_4CO_2)_3$. *Microporous and Mesoporous Materials* **2005,** *84* (1), 97-104.

72. Uemura, T.; Horike, S.; Kitagawa, K.; Mizuno, M.; Endo, K.; Bracco, S.; Comotti, A.; Sozzani, P.; Nagaoka, M.; Kitagawa, S., Conformation and Molecular Dynamics of Single Polystyrene Chain Confined in Coordination Nanospace. *Journal of the American Chemical Society* **2008,** *130* (21), 6781-6788.

73. Kolokolov, D. I.; Jobic, H.; Stepanov, A. G.; Guillerm, V.; Devic, T.; Serre, C.; Férey, G., Dynamics of Benzene Rings in MIL-53(Cr) and MIL-47(V) Frameworks Studied by ^{2}H NMR Spectroscopy. *Angewandte Chemie International Edition* **2010,** *49* (28), 4791-4794.

74. Kolokolov, D. I.; Stepanov, A. G.; Jobic, H., Guest Controlled Rotational Dynamics of Terephthalate Phenylenes in Metal–Organic Framework MIL-53(Al): Effect of Different Xylene Loadings. *The Journal of Physical Chemistry C* **2014,** *118* (29), 15978-15984.

75. Kolokolov, D. I.; Stepanov, A. G.; Guillerm, V.; Serre, C.; Frick, B.; Jobic, H., Probing the Dynamics of the Porous Zr Terephthalate UiO-66 Framework Using ^{2}H NMR and Neutron Scattering. *The Journal of Physical Chemistry C* **2012,** *116* (22), 12131-12136.

76. Khudozhitkov, A. E.; Kolokolov, D. I.; Stepanov, A. G.; Bolotov, V. A.; Dybtsev, D. N., Metal-Cation-Independent Dynamics of Phenylene Ring in Microporous MOFs: A ^{2}H Solid-State NMR Study. *The Journal of Physical Chemistry C* **2015,** *119* (50), 28038-28045.

77. Moreau, F.; Kolokolov, D. I.; Stepanov, A. G.; Easun, T. L.; Dailly, A.; Lewis, W.; Blake, A. J.; Nowell, H.; Lennox, M. J.; Besley, E.; Yang, S.; Schröder, M., Tailoring Porosity and Rotational Dynamics in a Series of Octacarboxylate Metal-Organic Frameworks. *Proceedings of the National Academy of Sciences* **2017,** *114* (12), 3056.

78. Shustova, N. B.; Ong, T.-C.; Cozzolino, A. F.; Michaelis, V. K.; Griffin, R. G.; Dincă, M., Phenyl Ring Dynamics in a Tetraphenylethylene-Bridged Metal–Organic Framework: Implications for the Mechanism of Aggregation-Induced Emission. *Journal of the American Chemical Society* **2012,** *134* (36), 15061-15070.

79. Li, B.; Wen, H.-M.; Wang, H.; Wu, H.; Tyagi, M.; Yildirim, T.; Zhou, W.; Chen, B., A Porous Metal–Organic Framework with Dynamic Pyrimidine Groups Exhibiting Record High Methane Storage Working Capacity. *Journal of the American Chemical Society* **2014,** *136* (17), 6207-6210.

80. Zhang, J.-P.; Chen, X.-M., Exceptional Framework Flexibility and Sorption Behavior of a Multifunctional Porous Cuprous Triazolate Framework. *Journal of the American Chemical Society* **2008,** *130* (18), 6010-6017.

81. Sato, H.; Kosaka, W.; Matsuda, R.; Hori, A.; Hijikata, Y.; Belosludov, R. V.; Sakaki, S.; Takata, M.; Kitagawa, S., Self-Accelerating CO Sorption in a Soft Nanoporous Crystal. *Science* **2014,** *343* (6167), 167.

82. Thommes, M.; Kaneko, K.; Neimark, A. V.; Olivier, J. P.; Rodriguez-Reinoso, F.; Rouquerol, J.; Sing, K. S. W., Physisorption of gases, with special reference to the evaluation of surface area and pore size distribution (IUPAC Technical Report). *Pure and Applied Chemistry* **2015,** *87* (9-10), 1051-1069.

83. Gu, Y.; Zheng, J.-J.; Otake, K.-i.; Sugimoto, K.; Hosono, N.; Sakaki, S.; Li, F.; Kitagawa, S., Structural-Deformation-Energy-Modulation Strategy in a Soft Porous Coordination Polymer with an Interpenetrated Framework. *Angewandte Chemie International Edition* **2020,** *59* (36), 15517-15521.

84. Hyun, S.-m.; Lee, J. H.; Jung, G. Y.; Kim, Y. K.; Kim, T. K.; Jeoung, S.; Kwak, S. K.; Moon, D.; Moon, H. R., Exploration of Gate-Opening and Breathing Phenomena in a Tailored Flexible Metal–Organic Framework. *Inorganic Chemistry* **2016,** *55* (4), 1920-1925.

85. Coudert, F.-X., Molecular Mechanism of Swing Effect in Zeolitic Imidazolate Framework ZIF-8: Continuous Deformation upon Adsorption. *ChemPhysChem* **2017,** *18* (19), 2732-2738.

86. Yue, Y.; Rabone, J. A.; Liu, H.; Mahurin, S. M.; Li, M.-R.; Wang, H.; Lu, Z.; Chen, B.; Wang, J.; Fang, Y.; Dai, S., A Flexible Metal–Organic Framework: Guest Molecules Controlled Dynamic Gas Adsorption. *The Journal of Physical Chemistry C* **2015,** *119* (17), 9442-9449.

87. Sakaida, S.; Otsubo, K.; Sakata, O.; Song, C.; Fujiwara, A.; Takata, M.; Kitagawa, H., Crystalline Coordination Framework Endowed with Dynamic Gate-Opening Behaviour byBeing Downsized to a Thin Film. *Nature Chemistry* **2016,** *8* (4), 377-383.

88. Ania, C. O.; García-Pérez, E.; Haro, M.; Gutiérrez-Sevillano, J. J.; Valdés-Solís, T.; Parra, J. B.; Calero, S., Understanding Gas-Induced Structural Deformation of ZIF-8. *The Journal of Physical Chemistry Letters* **2012,** *3* (9), 1159-1164.

89. Chaplais, G.; Fraux, G.; Paillaud, J.-L.; Marichal, C.; Nouali, H.; Fuchs, A. H.; Coudert, F.-X.; Patarin, J., Impacts of the Imidazolate Linker Substitution (CH_3, Cl, or Br) on the Structural and Adsorptive Properties of ZIF-8. *The Journal of Physical Chemistry C* **2018,** *122* (47), 26945-26955.

90. Sears, V. F., Neutron Scattering Lengths and Cross Sections. *Neutron News* **1992,** *3* (3), 26-37.

91. Peterson, V. K.; Liu, Y.; Brown, C. M.; Kepert, C. J., Neutron Powder Diffraction Study of D_2 Sorption in Cu_3(*1,3,5*-benzenetricarboxylate)$_2$. *Journal of the American Chemical Society* **2006,** *128* (49), 15578-15579.

92. Getzschmann, J.; Senkovska, I.; Wallacher, D.; Tovar, M.; Fairen-Jimenez, D.; Düren, T.; van Baten, J. M.; Krishna, R.; Kaskel, S., Methane Storage Mechanism in the Metal-Organic Framework $Cu_3(btc)_2$: An *in situ* Neutron Diffraction Study. *Microporous and Mesoporous Materials* **2010,** *136* (1), 50-58.

93. Hulvey, Z.; Vlaisavljevich, B.; Mason, J. A.; Tsivion, E.; Dougherty, T. P.; Bloch, E. D.; Head-Gordon, M.; Smit, B.; Long, J. R.; Brown, C. M., Critical Factors Driving the High Volumetric Uptake of Methane in $Cu_3(btc)_2$. *Journal of the American Chemical Society* **2015,** *137* (33), 10816-10825.

94. Lorzing, G. R.; Gosselin, A. J.; Trump, B. A.; York, A. H. P.; Sturluson, A.; Rowland, C. A.; Yap, G. P. A.; Brown, C. M.; Simon, C. M.; Bloch, E. D., Understanding Gas Storage in Cuboctahedral Porous Coordination Cages. *Journal of the American Chemical Society* **2019,** *141* (30), 12128-12138.

95. Li, L.; Lin, R.-B.; Krishna, R.; Wang, X.; Li, B.; Wu, H.; Li, J.; Zhou, W.; Chen, B., Efficient Separation of Ethylene from Acetylene/Ethylene Mixtures by a Flexible-Robust Metal–Organic Framework. *Journal of Materials Chemistry A* **2017,** *5* (36), 18984-18988.

96. Ryder, M. R.; Van de Voorde, B.; Civalleri, B.; Bennett, T. D.; Mukhopadhyay, S.; Cinque, G.; Fernandez-Alonso, F.; De Vos, D.; Rudić, S.; Tan, J.-C., Detecting Molecular Rotational Dynamics Complementing the Low-Frequency Terahertz Vibrations in a Zirconium-Based Metal-Organic Framework. *Physical Review Letters* **2017,** *118* (25), 255502.

97. Zhou, W.; Yildirim, T., Lattice Dynamics of Metal-Organic Frameworks: Neutron Inelastic Scattering and First-Principles Calculations. *Physical Review B* **2006,** *74* (18), 180301.

98. Zhou, W.; Wu, H.; Udovic, T. J.; Rush, J. J.; Yildirim, T., Quasi-Free Methyl Rotation in Zeolitic Imidazolate Framework-8. *The Journal of Physical Chemistry A* **2008,** *112* (49), 12602-12606.

99. Ryder, M. R.; Civalleri, B.; Bennett, T. D.; Henke, S.; Rudić, S.; Cinque, G.; Fernandez-Alonso, F.; Tan, J.-C., Identifying the Role of Terahertz Vibrations in Metal-Organic Frameworks: From Gate-Opening Phenomenon to Shear-Driven Structural Destabilization. *Physical Review Letters* **2014,** *113* (21), 215502.

100. Ryder, M. R.; Civalleri, B.; Cinque, G.; Tan, J.-C., Discovering Connections between Terahertz Vibrations and Elasticity Underpinning the Collective Dynamics of the HKUST-1 Metal–Organic Framework. *CrystEngComm* **2016,** *18* (23), 4303-4312.

101. Wu, Y.; Kobayashi, A.; Halder, G. J.; Peterson, V. K.; Chapman, K. W.; Lock, N.; Southon, P. D.; Kepert, C. J., Negative Thermal Expansion in the Metal–Organic Framework Material Cu_3(*1,3,5*-benzenetricarboxylate)$_2$. *Angewandte Chemie International Edition* **2008,** *47* (46), 8929-8932.

102. Kusaka, S.; Nakajima, Y.; Hori, A.; Yonezu, A.; Kikushima, K.; Kosaka, W.; Ma, Y.; Matsuda, R., Molecular Motion in the Nanospace of MOFs upon Gas Adsorption Investigated by *in situ* Raman Spectroscopy. *Faraday Discussions* **2021**.

103. Casco, M. E.; Fernández-Catalá, J.; Cheng, Y.; Daemen, L.; Ramirez-Cuesta, A. J.; Cuadrado-Collados, C.; Silvestre-Albero, J.; Ramos-Fernandez, E. V., Understanding ZIF-8 Performance upon Gas Adsorption by Means of Inelastic Neutron Scattering. *ChemistrySelect* **2017,** *2* (9), 2750-2753.

104. Butler, K. T.; Vervoorts, P.; Ehrenreich, M. G.; Armstrong, J.; Skelton, J. M.; Kieslich, G., Experimental Evidence for Vibrational Entropy as Driving Parameter of Flexibility in the Metal–Organic Framework ZIF-4(Zn). *Chemistry of Materials* **2019,** *31* (20), 8366-8372.

105. Lock, N.; Christensen, M.; Wu, Y.; Peterson, V. K.; Thomsen, M. K.; Piltz, R. O.; Ramirez-Cuesta, A. J.; McIntyre, G. J.; Norén, K.; Kutteh, R.; Kepert, C. J.; Kearley, G. J.; Iversen, B. B., Scrutinizing Negative Thermal Expansion in MOF-5 by Scattering Techniques and *ab initio* Calculations. *Dalton Transactions* **2013,** *42* (6), 1996-2007.

106. Rosenbach Jr, N.; Jobic, H.; Ghoufi, A.; Salles, F.; Maurin, G.; Bourrelly, S.; Llewellyn, P. L.; Devic, T.; Serre, C.; Férey, G., Quasi-Elastic Neutron Scattering and Molecular Dynamics Study of Methane Diffusion in Metal Organic Frameworks

MIL-47(V) and MIL-53(Cr). *Angewandte Chemie International Edition* **2008,** *47* (35), 6611-6615.

107. Stallmach, F.; Gröger, S.; Künzel, V.; Kärger, J.; Yaghi, O. M.; Hesse, M.; Müller, U., NMR Studies on the Diffusion of Hydrocarbons on the Metal-Organic Framework Material MOF-5. *Angewandte Chemie International Edition* **2006,** *45* (13), 2123-2126.

108. Kärger, J.; Binder, T.; Chmelik, C.; Hibbe, F.; Krautscheid, H.; Krishna, R.; Weitkamp, J., Microimaging of Transient Guest Profiles to Monitor Mass Transfer in Nanoporous Materials. *Nature Materials* **2014,** *13* (4), 333-343.

109. Heinke, L.; Tzoulaki, D.; Chmelik, C.; Hibbe, F.; van Baten, J. M.; Lim, H.; Li, J.; Krishna, R.; Kärger, J., Assessing Guest Diffusivities in Porous Hosts from Transient Concentration Profiles. *Physical Review Letters* **2009,** *102* (6), 065901.

110. Jobic, H.; Theodorou, D. N., Quasi-Elastic Neutron Scattering and Molecular Dynamics Simulation as Complementary Techniques for Studying Diffusion in Zeolites. *Microporous and mesoporous materials* **2007,** *102* (1-3), 21-50.

111. Salles, F.; Jobic, H.; Ghoufi, A.; Llewellyn, P. L.; Serre, C.; Bourrelly, S.; Férey, G.; Maurin, G., Transport Diffusivity of CO_2 in the Highly Flexible Metal–Organic Framework MIL-53(Cr). *Angewandte Chemie International Edition* **2009,** *48* (44), 8335-8339.

112. Prakash, M.; Jobic, H.; Ramsahye, N. A.; Nouar, F.; Damasceno Borges, D.; Serre, C.; Maurin, G., Diffusion of H_2, CO_2, and Their Mixtures in the Porous Zirconium Based Metal–Organic Framework MIL-140A(Zr): Combination of Quasi-Elastic Neutron Scattering Measurements and Molecular Dynamics Simulations. *The Journal of Physical Chemistry C* **2015,** *119* (42), 23978-23989.

113. Kolokolov, D. I.; Maryasov, A. G.; Ollivier, J.; Freude, D.; Haase, J.; Stepanov, A. G.; Jobic, H., Uncovering the Rotation and Translational Mobility of Benzene Confined in UiO-66 (Zr) Metal–Organic Framework by the ^{2}H NMR–QENS Experimental Toolbox. *The Journal of Physical Chemistry C* **2017,** *121* (5), 2844-2857.

114. Sayeed, A.; Mitra, S.; Anil Kumar, A. V.; Mukhopadhyay, R.; Yashonath, S.; Chaplot, S. L., Diffusion of Propane in Zeolite NaY: a Molecular Dynamics and Quasi-Elastic Neutron Scattering Study. *The Journal of Physical Chemistry B* **2003,** *107* (2), 527-533.

115. O'Malley, A. J.; Hitchcock, I.; Sarwar, M.; Silverwood, I. P.; Hindocha, S.; Catlow, C. R. A.; York, A. P. E.; Collier, P. J., Ammonia Mobility in Chabazite: Insight into the Diffusion Component of the NH_3-SCR Process. *Physical Chemistry Chemical Physics* **2016,** *18* (26), 17159-17168.

116. Hernandez-Tamargo, C.; O'Malley, A.; Silverwood, I. P.; de Leeuw, N. H., Molecular Behaviour of Phenol in Zeolite Beta Catalysts as a Function of Acid Site Presence: a Quasielastic Neutron Scattering and Molecular Dynamics Simulation Study. *Catalysis Science & Technology* **2019,** *9* (23), 6700-6713.

117. O'Malley, A. J.; Sarwar, M.; Armstrong, J.; Catlow, C. R. A.; Silverwood, I. P.; York, A. P. E.; Hitchcock, I., Comparing Ammonia Diffusion in NH_3-SCR Zeolite

Catalysts: a Quasielastic Neutron Scattering and Molecular Dynamics Simulation Study. *Physical Chemistry Chemical Physics* **2018,** *20* (17), 11976-11986.

118. Mukhopadhyay, R.; Sayeed, A.; Rao, M. N.; Anilkumar, A. V.; Mitra, S.; Yashonath, S.; Chaplot, S. L., Rotation of Propane Molecules in Supercages of Na–Y Zeolite. *Chemical Physics* **2003,** *292* (2), 217-222.

119. Pillai, R. S.; Jobic, H.; Koza, M. M.; Nouar, F.; Serre, C.; Maurin, G.; Ramsahye, N. A., Diffusion of Carbon Dioxide and Nitrogen in the Small-Pore Titanium Bis(phosphonate) Metal–Organic Framework MIL-91 (Ti): a Combination of Quasielastic Neutron Scattering Measurements and Molecular Dynamics Simulations. *ChemPhysChem* **2017,** *18* (19), 2739-2746.

Chapter 2

Experimental and Theoretical Methodologies

Details of relevant basic theories, experimental procedures, characterisation techniques, and data analysis used in this thesis are given in this chapter. Information on collaborative theoretical studies are also described in brief.

2.1) Background theories

2.1.1) Powder diffraction

Powder diffraction is one of the most powerful characterisation techniques, providing a wealth of information on the atomic structure and microstructural properties of materials. This technique is concerned with samples being polycrystalline or consisting of different crystals that large majorities of materials such as metal oxides, zeolites, and metal-organic frameworks (MOFs) exist. This is also a key strength of this technique to study the samples where a single-crystal form is not readily available and does not represent bulk materials under the measurement conditions such as high temperature, high pressure and gas loading. In Chapter 3 and 4, two types of powder diffractions: X-ray powder diffraction (XRD) and neutron powder diffraction (NPD) categorised by the type of scattering source, are intensely used to study structural responsive behaviours of MOFs towards external stimuli. The fundamental scattering processes of XRD and NPD are intrinsically different. While X-rays interact with electron clouds in an atom of a sample, neutrons interact with an atomic nuclei. This difference serves to make the two techniques complementary. The basic concept of the NPD will be discussed together with other neutron techniques in section 2.1.3

as they are strongly related to each other whereas that of the well-established XRD technique is briefly presented here.

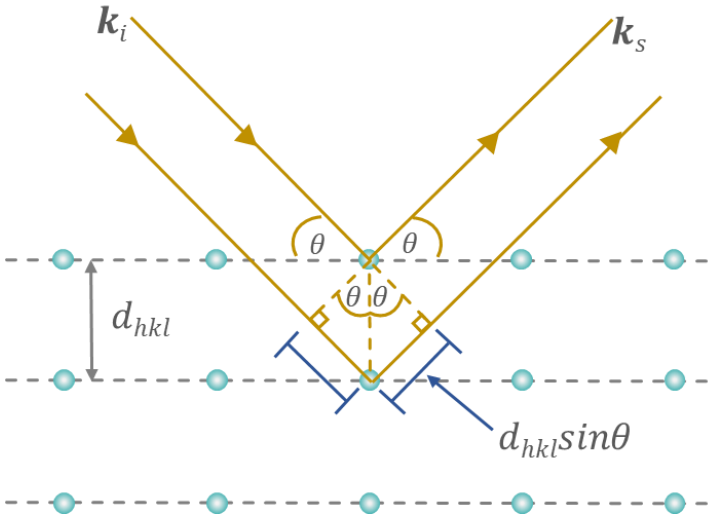

Figure 2.1 | Illustration of a beam that satisfies the Bragg's law, where d_{hkl}, $\boldsymbol{k}_i$ and $\boldsymbol{k}_s$ represent the inter-planar spacing, the incident vector and the scattered vector, respectively.

The first discovery of the structural information in powder diffraction is developed via the well-known Bragg's law [1] which describes the interference pattern of X-rays scattered by electrons of atoms in lattice planes. The lattice planes are crystallographic planes, characterised by the index hkl, the so-called Miller indices. To satisfy the Bragg's law, the wavelength λ is equivalent to the atomic or molecular distances, i.e. inter-planar spacing d_{hkl}. An interference occurs when the path length difference associated with reflections from adjacent lattice planes is equivalent to the wavelength λ (see Figure 2.1):

$$2d_{hkl}sin\theta = n\lambda \qquad \textit{Equation 2. 1}$$

where d_{hkl} is the inter-planar distance of lattice plane hkl,

θ is the scattering angle,

n is an integer, and

λ is the wavelength of the incident X-ray.

The Bragg's equation is applied to other diffraction techniques such as NPD. In principle, the distinction between XRD and NPD originates from their characteristic atomic form factors that contributes to the observed diffraction intensity. [2] The atomic form factor of X-rays is proportional to the atomic number *Z* and reduces monotonically with increasing θ and decreasing λ. As a result, XRD is more sensitive to heavy atoms and Bragg reflections at higher θ angles will generally exhibit a lower intensity compared to those at lower θ angles. On the other hand, the atomic form factor of neutrons tends to be independent of λ and θ, and the associated neutron scattering lengths (Section 2.1.3.2) do not simply vary with *Z*, permitting NPD to detect light elements (e.g. H, D, C, and O) with a wide range of data collection. Comparison of the X-ray and neutron atomic form factors of ${}^{12}_{6}\mathrm{C}$ with increasing momentum transfer $\boldsymbol{Q} = 4\pi \sin\theta/\lambda$ (Section 2.1.3.1) can be seen as an example in Figure 2.2.

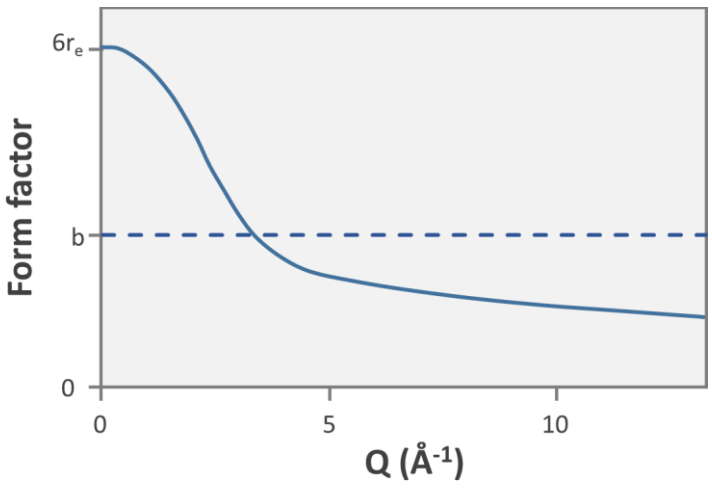

Figure 2.2 | Comparison of the X-ray and neutron atomic form factors for ${}^{12}_{6}\mathrm{C}$ as a function of the momentum transfer $\boldsymbol{Q} = 4\pi \sin\theta/\lambda$. While The X-ray form factor, having a

maximum value comparable to the atomic number Z= 6, decays to zero with increased the sin θ/λ (blue line), the neutron form factor is independent of sin θ/λ (dotted line) [3].

The details of how and why neutrons scatter differently from X-rays will be given in section 2.1.3. Here, it is sufficient to have a short summary as follows:

I) Unlike XRD, the intensity of NPD depends on the neutron scattering length/cross section (section 2.1.3.2), not atomic number-dependent. Thus, light elements (e.g. H, Li, C, and O) are more visible and adjacent elements in the periodic table are often readily distinguished.

II) Isotopes have different neutron scattering lengths, making contrast observation in random structures and allowing detection of different isotope behaviours such as H and D.

III) Neutron scattering is weak with a typically low absorption. This property can have positive and negative effects. On the positive side, neutrons can penetrate deeply into the sample of interest, allowing the study of bulk properties of the sample. On the negative side, neutron experiments require a greater quantity of sample (typically $\geq$ 1 g) and a relatively long time for data collection compared to X-ray experiments.

IV) No atomic form factor is applied in NPD, thus permitting a data collection over a large range of interplanar spacings d (i.e. $\boldsymbol{Q}$ range).

V) Neutrons also interact with unpaired electrons via magnetic dipole interaction which is beneficial for study of magnetic structure.

Although the powder X-ray and neutron diffraction techniques have different scattering characteristics, they both intrinsically suffer in peak overlapping that obstructs the accuracy of structure refinement. To achieve a better peak separation, it is thus essential to perform the powder diffraction experiments by using high resolution diffractometers especially whose X-rays and neutrons are generated by synchrotron and high-flux neutron

sources. In Chapter 3 and 4, I will discuss on the use of the high-resolution NPD supported by the high-resolution synchrotron X-ray diffraction (SXRD) for analysis of the structural changes in UiO-67 type MOFs under external stimuli.

2.1.2) Structure determination from powder diffraction data

2.1.2.1) Rietveld method

The most commonly used procedure for structure refinement from the powder diffraction data is the Rietveld method, developed by Hugo M. Rietveld [4]. The fundamental idea behind this method is to refine user-selected parameters to minimize the weighted differences between an experimental pattern and a model (calculated) pattern based on the postulated crystal structure and instrumental parameters by means of a non-linear least square regression. The Rietveld method circumvents a peak overlapping problem and allows an entire observed pattern to be used effectively. It can be used to refine structural parameters of crystalline solids such as cell parameters, atomic coordinates, site occupancies, and thermal displacements. According to the non-linear least squares algorithm, the square sum of differences between the N observed and calculated step-by-step intensities is subjected to minimisation:

$$\sum_i^N (w_i \left(y_{obs,i} - y_{calc,i}\right)^2) \rightarrow Min \qquad \textit{Equation 2. 2}$$

where w_i is the weight usually estimated from statistics on the observed $y_{\mathrm{obs},i}$ as $w_i \approx 1/y_{\mathrm{obs},i}$.

The calculated intensity $y_{\mathrm{calc},i}$ consists of mostly non-linear analytic functions and is defined as

$$y_{calc,i} = \sum_p \left(S_p \sum_{\boldsymbol{s}(p)} (\left|F_{calc,\boldsymbol{s},p}\right|^2 \boldsymbol{\Phi}_{\boldsymbol{s},p,i} Corr_{\boldsymbol{s},p,i})\right) + Bkg_i \qquad \textit{Equation 2. 3.}$$

For the above equation, p refers to the crystalline phase of the sample. Hence, the outer sum covers all the phases p involved in the diffraction pattern. The inner sum operates over all Bragg reflections **s**= *(hkl)* of a p phase, which corresponds to the position i in the diffraction pattern. S_{p} is the scaling factor, related to the weight fraction of phase p and thus contributing to the intensity of each phase. $F_{\mathrm{calc},\boldsymbol{s},\mathrm{p}}$ is called the structure factor of which the squared complex is proportional to the intensity of a Bragg reflection $\boldsymbol{s}$. This function is the vector sum of atomic form factors (for X-ray diffraction) or coherent scattering lengths (for neutron diffraction). The profile function $\boldsymbol{\Phi}_{\boldsymbol{s},p,i}$ represents the profile point i with respect to the position $s = |\boldsymbol{s}| = 2\sin\theta/\lambda$ of the Bragg peak $\boldsymbol{s}$ for the phase p. $Corr_{\boldsymbol{s},\mathrm{p},i}$ is the correction factor that need to be applied to the reflection intensities. This factor in fact has contributions from various correction factors such as multiplicity, Lorentz-polarisation factor, preferred orientation, etc. The final term is the observed background $\mathrm{Bkg_i}$ at position i in the diffraction profile.

This approach requires a reasonable starting model for the entire powder pattern, i.e. all the starting parameters need to be sensibly valued. To simplify and hence maximise the success rate of the Rietveld refinement, it can be useful to separate the above complex function into several subgroups of parameters depending on their relationship to the diffraction pattern [5]: I) peak position s (simply referred to as θ or d- spacing) is geometrically determined by the crystal lattice, space-group symmetry and instrumental profile; II) integrated peak intensity $\left|F_{calc,\boldsymbol{s},\mathrm{p}}\right|^2 Corr_{\boldsymbol{s},\mathrm{p}}$) is determined by the crystal structure and geometrical factors; III) peak profile $\boldsymbol{\Phi}_{\boldsymbol{s},\mathrm{p},i}$ is originated from the contributions of instrument and sample microstructure; IV) background Bkg_i is affected by both the

instrument and the sample, namely thermal diffuse scattering, incoherent scattering, inelastic scattering, sample environment and so on.

2.1.2.2) Judging quality of Rietveld refinement

Before assessing the quality of a Rietveld refinement, one should first visually check how well the calculated diffraction pattern fits the observed pattern. This is to verify any gross errors in the structural model used for the refinement. For a well-fitted diffraction pattern, the difference between the observed and the calculated diffraction profiles should be as low as possible without any poorly-fitted peaks. If any significant peak difference is observed, it may reflect an unsuitability of the proposed model.

Like other curve/peak fitting techniques, various statistical agreement (*R*-) factors can be used for determination of the quality of a Rietveld refinement. The most common one is the so-called profile *R*-factor, which is a measure of the difference between the observed and the calculated profiles:

$$R_p = \frac{\sum_{i=1}^{N} |y_{obs,i} - y_{calc,i}(p)|}{\sum_{i=1}^{N} y_{obs,i}} \qquad \textit{Equation 2. 4}$$

where $y_{\mathrm{obs},i}$ is the observed Bragg peak intensity at the i^{th} step,

$y_{\mathrm{calc},i}$ is the calculated Bragg peak intensity at the i^{th} step,

This simple sum of all differences relative to the sum of all observed values has several problems. First, it tends to overemphasise the strong reflections and it does not take experimental uncertainties into account. Both problems are overcome by applying a weighting scheme, where every data point get a weight W_i (see below):

$$R_{wp} = \sqrt{\frac{\sum_{i=1}^{N} w_i (y_{obs,i} - y_{calc,i}(p))^2}{\sum_{i=1}^{N} w_i {y_{obs,i}}^2}} \qquad \textit{Equation 2. 5}$$

Where w_i is the weight coefficient at the i^{th} step.

This *R*-factor is directly related to the Rietveld objective function of eq. 2.2.

The next problem is related to the influence of the background. If the peak to background ration is low, the profile *R*-value can be dominated by the well-fitted background points and relatively insensitive to the structural model. To avoid this problem, it is useful to subtract the background from the observed step scan intensities in the denominator:

$$R'_p = \frac{\sum_{i=1}^{N} |y_{obs,i} - y_{calc,i}(p)|}{\sum_{i=1}^{N} |y_{obs,i} - Bkg_i|} \qquad \textit{Equation 2. 6}$$

and

$$R'_{wp} = \sqrt{\frac{\sum_{i=1}^{N} w_i (y_{obs,i} - y_{calc,i}(p))^2}{\sum_{i=1}^{N} w_{i(y_{obs,i} - Bkg_i)^2}}} \qquad \textit{Equation 2. 7}$$

Despite these corrections, profile *R*-values of different refinements can only be compared for identical statistical conditions. The so-called expected *R*-factor, which is mainly determined by counting statistics, give a measure of the best profile fit:

$$R_{exp} = \sqrt{\frac{N-P}{\sum_{i=1}^{N} w_i y_{obs,i}^2}} \qquad \textit{Equation 2. 8}$$

and

$$R'_{exp} = \sqrt{\frac{N-P}{\sum_{i=1}^{N} w_{i(y_{obs,i} - Bkg_i)^2}}} \qquad \textit{Equation 2. 9}$$

with the number of observed data points *N* and the number of parameters *P*. On an absolute basis, the ratio χ between the weighted-profile *R*-value and the expected *R*-value (also called goodness of fit, *GOF*) is another good measure on the quality of the Rietveld refinement:

$$\chi^2 = \frac{{R_{wp}}^2}{{R_{exp}}^2} = \frac{\sum_{i=1}^{N} w_i (y_{obs,i} - y_{calc,i}(p))^2}{N - P} \qquad \textit{Equation 2. 10}$$

There have been many critical discussions on the fitting values to be accepted. For a general powder diffraction pattern, a well-fitted Rietveld refinement should have a R_{wp} value below 12% and a *GOF* value should reach unity [6]. However, a low R_{wp} value can be more difficult to obtain for a lower symmetric (more complex) crystal structure whose Bragg peaks are more observed [7]. As a result, acceptable R_{wp} values for crystal structures with low symmetry (e.g. monoclinic and triclinic) could be up to 15%. All the profile *R*-factors may be depreciated by a poorly-defined peak shape, even though a correct crystallographic model is used. On the other hand, the fitting values may look satisfactory even we use a wrong crystallographic model because the background is well fitted [8]. When a diffraction profile is derived from a high-resolution synchrotron or neutron source, a R_{exp} factor gets drastically reduced as the number of observables *N* is much higher than that of a laboratory X-ray source, as a consequence of better detector resolution and longer counting time. In this circumstance, the R_{exp} value is much lower than the R_{wp} one and hence renders a large χ^2 [3]. This indicates a less reliability of χ^2 when dealing with a high quality data from the synchrotron and neutron facilities. Thus, more meaningful factors such as R_{wp} should be used alternatively since it tells us directly how well the calculated pattern matches with the observed one. Finally, knowledge of crystallography is indeed a key factor to achieve a successful refinement. Without a sensible crystal structure, a refinement result will become meaningless even all the measures of fit are tremendously low.

2.1.2.3) Le Bail extraction

To facilitate a successful structure determination by the Rietveld method (2.1.2.1), it is helpful to have sensible starting parameters such as lattice parameters, space group, peak shape function factors, and background. The best way to achieve these parameters is to perform a structure-independent whole powder pattern fitting (WPPF) prior to the Rietveld refinement. Then, the obtained parameters can be straightforwardly transferred to the Rietveld analysis. The most frequently used WPPF methods are the Pawley (Pawley 1981) and the Le Bail (Le Bail, *et al*., 1988; Le Bail, 2005) methods. Both methods are based on the use of non-linear least squares minimisation but how they extract the integrated peak intensities are different. As these methods refine over an entire powder pattern, even the overlapped peaks can be calculated during the refinement, despite in a purely convoluted way. In this thesis, all the diffraction patterns of the MOF samples were primarily refined by the Le Bail approach.

Comparing to the regular Rietveld refinement, the Le Bail method follows the same least squares procedure to refine all parameters but exclude structural parameters: atomic coordinates, site occupancies, and thermal displacements. If we consider a diffraction pattern with a single phase, the Rietveld expression in Equation 2.2 can be reduced to

$$y_{calc,i} = S\sum_{\boldsymbol{s}}(\left|F_{calc,\boldsymbol{s}}\right|^2 \boldsymbol{\Phi}_{\boldsymbol{s},i} Corr_{\boldsymbol{s},i}) + Bkg_i. \qquad \textit{Equation 2. 11}$$

Without information on the structural parameters, the structure factor $\left|F_{\mathrm{calc},\boldsymbol{s}}\right|^2$ is initially treated as an arbitrary value, e.g. 1.0.

$$\left|F_{calc,\boldsymbol{s}}\right|^2 = 1.0. \qquad \textit{Equation 2. 12}$$

During the iteration process, the $\left|F_{calc,\boldsymbol{s}}\right|^2$ is freely refined like a virtual structure model to get a new value as

$$\left|F_{calc,\boldsymbol{s}}\right|^2_{new} = \frac{S\sum_{\boldsymbol{i}}(y_{obs,i}\left|F_{calc,\boldsymbol{s}}\right|^2 \boldsymbol{\Phi}_{\boldsymbol{s},i} Corr_{s,i})}{y_{calc,i}} \qquad \textit{Equation 2. 13}$$

The obtained $\left|F_{\mathrm{calc},\boldsymbol{s}}\right|^2_{\mathrm{new}}$ is subsequently used as a starting value for the next cycle of iteration until the convergence is done:

$$\left|F_{calc,\boldsymbol{s}}\right|^2 = \left|F_{calc,\boldsymbol{s}}\right|^2_{new}. \qquad \textit{Equation 2. 14}$$

2.1.3) Basic concepts of Neutron Scattering

While an X-ray electromagnetically interacts with electron clouds in a sample, a neutron interacts with atomic nuclei via the very short-range strong nuclear force. According to the de Broglie hypothesis, a neutron exhibits both particle-like and wave-like behaviours: it is a subatomic particle having zero charge, a spin ½, a mass close to that of a proton, and a wavelength λ. The neutron wavelength is associated to the de Broglie relationship as

$$\lambda = \frac{h}{mv} \qquad \textit{Equation 2. 15}$$

where h is Planck's constant, m is the neutron mass (1.67945×10^{-27} kg), and v is its velocity.

The associated wave vector $\boldsymbol{k}$ is given by

$$\boldsymbol{k} = \frac{2\pi}{\lambda} \qquad \textit{Equation 2. 16}$$

This allows the neutron momentum p to be written as

$$p = mv = \hbar \boldsymbol{k} \qquad \textit{Equation 2. 17}$$

where ħ is the reduced Planck constant.

Then, the neutron energy E is

$$E = \frac{1}{2}mv^2 = \frac{\hbar^2 \boldsymbol{k}^2}{2m} \qquad \textit{Equation 2. 18.}$$

For a thermal neutron corresponding to a moderator temperature of ca. 300 K, its energy is comparable to that of interatomic/intermolecular forces and its wave vector similar to interplanar *d*-spacings. This enables the study of structural and dynamical properties of materials.

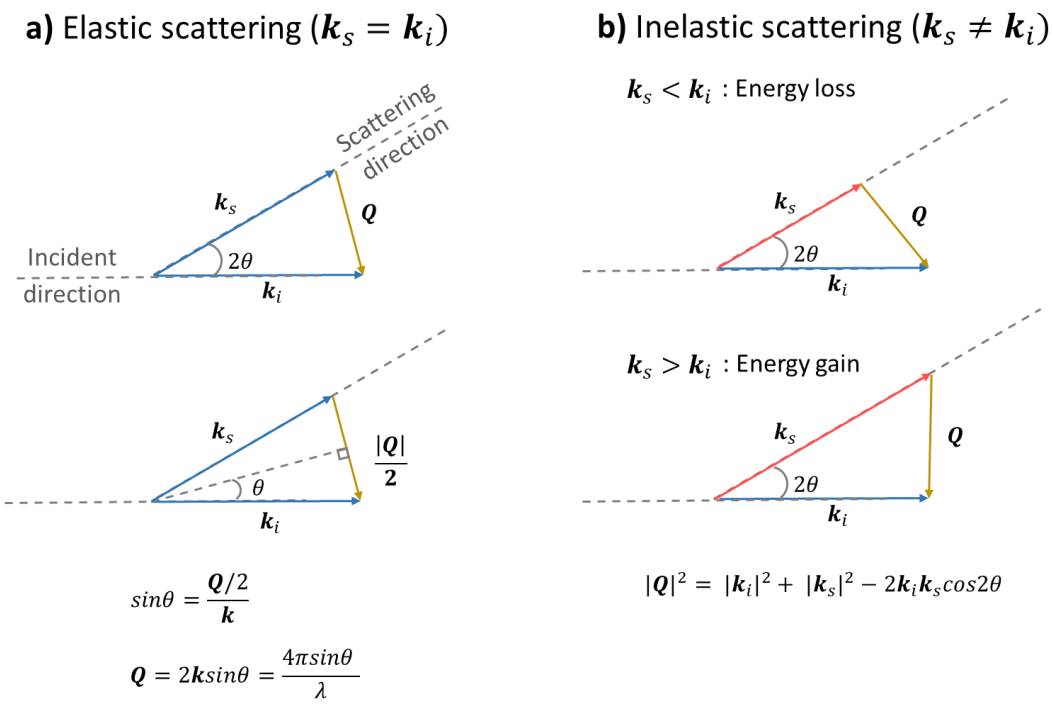

Figure 2.3 | Scattering triangles for elastic scattering (**a**) and inelastic scattering (**b**). During the scattering process, the scale and direction of the scattering vector $\boldsymbol{Q}$ is determined by the magnitudes of the incident wave vector $\boldsymbol{k}_i$ and the scattered wave vector $\boldsymbol{k}_s$ with respect to the scattering angle 2θ [9].

When a neutron collides with a scattering atom in matter, the total momentum and energy are preserved: the energy loss from the scattered neutron is gained by the sample.

The energy transfer $\hbar\omega$ is then written as

$$E = \hbar\omega = \hbar(\omega_i - \omega_s) \qquad \textit{Equation 2. 19}$$

where ω_{i} and ω_{s} are, respectively, the incident and the scattered angular frequencies.

The momentum transfer $\hbar Q$ is also given by

$$\hbar\boldsymbol{Q} = \hbar(\boldsymbol{k}_i - \boldsymbol{k}_s) \qquad \textit{Equation 2. 20}$$

and so,

$$\omega = \frac{\hbar}{2m}(\boldsymbol{k}_i{}^2 - \boldsymbol{k}_s{}^2) \qquad \textit{Equation 2. 21}$$

where k_{i} and $k_{\mathrm{s}}$are the incident and the scattered wave vector, respectively. The $\boldsymbol{Q} = \boldsymbol{k}_{\mathrm{i}} - \boldsymbol{k}_{\mathrm{s}}$ is known as the scattering vector and the relationship between these parameters can be described by using the so-called scattering triangles as depicted in Figure 2.1.

2.1.3.1) Elastic and inelastic scattering

There are two types of scattering: I) elastic and II) inelastic. The former occurs when there is no change in the energy of the incident neutron during the interaction; or in terms of the neutron's wave vector, the direction of the wave vector changes but not its magnitude ($\boldsymbol{k}_{\mathrm{s}} = \boldsymbol{k}_{\mathrm{i}}$ so $\hbar\omega = 0$, see Figure 2.3a). The magnitude of $\boldsymbol{Q}$ then depends only on the scattering angle 2θ between the incident and the scattered wave vectors. By using trigonometry, $\boldsymbol{Q}$ of an elastic scattering is written as

$$\boldsymbol{Q} = 2\boldsymbol{k}sin\theta = \frac{4\pi sin\theta}{\lambda} \qquad \textit{Equation 2. 22}$$

On the other hand, an inelastic scattering happens once a neutron exchanges energy and momentum with a scattered atom, causing both the direction and the magnitude of the neutron's wave vector to change (Figure 2.3b). This event results in either an energy loss ($\boldsymbol{k}_\mathrm{s} < \boldsymbol{k}_\mathrm{i}$) or an energy gain ($\boldsymbol{k}_\mathrm{s} > \boldsymbol{k}_\mathrm{i}$) of the scattered neutron. The scattering vector $\boldsymbol{Q}$ is hence dependent on both the scattering angle 2θ and the energy transfer $\hbar\omega$ and its magnitude can be derived from

$$|\boldsymbol{Q}|^2 = |\boldsymbol{k}_i|^2 + |\boldsymbol{k}_s|^2 - 2\boldsymbol{k}_i\boldsymbol{k}_s cos2\theta \qquad \textit{Equation 2. 23}$$

2.1.3.2) Scattering cross section

A scattering cross section σ can be used to determine how strongly an incident neutron interacts with a target nucleus; the larger the cross section the more likely an interaction. It is measured in a unit of barn (1 barn = 10×10^{-28} m^2) which represents an effective area presented by a nucleus to a passing neutron. In most neutron scattering experiments, scientists measure the double-differential scattering cross section defined as $\frac{\mathrm{d}^2\sigma}{\mathrm{d}\Omega \mathrm{d}E}$. This parameter is equivalent to the number of neutrons scattered into the solid angle $\mathrm{d}\Omega = \sin\theta\, \mathrm{d}\theta \mathrm{d}\phi$ with the energy range of $\mathrm{d}E$ (see Figure 2.4). The total cross section of each scattering atom is derived by integration of overall solid angles and energies:

$$\sigma = \int d\Omega \frac{d\sigma}{d\Omega} = \int dE \int d\Omega \frac{d^2\sigma}{d\Omega dE} = 4\pi\langle b^2 \rangle \qquad \textit{Equation 2. 24}$$

where b is the scattering length which varies irregularly from one atom to another or even from one isotope to another.

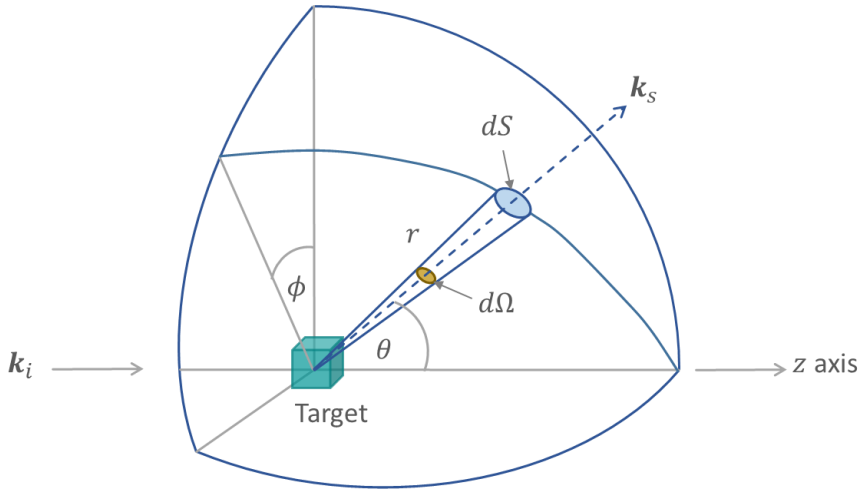

Figure 2.4 | Geometry of the neutron scattering experiment (Marshall and Lovesey 1971; Squirs 1978).

2.1.3.3) Coherent and incoherent scattering

As atoms of the same element usually have different isotopes and nuclear spin states, it is helpful to decompose the total cross section σ into two contributions; coherent and incoherent scatterings (σ_{coh} and σ_{inc}, respectively). An example of the decomposition is simply displayed in Figure 2.5. The coherent part corresponds to an average over all isotopes and spin states:

$$\sigma_{coh} = 4\pi\langle b\rangle^2 \qquad \textit{Equation 2. 25}$$

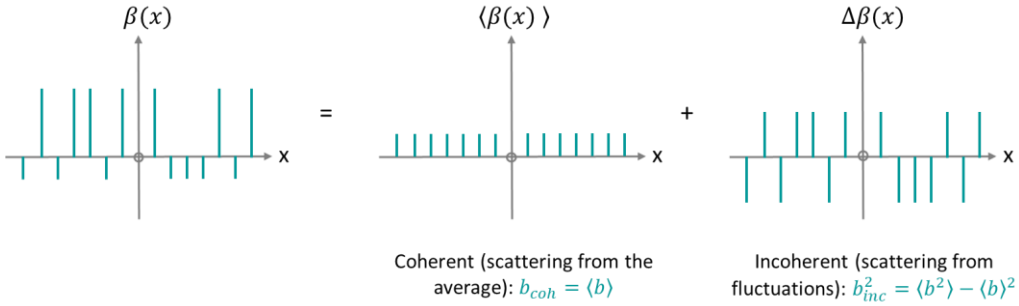

Figure 2.5 | Illustration of a very simple one-dimensional example of how a function, *β(x)*, can be decomposed into the sum of an average pattern, $\langle\beta(x)\rangle$, and a set of random fluctuations, $\Delta\beta(x)$ [2].

While the incoherent part is defined by the difference between the total and the coherent cross-sections:

$$\sigma_{inc} = 4\pi(\langle b^2 \rangle - \langle b \rangle^2) \qquad \textit{Equation 2. 26}$$

The neutron scattering lengths and cross-sections of the elements involved in MOF synthesis which is a central of this thesis are shown in Table 2.1.

Table 2.1 | Neutron scattering lengths (b) and cross sections (σ) of the elements typically used to synthesise MOFs [10].

Element	$\boldsymbol{b_{coh}}$ (fm)	$\boldsymbol{b_{inc}}$ (fm)	$\boldsymbol{\sigma_{coh}}$ (barn)	$\boldsymbol{\sigma_{inc}}$(barn)	$\boldsymbol{\sigma_{total}}$ (barn)
H	-3.74	25.27	1.76	80.27	82.03
D	6.67	4.04	5.59	2.05	7.64
C	6.65	-	5.55	0	5.55
N	9.36	-	11.01	0.50	11.51
O	5.80	-	4.23	0	4.23
Al	3.45	0.26	1.49	0.01	1.50
Cl	11.65	-	17.06	4.76	21.82
V	-0.38	-	0.02	5.08	5.10
Zr	7.16	-	6.44	0.02	6.46

Notes: b_{coh} is the bound coherent scattering length; b_{inc} is the bound incoherent scattering length; σ_{coh} is the coherent scattering cross section; σ_{inc} is the incoherent scattering cross section; σ_{total} is the total bound scattering cross; 1 barn = 100 fm^2= 10^{-28} m^2; Al has a

minimum neutron scattering cross-section so it is commonly used as a sample holder; V has a small scattering cross-section with almost incoherent contribution (i.e. nearly zero coherent contribution) making it suitable for standard calibration.

Similarly, the measured intensity can be also divided into coherent and incoherent parts.

$$\frac{d^2\sigma}{d\Omega dE} = \frac{\boldsymbol{k_S}}{\boldsymbol{k_i}}\frac{1}{4\pi\hbar}[\sigma_{coh}S_{coh}(\boldsymbol{Q},\omega) + \sigma_{inc}S_{inc}(\boldsymbol{Q},\omega)] \quad \textit{Equation 2. 27}$$

$$S(\boldsymbol{Q},\omega) = S_{coh}(\boldsymbol{Q},\omega) + S_{inc}(\boldsymbol{Q},\omega) \quad \textit{Equation 2. 28}$$

where $S(\boldsymbol{Q},\omega)$is the scattering function or dynamical structure factor.

The scattering function is the four-dimensional Fourier transform of the van Hove correlation function $G(\boldsymbol{r},t)$ and is given by

$$S(\boldsymbol{Q},\omega) = \frac{1}{2\pi}\int dt exp(-i\omega t)\int d\boldsymbol{r} exp(i\boldsymbol{Q}\cdot\boldsymbol{r})G(\boldsymbol{r},t) \quad \textit{Equation 2. 29}$$

It is useful to correlate the scattering function to the intermediate scattering function, $I(\boldsymbol{Q},t)$, which is described as

$$I(\boldsymbol{Q},t) = \int d\boldsymbol{r} exp(i\boldsymbol{Q}\cdot\boldsymbol{r})G(\boldsymbol{r},t) \quad \textit{Equation 2. 30}$$

And so

$$S(\boldsymbol{Q},\omega) = \frac{1}{2\pi}\int dt exp(-i\omega t)\, I(\boldsymbol{Q},t) \quad \textit{Equation 2. 31}$$

The inversion of Fourier transform can provide another expression for $I(\boldsymbol{Q},t)$:

$$I(\boldsymbol{Q},t) = \int d\omega exp(i\omega t)S(\boldsymbol{Q},\omega) \quad \textit{Equation 2. 32}$$

The coherent and incoherent scattering functions are associated with the pair- and self- correlation functions:

$$S_{coh}(\boldsymbol{Q},\omega) = \frac{1}{2\pi}\int dt exp(-i\omega t)\int d\boldsymbol{r} exp(i\boldsymbol{Q}\cdot\boldsymbol{r})G_p(\boldsymbol{r},t) \qquad \textit{Equation 2. 33}$$

$$S_{inc}(\boldsymbol{Q},\omega) = \frac{1}{2\pi}\int dt exp(-i\omega t)\int d\boldsymbol{r} exp(i\boldsymbol{Q}\cdot\boldsymbol{r})G_s(\boldsymbol{r},t) \qquad \textit{Equation 2. 34}$$

The pair-correlation function $G_{\mathrm{p}}(\boldsymbol{r},t)$ corresponds to the possibility of finding any particle at a position $\boldsymbol{r}$ at time t, giving information on spatial correlations and collective motions of overall scattering particle in the sample. In contrast, the self-correlation function $G_{\mathrm{s}}(\boldsymbol{r},t)$ represents the possibility of finding a particle at a position $\boldsymbol{r}$ at time, if the same particle was at the origin at time zero; i.e. the interaction of an incident neutron with the same atom but at different positions and different time). This, as a result, tells us about the behaviour of individual scattering particle in the sample such as diffusion, rotation, and incoherent vibration.

2.1.4) Neutron powder diffraction (NPD)

Neutron powder diffraction (NPD) is an elastic scattering technique that measures the differential cross section, $\frac{d\sigma}{\mathrm{d}\Omega}$, which corresponds to the number of neutrons scattered through angle 2θ per second into the solid angle $\mathrm{d}\Omega$ (Figure 2.4). Hence, this technique provides an information on static structural properties of materials.

Similar to the well-known X-ray and electron diffractions, the Bragg's law ($2d_{hkl}\sin\theta = n\lambda$, Equation 2.1) is also applied to describe the interference pattern of neutrons scattered by atoms in a sample. As NPD is elastic ($\boldsymbol{k}_{\mathrm{i}} - \boldsymbol{k}_{\mathrm{s}}$ and $\omega = 0$), a combination of Equation 2.1 and 2.21 where $n = 1$ is given by

$$\frac{2\pi}{\boldsymbol{Q}} = d_{hkl} = \frac{\lambda}{2sin\theta} \qquad \textit{Equation 2. 35}$$

A correlation between a scattering wave vector $\boldsymbol{Q}$ in real space and a reciprocal lattice vector $\boldsymbol{G}_{hkl}$ can also written as

$$\left(\frac{d\sigma}{d\Omega}\right)_{Bragg} = N\frac{(2\pi)^3}{V_0}\sum_{hkl}\delta(\boldsymbol{Q}-\boldsymbol{G}_{hkl})|F_{hkl}(\boldsymbol{Q})|^2 \qquad \textit{Equation 2. 36}$$

where the unit-cell structure factor $F_{hkl}(\boldsymbol{Q})$ is given by

$$F_{hkl}(\boldsymbol{Q}) = \sum_d \boldsymbol{b}_d e^{i\boldsymbol{Q}d}e^{-W_d} \qquad \textit{Equation 2. 37}$$

and W_d is called the Debye-Waller factor associated to thermal motions of atoms and hence peak broadening. To reduce the effect of the peak broadening, ones should collect the NPD data at cryogenic temperature.

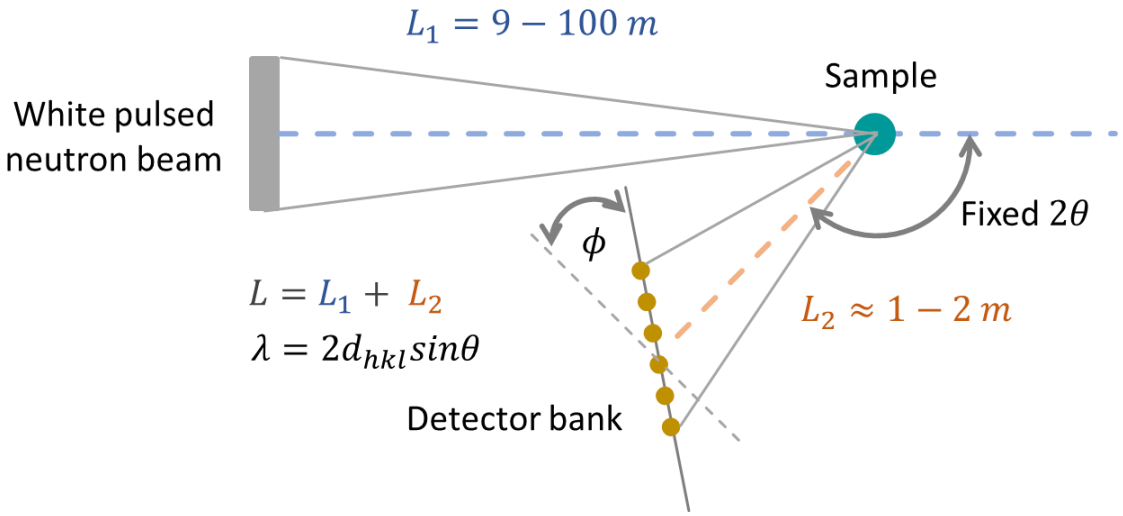

Figure 2.6 | Schematic illustration of the time-of-flight (TOF) instrumental configuration for NPD measurement. A broad spectrum of neutron energies (proportional to velocities) from a pulsed source is separated by time of arrival, facilitating the measurement of different interplanar distances d_{hkl} at a fixed scattering angle 2θ.

At a neutron pulsed source such as ISIS, neutrons are generated by high-energy protons, primarily accelerated in a proton synchrotron, strike into a heavy-metal target (e.g.

Ta, W, or Pb) [11]. The concept of time of flight T is universally applied to determine λ over a known total flight path L of the scattered neutron from the source (T=0) to the sample L_1 and subsequently over the scattering path to the detector L_2 as shown in Figure 2.5. Based on the de Broglie relationship in Equation 2.14 together with the measurable T and L of the neutron, we can calculate its wavelength λ by

$$\lambda = \frac{hT}{mL}. \qquad \textit{Equation 2. 38}$$

where λ is in Å, T is in μs and L is in m.

Combining Equation 2.38 with the Bragg's law in Equation 2.1, we obtain a relationship between T and d_{hkl} as

$$d_{hkl} = \frac{T}{505.56Lsin\theta}. \qquad \textit{Equation 2. 39}$$

2.1.5) Inelastic neutron scattering (INS)

INS is a spectroscopic technique that uses neutrons to probe atomic and molecular motions in solids [12]. In direct comparison to conventional infrared and Raman spectroscopies whose spectra depend on electro-optic interactions, INS has tremendous advantages over them:

I) INS spectra are readily and accurately modelled.

Observed INS intensities are directly related to the atomic displacements of the scattering atom without any complications from electro-optic parameters. Moreover, the vibrational frequencies and intensities of most molecular systems can be accurately simulated by means of evolving *ab-initio* calculations, providing us an invaluable information on the dynamics of molecular structures.

II) INS spectra are sensitive to hydrogen atom vibrations.

Owing to the very large neutron incoherent scattering cross section of H atom, this allows about ten times higher contrast of H signal to be observed over other elements.

III) Unlike optical spectroscopic techniques, no selection rules are applied to INS spectra.

All vibrations are active in INS and principally measureable simply because an incident neutron (ca. 1 atomic mass unit) transfer momentum to a scattering atom. Measurement of INS is not limited to the Brillouin zone centre, contrast to the optical methods. The observed INS intensity is therefore proportional to concentration of each element in a sample.

IV) Neutrons are highly penetrating and so can probe bulk properties of the sample.

Neutrons can penetrate into a typical solid sample with the order of millimetres in depth and pass readily through the walls of the sample container, allowing the observation of bulk properties rather than a molecule adsorbed on a sample surface.

V) INS spectrometers cover a wide range of molecular vibrations.

An INS spectral region of 16-4000 cm^{-1} is closely associated to both intramolecular and lattice vibrations (Figure 2.7). The lower energy transfer below 400 cm^{-1}, where key information on the lattice dynamics and translational/rotational motions of adsorbed gas molecules is increasingly found, is readily accessible. Moreover, modern INS instruments also provide a quality of spectra that mostly equivalent to that of IR and Raman analogue under the same system and conditions.

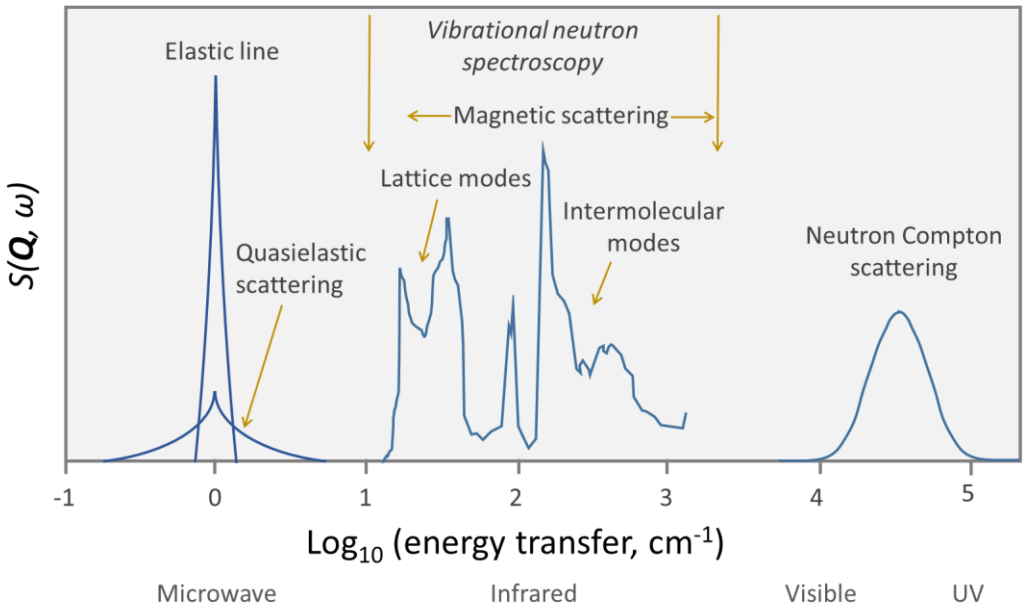

Figure 2.7 | INS spectroscopy in comparison with optical (photon) spectroscopies. The neutron scattering intensity in the y axis is represented by the neutron scattering function, $S(\boldsymbol{Q},\omega)$ [12]. An observed INS spectrum elucidates a change of the neutron scattering intensity as a function of the energy transfer and the momentum transfer. The spectrum is typically expressed as a neutron energy loss resulting from the energy transfer from the incident neutrons to the individual scattering atom in a sample. The energy range for the INS experiment is 16-4000 cm^{-1} which is comparable to that of mid-infrared region.

2.1.5.1) INS experiments

INS experiments aim to determine the scattering intensity $S(\boldsymbol{Q},\omega)$ as a function of $\boldsymbol{Q}$ and ω. Thus, the knowledge of energy transfer and momentum transfer previously expressed in Equation 2.12- 2.14 is required. The INS experiments throughout this thesis were performed on TOSCA instrument [13], an indirect geometry time-of-flight spectrometer at the ISIS pulsed spallation neutron source at the Rutherford Appleton Laboratory. TOSCA is optimised for high-resolution vibrational spectroscopy in the energy-transfer range 0–4000 cm^{-1} (0 - 500 meV) with the best results below 2000 cm^{-1},

(250 meV). Details of the experiments using TOSCA is given in the 2.2.3 Characterisation techniques and Chapter 5. In this stage, I will mainly focus on how the instrument works and how to acquire the data from it.

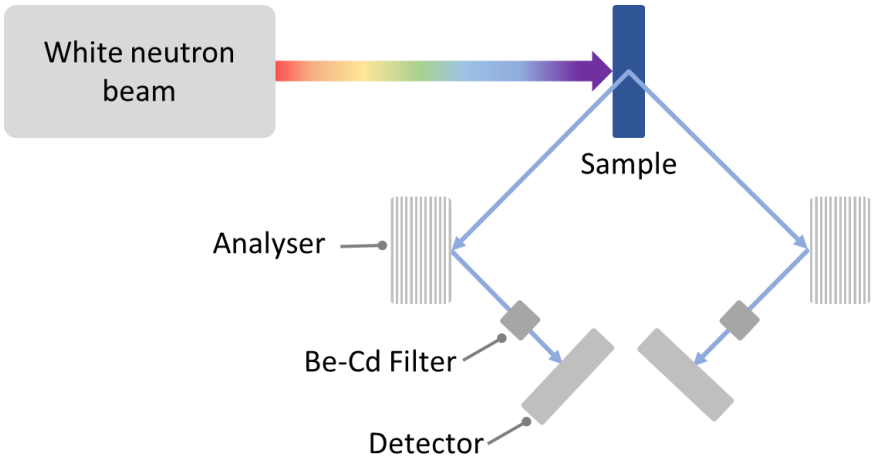

Figure 2.8 | Schematic diagram of the TOSCA indirect geometry time-of-flight (TOF) spectrometer.

As mentioned earlier in the NPD section, The INS experiment on TOSCA is also based on measuring the neutron energies/wavelengths by discriminating their time of arrival at the detector [14]. The TOSCA has an indirect geometry of which the final energy of neutron scattered from a sample is fixed by a Be-Cd filter and a pyrolytic graphitic analyser before travelling to the detector (Figure 2.8). For elastic scattering, the energy transferred to the sample is defined as

$$E_{trans} = E_i - E_s \qquad \textit{Equation 2. 40}$$

where E_i and E_s are the incident and scattered energies, respectively. Thus, the relationship between the time of flight T and the energy transfer can be written as

$$T = t_i + t_s = \frac{L_1}{v_i} + \frac{L_2}{v_s} = \frac{L_1}{\sqrt{\frac{2E_i}{m}}} + \frac{L_2}{\sqrt{\frac{2E_s}{m}}} \qquad \textit{Equation 2. 41}$$

Since the values of the scattered energy E_s, the mass of a neutron m, path length from the neutron source to the sample L_1, and path length from the sample to the detector L_2 are all fixed and known, the measurement of the time of flight T allows the calculation of the associated E_i and hence the energy transfer at the sample E_{trans}.

At TOSCA, it is designed in such a way that there is only single value of momentum transfer for each energy transfer, $E_{trans} \approx 16\boldsymbol{Q}^2$. This relation originates from the fact that a mass of neutron is largely close to that of hydrogen (H). Therefore, an inelastic scattering undergoes a significant transfer of momentum and energy. The correlation of the energy transfer and the intensity of the *i*th molecular vibrational transition I_i can be written as:

$$S(\boldsymbol{Q}, \omega_i) \approx I_i \propto \boldsymbol{Q}^2 U_i^2 exp(-\boldsymbol{Q}^2 U_{total}^2)\sigma \qquad \textit{Equation 2. 42}$$

where U_i is the amplitude of vibration of the atoms involved in the vibrational mode. The exponential term in Equation 2.36 is referred to the Debye-Waller factor; U_{total} is the mean square displacement of the molecule whose magnitude is related to the thermal motion. This equation emphasises scientists to perform INS experiments at cryogenic temperature (typically below 50 K) to reduce the value of U_{total} and hence increase the observed intensity of the molecular vibration I_i. The final parameter σ is the neutron scattering cross-section of all the atoms involved in the vibrational mode. The σ varies from one atom/isotope to another and is independent of the chemical environment. The detail of σ is formerly discussed in 2.1.4.2 and Table 2.1. It is worth noting that the neutron scattering cross-section for H is ~80 barns, about ten times larger than all other elements. This indicates that any vibrational modes involved the displacement of H atoms will prominently direct the overall spectrum. This H dependency is indeed a key strength of INS to probe molecular motions of hydrogen-rich materials which will be presented in Chapter 5.

2.1.6) Quasielastic neutron scattering (QENS)

2.1.6.1) Fundamentals and type of information provided

QENS has made many important contributions to the atomistic elucidation of diffusive motions in porous materials. It is a sub-branch of INS that is principally used to monitor an exchange of energy from the neutron to the sample. Unlike regular INS whose energy exchanges involve excitations of molecular vibrations, smaller energy transfers ($\hbar\omega \neq 0 \approx$ neV or μeV) in QENS is related to diffusive motions appearing as wings (peak broadenings) of the elastic peak (see Figure 2.7). Diffusive motions are not quantised and hence the energy transfer can be extremely small. Owing to a large incoherent cross-section of H (~80 barns), QENS is one of the most powerful tools to study diffusions in hydrogenous materials. The diffusion process can be measured on atomic scales of space and time simultaneously, making QENS unique from other conventional methods such as X-ray and Raman spectroscopy. The most valuable feature of QENS is its ability to elucidate atomic diffusions and rotation mechanism which is a core information for a wide range of science areas.

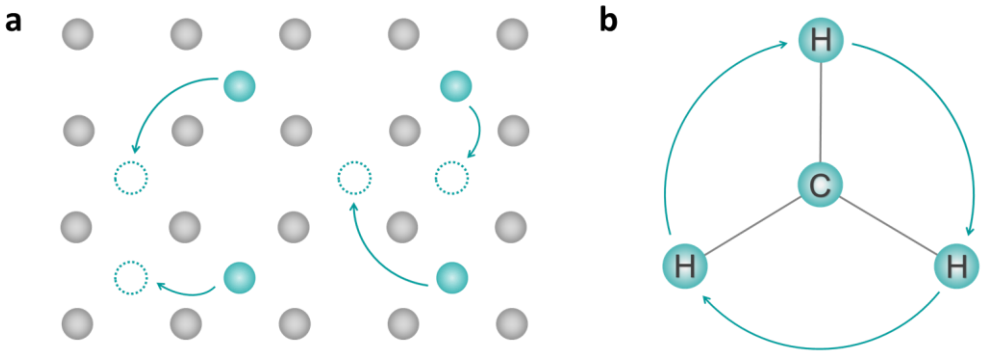

Figure 2.9 | Two types of diffusional motions of a particle (teal sphere) in a porous solid (grey sphere): **a**) translational diffusion and **b**) rotational diffusion such as a methyl ($-CH_3$) group.

Diffusional motions can be categorised into two main subgroups: translational diffusion and rotational diffusion (Figure 2.9) [15]. The former refers to the movement where the centre of mass moves within the crystalline lattice of the observed material. On the other hand, the latter involves rotation/reorientation of a molecule or part of a molecule with its centre of mass remaining static in space. These modes of diffusions can occur simultaneously with different time scales. The relation of the energy resolution of a spectrometer ΔE and the time scale of the diffusive motion τ can be described by the Heisenburg uncertainty principle:

$$\Delta E \cdot \tau \geq \frac{h}{2\pi}. \qquad \textit{Equation 2. 43}$$

From Equation 2.43, we can see that the slower the diffusive motion to be observable, the better energy resolution is required. Table 2.2 provides information on the time scale of diffusive motions, the ΔE required to detect the motion and the instrumental technique to attain this ΔE.

Table 2.2 | Time scale, energy resolution and spectroscopic technique for QENS experiment.

Time scale τ (sec)	**Energy resolution ΔE (μeV)**	**Instrumental technique**
10^{-11}	10-100	Direct-geometry time-of-flight
10^{-9}	0.3-20	Backscattering crystal analyser
10^{-7}	0.005-1	Spin-echo

Momentum transfer $\boldsymbol{Q}$ is another key factor to consider before acquiring a QENS experiment. It can give information on diffusional jump distances and on the geometry of

these jumps. From Equation 2.22 where $\boldsymbol{Q} = \frac{2\pi}{d} = \left(\frac{4\pi}{\lambda}\right)\sin\theta$, the cold neutrons ($E < 5\ meV\ or\ \lambda > 4$ Å typically used in a modern QENS instrument give a $\boldsymbol{Q}$ range from 0.05 to 2.5 Å^{-1}. This range is associated to the distances from 1 to 100 Å, where the atomic or microscopic diffusion takes place.

2.1.6.2) QENS experiments

QENS experiments were conducted on OSIRIS instrument at the ISIS pulsed spallation neutron source at the Rutherford Appleton Laboratory [16]. The OSIRIS is an inverted-geometry and time-of-flight spectrometer. It measures the incident neutron energy by a time-of-flight technique over known neutron path length and selects the single scattered neutron energy by using a single crystal analyser (in the case of this work, a pyrolytic graphite). The resolution can be derived by differentiating the Bragg's equation ($\lambda = 2d\sin\theta$) to give

$$\frac{\Delta E}{E} = 2\frac{\Delta\lambda}{\lambda} = 2\left[(cot\theta \cdot \Delta\theta)^2 + \left(\frac{\Delta d}{d}\right)^2\right]^{1/2}. \qquad \textit{Equation 2. 44}$$

The $\frac{\Delta d}{d}$ value for commonly-used single crystals is as low as 10^{-4} and hence negligible. The $\cot\theta \cdot \Delta\theta$ term then dominates the overall resolution. When the Bragg scattering angle approaches 90°, the $\cot\theta$ tends to reach zero and consequently gives the extremely high energy resolution. Therefore, the inverted-geometry spectrometer is often referred to as a back-scattering spectrometer. In addition to being used as a spectrometer, the OSIRIS can be operated as a long-wavelength diffractometer simultaneously with the QENS measurement. This enables a direct comparison of the data obtained from both quasi-elastic and elastic neutron scatterings. Details of the OSIRIS specification and sample environments are given in section 2.2.3 Characterisation techniques and Chapter 5.

2.1.6.3) Information derived from QENS data

For an atom diffusing in a certain volume, the incoherent scattering law $S_{\mathrm{incoh}}(\boldsymbol{Q},\omega)$ in the elastic region can be commonly separated into two components: purely elastic scattering and quasi-elastic scattering centred at $\omega = 0$ [17]. The law is ascribed as

$$S_{inc}(\boldsymbol{Q},\omega) = I_{elastic}(\boldsymbol{Q})\delta(\omega) + I_{quasi}(\boldsymbol{Q})L(\omega) \qquad \textit{Equation 2. 45}$$

Where $\delta(\omega)$ and $L(\omega)$ are the delta and the Lorentzian functions, respectively. This convoluted equation is fitted with the measured QENS data to achieve diffusive behaviours of the system. The delta function provides information on a geometrical structure (static atoms) and the Lorentzian term gives details of the diffusion rate τ by analysing the shape of its half-width at the half-maximum (HWHM) at a given $\boldsymbol{Q}$ or scattering angle 2θ. For a simple translational diffusion, the relation between τ and $\boldsymbol{Q}$ can give information on a diffusion coefficient D:

$$\tau = \hbar D\boldsymbol{Q}^2 \qquad \textit{Equation 2. 46}$$

This type of diffusion is isotropic and long-range (i.e. small $\boldsymbol{Q}$) obeying the Fick's second law of diffusion [18]. However, such simple motion is not commonly the case, especially for a molecular diffusion in porous materials where a short-range diffusion (a large $\boldsymbol{Q}$ value) usually occurs. The diffusion process in this system normally displays a strong dependency on $\boldsymbol{Q}$ and gives a unique shape of the HWHM [19]. The diffusion can be regulated by several factors such as confined spaces, binding interactions, or concentration gradients of the adsorbates. This short-range diffusion can be described by the so-called jump diffusion models. These models view the diffusion as sequential jumps and contain dynamical parameters such as the diffusion coefficient D, the residence time τ, and the mean-jump length r. For example, the model proposed by Chudley and Elliott (CE) [20] expresses

discrete jumps between the atoms oscillating around a point with a fixed jump length. The model is expressed as:

$$\Gamma(\boldsymbol{Q}) = \frac{\hbar}{\tau}\left(1 - \frac{sin(\boldsymbol{Q}r)}{\boldsymbol{Q}r}\right) \qquad \textit{Equation 2. 47}$$

where τ refers to the time each of the atoms spends at any position before jumping to another position. Then, D can be calculated from:

$$D = \frac{r^2}{6\tau} \qquad \textit{Equation 2. 48}$$

Hall and Ross (HR) [21] proposed another model based on a Gaussian distribution of jump lengths and written as $\rho(r) = \frac{2r^2}{r_0^3\sqrt{2\pi}} \cdot e^{-r^2/2r_0^2}$. The mean-square-displacement (msd, $\langle r^2 \rangle$) is defined as $\langle r^2 \rangle = \int_0^\infty r^2 \rho(r) \mathrm{d}r = 3r_0^2$. The peak broadening is then given by

$$\Gamma(\boldsymbol{Q}) = \frac{\hbar}{\tau}\left(1 - e^{-\boldsymbol{Q}^2 r_0^2/6}\right) \qquad \textit{Equation 2. 49}$$

The model proposed by Singwi and Sjölander (SS) [22] considers an exponential distribution of jump lengths: $\rho(r) = \frac{r}{r_0^2} \cdot e^{-r/r_0}$. Thus, the HWHM of Lorentzian function is achieved by

$$\Gamma(\boldsymbol{Q}) = \frac{\hbar}{\tau}\left(\frac{\boldsymbol{Q}^2 r_0^2}{1+\boldsymbol{Q}^2 r_0^2}\right) \qquad \textit{Equation 2. 50}$$

with a given msd value of $\langle r^2 \rangle = 6r_0^2$.

It is worth noting that the diffusion models expressed in Equation 2.47, 2.49 and 2.50 become a Fickian motion (see Equation 2.46) at the small $\boldsymbol{Q}$ limit which corresponds to a long-range diffusion. Comparison of the different diffusion models are demonstrated in Figure 2.10.

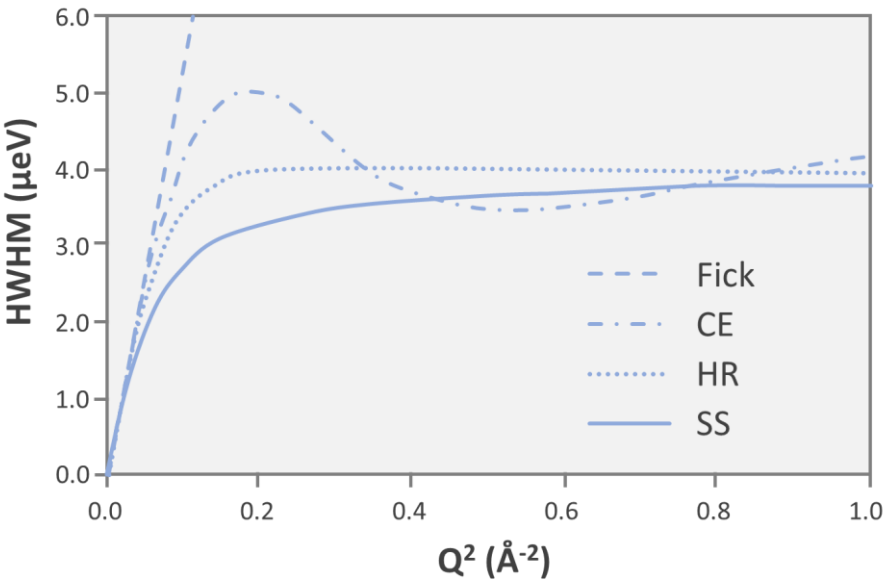

Figure 2.10 | The broadenings (HWHM) of Lorentzian functions as a function of $\boldsymbol{Q^2}$ fitted with different diffusion models: Fick (dashed line), Chudley-Elliott (dotted-dashed line), Hall-Ross (dotted line), and Singwi-Sjölander (solid line). All models are derived from the same values of $\langle r^2 \rangle = 100$ Å^2, jumping rate $\frac{1}{\tau} = 4$ μeV, and hence diffusion coefficient $D = 1.0 \times 10^{-9}$ m^{2}s^{-1} . [23]

In addition to the translational diffusion, localised diffusions such as rotations and molecular reorientations can be observed in a time scale of QENS instruments. The rotational motion features a $\boldsymbol{Q}$-independent HWHM of any fitted Lorentzian functions. This type of diffusion can be further analysed by the elastic incoherent structure factor (EISF) introduced by R. Lechner in 1971. [24] The EISF is defined .as:

$$EISF = \frac{I_{elastic}(\boldsymbol{Q})}{I_{elastic}(\boldsymbol{Q}) + I_{quasi}(\boldsymbol{Q})} = \frac{elastic\ intensity}{total\ intensity} \qquad \textit{Equation 2. 51}$$

where I_{elastic} $(\boldsymbol{Q})$ and I_{quasi} $(\boldsymbol{Q})$ represent the integrated elastic intensity and the integrated quasielastic intensity, respectively. The EISF is a very important factor to analyse the QENS

data since its precise shape as a function of $\boldsymbol{Q}$ refers to the geometry of the diffusion pathway and is sensitive to the model in the certain $\boldsymbol{Q}$ region [15].

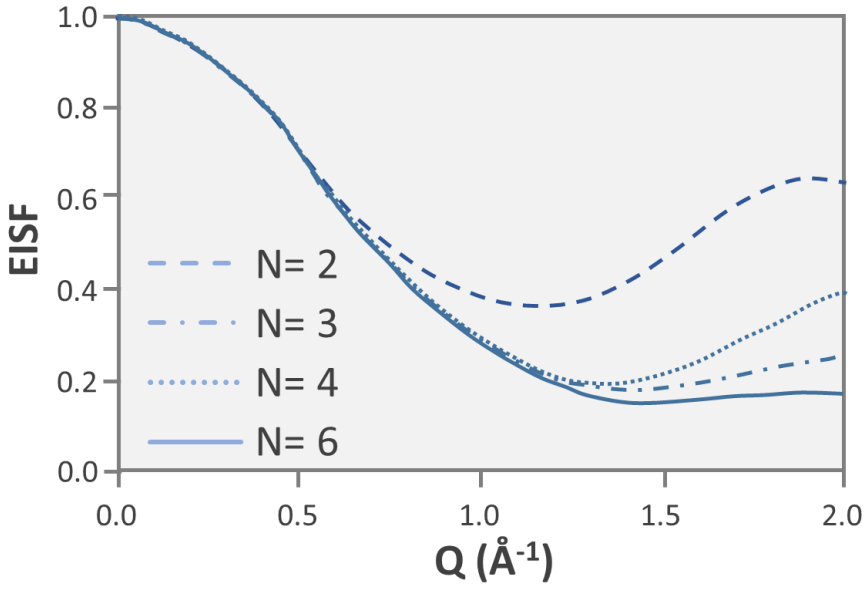

Figure 2.11 | Elastic incoherent structure factor (EISF) as a function of $\boldsymbol{Q}$ simulated from the uniaxial jump rotation model with a constant radius of rotation $r = 2.0$ Å but various equivalent N sites.

Several models are proposed and compared to the experimental EISF to describe the geometry of rotational motions. For instance, isotropic rotation around a sphere, rotational diffusion on a circle, diffusion within a sphere, and uniaxial jump rotation over a circle. [17] An example of the fitted Q-dependent EISF profiles that follow the uniaxial rotation model with different N sites equally spaced on a circle is depicted in Figure 2.11. For the jump between two equivalent sites (N = 2) such as a water molecule bound to a surface, the corresponding EISF is written by

$$EISF = \frac{1}{2}[1 + j_0(\boldsymbol{Q}r)] \qquad \textit{Equation 2. 52}$$

where j_l and r are the l^{th} spherical Bessel function and the jump distance, respectively. In the case of the rotation among three sites on a circle with a radius r, e.g. a methyl ($-CH_3$) group, the EISF is ascribed as

$$EISF = \frac{1}{3}[1 + 2j_0(\boldsymbol{Q}r\sqrt{3})] \qquad \textit{Equation 2. 53}$$

The two site- and three site-jumping models give rise to a single Lorentzian function of the quasielastic component of the scattering law (Equation 2.45) and lead to a consequent ***Q***-independency of the HWHM.

For the complex systems where multiple dynamical processes are coupled, the interpretation of QENS data may be substantially supported by the use of molecular dynamics simulations (MD). This is the key strength of QENS over other dynamics-probing techniques since its dynamics length and timescale match well with those of the MD simulations. The modern MD simulations can enable not only qualitative verification of the diffusion behaviours observed from the QENS experiments, but also quantitative analysis and reproduction of the QENS data [19]. In Chapter 5, analysis of the QENS data will be presented to get insight into the NH3 diffusion in UiO-type MOFs with a brief introduction of the supportive simulations which are currently under investigation.

2.2) Experimental procedures

2.2.1) Chemicals

All chemicals and solvents in this work were commercially available (Sigma Aldrich and Fluorochem), with 98 % purity or above, and used as received.

2.2.2) Sample preparation

UiO-67 was prepared according to a procedure reported by J. F. Cavka *et al*. with some modifications [25]. 8 mL of *N,N*-dimethylformamide (DMF) was added into a glass vial containing 49 mg of zirconium tetrachloride ($ZrCl_4$), 378 mg of glacial acetic acid, and 52 mg of biphenyl-*4,4′*-dicarboxylic acid (H_2BPDC). The mixture was homogenised via sonication for 10 min, followed by solvothermal treatment at 393 K for 24 h. The solid product was washed with DMF three times, methanol three times, followed by methanol exchange for three days. During this period, methanol was exchanged daily. The final product was collected by centrifugation and activated at 423 K under vacuum for 12 h before storing in a desiccator. Anal. Calcd for $Zr_6O_{32}H_{48}C_{64}$ (i.e. $Zr_6O_4(OH)_4(bpdc)_{6-x}(acetate)_{2x}$ where x= 2.0): C/Zr, 1.40. Found: C/Zr, 1.41± 0.5.

UiO-bpydc was prepared by using the procedure similar to UiO-67, except 52 mg of *2,2′*-bipyridine-*5,5′*-dicarboxylic acid (H_2BPYDC) was used instead of H_2BPDC. Anal. Calcd for $Zr_6O_{32}H_{40}C_{60}N_9$ (i.e. $Zr_6O_4(OH)_4(bpydc)_{6-x}(acetate)_{2x}$ where x= 1.5): C/Zr, 1.32. Found: C/Zr, 1.31± 0.5.

Healed UiO-67 and UiO-bpydc were synthesised according to the procedure published by O. V. Gutov *et al*. with some modifications [26]. 100 mg of each sample and 60 mg of its corresponding linker were dispersed in a vial containing 10 ml DMF solution. The mixture vial was sealed securely and sonicated for 15 minutes before placing in an oven at 393 K for 48 h. The precipitate was separated from the suspension by centrifugation and intensively washed five times with hot DMF and four times with methanol, followed by methanol exchange for three days. The final product was evacuated with gradual heating to 423 K for 12 h and kept in a desiccator. Anal. Calcd for healed UiO-67 $Zr_6O_{32}H_{52}C_{84}$ (i.e.

$Zr_6O_4(OH)_4(bpdc)_{6-x}(acetate)_{2x}$ where x= 0.0): C/Zr, 1.84. Found: C/Zr, 1.83± 0.5. Anal. Calcd for healed UiO-bpydc $Zr_6O_{32}H_{40}C_{65.6}N_{10.4}$ (i.e. $Zr_6O_4(OH)_4(bpydc)_{6-x}(acetate)_{2x}$ where x= 0.8): C/Zr, 1.44. Found: C/Zr, 1.43± 0.5.

2.2.3) Characterisation techniques

2.2.3.1) X-ray powder diffraction (XRD)

Laboratory XRD was performed by using a Bruker D8 Advance X-ray diffractometer operated at 40 kV and 40 mA with Cu Kα1 radiation (λ = 1.54056 Å) over the 2θ range of 5 to 70 °. Prior to the measurement, a powder sample (10-15 mg) was finely ground, spread onto a poly(methyl methacrylate) sample holder, and flattened to obtain a smooth surface.

2.2.3.2) Thermogravimetric analysis (TGA)

TGA was performed on a TA Instruments TGA Q600 under an airflow of 100 ml/min. A sample with an exact amount (10-15 mg) was added into an alumina pan and heated from room temperature to 1173 K using the heating rate of 10 K/min. A corresponding TGA curve together with its first derivative was collected simultaneously.

2.2.3.3) Elemental analysis

C H N elemental analysis was acquired on a LECO brand CHNS-932 Analyzer. Quantity of Zr in an acid-digested sample was confirmed by inductively coupled plasma mass spectrometry (ICP-MS) with an Agilent 7800 ICP-MS instrument.

2.2.3.4) ^{1}H Nuclear magnetic resonance (NMR) of digested samples

Prior to the ^{1}H NMR measurement, sample digestion was conducted as follows: 1 mL of 0.1 M NaOH in D_2O was placed into a glass vial containing 10 mg of a MOF sample.

The mixture was sonicated for 5 min and left overnight to allow complete decomposition of the MOF framework, i.e. Zr oxoclusters are precipitated out as zirconium oxides (ZrO_2) and the other components such as organic linkers and capping species are entirely dissolved in the basic solution. NMR spectra of the digested MOF solution were recorded on a Bruker AVIIIHD 400 nanobay NMR spectrometer.

2.2.3.5) N_2 physisorption

N_2 adsorption isotherm (at 77 K) up to 1 bar was analysed using a Micromeritics Tristar instrument. All sorption isotherms were obtained using ultrahigh purity gases (99.999%). Before the sorption analysis, a sample (0.1−0.2 g) was loaded into a sample cell and subjected to a vacuum of 10^{-5} Pa at 423 K for 12 h. N_2 adsorption data with an initial slope (0.01 to 0.1 P/P_0) permitted calculation of the apparent surface areas based on the Brunauer Emmett Teller (BET) equations.

2.2.3.6) NH_3 temperature-programmed desorption (NH_3-TPD)

NH_3-TPD spectrum was measured with a Micromeritics AutoChem II 2910 apparatus. Detection of desorbed molecules was done by a thermal conductivity detector. About 100 mg of sample was degassed in a quartz cell at 573 K for 1 h, exposed to NH_3 which was used as a probe molecule at 373 K for 30 min, and then evacuated at 373 K for 15 min by purging with He gas. TPD measurement was done from room temperature to 593 K with a heating rate of 10 K/min and with He as carrier gas having a flow rate of 40 cm^3/min.

2.2.3.7) Volumetric analysis of NH_3 sorption isotherms

NH_3 sorption isotherms of the samples were carried out by using a gas adsorption analyser (Quantachrome Autosorb iQ-Chemi). Each sample was placed in a chamber and

outgassed under vacuum at 423 K for 24 h before testing. 99.9% NH_3 gas was loaded into the sample chamber at 298 K with a loading of 5 cm^3/time from 0 up to 1100 mbar.

2.2.3.8) Gravimetric analysis of NH_3 sorption isotherms

The Intelligent Gravimetric Analyser (IGA-001, Hiden) was employed to measure the cycling stability of MOF samples upon NH_3 uptake. The NH_3 gas used is 99.999% purity, CK Gas Company. Prior to the measurement, a sample in a vessel of IGA was degassed under 10^{-5} Pa at 423 K for 8 h. A built-in water bath was used to keep the temperature isothermally at 298 K. NH_3 was dosed to the sample at a maximum rate from 0 to 600 mbar. Then, the sample was evacuated at 298 K for 1 h and heated at 423 K until the sample weight stabilized. The sample was cooled down to 298 K again before repeating the cycle test for three times.

2.2.3.9) Synchrotron powder X-ray diffraction (SXRD):

SXRD data were collected on Beamline I11[27], Diamond Light Source, UK. The energy of the incident X-ray flux was set at 15 keV. The wavelength and the 2θ-zero point were refined using a diffraction pattern obtained from a high-quality silicon powder (SRM640c). For the gas-free samples, each sample powder was ground and loaded in a 0.5 mm borosilicate glass capillary and then activated under vacuum at 423 K for 2 h. For the NH_3-loaded samples, each sample was degassed at 473 K for 3 h under reduced pressure using a Schlenk line. The sample was then naturally cooled down to the room temperature and exposed to an NH_3 vapour for 30 min. The sample was loaded into a quartz-type capillary with a diameter of 0.5 mm and sealed perfectly by using a flame. High-resolution SXRD data of all samples were achieved by using the multi-analyser crystals (MAC)

detectors in the 2θ range of 0-150 ° with 0.001 ° data binning. Each MAC pattern was collected for an hour to get satisfying statistics.

2.2.3.10) In situ synchrotron powder X-ray diffraction (*In situ* SXRD) for NH_3 desorption study:

In situ SXRD pattern of the NH_3-loaded UiO-bpydc (NH_3@UiO-bpydc) was collected at Beamline BL02B2, Spring 8, Japan. The energy of the incident X-ray flux was set at 37 keV. The wavelength and the 2θ-zero point were refined using a diffraction pattern obtained from a Si (1 1 1) double-crystal monochromator. High-resolution SXRD data of all samples were achieved by using the position-sensitive detectors (PSDs) in the 2θ range of 2-80 ° with 0.001 ° data binning. The capillary was mounted to a sample holder and heated up from room temperature to 773 K with a ramping rate of 5 K/min. Each PSD pattern was collected every 2 K of increasing temperature with a scanning time of 2 s. At 373, 473, 573, 673 and 773 K, The diffraction patterns were scanned by using a time per step of 120 s for good statistics.

2.2.3.11) *In situ* neutron powder diffraction (*In situ* NPD) for ammonia adsorption analysis:

An *in situ* NPD at WISH instrument[28] was used to study the binding sites of fully-deuterated ammonia (ND_3, 99 %) and the structural change of the Zr-based MOFs as a function of increased ND_3 loading. This structural information was achieved by the use of Rietveld refinement. Prior to the measurement, a sample was loaded into an 11 mm diameter vanadium can with quartz wool on top. The sample was degassed under high vacuum at 373 K (5 K/min heating rate) for 24 h to remove any guest molecules and then naturally cooled down to room temperature. The sample holder was transferred to a vacuum chamber

connected to a gas handling system. An NPD pattern of the desolvated sample was first collected at 300 K for 20 min. After that, a He cryostat was used to cool down the sample can to 7 K, where the thermal motion of the MOF sample and adsorbed ND_3 molecules can be significantly reduced. High-resolution NPD of this sample was carried out for 1 hour to get good statistics. After the measurement, the sample was gently heated up to 300 K before dosing with ND_3 gas by using a calibrated volume. Each of the loading steps required half an hour to enable the homogenous dispersion of ND_3 molecules inside the crystalline sample. NPD patterns after each ND_3 loading were measured at 300 K and 7 K for 20 min and 1 h, respectively. Prior to the low-temperature data collection at 7 K, the system was cooled down to 7 K slowly over 3 h in order to eliminate the gas condensation outside the sample. The gas handling system and sample environment at WISH are demonstrated in Figure 2.12.

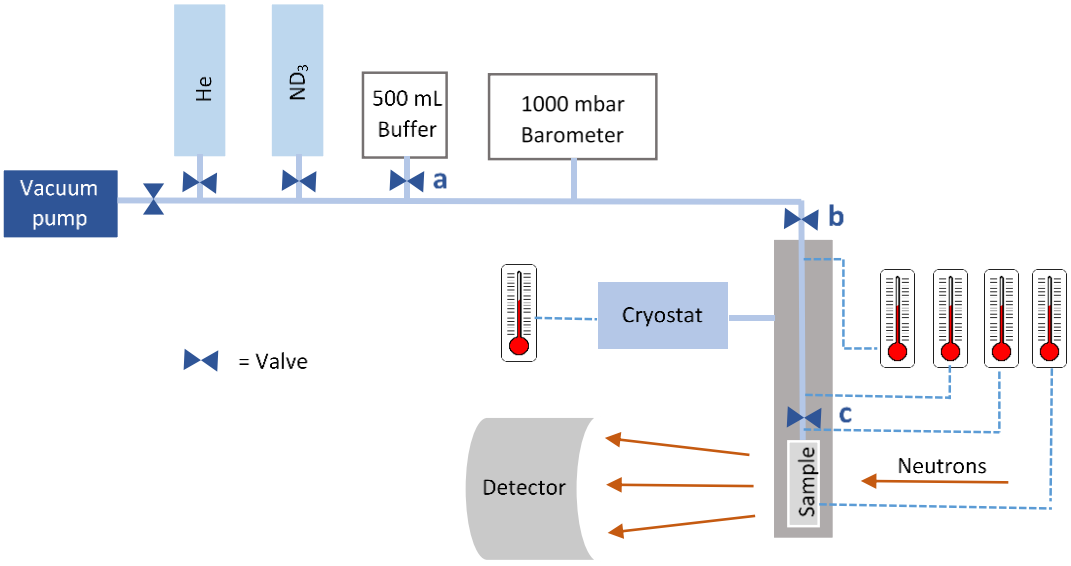

Figure 2.12 | Schematic diagram of the neutron diffraction set up at WISH beamline, ISIS.

Volume calibration along with ND_3 dosing was performed at 298 K by using the procedure adopted from the literature [29]. Helium (He) was used as a calibration gas. According to Figure 2.12, a certain pressure of He (P_a) was loaded into a known volume

(V_a) of a 500 mL buffer while keeping the other parts evacuated. An actual volume of the system excluding the sample stick and the sample cell (V_b, to the valve b) was then calculated by using a final pressure of He (P_b) after closing a vacuum valve and opening a buffer valve to reach the V_b volume. From the ideal gas law, we can achieve the value of V_b:

$$V_b = \frac{V_a P_a}{P_b} \qquad \textit{Equation 2. 54}$$

The same procedure was also applied to determine an actual volume of the whole system including the sample stick and the sample cell (V_c). Assuming that the He adsorption capacity of UiO-67 and UiO-bpydc is negligible at 298 K, [30] V_c is then the total volume of the system. After the volume calibration, the sample together with the rest of the gas handling system was evacuated to 10^{-5} Pa for 1 h to completely remove the He gas. The valve b was closed prior to dosing the ND_3 gas into the system with a set pressure of P_2. The initial amount of ND_3 in the system (n_2) can be derived from the following equation:

$$P_2V_b = n_2RT \qquad \textit{Equation 2. 55}$$

where R and T are the ideal gas constant and the temperature, respectively.

When the valve b is open to allow ND_3 adsorption into the sample, the final ND_3 pressure will stabilize at P_3. Then we can get the amount of residual ND_3 left in the system (n_3):

$$P_3V_c = n_3RT \qquad \textit{Equation 2. 56}$$

The actual amount of ND_3 adsorbed (n) by the sample is then calculated:

$$n = n_2 - n_3 \qquad \textit{Equation 2. 57}$$

The precise dosing amount of ND_3 in a unit of mmol/g can be obtained since we know the weight of the sample used.

In the temperature-dependent study by *in situ* NPD, it is essential to keep the same ND_3 quantity in the internal pores of the powder sample as close as possible. As shown in the set up above (based on the similar BET/Chemisorption equipment and procedure), the sample was first placed in the sample tube with repeated flushing and evacuation. We then loaded pure ND_3 stepwise through opening the valves b and c. Notice that the dosing volume (deliver volume up to valve b) and the volume in the sample tube with the sample (between valve b to the sample bottom) were carefully pre-calibrated with inert gas. As a result, the total desired gas loading to the sample can be precisely worked out from the pressure transducers (pressure differences) before dosage and after equilibration for the subsequent dosing at different pressures before saturation. Given the high surface area of the powder MOF sample (at high loading) compared to the small top gas volume and the closure of the valve b, the data collection at room temperature (298 K) was first collected. Following on this, the cooling process was taken slowly until reaching 7 K with the valve b remained closed.

2.2.4) Inelastic neutron scattering (INS) at TOSCA

TOSCA [13] instrument, an INS spectrometer with an indirect time-of-flight (TOF) geometry at the ISIS Pulsed Neutron and Muon Source, Rutherford Appleton Laboratory, was used to study the dynamic interactions between stored NH_3 (99.9%) and the host structures of UiO-67 and UiO-bpydc, as a function of increased NH_3 loading. The TOSCA has a wide energy transfer range of 0- 4000 cm^{-1} (0- 500 meV) and a high resolution of 1.5% $\Delta E/E$ with the best results below 2000 cm^{-1} (250 meV). A pulsed polychromatic beam of neutrons hit a sample at a certain flight path of 17 m from the source. The neutrons inelastically scattered by the sample were then reflected by a pyrolytic graphite *(002)*

analyser combined with a cooled Be filter to give a unique final energy of ~32 cm^{-1}. The fixed energy neutrons finally travelled towards ten detector banks each having thirteen ^3He tubes. Five banks are located in forward scattering and the other five in backward scattering geometries with scattered angles of 45 ° and 135 °, respectively. Thanks to the low final energy, a relationship between energy transfer (E_T, cm^{-1}) and momentum transfer ($\boldsymbol{Q}$, $Å^{-1}$) are directly translated to $E_T \approx 16\boldsymbol{Q}^2$. The TOF data were converted to energy transfer and spectral intensity, i.e. $S(\boldsymbol{Q}, \omega)$, by using the Mantid software developed at ISIS facility [31].

Prior to the measurement, a sample (1.0-1.5 g) was loaded into a 11 mm diameter vanadium can with quartz wool on top and sealed with an Indium wire. The sample was degassed under high vacuum at 373 K (5 K/min heating rate) for 24 h to remove any guest molecules and then naturally cooled down to room temperature. The sample can was mounted at the end of the stick and connected to a gas handling and a temperature control system. Leak check was done before cooling down the sample can to below 10 ± 0.1 K within a closed cycle refrigerator (CCR) cryostat, where the thermal motion of the MOF sample and adsorbed NH_3 molecules can be significantly reduced. An INS spectrum of the desolvated sample was carried out for at least 4 hours for a good statistics. After the measurement, the sample was gently heated up to 300 K before dosing with NH_3 gas at the desired amount by using a calibrated volume. Each of the loading step required half an hour to enable homogenous dispersion of NH_3 molecules inside the crystalline sample. The INS spectrum of each ammoniated sample was measured below 10 K similar to its pristine sample. Since we used the hydrogen-rich samples featuring strongly neutron scattering, the effect of the background from the instrument and the vanadium sample holder could be neglected; i.e. data collection of the empty holder was skipped. The gas handling system and

sample environment at TOSCA are similar to one at WISH beamline, except gaseous ND_3 was replaced by NH_3.

Calculation of area under INS curve: The Integrate Gadget in OriginPro was used to perform the numerical integration on the INS spectra to determine the area under the curve of specific vibrational modes. The range of data was selected to include the peaks of the vibrational modes of interest, using the x-axis as the baseline.

2.2.5) Quasi-elastic neutron scattering (QENS) at OSIRIS

QENS experiments were performed on the OSIRIS [16] instrument, a high-flux backscattering, time-of-flight (TOF) spectrometer with an inverted geometry at the ISIS Pulsed Neutron and Muon Source, Rutherford Appleton Laboratory. QENS technique was used to study the ammonia kinetics in the host structures of UiO-67 and UiO-bpydc, as a function of increased NH_3 loading. A white beam of neutrons first illuminated the sample. After scattering, the neutrons were Bragg reflected by the crystal analyser (the *(002)* plane of pyrolitic graphite) to define a single final energy (1.845 meV). The scattered neutrons with fixed energy then travelled towards the 42-element ^{3}He detectors. The scattered neutrons were detected over an angular range of 2θ = 11- 155 °. The instrumental resolution and detector efficiencies were calibrated by fitting the spectrum of a vanadium standard. The elastic energy resolution was 24.5 μeV. The energy transfer (ΔE) range was -0.4- 0.4 meV and the momentum transfer (***Q***) range was 0.18- 1.8 Å^{-1}. The OSIRIS was also used as a long-wavelength diffractometer. The d range was 0.8- 35 Å with $\Delta d/d$ between 5x 10^{-3} and 6x 10^{-3}. All the TOF data were analysed by using the Mantid software [31].

Sample environment set up at the OSIRIS instrument was similar to that at the WISH one, except NH_3 was used instead of ND_3. A sample (~2.2 g) was loaded into a thin walled

aluminium can of annular geometry. To prevent a sample spillage, quartz wool was placed on top of the can before sealing with an Indium wire. The sample can was degassed under high vacuum at 373 K (5 K/min heating rate) for 24 h to remove any guest molecules and then naturally cooled down to room temperature. The sample can was mounted at the end of the stick and connected to a gas handling and a temperature control system. During data collection, the temperature of the sample was controlled by a He cryostat and thermocouples. Leak check was done before cooling down the sample can to below 10 K, where the Debye-Waller factor resulting from thermal motion of the MOF sample can be significantly reduced. A QENS spectrum of the desolvated sample was carried out at least 4 hours to get an accumulated proton current of 900 μA for a good statistics. After the measurement at cryogenic temperature, the sample was gently heated up to 298 K and equilibrated for half an hour before collecting the data again for 4 hours. Next, a precise amount of NH_3 was loaded into the sample by using a calibrated volume. Each of the loading step required half an hour to enable homogenous dispersion of NH_3 molecules inside the crystalline sample. The QENS spectrum of each ammoniated sample was measured at 298 K with a total proton current above 900 μA. Neutron diffraction measurement was performed simultaneously during the QENS data collection.

2.2.6) Data analysis

2.2.6.1) For XRD and NPD experiments

Rietveld refinement of gas-free samples:

TOPAS-academic 5 software [32], containing Rietveld refinement methods, was used to analyse the structural information of the diffraction patterns. For structural refinement, the initial MOF models were based on crystallographic data of UiO-67 [33], and UiO-bpydc [34]. The diffraction patterns were refined by optimisation of the scale factor

and lattice parameters. The background was described by a shifted Chebyschev function. A back-to-back exponential convoluted with pseuduo-voigt peakshape function was used to describe the peak asymmetry in the time-of-flight (tof) data. Both biphenyl-*4,4′*-dicarboxylate (bpdc) and *2,2′*-bipyridine-*5,5′*-dicarboxylate (bpydc) linkers were treated as rigid bodies using Cartesian coordinates to reduce the number of variables. Dummy atoms were added to define the origins of the rigid bodies. The refined structural parameters for all atoms of each pattern were the coordinates (x, y, z) and isotropic displacement factors (B_{eq}). The quality of the Rietveld refinements of diffraction data was confirmed by low values of goodness-of-fit (GOF, χ^2) and *R* factors (R_{wp}, R_p, R_{exp}) and a well fitted pattern with acceptable B_{eq} within experimental errors. All the errors of the atom−atom distances were calculated using the following equation:

$$r_{error} = \sqrt{(x_{error})^2 + (y_{error})^2 + (z_{error})^2} \times r_{measure} \qquad \textit{Equation 2. 58}$$

where r_{error} is the error of the measured atom−atom distance, x_{error}, y_{error}, z_{error} are the errors of the fractional coordinates (*x*, *y*, *z*) respectively, r_{measure} is the measured atom−atom distance.

Rietveld refinement of ND_3-loaded samples:

For the ammoniated samples, the possible locations of ND_3 molecules inside the MOF cavities were determined by using a Fourier difference map, generated in the TOPAS-5 software. The structures of the guest-free UiO-67 and UiO-bpydc were used as starting models with constant occupancies and isotropic displacement factors. Thanks to the porous structure and chemical properties of the MOFs, interacting ND_3 molecules with a dynamic size of 2.5 Å were expected to adsorb inside the pore, on the basal planes of linkers, and close to metal nodes. Each ND_3 molecule was treated as a rigid body described by Z-matrix

with N–H bond distance and H–N–H bond angle constrained in the range of 1.04-1.07 Å and 106.0-107.0 °, respectively. The ND_3 molecule was added into the MOF structure one by one. Coordinates and site occupancy of the ND_3 molecule were freely refined. Fitting parameters including *GOF* and *R* factors, were used to prove the quality of the refinement. The lower values of these factors, the more accurate refinement close to the real structure.

Neutron diffraction: Rietveld refinement was performed over the diffraction data recorded on the average $2\theta = 58.3^{o}$ detector bank.

Synchrotron diffraction: Rietveld refinement was performed over the whole data range ($2\theta = 5{-}40\ ^{o}$).

CCDC 2047200, 2047201, 2047202, 2047203, 2047204, and 2047205 contain the supplementary crystallographic data for this paper. The data can be obtained free of charge from The Cambridge Crystallographic Data Centre via www.ccdc.cam.ac.uk/structures. A list of the crystal structures obtained from the Rietveld refinements of the NPD data at 300 K and their corresponding CCDC Deposition numbers is given below;

CCDC 2047200: UiO-67 with the first ND_3 loading

CCDC 2047201: UiO-67 with the third ND_3 loading

CCDC 2047202: UiO-bpydc with the first ND_3 loading

CCDC 2047203: UiO-bpydc with the second ND_3 loading

CCDC 2047204: UiO-bpydc with the third ND_3 loading

CCDC 2047205: UiO-67 with the second ND_3 loading

2.2.6.2) For INS and QENS experiments

TOF datasets were converted to the dynamic structure factor, $S(\boldsymbol{Q},\omega)$, and rebinned in energy transfer using the Mantid data analysis suite developed at ISIS [31]. Details of data analysis will be presented in Chapter 5.

2.3) Theoretical calculations

The computational calculations were performed in collaboration with Dr. Xin Ping from East China University of Science and Technology, P.R. China (for DFT) and Dr. Nakul *et al*. from University of Cambridge, UK (for GCMC). The details of these calculations are briefly presented.

2.3.1) Density Functional Theory (DFT) calculations

2.3.1.1) Optimisation of NH_3-MOF structures

The valence-core interactions were described by using the projector-augmented wave (PAW) method [35] at a kinetic energy cutoff of 500 eV. The 2×2×2 *k*-point mesh was used for Brillouin zone integrations. For geometry optimisations, we used a Hellman−Feynman force criterion of 0.02 eV/Å on each ion.

Binding energy per NH_3 molecule (E_b) of a MOF-$n$$NH_3$ system was calculated as follows:

$$E_b = \frac{1}{n}\{E[MOF] + nE[NH_3] - E[MOF-nNH_3]\}, \qquad \textit{Equation 2. 59}$$

where n is the number of NH_3 molecules in the MOF-$n$$NH_3$ system and $E[\mathrm{MOF}]$, $E[\mathrm{NH_3}]$, and $E[\mathrm{MOF}-n\mathrm{NH_3}]$ are the DFT calculated energies of the bare MOF, NH_3 molecule, and MOF-$n$$NH_3$ system, respectively.

Due to the large size of the MOF systems, we were not able to include dispersion corrections (e.g., the DFT-D3 scheme [36] of Grimme) in our DFT calculations because dispersion-corrected DFT calculations require much larger memory in computations than normal DFT calculations. Although the binding energies obtained from normal DFT calculations are underestimated, the differences of binding energies from normal DFT calculations are expected to be similar to that from dispersion-corrected DFT calculations.

2.3.1.2) Calculations of rotational energy barriers

The rotational energy barriers of NH_3-free and NH_3-loaded UiO-67 and UiO-bpydc were estimated by calculations on cluster models using M06-2X [37] functional with the def2-TZVP [38-39] basis set. Specifically, we considered four cases, namely the guest-free UiO-67, UiO-67-1NH_3, guest-free UiO-bpydc, and UiO-bpydc-1NH_3; the corresponding cluster models are proton-capped bpdc, bpdc-1NH_3, bpydc, and bpydc-1NH_3 which were cut from the optimised periodic structures. The rotational groups (dihedral angle O1-C1-C2-C3, see Figure 4.7 in Chapter 4) were rotated between γ (i.e., the dihedral angle O1-C1-C2-C3 of the most stable configuration) and γ+180° (half a period) with 10° increments to scan the potential energy surfaces. During the scan, only the dihedral angle and the COO groups were fixed. The rotation energy barriers were computed as the energy difference between the most unstable and the most stable configurations (Table 4.3 in Chapter 4). These cluster calculations were carried out with the *Gaussian 16* program [40].

2.3.1.3) Calculations of vibrational (phonon) frequencies of NH_3-MOF structures

Models for the DFT calculations were built based on the refined crystal structures from neutron diffraction data. According to the crystallographic models of the NH_3-MOF

adducts, some of the organic linkers and all of the NH_3 sites are partially occupied due to missing linker defects and symmetry, respectively. To achieve a proper computed result, a supercell calculation would be required. However, this approach is far too costly in practice. In this work, single unit cells of non-defective UiO-67 and UiO-bpydc structures were used instead. The occupancies of NH_3 molecules were modified to be either fully occupied (i.e. 100% occupancy) or unoccupied with respect to their local environment and symmetry (the overall occupancy might not be proportional to the actual occupancy). The Perdew-Burke-Ernzerhof (PBE) functional based on generalized gradient approximation (GGA) [41] implemented in the VASP [42] package was used. The projector augmented wave (PAW) [35] method was employed. Due to the large unit cells of UiO-67 type MOFs, only Gamma (Γ) point was sampled. The cutoff energy was 500 eV. The shape of the unit cell and atomic positions were allowed fully relaxed without imposed symmetry during the optimisation. The energy convergence for the self-consistent electronic relaxation was set to be 10^{-5} eV and the force convergence was set to be 0.02 eV/Å. We were unable to count in the weak dispersion interactions in our DFT calculations since it requires much greater memory for the data storage compared to using the standard DFT calculations. The calculated INS spectra and their corresponding vibrational modes were generated by OCLIMAX [43] and Jmol [44] software, respectively. The theoretical spectrum included overtones to the 10^{th} order. The scaling factor of 0.985 was applied to all the calculated INS spectra for vibrational frequency correction.

2.3.2) Grand cononical Monte Carlo (GCMC) simulations:

In Chapter 5, the adsorption isotherms of N_2 at 77 K and NH_3 at 298 K in defective UiO-67 type MOFs were simulated using the grand canonical Monte Carlo method as

implemented in the RASPA simulation package. [45] Models of UiO-67 and UiO-bpydc with missing linker defects were built based on the crystal structures from neutron diffraction data. A 2x2x2 supercell was constructed to represent each of the MOF models. Framework atoms were kept fixed at the crystallographic positions thereby ignoring the skeleton stretching and bending vibration as these materials did not show significant volume change. Monte Carlo moves consisted of insertion, deletion, rotation and translation moves, each with equal probabilities. For all the pressure points, 20,000 cycles for equilibration and another 10,000 cycles to average the properties were applied. A cycle was defined as the maximum of 20 steps or the number of molecules in the system. A step was when any one of the randomly selected Monte Carlo moves was attempted on any one molecule of the system. This implied that on an average a Monte Carlo move had been attempted on all the molecules during each cycle. Intermolecular interactions were modeled using the Lennard-Jones (LJ) potential with a cutoff of 12.8 Å. Lorentz Berthelot mixing rules were used for all the cross-interaction terms. Electrostatic interactions were modeled using the coulombic potential and were computed using the Ewald summation method with the precision set to 10^{-6}. N_2 and NH_3 were modeled using parameters taken from the TraPPE force field. [46] The framework atoms were modeled using LJ parameters taken from the DREIDING force field. [47] For metals in the framework not described in the DREIDING force field, their LJ parameters were taken from the UFF force field. [48] All the frameworks were modeled as rigid structures with periodic boundary conditions applied in all directions. The number of unit cells in the simulation box was computed individually for each of the frameworks to make sure the simulation box was large enough to ensure that a distance of at least twice the cutoff radius was maintained between the periodic images. The charges for the framework

were computed using the EQeq protocol. [49] The geometric properties were calculated using Poreblazer [50].

2.4) Chapter summary

Information on the fundamentals and unique features of the major techniques used in this thesis (e.g. neutron diffraction and neutron spectroscopy) are presented. The experimental procedures, characterisation techniques, data analysis, as well as collaborative theoretical studies are also included.

2.5) References

1. Bragg, W. L., The Specular Reflection of X-rays. *Nature* **1912,** *90* (2250), 410-410.
2. Sivia, D. S.; Sivia, D., *Elementary Scattering Theory: For X-ray and Neutron Users*. Oxford University Press: 2011.
3. David, B.; Shankland, K.; McCusker, L. B., *Structure Determination from Powder Diffraction Data*. 2006.
4. Young, R. A., *The Rietveld Method*. International Union of Crystallograhy: Chester, England, 1993.
5. Robert E. Dinnebier, A. L., John S. O. Evans, *Rietveld Refinement- Practical Powder Diffraction Pattern Analysis Using TOPAS*. Walter de Gruyter GmbH: Berlin, 2019.
6. David, W. I. F., Powder Diffraction: Least-Squares and Beyond. *J Res Natl Inst Stand Technol* **2004,** *109* (1), 107-123.
7. Lutterotti, L.; Scardi, P., Simultaneous Structure and Size–Strain Refinement by the Rietveld Method. *Journal of Applied Crystallography* **1990,** *23* (4), 246-252.
8. Kisi, E. H.; Howard, C. J., *Applications of Neutron Powder Diffraction*. Oxford University Press: Oxford, 2008.
9. Pynn, R., Neutron Scatterring- A Primer. 1990. https://fas.org/sgp/othergov/doe/lanl/pubs/00326651.pdf.
10. Sears, V. F., Neutron Scattering Lengths and Cross Sections. *Neutron News* **1992,** *3* (3), 26-37.
11. Characteristics of a Pulsed Source. https://www.isis.stfc.ac.uk/Pages/Characteristics-of-a-pulsed-source.aspx
12. Mitchell, P. C. H., *Vibrational Spectroscopy with Neutrons: with Applications in Chemistry, Biology, Materials Science and Catalysis*. World Scientific: New Jersey

London, 2005.

13. Pinna, R. S.; Zanetti, M.; Rudić, S.; Parker, S. F.; Armstrong, J.; Waller, S. P.; Zacek, D.; Smith, C.; Harrison, S. M.; Gorini, G.; Fernandez-Alonso, F., The TOSCA Spectrometer at ISIS: the Guide Upgrade and Beyond. *Journal of Physics: Conference Series* **2018,** *1021*, 012029.

14. Timmy Ramirez-Cuesta, S. P., John Tomkinson. TOSCA User Manual. https://www.isis.stfc.ac.uk/Pages/tosca-user-manual6685.pdf.

15. Willis, B. T. M.; Carlile, C. J., *Experimental Neutron Scattering*. Oxford University Press: Oxford, 2008.

16. Telling, M. T. F.; Andersen, K. H., Spectroscopic Characteristics of the OSIRIS Near-Backscattering Crystal Analyser Spectrometer on the ISIS Pulsed Neutron Source. *Physical Chemistry Chemical Physics* **2005,** *7* (6), 1255-1261.

17. Bée, M., *Quasielastic Neutron Scattering : Principles and Applications in Solid State Chemistry, Biology, and Materials Science*. Adam Hilger: Bristol, 1988.

18. Jan Peter Embs, F. J., Rolf Hempelmann, Introduction to Quasielastic Neutron Scattering. *Zeitschrift für Physikalische Chemie* **2010,** *224*, 28.

19. Armstrong, J.; O'Malley, A. J.; Ryder, M. R.; Butler, K. T., Understanding Dynamic Properties of Materials Using Neutron Spectroscopy and Atomistic Simulation. *Journal of Physics Communications* **2020,** *4* (7), 072001.

20. Chudley, C. T.; Elliott, R. J., Neutron Scattering from a Liquid on a Jump Diffusion Model. *Proceedings of the Physical Society* **1961,** *77* (2), 353-361.

21. Hall, P. L.; Ross, D. K., Incoherent Neutron Scattering Functions for Random Jump Diffusion in Bounded and Infinite Media. *Molecular Physics* **1981,** *42* (3), 673-682.

22. Singwi, K. S.; Sjölander, A., Diffusive Motions in Water and Cold Neutron Scattering. *Physical Review* **1960,** *119* (3), 863-871.

23. Jobic, H.; Theodorou, D. N., Quasi-Elastic Neutron Scattering and Molecular Dynamics Simulation as Complementary Techniques for Studying Diffusion in Zeolites. *Microporous and mesoporous materials* **2007,** *102* (1-3), 21-50.

24. Lechner R.E., L. S., *Quasielastic Neutron Scattering in Biology, Part I: Methods.* Springer: Berlin, 2006.

25. Cavka, J. H.; Jakobsen, S.; Olsbye, U.; Guillou, N.; Lamberti, C.; Bordiga, S.; Lillerud, K. P., A New Zirconium Inorganic Building Brick Forming Metal Organic Frameworks with Exceptional Stability. *Journal of the American Chemical Society* **2008,** *130* (42), 13850-13851.

26. Gutov, O. V.; Hevia, M. G.; Escudero-Adán, E. C.; Shafir, A., Metal–Organic Framework (MOF) Defects under Control: Insights into the Missing Linker Sites and Their Implication in the Reactivity of Zirconium-Based Frameworks. *Inorganic Chemistry* **2015,** *54* (17), 8396-8400.

27. Thompson, S. P.; Parker, J. E.; Potter, J.; Hill, T. P.; Birt, A.; Cobb, T. M.; Yuan, F.; Tang, C. C., Beamline I11 at Diamond: A New Instrument for High Resolution Powder Diffraction. *Review of Scientific Instruments* **2009,** *80* (7), 075107.

28. Chapon, L. C.; Manuel, P.; Radaelli, P. G.; Benson, C.; Perrott, L.; Ansell, S.; Rhodes, N. J.; Raspino, D.; Duxbury, D.; Spill, E.; Norris, J., Wish: The New Powder and Single Crystal Magnetic Diffractometer on the Second Target Station. *Neutron News* **2011,** *22* (2), 22-25.

29. Zhao, P.; Fang, H.; Mukhopadhyay, S.; Li, A.; Rudić, S.; McPherson, I. J.; Tang, C. C.; Fairen-Jimenez, D.; Tsang, S. C. E.; Redfern, S. A. T., Structural Dynamics of a Metal–Organic Framework Induced by CO_2 Migration in Its Non-Uniform Porous Structure. *Nature Communications* **2019,** *10* (1), 999.

30. Wang, B.; Huang, H.; Lv, X.-L.; Xie, Y.; Li, M.; Li, J.-R., Tuning CO_2 Selective Adsorption over N_2 and CH_4 in UiO-67 Analogues through Ligand Functionalization. *Inorganic Chemistry* **2014,** *53* (17), 9254-9259.

31. Arnold, O.; Bilheux, J. C.; Borreguero, J. M.; Buts, A.; Campbell, S. I.; Chapon, L.; Doucet, M.; Draper, N.; Ferraz Leal, R.; Gigg, M. A.; Lynch, V. E.; Markvardsen, A.; Mikkelson, D. J.; Mikkelson, R. L.; Miller, R.; Palmen, K.; Parker, P.; Passos, G.; Perring, T. G.; Peterson, P. F.; Ren, S.; Reuter, M. A.; Savici, A. T.; Taylor, J. W.; Taylor, R. J.; Tolchenov, R.; Zhou, W.; Zikovsky, J., Mantid—Data Analysis and Visualization Package for Neutron Scattering and μ SR Experiments. *Nuclear Instruments and Methods in Physics Research Section A: Accelerators, Spectrometers, Detectors and Associated Equipment* **2014,** *764*, 156-166.

32. Coelho, A., TOPAS and TOPAS-Academic: an Optimization Program Integrating Computer Algebra and Crystallographic Objects Written in C++. *Journal of Applied Crystallography* **2018,** *51* (1), 210-218.

33. Ko, N.; Hong, J.; Sung, S.; Cordova, K. E.; Park, H. J.; Yang, J. K.; Kim, J., A Significant Enhancement of Water Vapour Uptake at Low Pressure by Amine-Functionalization of UiO-67. *Dalton Transactions* **2015,** *44* (5), 2047-2051.

34. Gonzalez, M. I.; Bloch, E. D.; Mason, J. A.; Teat, S. J.; Long, J. R., Single-Crystal-to-Single-Crystal Metalation of a Metal–Organic Framework: A Route toward Structurally Well-Defined Catalysts. *Inorganic Chemistry* **2015,** *54* (6), 2995-3005.

35. Blöchl, P. E., Projector Augmented-Wave Method. *Physical Review B* **1994,** *50* (24), 17953-17979.

36. Grimme, S.; Antony, J.; Ehrlich, S.; Krieg, H., A Consistent and Accurate *ab initio* Parametrization of Density Functional Dispersion Correction (DFT-D) for the 94 Elements H-Pu. *The Journal of Chemical Physics* **2010,** *132* (15), 154104.

37. Zhao, Y.; Truhlar, D. G., The M06 Suite of Density Functionals for Main Group Thermochemistry, Thermochemical Kinetics, Noncovalent Interactions, Excited States, and Transition Elements:Two New Functionals and SystematicTesting of Four M06-Class Functionals and 12 Other Functionals. *Theoretical Chemistry Accounts* **2008,** *120* (1), 215-241.

38. Weigend, F.; Ahlrichs, R., Balanced Basis Sets of Split Valence, Triple Zeta Valence and Quadruple Zeta Valence Quality for H to Rn: Design and Assessment of Accuracy. *Physical Chemistry Chemical Physics* **2005,** *7* (18), 3297-3305.

39. Weigend, F., Accurate Coulomb-Fitting Basis Sets for H to Rn. *Physical Chemistry Chemical Physics* **2006,** *8* (9), 1057-1065.

40. Frisch, M. J.; Trucks, G. W.; Schlegel, H. B.; Scuseria, G. E.; Robb, M. A.; Cheeseman, J. R.; Scalmani, G.; Barone, V.; Petersson, G. A.; Nakatsuji, H.; Li, X.; Caricato, M.; Marenich, A. V.; Bloino, J.; Janesko, B. G.; Gomperts, R.; Mennucci, B.; Hratchian, H. P.; Ortiz, J. V.; Izmaylov, A. F.; Sonnenberg, J. L.; Williams; Ding, F.; Lipparini, F.; Egidi, F.; Goings, J.; Peng, B.; Petrone, A.; Henderson, T.; Ranasinghe, D.; Zakrzewski, V. G.; Gao, J.; Rega, N.; Zheng, G.; Liang, W.; Hada, M.; Ehara, M.; Toyota, K.; Fukuda, R.; Hasegawa, J.; Ishida, M.; Nakajima, T.; Honda, Y.; Kitao, O.; Nakai, H.; Vreven, T.; Throssell, K.; Montgomery Jr., J. A.; Peralta, J. E.; Ogliaro, F.; Bearpark, M. J.; Heyd, J. J.; Brothers, E. N.; Kudin, K. N.; Staroverov, V. N.; Keith, T. A.; Kobayashi, R.; Normand, J.; Raghavachari, K.; Rendell, A. P.; Burant, J. C.; Iyengar, S. S.; Tomasi, J.; Cossi, M.; Millam, J. M.; Klene, M.; Adamo, C.; Cammi, R.; Ochterski, J. W.; Martin, R. L.; Morokuma, K.; Farkas, O.; Foresman, J. B.; Fox, D. J. *Gaussian 16 Rev. C.01*, Wallingford, CT, 2016.

41. Perdew, J. P.; Burke, K.; Ernzerhof, M., Generalized Gradient Approximation Made Simple. *Physical Review Letters* **1996,** *77* (18), 3865-3868.

42. Kresse, G.; Furthmüller, J., Efficiency of *ab-initio* Total Energy Calculations for Metals and Semiconductors Using a Plane-Wave Basis Set. *Computational Materials Science* **1996,** *6* (1), 15-50.

43. Cheng, Y. Q.; Daemen, L. L.; Kolesnikov, A. I.; Ramirez-Cuesta, A. J., Simulation of Inelastic Neutron Scattering Spectra Using OCLIMAX. *Journal of Chemical Theory and Computation* **2019,** *15* (3), 1974-1982.

44. Jmol: an Open-Source Java Viewer for Chemical Structures in 3D. http://www.jmol.org/.

45. Dubbeldam, D.; Calero, S.; Ellis, D. E.; Snurr, R. Q., RASPA: Molecular Simulation Software for Adsorption and Diffusion in Flexible Nanoporous Materials. *Mol Simulat* **2016,** *42* (2), 81-101.

46. Potoff, J. J.; Siepmann, J. I., Vapor–Liquid Equilibria of Mixtures Containing Alkanes, Carbon Dioxide, and Nitrogen. *Aiche J* **2001,** *47* (7), 1676-1682.

47. Mayo, S. L.; Olafson, B. D.; Goddard, W. A., DREIDING: a Generic Force Field for Molecular Simulations. *Journal of Physical chemistry* **1990,** *94* (26), 8897-8909.

48. Rappé, A. K.; Casewit, C. J.; Colwell, K.; Goddard Iii, W.; Skiff, W., UFF, a Full Periodic Table Force Field for Molecular Mechanics and Molecular Dynamics Simulations. *Journal of the American chemical society* **1992,** *114* (25), 10024-10035.

49. Wilmer, C. E.; Kim, K. C.; Snurr, R. Q., An Extended Charge Equilibration Method. *J Phys Chem Lett* **2012,** *3* (17), 2506-2511.

50. Sarkisov, L.; Harrison, A., Computational Structure Characterisation Tools in Application to Ordered and Disordered Porous Materials. *Molecular Simulation* **2011,** *37* (15), 1248-1257.

Chapter 3

Responsive behaviours of Defect-Rich Zr-Based Metal-Organic Frameworks toward NH_3 Adsorption

Understanding structural responses of metal-organic frameworks (MOFs) to external stimuli such as the inclusion of guest molecules, temperature/pressure has gained increasing attention in many applications, for example, manipulation and manifesto smart materials for gas storage, energy storage, controlled drug delivery, tunable mechanical properties, and molecular sensing, to name but a few. This chapter presents the use of high-resolution *in situ* neutron and synchrotron diffractions combined with Rietveld refinement and density functional theory (DFT) calculations to investigate structural responses at a molecular level of defective Zr-based MOFs upon progressive adsorption of ammonia (NH_3) as an external stimulus. UiO-67 and UiO-bpydc containing biphenyl dicarboxylate and bipyridine dicarboxylate linkers, respectively, were selected due to their high thermal and chemical stability. The results establish the paramount influence of functional linkers of the MOFs on their NH_3 affinity, which leads to stimulus-tailoring properties such as gate-controlled porosity by dynamic linker flipping, disorder, and structural rigidity. Despite their structural similarities, we show for the first time the dramatic alteration of NH_3 adsorption profiles when the phenyl groups are replaced by the bipyridine in the organic linker. These molecular controls stem from controlling the degree of H-bonding networks/distortions between the bipyridine scaffold and the adsorbed NH_3 without significant change in pore volume and unit cell parameters. This strikes the delicate control in material properties at a molecular level. Dr. Pu Zhao from our research group contributed equally to this study. The DFT

calculations in this work were acquired in collaboration with Dr. Xin-Ping Wu at Key Laboratory for Advanced Materials, Center for Computational Chemistry and Research Institute of Industrial Catalysis, East China University of Science and Technology, P.R. CHINA. The results in this Chapter have been published in Journal of the American Chemical Society (DOI: 10.1021/jacs.0c12483).

3.1) Introduction

The development of smart materials for stimuli-responsive recognition, wherein a complex form in a manner that is sensitive to, or can be governed by, externally applied triggers such as light, temperature, pressure, magnetic or electric field has recently been receiving a lot of attention. Molecular engineering, biometric and design approaches offer an assortment of new chemistry and material design tools toward improving precision in tailoring properties. For example, understanding and controlling molecular motions of synthetic materials towards stimulus for their order-disorder transformation, reorientational and rotational motion associated with phase transitions may allow switching back and forth between hard or soft state, a breakthrough that offers an innovative solution to a long-standing challenge with synthetic materials by giving them both strength and shape adaptability. [1-3]

Metal-organic frameworks (MOFs) [4] or porous coordination polymers (PCPs) [5] are highly topical classes of porous crystalline solids, constructed by metal ions/clusters coordinated to functional organic linkers that are suitably under exploration in this area. They possess large surface area, high porosity, functional diversity and structural flexibility, which tremendously excites their use in many applications. [6-8] The rational design of

MOF materials for applications heavily relies on a thorough understanding of the host-guest interactions of the frameworks with exterior triggers. The nature of these interactions if controllable has been considered to primarily manipulate the MOF structural properties such as disorder, flexibility, compressibility as well as chemical reactivity. [3] Recently, different gas sorption phenomena in MOFs have been recognized for efficient gas separation application. [9-14] Sequential pore filling in non-uniform MOF pores has also been attributed for differential gas sorption phenomena. [9-10, 15] Flexible and dynamics motions of MOF linkers that undergo rotation or libration have been elucidated to play a dramatic role in guest-induced gate opening phenomena in many MOFs such as ZIF-8 [16], DUT-98 [17], and Cu-based PCPs [14].

The previously introduced structural transitions of MOFs, however, experience large volume change both in the nanospace and in the bulk solids challenging the practical use of these materials, especially in sorption-based applications. [18] This volume expansion in the adsorbent solid is disadvantageous as it may damage the storage tank, decompose the moldings, and also may result in slower diffusion of gases in the tank. Consequently, design of new porous 'rigid' materials that can show guest adsorption and desorption with specific interaction(s) without significant volume change is highly desirable and technologically important. For example, Kitagawa and co-workers showed by SXRD and refinement of their crystalline MOFs and porous coordination polymer (PCP) that the polarised CH_2Br (also Cl and I) linker with CO_2 interaction can account for the additional CO_2 stepped uptake without significant structural or volume changes. [18] Similarly, Bärwinkel and co-workers demonstrate that additional capacity of adsorption for CO_2 was realized by their crystalline microporous organically pillared layered silicates (MOPS) from their SXRD and refinement

using the interaction of CO_2 with the organic cationic pillar based on electrostatic interactions without any framework and macroscopic pore volume changes. [19]

In addition, studying the flexibility of MOF's organic linker by guest molecule stimulus at variable temperature may provide hints about their molecular interaction. To our understanding, flexible MOFs are characterised mainly by changes in the pore structure. For example, the "flexibility" is well-known to occur in phenylene-based ligand systems. [14, 20-21] Gonzalez-Nelson *et al*. [2] have recently reviewed the studies of rotational barriers and dynamics of such ligand motives upon guest inclusion from the literature. However, these works were set in context to materials that exhibit large changes in unit cell and pore volume upon guest inclusion and other stimuli. The framework flexibility in the context of mainly ligand "flipping" but without significant pore volume alteration remains almost unexplored.

Zr-based MOFs UiO-66 and UiO-67 [22] are well known for their robust yet defect-rich structures. [23-24] The effect of defects on the CO_2 adsorption behaviour of UiO-66 has been demonstrated previously. [25] Thus, the tailoring the framework to accommodate controllable missing linkers as demonstrated can have a strong impact on the materials' properties, both by changing the characteristics of the pore windows of the MOF and by controlling the access to internal sites in pore cavities. Further incorporation of hydrogen bond functionality directly into MOF for gas uptake and molecular recognition is also thought to be important for the fine-control. [3, 26] As a result, new properties such as flexible gate-opening behaviour (transition between a closed and open form) with higher resistance to structural collapse can be anticipated for a wide range of future nanotechnology applications. [3, 14-19, 21, 27]

Here, defective UiO-67 with its organic linkers is selected to demonstrate how its non-monodisperse pore structure created by missing linker defects affect its NH_3 adsorption behaviour. Sequential pore filling induced by different pore openings created by ligand defects leads to a two-step NH_3 adsorption isotherm in UiO-67. While responsive behaviours of MOFs to weakly interacting molecules such as hydrogen, carbon dioxide, and hydrocarbon have been widely explored, [9-11, 27-29] only a few reports focused on more polar coordinating gases such as water, alcohols, and NH_3. [12, 17, 30-31] In addition, although unusual adsorption behaviours for polar coordinating gases have been observed [12, 17, 30, 32], in-depth study on sorption mechanisms and structural responses of MOFs is rarely explored at the molecular level. In this study, *in situ* high-resolution neutron and synchrotron powder diffractions (NPD and SXRD) combined with density functional theory (DFT) calculations were used to study the precise binding domains and the structural interactions of NH_3 with UiO-67 framework. Although NPD has been used to study NH_3 adsorption in UiO-67 [33], detailed investigation of host-guest interactions in this material has not been reported before. To further engineer defects in UiO-67 to create a polar surface porous structure for controlled NH_3 adsorption, we synthesised defective UiO-bpydc by replacing the phenyl groups of biphenyl-*4,4′*-dicarboxylate (bpdc) linkers in UiO-67 with pyridine groups.[34-35] Thus a UiO-67 isostructure with different pore surface polarity is designed to fine-tune its NH_3 adsorption profile. Here, we show that H-bonding networks can be formed between the bipyridine scaffold and the adsorbed NH_3. They offer a steric hindrance to modify the NH_3 adsorption behaviour, disorder, and structural flexibility of the framework without major structural or pore volume change, indicating the importance of host-guest interactions on controlling the responsive behaviours of the MOFs with the trapped molecules upon external triggers. This work provides a microscopic picture of

porosity tailoring, disorder, and flexibility of MOFs with designated functional linkers by tunable NH_3 adsorption.

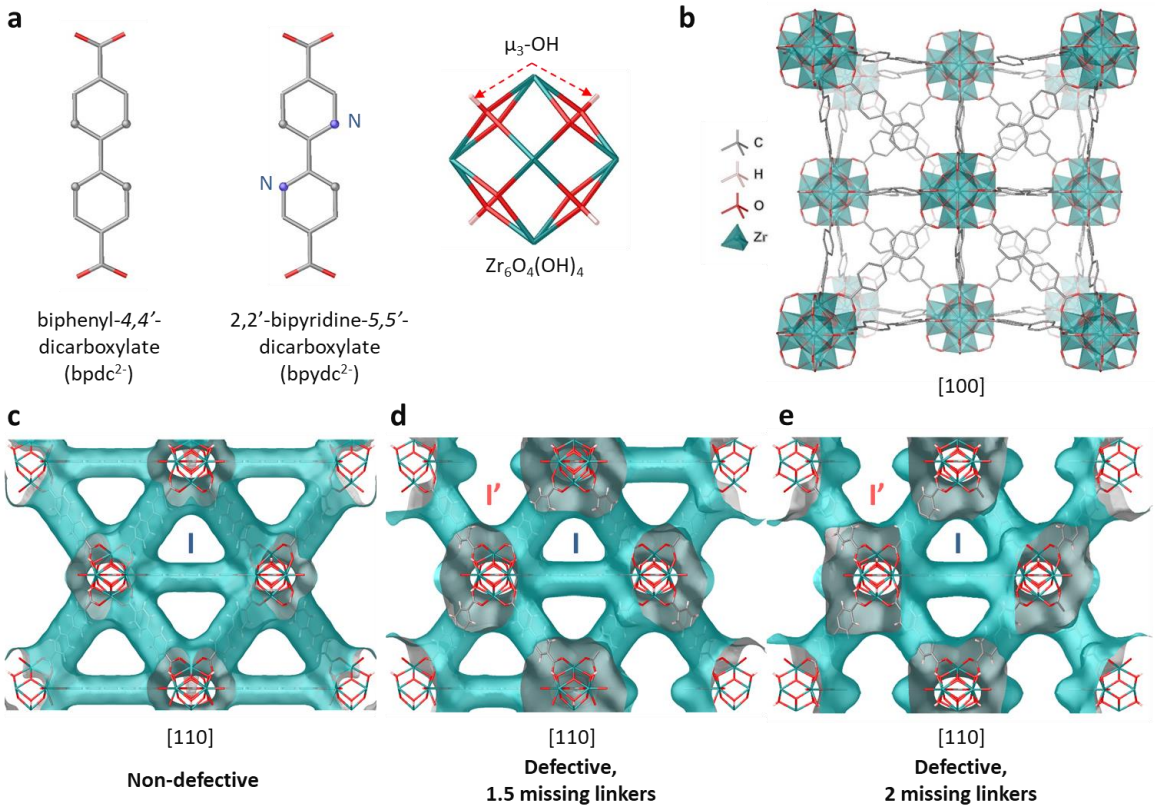

Figure 3.1 | Visualisation of the UiO-67 type MOFs. (**a**) Components including organic linkers and $Zr_6O_4(OH)_4$ nodes and (**b**) Crystal structure with a reticular formula of $Zr_6O_4(OH)_4(linker)_{6-x}(anionic\ capping\ species)_{2x}$, where x refers to the number of missing linkers per formula. (**c**) Solvent-excluded surface maps of non-defective and defective structures of the UiO-67-type MOFs with (**d**) 1.5 missing linkers per reticular formula and (**e**) 2.0 missing linkers per reticular formula. The radius of the probe sphere is 1.826 Å equivalent to the approximate van der Waals radius of an NH_3 molecule. I and I' represent primitive triangular and lozenge windows caused by missing linker defects, respectively.

The structures are illustrated by using polyhedral and stick models; Zr: teal, O: red, C: grey, N: Blue, H: pale pink. H atoms in the linkers in (**b**) are omitted for clarity.

3.2) Results and Discussion

UiO-67 [22] and UiO-bpydc [34-35] are isostructural MOFs consisted of Zr_6 oxoclusters coordinatively bound with biphenyl-*4,4′*-dicarboxylate (bpdc) and *2,2′*-bipyridine-*5,5′*-dicarboxylate (bpydc) linkers, respectively. Thanks to the high connectivity of Zr_6 oxoclusters, UiO-67 and UiO-bpydc can retain their crystal structures even with the occurrence of missing linkers. The degree of defects induced by missing linker can be manipulated during the synthesis procedure by using various capping molecules (e.g. acetate). The chemical formula of the UiO-67 and the UiO-bpydc are written as $Zr_6O_4(OH)_4(bpdc)_{6-x}$(anionic capping species)$_{2x}$ and $Zr_6O_4(OH)_4(bpydc)_{6-x}$ (anionic capping species)$_{2x}$ where x refers to the number of the missing linkers per formula. UiO-67 and UiO-bpydc exhibit the same crystal structures with space group *Fm*-3*m*. Their crystal structures with fcu topology are depicted in Figure 3.1. Without defects, the structures consist of uniform trigonal windows with the diameter of 11 Å that lead to interconnected tetrahedral and octahedral pores inside the structures (Figure 3.1c). For the tetrahedral and octahedral pores, their pore size is defined as the diameter of the biggest sphere that can be fitted into the specific pore (12 and 16 Å). In the presence of missing linker defects, the trigonal windows surrounding the defects are merged into lozenge windows with a dynamic size larger than 14 Å (Figure 3.1d and 3.1e). For clarity, UiO-67 and UiO-bpydc with defects will be referred to as “UiO-67” and “UiO-bpydc” throughout the paper, respectively, unless otherwise specified.

In this study, UiO-67 and UiO-bpydc were solvothermally prepared by using acetic acid (CH_3COOH) as a modulator. $ZrCl_4$, glacial CH_3COOH, and a linker of choices (H_2BPDC or H_2BPYDC for UiO-67 and UiO-bpydc, respectively) were mixed well in DMF solvent. The mixture was then kept at 393 K for 24 h. After the solvothermal treatment, the white precipitate was washed thoroughly with DMF three times, MeOH three times, followed by MeOH exchange for three days to remove any unreacted species and non-volatile DMF from the products. The final product was collected by centrifugation and activated at 423 K under vacuum for 12 h before storing in a desiccator. Detailed synthesis of the MOF samples are given in Section 2.2 of Chapter 2.

Table 3.1 | Sample information used in the *in situ* NPD experiments.

Sample	**UiO-67**				**UiO-bpydc**			
Reticular formula	$Zr_6O_4(OH)_4(bpdc)_{6-x}(acetate)_{2x}$				$Zr_6O_4(OH)_4(bpdc)_{6-x}(acetate)_{2x}$			
Actual reticular formula[a]	$Zr_6O_4(OH)_4(bpdc)_4(acetate)_4$				$Zr_6O_4(OH)_4(bpydc)_{4.5}(acetate)_3$			
Loading amount of ND_3 (mmol/g)	0.00	1.23	4.63	7.60	0.00	4.15	4.27	6.06
Loading amount of ND_3 (molecule/unit cell)	0.00	9.65	36.3	59.6	0.00	32.6	33.6	47.6
Loading temperature (K)	300				300			
Measurement temperature (K)	300				300			

[a] Based on the ICP-MS data in the Appendices of Chapter 3.

XRD, elemental analyses, TG, and N_2 sorption analyses were employed to verify structural properties and compositions of the prepared MOF samples (Figures A3.1-A3.8).

These values suggest a significant degree of missing linker (defects), which generally agree well with the previous report that used monocarboxylic acid as the modulator. [22] The analysis results of the defective MOFs after healing process [36] also reveal the repairing some of the linker density for the UiO-67 and the UiO-bpydc samples. The post-healing process gives narrower pore size distributions which can be clearly observed (Figures A3.7 and A3.8). There is a sharp increase of the pores centred at around 11 Å along with a general reduction of larger pores after the defect healing process. These observations confirm that the missing linker defects indeed pervasively exist and potentially affect the pore structure. After the healing process, we did not observe any significant change in the pore volume as similar to that of the previous works. [18-19] Although it is known that defects could affect pore volume, the observed change in the pore size distribution is more likely to reflect the change in the quantities of the windows rather than the interior pores.

3.2.1) NH_3 adsorption in defective UiO-67

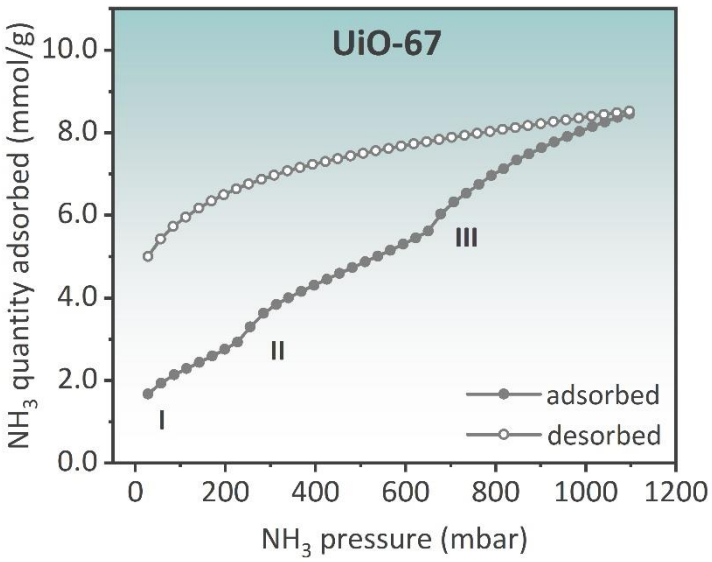

Figure 3.2 | NH_3 sorption isotherm of UiO-67. The isotherm was measured at 298 K and up to 1100 mbar of NH_3 pressure. Under room temperature the open-ended desorption isotherm clearly indicates that some adsorbed NH_3 molecules partially retain in the MOF sample due to the strongly binding interaction (potentially at μ_3-OH sites). A more dramatic treatments including the uses of higher temperature and evacuation should be done to complete the desorption in a complete cycle.

All the NH_3 sorption experiments were performed collaboratively by Dr. James Taylor at the ISIS facilities. Information on the sample properties involved in the NH_3 adsorption analyses and the NPD experiments are summarized in Table 3.1. NH_3 sorption isotherms measured at 298 K and up to 1100 mbar of NH_3 pressure are shown in Figure 3.2. First, the profile of adsorption clearly displays a 'step-like shape' with two clear transitions. Such behaviour in MOFs is mainly caused by a gate-opening phenomenon: the interaction between guest molecules and pore walls, or a pore filling process, in particular for a polar

fluid such as water and NH_3 with nonpolar walls, whereas the change in framework size plays a minor role. [18-19] At the beginning of adsorption, there is a rapid and abrupt increase of over 1.70 mmol/g NH_3 uptake at an NH_3 pressure lower than 30 mbar (Position I). This result indicates the presence of strong adsorption sites inside the framework, likely due to the readily binding of NH_3 with either μ_3-OH in Zr_6 oxoclusters or missing linker defects. According to defect stoichiometry, the concentration of μ_3-OH of UiO-67 is estimated to be 1.91 mmol/g, which is comparable to the amount of NH_3 adsorbed. Therefore, we assign the majority of the initial adsorption to the NH_3 interaction with μ_3-OH. The uptake suddenly increased from 2.40 to 4.40 mmol/g at an NH_3 pressure of 250 mbar (Position II) and 5.60 to 8.40 mmol/g at an NH_3 pressure of 650 mbar (Position III) as the two transition points. These results suggest two strong but discrete changes in the interaction(s) of the MOF-NH_3 system upon increasing NH_3 partial pressure. In the desorption isotherms, large opened hysteresis loops were found, implying that the strongly bound NH_3 molecules resistively remain inside the framework, defying the adsorption-desorption reversibility. However, these bound NH_3 molecules can be fully desorbed by treating the samples at 423 K for 1 h under dynamic vacuum (Figure A3.9). NH_3 stability of UiO-67 was investigated by testing NH_3 sorption for three cycles and exposing the materials to NH_3 vapor for one week. In contrast with previous work, [33] no significant change of structures was found in XRD patterns of NH_3-loaded MOFs (Figure A3.10) and no shift of IR spectra in carbonyl region indicating the same binding mode of carboxylate linkers upon NH_3 incorporation (Figure A3.11). These results confirm the high stability of the materials for the NH_3 uptake experiments.

3.2.2) Elucidation of ND_3 adsorption sites inside defective UiO-67 by *in situ* powder diffraction

To understand the origin of the interesting stepwise MOF-NH_3 interactions at the molecular level, *in situ* high-resolution neutron powder diffraction (NPD) experiments supported by synchrotron X-ray powder diffraction (SXPD) were carried out at WISH beamline, ISIS Neutron, and Muon Source, and Diamond of the UK STFC facilities, respectively. This analysis, particularly the NPD, is a powerful tool to study MOF materials that contains both heavy and light elements. Unlike X-ray diffraction, neutron diffraction is sensitive to both organic linkers and metal clusters because the coherent neutron scattering cross-sections (σ_c) are independent of Z^2, where Z is an atomic number. The σ_c values of Zr, O, C, N, and D are 6.44, 4.23, 5.55, 11.01, and 5.59 barns, respectively. [37] Fully deuterated ammonia (ND_3) was used in these NPD experiments to minimize the incoherent scattering from H. This allows for a high diffraction contrast between the ND_3-loaded and the guest-free materials. The use of SXPD allowed complementary analysis (see in the Appendices of Chapter 3)

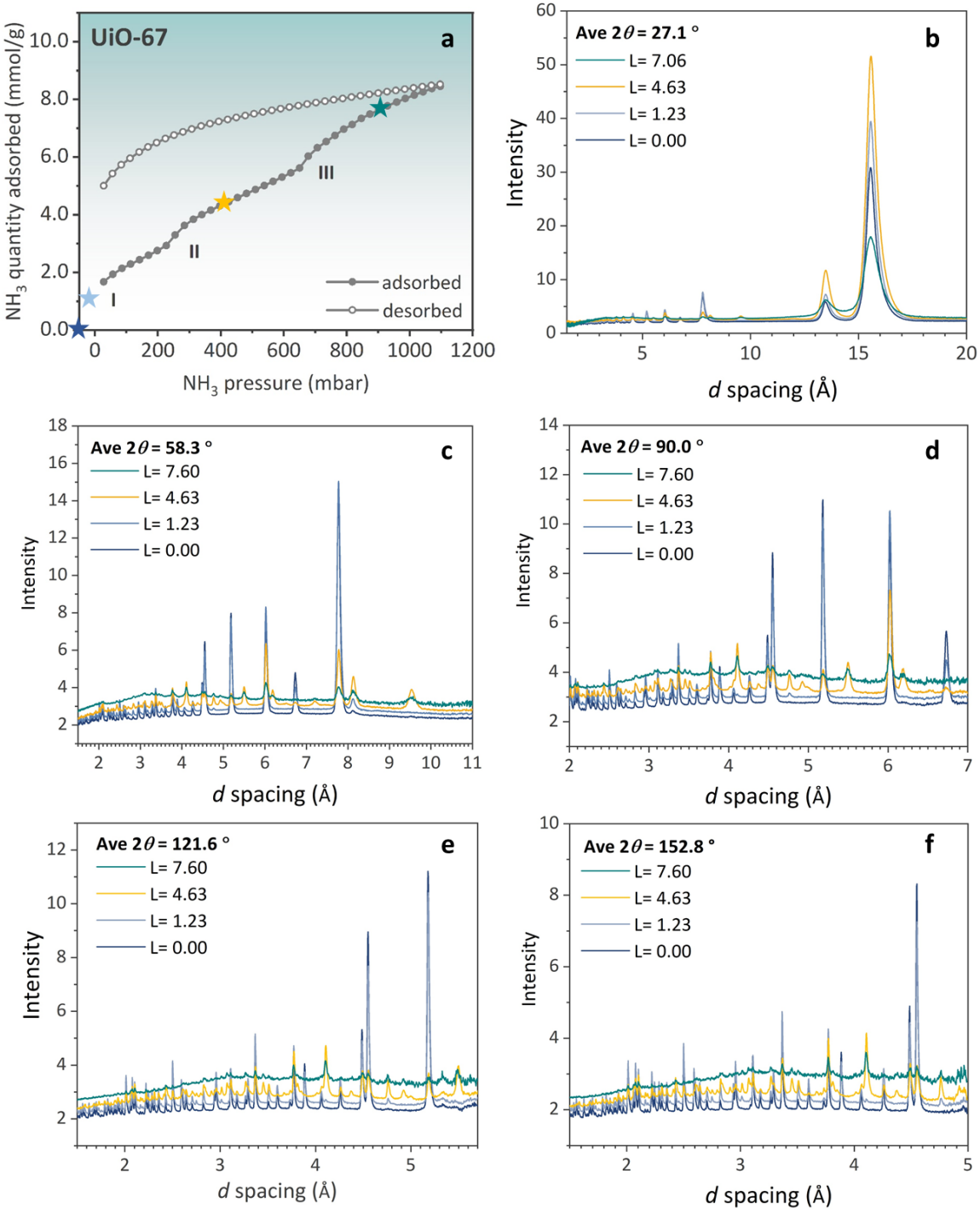

Figure 3.3 | *In situ* NPD patterns of UiO-67 at various loadings of ND_3. Each dosing point is marked as a star symbol in the stepwise NH_3 adsorption isotherm measured at 298 K and up to 1100 mbar of NH_3 pressure (**a**). The corresponding NPD patterns collected at 300 K

were normalized from different detector banks with the average 2θ of 27.1 ° (**b**), 58.3 ° (**c**), 90.0 ° (**d**), 121.6 ° (**e**), and 152.8 ° (**f**). *L* refers to the dosing capacity of ND_3 in mmol/g.

The NPD data of UiO-67 at different dosing amount of ND_3 were measured at 300 K to correlate the refined adsorption structures to the observed adsorption profiles at 298 K. The corresponding structural information, including atomic coordinates, orientations, and occupancies, were thoroughly analysed by using Rietveld refinement method [38] in TOPAS-Academic 5 software [39]. Details of data analysis are available in Section 2.2.4 of Chapter 2.

A series of NPD patterns for the adsorption of ND_3 by UiO-67 is shown in Figure 3.3. The diffraction patterns were plotted at different detector banks in order to compare data sensitivity and resolution. Some new Bragg peaks were clearly observed with a significant increase of peak intensity at the increasing quantity of ND_3 dosing. In contrast, the relative intensities of original peaks became reduced and their peak ratios significantly altered. These results can be caused by a structural modification of the MOF structure induced by both the orderly binding of the ND_3 molecules [33] and the dynamic motions of the MOF linkers. One might attribute the pronounced changes in diffraction patterns to the subtle deformation of the framework. However, Rietveld refinement confirms that there is no apparent change of the unit cell parameters upon the ND_3 inclusion over the range of NH_3 pressure used in this study (Figure A3.13). This observation suggests that peak intensities and positions can also be altered by guest loading without any change in structure.

Crystal structure refinement based on the high-resolution NPD data can directly reveal the existence of missing linker defects. [25] If the missing linker defects occur randomly in the MOF structure, the linker occupancies in the lattice points should be lower

than unity in the refinement. We, therefore, investigated this hypothesis by refining the structures of guest-free UiO-67 using the hydroxylated structure models reported in the literature. [34, 40] All atoms of the organic linkers were freely refined. The initial refinements revealed that the linker occupancies of the UiO-67 sample were clearly much less than 100 %. The much-improved values of fitting for bare UiO-67 with negligible residual nuclear density were achieved when we freely refined the occupancies of the central part of its corresponding linker ($[C_{12}H_8C_2]$), but left Zr fully coordinated by carboxylate O. The obtained occupancy of the UiO-67 linker was determined to be 48.38 % with R_{wp}/ R_p/ R_{exp}/ GOF values of 1.77 %/ 1.32 %/ 0.47 %/ 3.78 (Table 3.2). These values are in an agreement with the elemental analysis within experimental error, which confirms the presence of missing linker defects in these samples (Table A3.1 and A3.2).

Table 3.2 | Crystallographic data and details of ND_3@UiO-67 samples at various ND_3 dosing.

	Loading amount of ND_3 (mmol/g)			
	0.00	**1.23**	**4.63**	**7.60**
Reticular formula[a]	$Zr_6O_4(OH)_4(bpdc)_4(acetate)_4$			
Crystal system	Cubic			
Space group	*Fm*-3*m*			
Molar mass of MOFs (g/unit cell)[a]	7505.56			
ND_3 per unit cell (molecule)[a]	0.00	9.65	36.3	59.6
Detector	pixellated ^{3}He tube			

	Loading amount of ND_3 (mmol/g)			
	0.00	**1.23**	**4.63**	**7.60**
Measurement temperature (K)/ Counting time (minutes)	300/20	300/20	300/20	300/20
Refinement method	Rietveld			
Average 2θ for the refinement (°)	58.3			
a=b=c (Å)	26.88(4)	26.83(5)	26.83(7)	26.82(16)
V(Å^3)	19426(8)	19310(10)	19317(15)	19299(3)
R_{wp}/ R_p/ R_{exp} (%)	1.77/1.32/0.47	2.18/1.84/0.38	1.87/1.46/0.50	1.39/1.09/0.49
GOF (χ^2)	3.79	5.68	3.63	2.85

[a] Based on the UiO-67 structure with missing linkers obtained from ICP-MS results.

During the refinement, as previously stated, there is consistently lower occupancy of organic linker than carboxylate O atoms which implies that some O-type terminal groups still bind to unoccupied Zr nodes in the missing linker defects even after activation at 423 K for 24 hours under dynamic vacuum. We ruled out water (H_2O) as the defect-capping group since there were no significant nuclear residues at a position that was reported to be a site of the bound water molecule. [41] This sounds sensible because the activation condition should be sufficient to completely remove the trapped water from the samples. We then considered hydroxyl (–OH) and acetate (–$OOCCH_3$), as possible candidates. The latter was more likely to us since the best fitting values were gained when the Zr nodes were fully coordinated by carboxylate O atoms as mentioned above. Site occupancies of the carboxylate C and the *Ipso* C of the aromatic rings are also 11.79% higher than those of the remaining linker atoms,

suggesting that additional carboxylate molecules could possibly locate at the defect sites, yet in a disorderly binding configuration. The occurrence of acetates as the terminating groups is further confirmed by the ^1H NMR spectrum of the digested UiO-67 and UiO-bpydc samples (Figures A3.3 and A3.4). We thus used these refined structures as initial models for refinement of the ND_3-loaded samples.

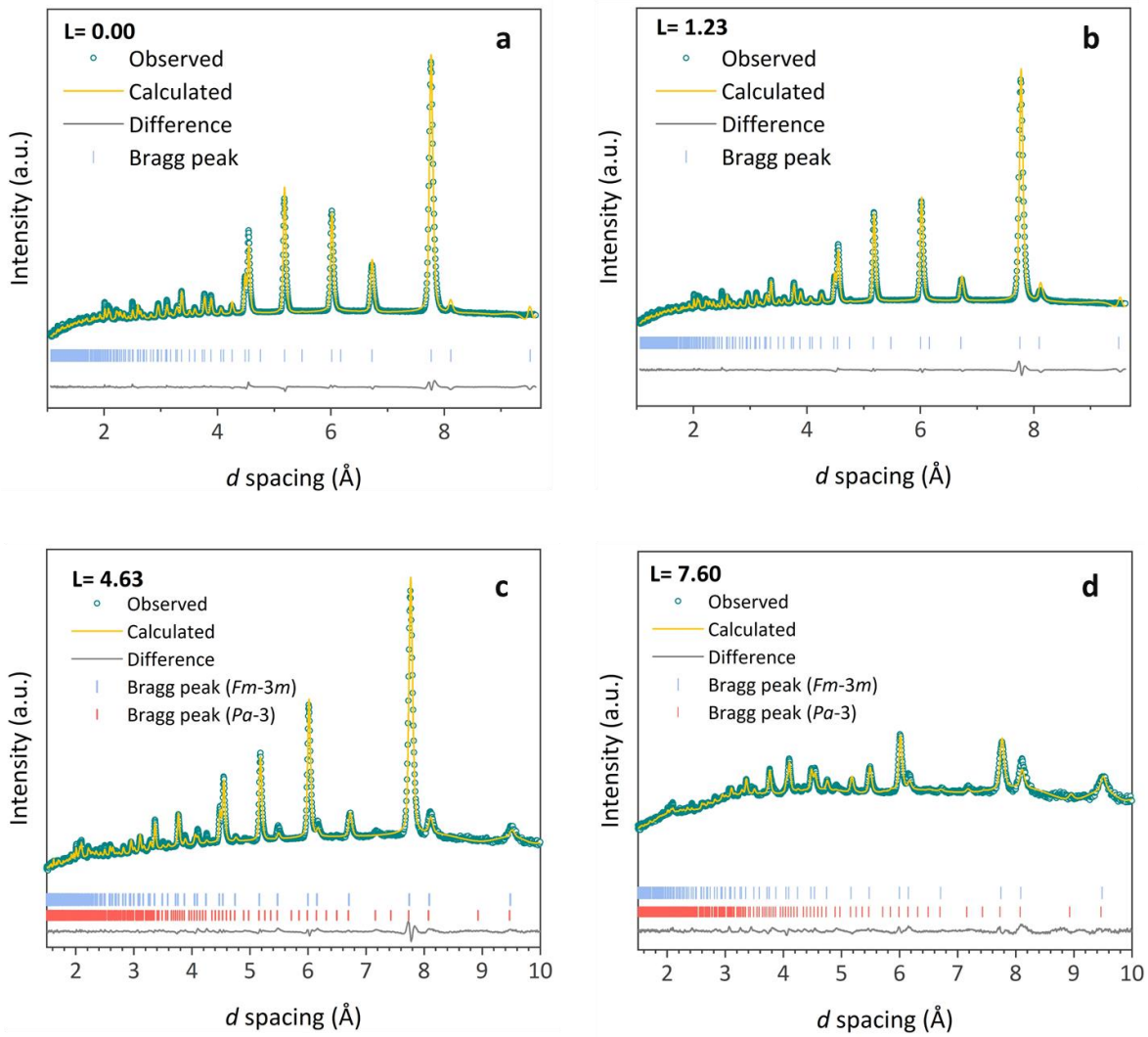

Figure 3.4 | Fitted NPD data of UiO-67 as a function of ND_3 adsorption. The refinements were conducted by using the data collected at 300 K from the average 2θ = 58.3 ° detector bank. *L* refers to the dosing amount of ND_3 in mmol/g. At this high ND_3 loading, small but

unindexed extra peaks was clearly found in the NPD pattern which is due to the distortion of the cubic *Fm*-3*m* MOF structure by the inhomogeneous ND_3 uptake (only a small quantity). Thus, in addition to using the single perfect MOF model (i.e. the model based on published crystal data and the occupancy number of linker with the assumption that the missing linker occurs randomly, the second MOF model with lowering the symmetry to cubic primitive cell (*Pa*-3 space group) to represent a small-distorted phase [42] was applied to achieve the best fit of the structure refinement. The weight percentage of each phase was freely refined to give the final phase composition of 78.16% (*Fm*-3*m*) and 21.84% (*Pa*-3) with all the diffraction peaks well fitted.

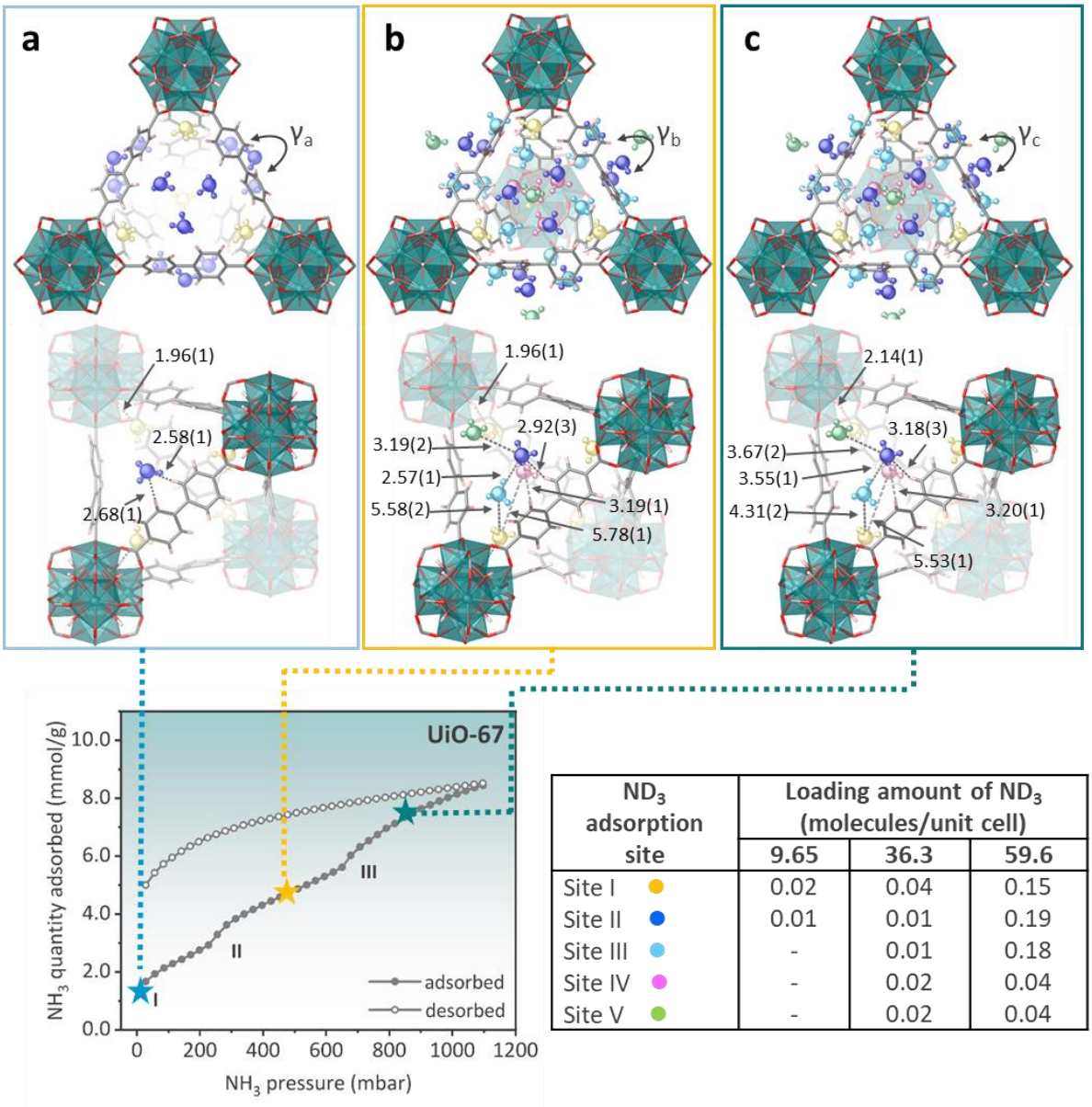

ND_3 adsorption site	Loading amount of ND_3 (molecules/unit cell)		
	9.65	36.3	59.6
Site I	0.02	0.04	0.15
Site II	0.01	0.01	0.19
Site III	-	0.01	0.18
Site IV	-	0.02	0.04
Site V	-	0.02	0.04

Figure 3.5 | ND_3 responsive behaviours of the defective UiO-67. Refined ND_3 positions in the UiO-67 structure at the ND_3 loading of **a**) 1.23, **b**) 4.63, and **c**) 7.60 mmol/g obtained from NPD data at 300 K which are equivalent to 9.65, 36.3, and 59.6 ND_3 molecules per unit cell. Each of the structures is refined and shown in top and side views of the trigonal window. Ball and stick models with different colors represent ND_3 molecules at different binding sites; site I: yellow, site II: blue, site III: light blue, site IV: pink, and site V: green. The host structures are illustrated by using polyhedral and stick models; Zr: teal, O: red, C:

grey, H: pale pink. Only tetragonal pores are depicted and the symmetry of ND_3 is disregarded for clarity. The dihedral angles between two phenyl rings (γ) are 32.19(1)°, 55.20(1) °, and 63.62(2) ° for γ_a, γ_b, and γ_c, respectively. The number in round brackets are referred to as an estimated standard deviation. The associated NH_3 sorption isotherm at the bottom left was measured at 298 K and up to 1100 mbar of NH_3 pressure; adsorption: closed circles; desorption: open circles).

For the Rietveld refinement of the ND_3-loaded UiO-67, as previously stated, small but unindexed extra peaks was clearly found in the NPD patterns of the samples with 4.63 and 7.60 mmol/g ND_3 loadings (Figure 3.4c and 3.4d). This observation can be ascribed to the distortion of the cubic *Fm*-3*m* MOF structure by the inhomogeneous ND_3 uptake [42] (only a small quantity). Thus, in addition to using the single perfect MOF model (i.e. the model based on published crystal data and the occupancy number of linker with the assumption that the missing linker occurs randomly, the second MOF model with lowering the symmetry to cubic primitive cell (*Pa*-3 space group) to represent a small-distorted phase was applied to achieve the best fit of the refinement. The weight percentage of each phase was freely refined to give the final phase composition of 78.16% (*Fm*-3*m*) and 21.84% (*Pa*-3) with all the diffraction peaks well fitted (Figures 3.4c and 3.4d and Table A3.3). The refined crystal structures of the ND_3-loaded samples are available to download with free of charge from The Cambridge Crystallographic Data Centre (see the Appendices of Chapter 3 for details of these crystal structures).

Figure 3.5a-c demonstrates the refined structures of UiO-67 at different ND_3 dosing derived from the NPD data at 300 K. All ND_3-loaded samples retain the *Fm*-3*m* space group but have crystallographic independent NH_3 binding sites resolved in each case. For ND_3-

loaded UiO-67 with the lowest uptake before any pore filling (Figure 3.5a), there are two sites for ND_3 binding to the frameworks; site I (occupancy 0.02) and site II (occupancy 0.01). At site I, ND_3 molecule primarily adsorbs close to the μ_3-OH with a $OH\cdots N_I$ distance of 1.96(1) Å ($O\cdots N_I$ = 2.80(1) Å), as we previously discussed. This result indicates the formation of H-bonding interaction between the μ_3-OH and ND_3, comparable to the recent report from Godfrey *et al*. [43] Interestingly, ND_3 molecules at site II located near the walls of the trigonal windows indicative of some degree of interactions with the MOF organic linkers ($H_{linker}\cdots N_{II}$= 2.58(1) and 2.68 (1) Å). Notice that the nonpolar phenyl rings of the biphenyl-*4,4′*-dicarboxylate (bpdc) linker may have formed a very weak dipole-induced dipole with each ND_3 molecule under this low adsorption quantity. Upon increasing the ND_3 dosing to 4.63 mmol/g or 36.3 ND_3 molecules/unit cell (Figure 3.5b), the site I occupancy clearly increase, indicating that more ND_3 molecules are adsorbed near the μ_3-OH. Apparently, further ND_3 molecules can be undoubtedly identified near the tetragonal pore by the structural refinement (site III and site IV). At site III, the ND_3 molecule filled the shallow pore positions with $N_{II}\cdots N_{III}$ bond distances among these ND_3 sites are in the range of 2.33(1) and 2.57(1) Å, indicating a H-bond network of these ND_3 molecules [44] spreading towards the filling of tetragonal pores from the ND_3 site II, presumably through the trigonal windows. Similarly, the inner pore site IV and a deep octahedral pore site V are also found occupied with ND_3, presumably through the growth of the H-bonding network. The progressive step-wise filling of the tetragonal pore is clearly shown due to the larger internal volume of the pore compared to the surface linker sites in the first transition step. When further dosing ND_3 beyond the second transition step (Figure 3.5c), higher occupancies of all the readily adsorbed sites are clearly observed. According to the refined structure, site V with interior filling of octahedral pores were observed along with an

increase in its occupancy. Again, the $N_V \cdots N_{II}$ bond distances of ND_3 at site V from site II are in the range of 3.67(2) and 4.20(2) Å, indicating the growth of H-bonding network in filling the octahedral pores presumably through the lozenge windows. The larger second transition step than the first one in the adsorption isotherm is in line with the expectation of the larger volume of octahedral pore and the higher partial pressure is required to fill the larger pore window.

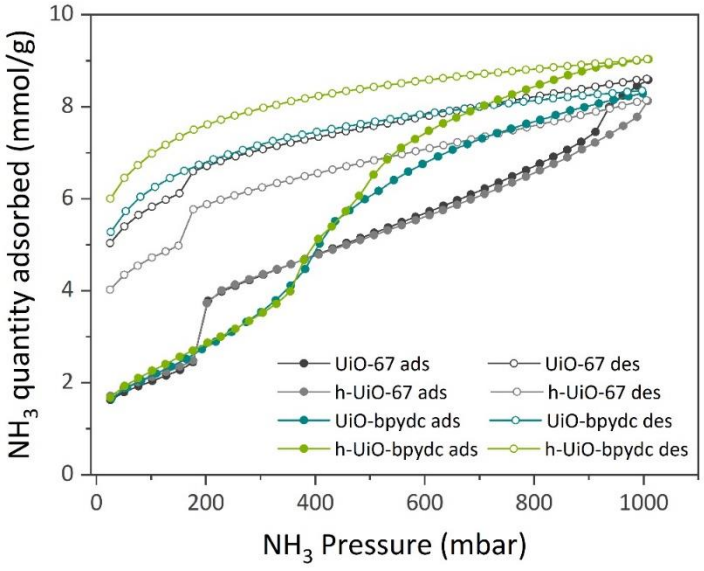

Figure 3.6 | Uptake data for NH_3 adsorption of MOF samples before and after the healing process. The isotherms were measured from 0 to 1000 mbar of NH_3 pressure at 298 K showing the similar sorption profiles as shown in Figure 3.2. The healed samples are denoted with h alphabets. Adsorption and desorption branches are labeled as ads and des, respectively. For UiO-67 sample, the two stepped uptakes at ~200 mbar and at ~800 mbar can also be seen, however, due to the different nature and smaller quantity of defects in this sample (~1 missing linker out of 6 by ICP-MS) smaller step changes occur at slightly different pressures. Notice that the second transition was disappeared from the healed UiO67, which was due to the total repair of the missing linker during healing (ICP-MS). On

the other hand, the NH_3 uptake of the healed UiO-bpydc increased from 8.4 to 9.0 $mmolg^{-1}$ with no significant change of the transition pressure. This result could be explained by the increase of NH_3 binding sites due to more bipyridine linkers available for binding in the healed UiO-bpydc.

In parallel with the trigonal windows in defect-free structure, the larger lozenge windows in our synthesised sample with the second transition (position III in Figure 3.5, bottom left) are thought to be generated by the missing linker defects, resulting in two distinctive stepwise adsorptions. The differences in pore shapes (tetragonal and octahedral) are not considered in the explanation of stepped NH_3 adsorption. This is because multilayer adsorption is not reflected in the adsorption isotherm of microporous materials and monolayer adsorption is hardly effected by pore shapes. [45] Comparison of NH_3 adsorption isotherms of unhealed (defective) and healed UiO-67 samples also supports this explanation (Figure 3.6). The adsorption step of the healed UiO-67 at higher NH_3 relative pressure was found almost disappeared. This undoubtedly reflects the relationship of the lozenge windows with the second transition step of NH_3 adsorption. The relative site occupancies of the material under exposure to ND_3 at different loadings with sufficient equilibration time may be more related to their adsorption affinity of the linker to the adsorbate rather than the molecular pathway for filling, which have not yet been studied in detail. [18-19]

3.2.3) NH_3-induced linker flipping in defective UiO-bpydc

To further engineer defective UiO-67 for controlled NH_3 adsorption, we synthesised defective UiO-bpydc by replacing the phenyl groups of biphenyl-*4,4′*-dicarboxylate (bpdc) linkers in UiO-67 with bi-pyridine groups. [34-35] It is anticipated that UiO-bpydc will have stronger H-bonding interactions with NH_3. NH_3-TPD data (Figure A3.14) can demonstrate

the above point. Three different desorption temperatures at approximately 140, 200, and 230 °C were observed for UiO-67 and these desorption temperatures are assigned to that of reversed filling from weaker binding to stronger binding (higher site number to lower site number). Notice that the desorption peaks of UiO-bpydc are shifted to higher temperatures, indicating that UiO-bpydc has stronger interactions with NH_3 molecules.

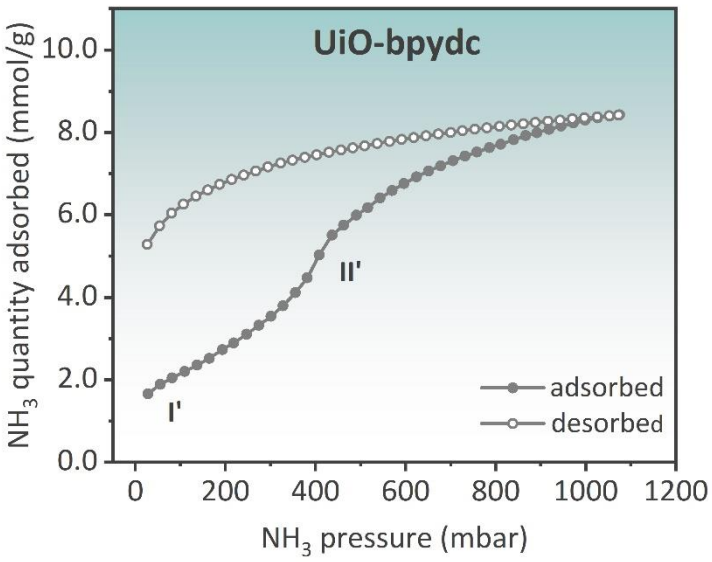

Figure 3.7 | NH_3 sorption isotherm of UiO-bpydc. The isotherm was measured at 298 K and up to 1100 mbar of NH_3 pressure. Under room temperature the open-ended desorption isotherm clearly indicates that some adsorbed NH_3 molecules partially retain in the MOF sample due to the strongly binding interaction (potentially at μ_3-OH sites). A more dramatic treatments including the uses of higher temperature and evacuation should be done to complete the desorption in a complete cycle.

According to the NH_3 adsorption isotherm in Figure 3.7, UiO-bpydc exhibits NH_3 uptake as high as 8.4 mmol/g at 298 K and 1100 mbar of pure NH_3 gas, which is comparable to that of UiO-67 with similar unit cell parameters and pore sizes. However, unlike UiO-67,

UiO-bpydc only has one large and sharper transition step (position II') in its NH_3 adsorption isotherm. The transition pressure *P* of 400 mbar is in between of those two (250 and 650 mbar) in the NH_3 adsorption isotherm of UiO-67. To further understand the origin of the interactions between NH_3 and UiO-bpydc, *in situ* NPD experiments were also carried out. NH_3 gas was replaced by ND_3 to get a better scattering signal. Diffraction patterns of the bare and ND_3-adsorbed UiO-bpydc are shown in Figure 3.8. Upon ND_3 dosing, peak intensities that correspond to the framework structure became weaker while small extra peaks with increasing intensities were observed. The positions of the extra peaks differ from ones observed in UiO-67 samples. This implies different binding domains of the ND_3 molecules inside the structure of ND_3-filled UiO-bpydc. The existence of missing linker defects was also confirmed by Rietveld refinements of the NPD results (Table A3.10-A3.12), giving the quantification of defects comparable to the elemental analyses and TG data (Table A3.1 and A3.2).

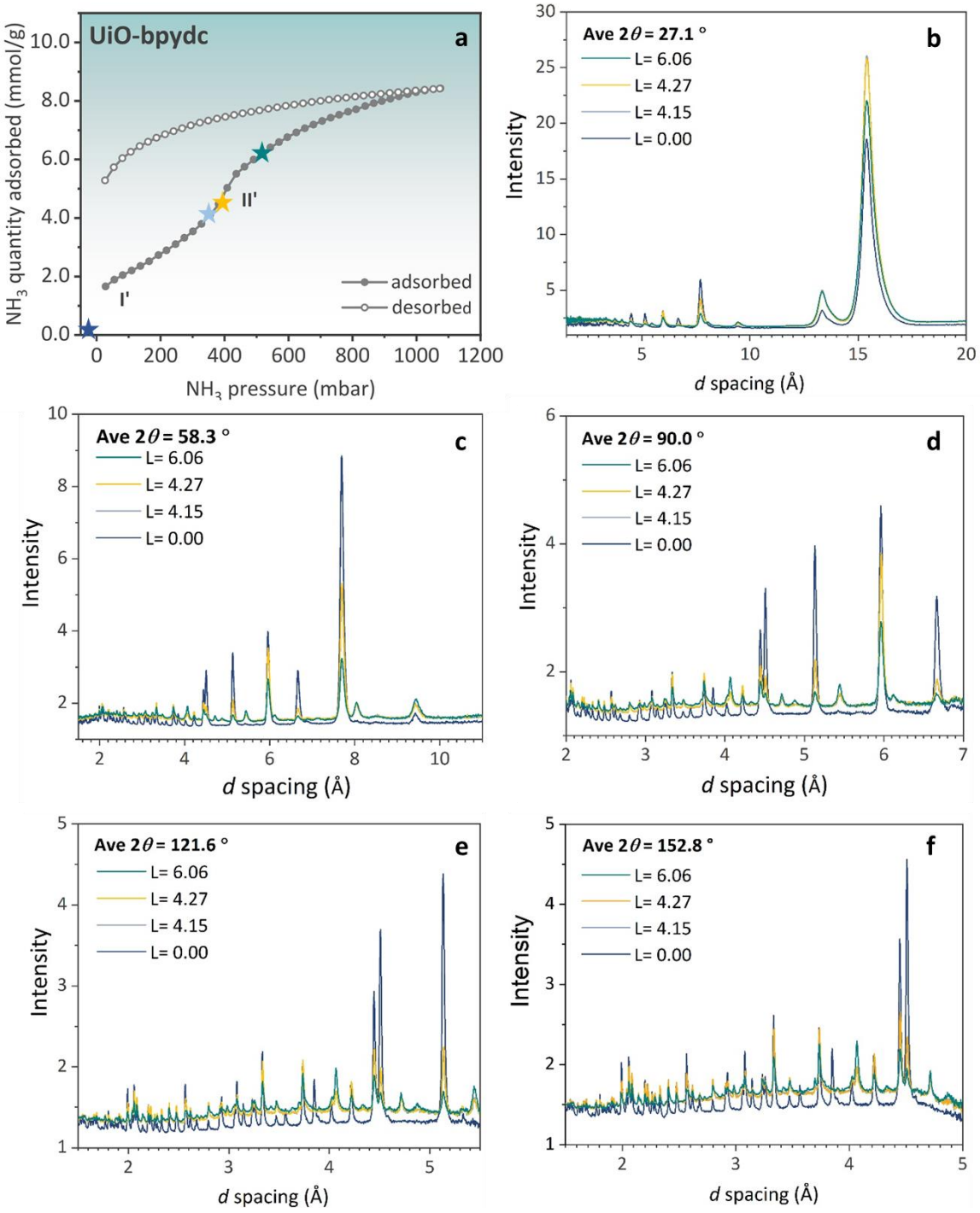

Figure 3.8 | *In situ* NPD patterns of UiO-bpydc at various loadings of ND_3. Each dosing point is marked as a star symbol in the stepwise NH_3 adsorption isotherm measured at 298 K and up to 1100 mbar of NH_3 pressure (**a**). The corresponding NPD patterns collected at

300 K were normalized from different detector banks with the average 2θ of 27.1 ° (**b**), 58.3 ° (**c**), 90.0 ° (**d**), 121.6 ° (**e**), and 152.8 ° (**f**). *L* refers to the dosing capacity of ND_3 in mmol/g.

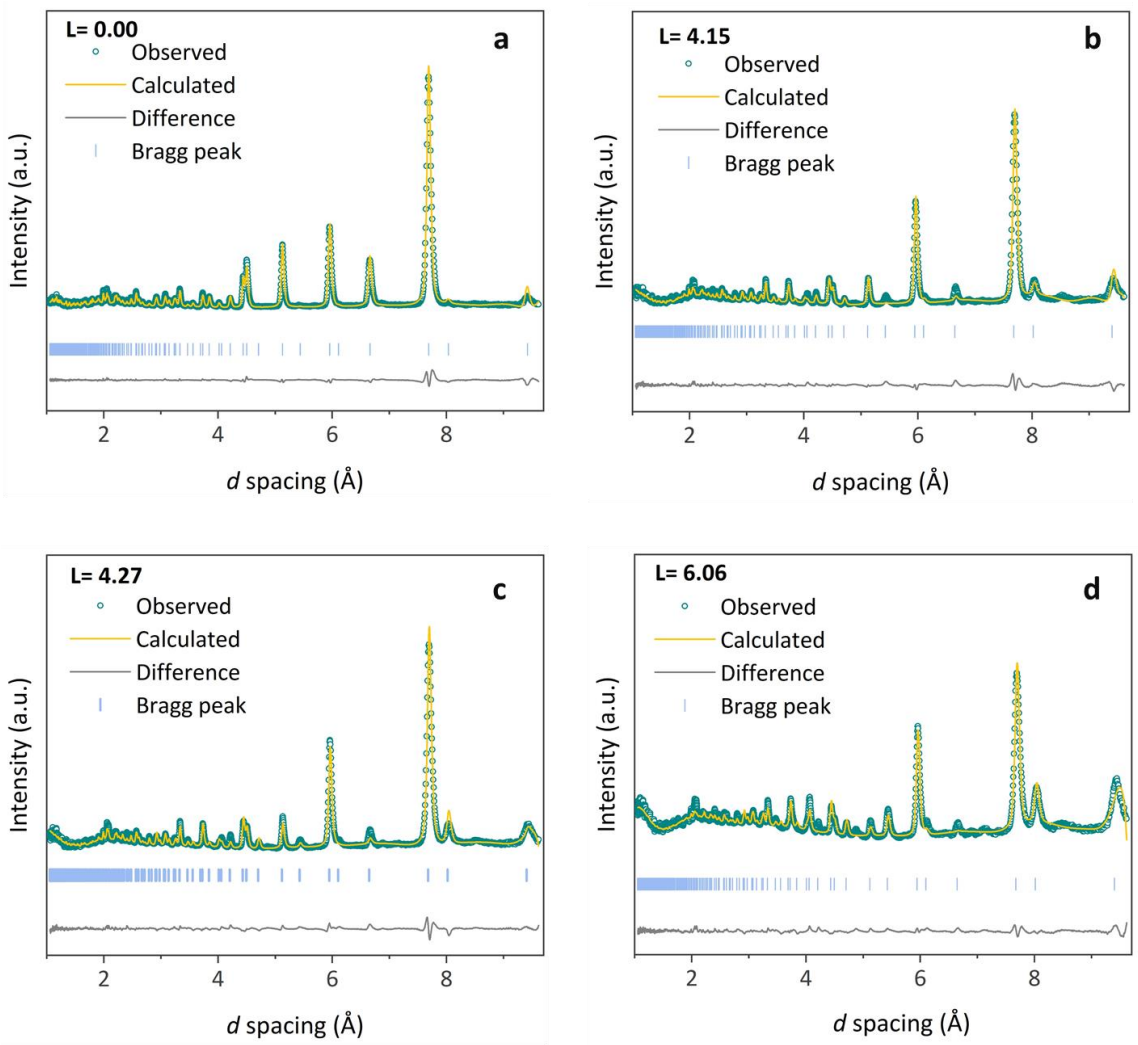

Figure 3.9 | Fitted NPD data of UiO-bpydc as a function of ND_3 adsorption. The refinements were conducted by using the data collected at 300 K from the average 2θ = 58.3 ° detector bank. *L* refers to the dosing amount of ND_3 in mmol/g.

Table 3.3 | Crystallographic data and details of ND_3@UiO-bpydc samples at various ND_3 dosing.

	Loading amount of ND_3 (mmol/g)			
	0.00	**4.15**	**4.27**	**6.06**
Reticular formula[a]	$Zr_6O_4(OH)_4(bpydc)_{4.5}(acetate)_3$			
Crystal system	Cubic			
Space group	*Fm*-3*m*			
Molar mass of MOFs (g/unit cell)[a]	7785.36			
ND_3 per unit cell (molecule)[a]	0.00	32.6	33.6	47.6
Detector	pixellated ^{3}He tube			
Measurement temperature (K)/ Counting time (minutes)	300/20			
Refinement method	Rietveld			
Average 2θ for the refinement (°)	58.3			
a=b=c (Å)	26.62(7)	26.57(7)	26.58(7)	26.57 (12)
V(Å^3)	18869(14)	18768(16)	18771(15)	18764(3)
R_{wp}/ R_p/ R_{exp} (%)	2.56/1.82/0.77	1.99/1.66/0.75	1.66/1.41/0.61	1.55/1.30/0.53
GOF (χ^2)	2.80	2.66	2.74	2.94

[a] Based on the UiO-bpydc structure with missing linkers obtained from ICP-MS results.

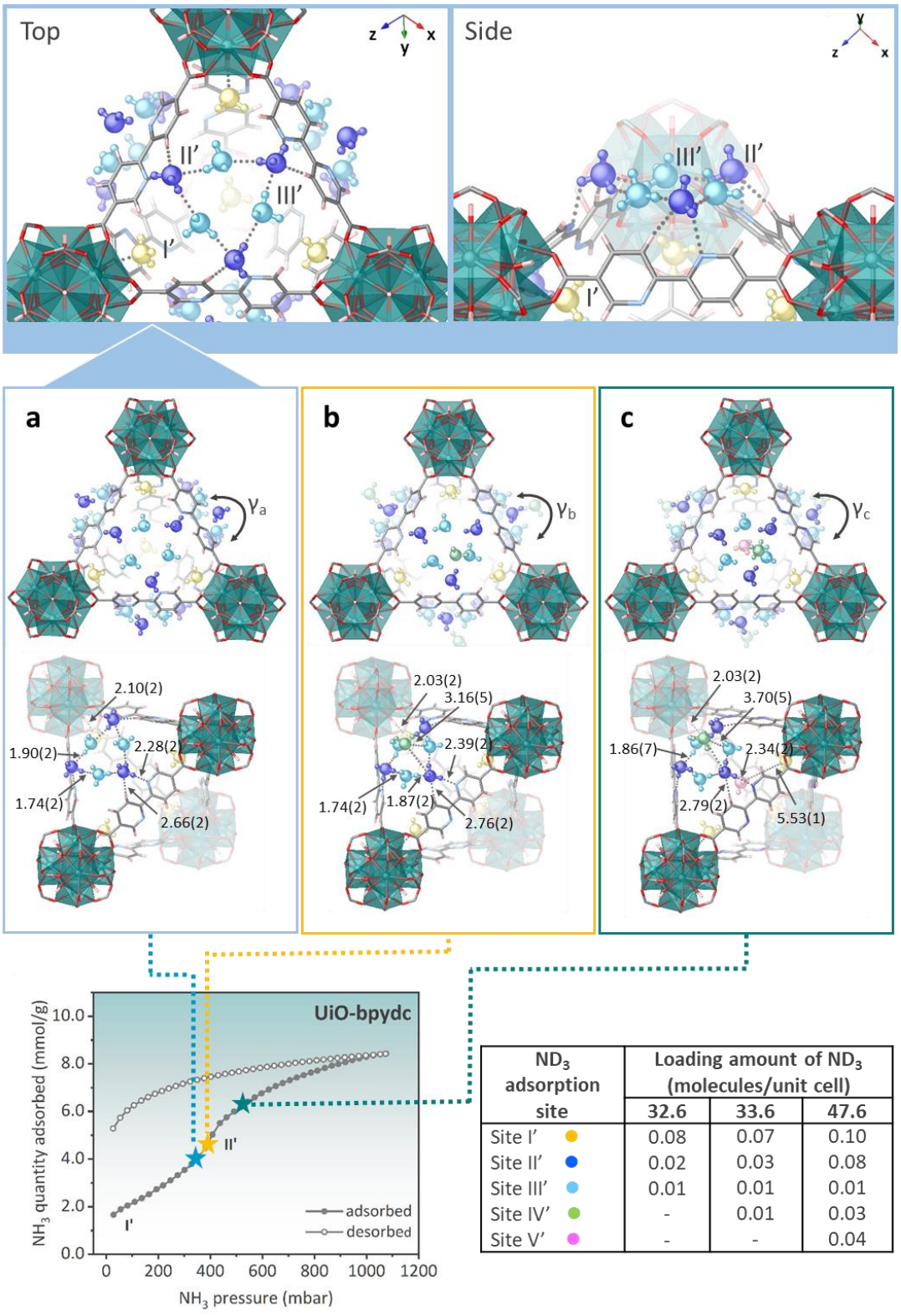

ND_3 adsorption site	Loading amount of ND_3 (molecules/unit cell)		
	32.6	33.6	47.6
Site I'	0.08	0.07	0.10
Site II'	0.02	0.03	0.08
Site III'	0.01	0.01	0.01
Site IV'	-	0.01	0.03
Site V'	-	-	0.04

Figure 3.10 | ND_3 responsive behaviours of the defective UiO-bpydc. Refined ND_3 positions of the UiO-bpydc structure at ND_3 dosing of **a**) 4.15, **b**) 4.27, and **c**) 6.06 mmol/g obtained

from NPD data at 300 K which are equivalent to 32.6, 33.6, and 47.6 ND_3 molecules per unit cell. Each of the structures is shown in top and side views of the window. Ball and stick models with different colors represent ND_3 molecules at different binding sites; site I': yellow, site II': blue, site III': light blue, site IV': green, site V': pink. The host structures are illustrated by using polyhedral and stick models; Zr: teal, O: red, C: grey, N: blue, H: pale pink. Only tetragonal pores are depicted and the symmetry of ND_3 is disregarded for clarity. Units of bond distances are in angstrom (Å). The dihedral angles between two pyridine rings (γ) are 19.95(1) °, 16.77(3) °, and 10.00(4) ° for γ_a, γ_b, and γ_c, respectively. The number in round brackets are referred to as an estimated standard deviation. The associated NH3 sorption isotherm at the bottom left was measured at 289 K and up to 1100 mbar of NH_3 pressure; adsorption: closed circles; desorption: open circles).

The fitted NPD data of UiO-67 as a function of ND_3 adsorption obtained from the Rietveld refinement and their corresponding crystallographic data are presented in Figure 3.9 and Table 3.3, respectively. These excellent fits with the low values of *R* factors and *GOF* reflect the high reliability of the fitting. Figure 3.10a-c demonstrates the refined structures of UiO-bpydc at different ND_3 dosings. First, we have considered the two points just below the transition step in the NH_3 adsorption. The UiO-bpydc displays much higher ND_3 loadings of 4.15 mmol/g (32.6 ND_3 molecules/unit cell, Figure 3.10a) and 4.27 mmol/g (33.6 ND_3 molecules/unit cell, Figure 3.10b) as compared to ~2.5 mmol/g of pre-step adsorption value in the case of the UiO-67. In the first pre-step point, we again observed two independent binding sites of ND_3 lying close to the μ_3-OH moiety (site I') and the organic linkers (site II', but this time, the bipyridine linker), respectively, before the extensive filling of the pores. This indicates that the adsorption of ND_3 readily takes place, particularly at site

II', giving higher occupancy numbers. For site I', the $OH\cdots N_I$ bond distance is 2.10(2) Å, which is comparable to that found in the isostructural UiO-67 samples. This similarity of the $OH\cdots N_I$ distance in both UiO-67 and UiO-bpydc are indicative of identical primary strongest binding sites which result in the initial adsorption at the lowest partial pressure of ND_3 gas (position I' in Figure 3.10, bottom left). However, the three ND_3 at site II' of UiO-bpydc resides closer to each of the three organic linkers in the trigonal window with $N_{linker}\cdots D_{II'}$ and $H_{linker}\cdots N_{II'}$ lengths of 2.28(2) and 2.66(2) Å, respectively. This observation shown in Figure 3.10a reveals that the ND_3-bipyridine linker interaction is even stronger than the ND_3-biphenyl linker interaction with longer distances ($H_{linker}\cdots N_{II}$= 2.68(1), 3.19(1) and 3.20(1)) Å, Figures 3.5a, 3.5b, and 3.5c, respectively). Surprisingly, an extra binding of ND_3 at site III' was also observed in the shallow tetragonal pore, presumably forming the H-bonding network with the adsorbed three ND_3 molecules on each of the pyridine linkers of the trigonal window to give six bound ND_3 in total in this region. Thus, in UiO-bpydc, the measured $N_{II'}\cdots D_{III'}$ and $N_{III'}\cdots D_{II'}$ H-bonding distances between site II' and site III' initially built from adsorbed ND_3 on the N-containing linker around the trigonal window are 1.74(2) and 1.90(2) Å, respectively. This ND_3 configuration clearly depicts a H-bonding network of six ND_3 molecules with the three bipyridine linkers around the trigonal window. Further dosing of ND_3 molecules to the frameworks in the second pre-step point results in a surface closer site IV' above a H-bond packing of site II' and III' with a very low occupancy (0.01) (Figure 3.10b). Interestingly, almost no filling of any sites locating inside the tetragonal pore in this bipyridine linker which is significantly different from that of site III (0.01) and site IV (0.02) of UiO-67 at comparable ND_3 pressure (Figure 3.5b). The H-bonding network of ammonia appears to have blocked up further ND_3 molecules to gain access to the interior pores through the trigonal window as that of the UiO-67 (Figure 3.10).

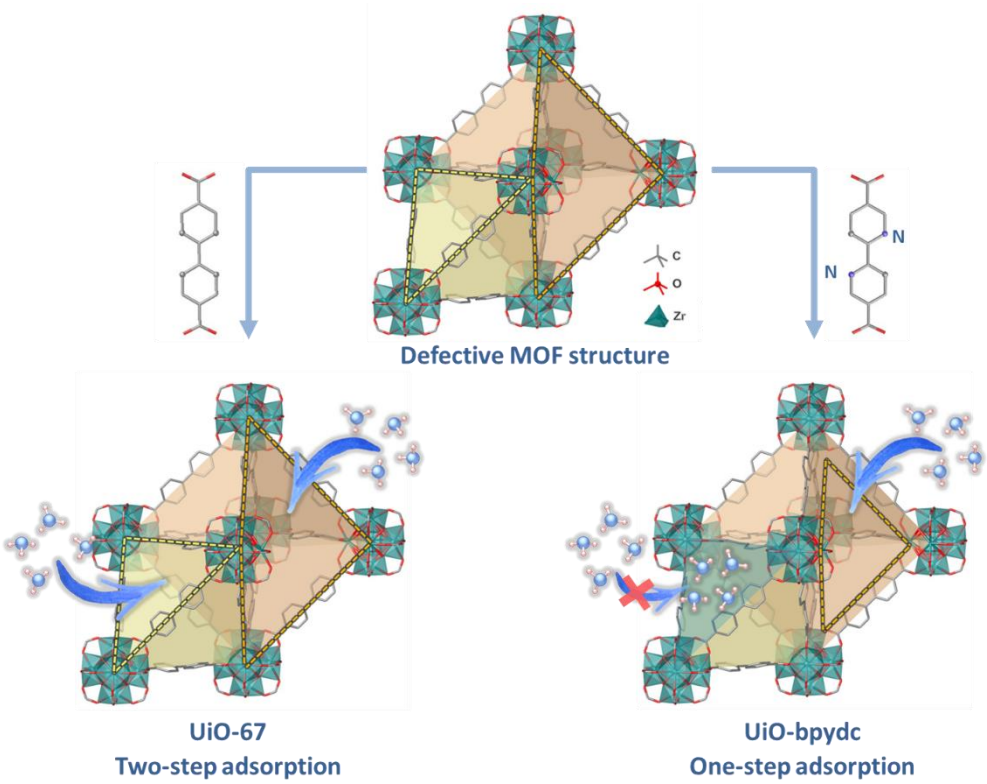

Figure 3.11 | Proposed NH_3 responsive behaviours of the defective UiO-67 type MOFs. The structures of the MOFs are illustrated by using polyhedral and ball& stick models; Zr: teal, O: red, C: grey, N: blue, H: pale pink. H atoms in the linkers are omitted for clarity. Yellow and orange areas refer to tetragonal and octahedral pores, respectively, whereas yellow and orange dashed lines represent trigonal and lozenge windows, respectively.

It is interesting to see the drastic increase in the ND_3 loading to 6.06 mmol/g or 47.6 ND_3 molecules/unit cell at the post-step point (Figure 3.10c), approaching to the status that all pores are filled up by the ND_3 molecules (site occupancies are high). Before saturation, we also anticipate that a similar H-bonding network between ND_3 molecules with remaining organic linkers in defective MOF structure can be built up to modify the lozenge windows under intermediate ND_3 pressures. Dissimilar to the closing up of the trigonal windows by the imperative H-bonding network with the six ND_3 molecules, the larger lozenge windows

created by missing and perhaps less ordered linkers may likely be modified to become new but smaller windows with the average size between the trigonal and lozenge windows (Figure 3.11). This can account for the merging of the two transition steps in UiO-67 to one in UiO-bpydc at the NH_3 pressure intermediate to those two step-pressures observed in the NH_3 adsorption isotherm of UiO-bpydc. This hypothesis is supported by realization of the correlation between the degree of missing linker defects and ND_3 adsorption behaviours using the defect-healed samples (Figure 3.6). For the healed UiO-67 sample, the total uptake did not change but the second transition step almost disappeared. In UiO-67, the second transition step is believed to strongly relate to the larger lozenge windows created by missing linker defects. According to the crystal structure of UiO-bpydc obtained at a ND_3 loading of 47.6 ND_3 molecules/unit cell (Figure 3.10c), a ND_3 molecule can be readily located inside the octahedral pore (site IV') presumably through the ND_3 modified lozenge windows since the trigonal windows are blocked up. Because the adsorption transition pressure is lower than the second transition pressure in UiO-67 attributed to adsorption through non-modified lozenge windows, lozenge windows in UiO-bpydc at high ND_3 loadings should have smaller diameters than the non-modified ones in UiO-67. This indeed indicates that the lozenge window is partially blocked by adsorbed ND_3. Thus, we show the gate-opening/closing behaviour via linker flipping of UiO-bpydc upon ND_3 adsorption for potential applications that heavily involve the dynamics of the linkers and kinetically-controlled processes such as gas separation, molecular sieving, and molecular sensing (Figure 3.11).

3.2.4) Analyses of the MOF-NH_3 interactions by DFT calculations

DFT calculations were performed to investigate the role of the bipyridine linkers of UiO-bpydc in forming the H-bonding network with NH_3 molecules, in comparison with the biphenyl ones of UiO-67. The structures of UiO-67 and UiO-bpydc from Rietveld refinements with slight modifications were used as initial models for geometry optimisation. Since we focused on whether the extensive imperative H-bonding network could form at the trigonal windows of the two MOFs, we used the non-defective MOF structures for DFT calculations. The optimised configurations of the NH_3 molecules at the trigonal windows of UiO-67 and the corresponding binding energies are shown in Figure 3.12. The optimised desolvated structure of UiO-67 without NH_3 shows that the two phenyl rings with a freely rotated single C−C bond in the linkers prefer to align with each other with a dihedral angle (γ) of 31.27 °: this matches well with the literature value. [40] The calculated binding energy of 0.05 eV indicates the very weak interaction with NH_3 molecule, which may be overcome at elevated temperature, giving no specific site binding (Figure 3.12a). Nevertheless, even in the absence of H bonding with the biphenyl linker of UiO-67, the NH_3 molecule at 0 K is still located near to the non-N containing linker due to dipole-induced dipole interaction. The binding energy is slightly enhanced to 0.06 eV per NH_3 molecule (Figure 3.12b) by further adding two more NH_3 molecules to the two remaining linkers of the trigonal window as similar to the refined structure in Figure 3.5a, depicting the consistent weak interactions. No further gain in binding energy (per NH_3 molecule) if NH_3 molecules were further added up to six.

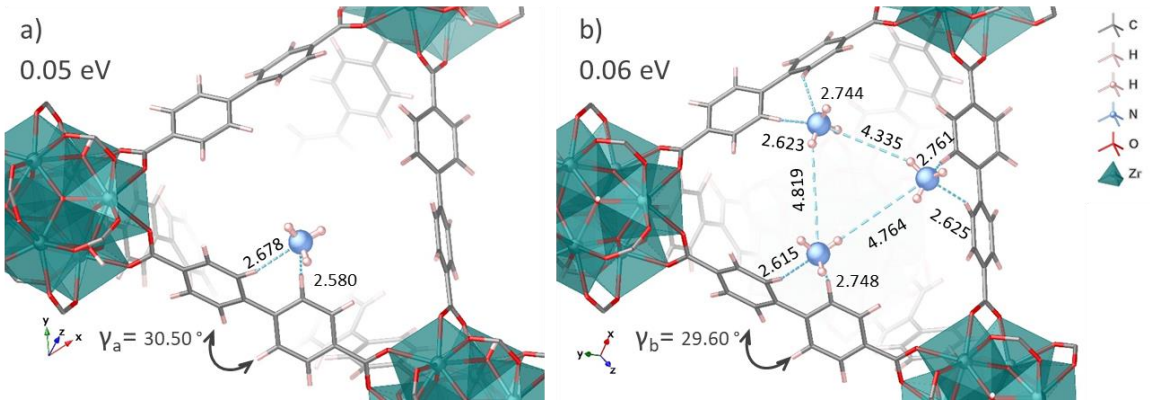

Figure 3.12 | Comparison of the UiO-67-NH_3 interactions by DFT calculations. DFT optimised structures of non-defective UiO-67 with *n* NH_3 molecules at the trigonal window: **a**) *n*= 1 and **b**) *n*= 3. The corresponding binding energies are depicted at the top left of each image. The units of the H bond lengths and the specific atom−atom distances are in angstrom (Å). The dihedral angles between two aromatic rings are denoted as *γ*.

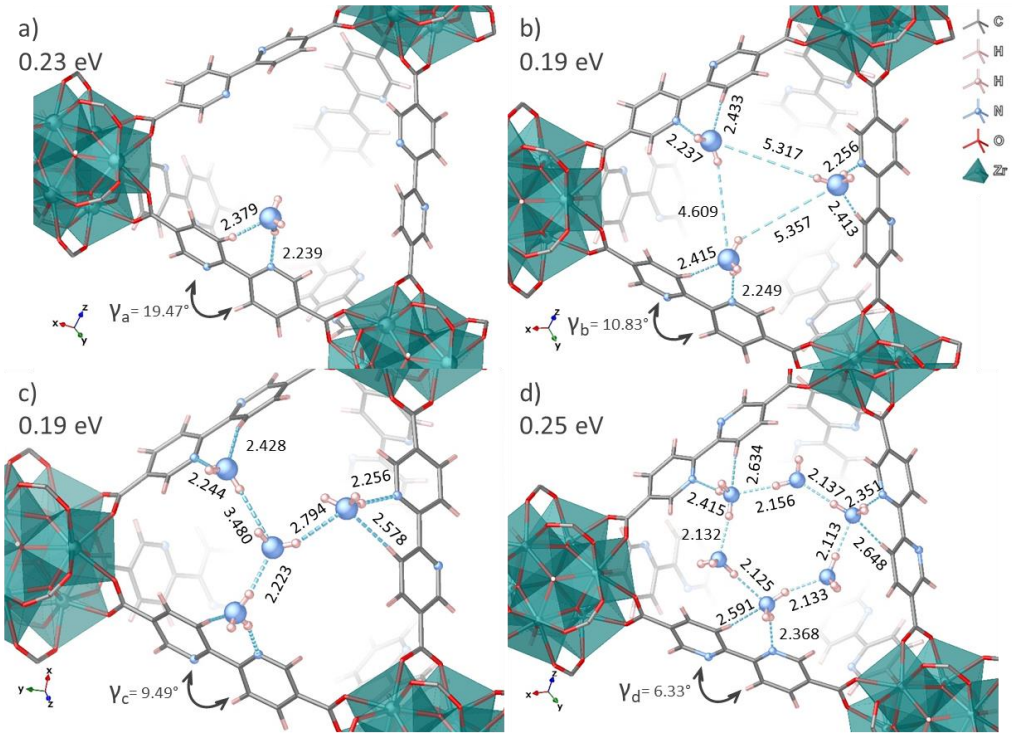

Figure 3.13 | Comparison of the UiO-bpydc-NH_3 interactions by DFT calculations. DFT optimised structures of non-defective UiO-bpydc with *n* NH_3 molecules at the trigonal

window: a) *n*=1; b) *n*= 3; c) *n*= 4; and d) *n*= 6. The corresponding binding energies are depicted at the top left of each image. The units of the H bond lengths and the specific atom−atom distances are in angstrom (Å). The dihedral angles between two aromatic rings are denoted as γ.

Figure 3.13 demonstrates the optimised configurations and the binding energies of the NH_3 molecules at the trigonal windows of UiO-bpydc. It is clear to note that the binding energy for one NH_3 adsorption at the linker of UiO-bpydc (0.23 eV, Figure 3.13a) is much stronger than that of UiO-67 (0.05 eV, Figure 3.12a). In the case of UiO-bpydc, the binding energy is slightly attenuated to 0.19 eV per NH_3 molecule by adding two or three more NH_3 molecules (Figure 3.13b and 3.13c), presumably the extra NH_3 molecules may disrupt the overall stability. Intriguingly, the highest binding energy of 0.25 eV per NH_3 molecule is obtained when six NH_3 molecules interconnected through H-bonding network with three linkers around the trigonal window (Figure 3.13d). Noticeably, the DFT optimised structures display the progressive distortion of the aligned bipyridine linkers with γ changed from 20.34 ^{o} (which is well matched with the NPD refined desolvated structure of UiO-bpydc with no NH_3) to 19.47 °, 10.83 °, 9.49 °, and 6.33 ° by increasing the number of NH_3 molecules at the trigonal window (Figure 3.13a-3.13d). Interestingly, for the case of UiO-bpydc with six NH_3 molecules (Figure 3.13d), the dihedral angles are twisted to nearly planar (γ = 6.33 °) in order to maximize the H-bonding geometry for all the molecules involved. This observation clearly corresponds to the NPD refined structure collected at 7 K at the highest loading (γ= 7.15(3)°), which will be discussed in more detail in Chapter 4. According to our molecular modelling, the close inter-linked NH_3 molecules block up the trigonal window and prevent NH_3 molecules from entering the interior pore. These DFT results are in good

agreement with the experimental observations and provide us with a further endorsement in the assembled H-bonding network with NH_3 adsorbates that governs the guest-responsive behaviours of this MOF-NH_3 system.

3.3) Chapter summary

High-resolution *in situ* neutron diffraction along with Rietveld refinement and DFT calculations have been used to elucidate the structural responses of defective UiO-67 and its derivatives upon the inclusion of NH_3. It is demonstrated that the different pore openings (windows) induced by missing linkers can introduce stepped and hysteresis NH_3 sorption in UiO-type MOFs. Results also establish the influence of functional linkers of these isostructural MOFs on their NH_3 affinity and flexibility. The great alteration of stepped NH_3 adsorption behaviours can take place when the phenyl groups are replaced by the pyridine ones. This unusual adsorption transition results from the steric hindrance of H-bond networks between the bipyridine scaffold and the adsorbed NH_3 molecules, forcing the linkers to adopt planar geometry to block up the pore and making the structure rigid. We demonstrate, for the first time, that the structural flexibility of the linkers on UiO-type MOFs can play a significant role in the type of gas uptake dependent on guest loading without significant change in pore volume and unit cell parameters, which otherwise are believed to be rigid and non-interactive.

Understanding the structure-function relationship of the MOF-NH_3 systems will enable the rational design of potential materials with controllable properties for not only strongly interacting gas storage, but also other applications such as controlled drug delivery and molecular sensing upon the use of external stimuli. Our study of utilising H-bonding

interactions of NH_3 with tailored linkers (and healing) merited as the first example of this kind, which plays a key role to stabilise the dynamical structures of the flexible biphenyl group for stepwise adsorption of NH_3 without major structural or pore volume change.

The work in this section has been published in Journal of the American Chemical Society (DOI: 10.1021/jacs.0c12483).

3.4) References

1. Budrikis, Z., Making the Switch. *Nature Reviews Materials* **2018,** *3* (6), 72-72.
2. Gonzalez-Nelson, A.; Coudert, F.-X.; van der Veen, M. A., Rotational Dynamics of Linkers in Metal–Organic Frameworks. *Nanomaterials* **2019,** *9* (3).
3. Krause, S.; Hosono, N.; Kitagawa, S., Chemistry of Soft Porous Crystals: Structural Dynamics and Gas Adsorption Properties. *Angewandte Chemie International Edition* **2020,** *59* (36), 15325-15341.
4. Zhou, H.-C.; Long, J. R.; Yaghi, O. M., Introduction to Metal–Organic Frameworks. *Chemical Reviews* **2012,** *112* (2), 673-674.
5. Kitagawa, S.; Kitaura, R.; Noro, S.-i., Functional Porous Coordination Polymers. *Angewandte Chemie International Edition* **2004,** *43* (18), 2334-2375.
6. Easun, T. L.; Moreau, F.; Yan, Y.; Yang, S.; Schröder, M., Structural and Dynamic Studies of Substrate Binding in Porous Metal–Organic Frameworks. *Chemical Society Reviews* **2017,** *46* (1), 239-274.
7. Karmakar, A.; Samanta, P.; Desai, A. V.; Ghosh, S. K., Guest-Responsive Metal–Organic Frameworks as Scaffolds for Separation and Sensing Applications. *Accounts of Chemical Research* **2017,** *50* (10), 2457-2469.
8. Wu, X.-P.; Gagliardi, L.; Truhlar, D. G., Cerium Metal–Organic Framework for Photocatalysis. *Journal of the American Chemical Society* **2018,** *140* (25), 7904-7912.
9. Zhao, P.; Fang, H.; Mukhopadhyay, S.; Li, A.; Rudić, S.; McPherson, I. J.; Tang, C. C.; Fairen-Jimenez, D.; Tsang, S. C. E.; Redfern, S. A. T., Structural Dynamics of a Metal–Organic Framework Induced by CO_2 Migration in Its Non-Uniform Porous Structure. *Nature Communications* **2019,** *10* (1), 999.
10. Krause, S.; Bon, V.; Senkovska, I.; Stoeck, U.; Wallacher, D.; Többens, D. M.; Zander, S.; Pillai, R. S.; Maurin, G.; Coudert, F.-X.; Kaskel, S., A Pressure-Amplifying Framework Material with Negative Gas Adsorption Transitions. *Nature* **2016,** *532*, 348.

11. Yang, S.; Lin, X.; Lewis, W.; Suyetin, M.; Bichoutskaia, E.; Parker, J. E.; Tang, C. C.; Allan, D. R.; Rizkallah, P. J.; Hubberstey, P.; Champness, N. R.; Mark Thomas, K.; Blake, A. J.; Schröder, M., A Partially Interpenetrated Metal–Organic Framework for Selective Hysteretic Sorption of Carbon Dioxide. *Nature Materials* **2012,** *11* (8), 710-716.

12. Zhang, S.-Y.; Jensen, S.; Tan, K.; Wojtas, L.; Roveto, M.; Cure, J.; Thonhauser, T.; Chabal, Y. J.; Zaworotko, M. J., Modulation of Water Vapor Sorption by a Fourth-Generation Metal–Organic Material with a Rigid Framework and Self-Switching Pores. *Journal of the American Chemical Society* **2018,** *140* (39), 12545-12552.

13. McDonald, T. M.; Mason, J. A.; Kong, X.; Bloch, E. D.; Gygi, D.; Dani, A.; Crocellà, V.; Giordanino, F.; Odoh, S. O.; Drisdell, W. S.; Vlaisavljevich, B.; Dzubak, A. L.; Poloni, R.; Schnell, S. K.; Planas, N.; Lee, K.; Pascal, T.; Wan, L. F.; Prendergast, D.; Neaton, J. B.; Smit, B.; Kortright, J. B.; Gagliardi, L.; Bordiga, S.; Reimer, J. A.; Long, J. R., Cooperative Insertion of CO_2 in Diamine-Appended Metal-Organic Frameworks. *Nature* **2015,** *519* (7543), 303-308.

14. Gu, C.; Hosono, N.; Zheng, J.-J.; Sato, Y.; Kusaka, S.; Sakaki, S.; Kitagawa, S., Design and Control of Gas Diffusion Process in a Nanoporous Soft Crystal. *Science* **2019,** *363* (6425), 387.

15. Cho, H. S.; Yang, J.; Gong, X.; Zhang, Y.-B.; Momma, K.; Weckhuysen, B. M.; Deng, H.; Kang, J. K.; Yaghi, O. M.; Terasaki, O., Isotherms of Individual Pores by Gas Adsorption Crystallography. *Nature Chemistry* **2019,** *11* (6), 562-570.

16. Fairen-Jimenez, D.; Moggach, S. A.; Wharmby, M. T.; Wright, P. A.; Parsons, S.; Düren, T., Opening the Gate: Framework Flexibility in ZIF-8 Explored by Experiments and Simulations. *Journal of the American Chemical Society* **2011,** *133* (23), 8900-8902.

17. Krause, S.; Bon, V.; Stoeck, U.; Senkovska, I.; Többens, D. M.; Wallacher, D.; Kaskel, S., A Stimuli-Responsive Zirconium Metal–Organic Framework Based on Supermolecular Design. *Angewandte Chemie International Edition* **2017,** *56* (36), 10676-10680.

18. Kanoo, P.; Matsuda, R.; Sato, H.; Li, L.; Hosono, N.; Kitagawa, S., Pseudo-Gated Adsorption with Negligible Volume Change Evoked by Halogen-Bond Interaction in the Nanospace of MOFs. *Chemistry – A European Journal* **2020,** *26* (10), 2148-2153.

19. Bärwinkel, K.; Herling, M. M.; Rieß, M.; Sato, H.; Li, L.; Avadhut, Y. S.; Kemnitzer, T. W.; Kalo, H.; Senker, J.; Matsuda, R.; Kitagawa, S.; Breu, J., Constant Volume Gate-Opening by Freezing Rotational Dynamics in Microporous Organically Pillared Layered Silicates. *Journal of the American Chemical Society* **2017,** *139* (2), 904-909.

20. Jiang, X.; Duan, H.-B.; Khan, S. I.; Garcia-Garibay, M. A., Diffusion-Controlled Rotation of Triptycene in a Metal–Organic Framework (MOF) Sheds Light on the Viscosity of MOF-Confined Solvent. *ACS Central Science* **2016,** *2* (9), 608-613.

21. Krause, S.; Evans, J. D.; Bon, V.; Senkovska, I.; Iacomi, P.; Kolbe, F.; Ehrling, S.; Troschke, E.; Getzschmann, J.; Többens, D. M.; Franz, A.; Wallacher, D.; Yot, P. G.; Maurin, G.; Brunner, E.; Llewellyn, P. L.; Coudert, F.-X.; Kaskel, S., Towards General Network Architecture Design Criteria for Negative Gas Adsorption Transitions in Ultraporous Frameworks. *Nature Communications* **2019,** *10* (1), 3632.

22. Cavka, J. H.; Jakobsen, S.; Olsbye, U.; Guillou, N.; Lamberti, C.; Bordiga, S.; Lillerud, K. P., A New Zirconium Inorganic Building Brick Forming Metal Organic Frameworks with Exceptional Stability. *Journal of the American Chemical Society* **2008,** *130* (42), 13850-13851.

23. Shearer, G. C.; Chavan, S.; Bordiga, S.; Svelle, S.; Olsbye, U.; Lillerud, K. P., Defect Engineering: Tuning the Porosity and Composition of the Metal–Organic Framework UiO-66 via Modulated Synthesis. *Chemistry of Materials* **2016,** *28* (11), 3749-3761.

24. Cliffe, M. J.; Wan, W.; Zou, X.; Chater, P. A.; Kleppe, A. K.; Tucker, M. G.; Wilhelm, H.; Funnell, N. P.; Coudert, F.-X.; Goodwin, A. L., Correlated Defect Nanoregions in a Metal–Organic Framework. *Nature Communications* **2014,** *5* (1), 4176.

25. Wu, H.; Chua, Y. S.; Krungleviciute, V.; Tyagi, M.; Chen, P.; Yildirim, T.; Zhou, W., Unusual and Highly Tunable Missing-Linker Defects in Zirconium Metal–Organic Framework UiO-66 and Their Important Effects on Gas Adsorption. *Journal of the American Chemical Society* **2013,** *135* (28), 10525-10532.

26. Forgan, R. S.; Marshall, R. J.; Struckmann, M.; Bleine, A. B.; Long, D.-L.; Bernini, M. C.; Fairen-Jimenez, D., Structure-Directing Factors when Introducing Hydrogen Bond Functionality to Metal–Organic Frameworks. *CrystEngComm* **2015,** *17* (2), 299-306.

27. Yang, Q.-Y.; Lama, P.; Sen, S.; Lusi, M.; Chen, K.-J.; Gao, W.-Y.; Shivanna, M.; Pham, T.; Hosono, N.; Kusaka, S.; Perry Iv, J. J.; Ma, S.; Space, B.; Barbour, L. J.; Kitagawa, S.; Zaworotko, M. J., Reversible Switching between Highly Porous and Nonporous Phases of an Interpenetrated Diamondoid Coordination Network That Exhibits Gate-Opening at Methane Storage Pressures. *Angewandte Chemie International Edition* **2018,** *57* (20), 5684-5689.

28. Lama, P.; Barbour, L. J., Distinctive Three-Step Hysteretic Sorption of Ethane with *in situ* Crystallographic Visualization of the Pore Forms in a Soft Porous Crystal. *Journal of the American Chemical Society* **2018,** *140* (6), 2145-2150.

29. Sikiti, P.; Bezuidenhout, C. X.; van Heerden, D. P.; Barbour, L. J., Direct *in situ* Crystallographic Visualization of a Dual Mechanism for the Uptake of CO_2 Gas by a Flexible Metal–Organic Framework. *Inorganic Chemistry* **2019,** *58* (13), 8257-8262.

30. Rieth, A. J.; Dincă, M., Controlled Gas Uptake in Metal–Organic Frameworks with Record Ammonia Sorption. *Journal of the American Chemical Society* **2018,** *140* (9), 3461-3466.

31. Rieth, A. J.; Hunter, K. M.; Dincă, M.; Paesani, F., Hydrogen Bonding Structure of Confined Water Templated by a Metal-Organic Framework with Open Metal Sites. *Nature Communications* **2019,** *10* (1), 4771.

32. Leroux, M.; Mercier, N.; Allain, M.; Dul, M.-C.; Dittmer, J.; Kassiba, A. H.; Bellat, J.-P.; Weber, G.; Bezverkhyy, I., Porous Coordination Polymer Based on Bipyridinium Carboxylate Linkers with High and Reversible Ammonia Uptake. *Inorganic Chemistry* **2016,** *55* (17), 8587-8594.

33. Barter, M.; Hartley, J.; Yazigi, F.-J.; Marshall, R. J.; Forgan, R. S.; Porch, A.; Jones, M. O., Simultaneous Neutron Powder Diffraction and Microwave Dielectric Studies of Ammonia Absorption in Metal–Organic Framework Systems. *Physical Chemistry Chemical Physics* **2018,** *20* (15), 10460-10469.

34. Gonzalez, M. I.; Bloch, E. D.; Mason, J. A.; Teat, S. J.; Long, J. R., Single-Crystal-to-Single-Crystal Metalation of a Metal–Organic Framework: A Route toward Structurally Well-Defined Catalysts. *Inorganic Chemistry* **2015,** *54* (6), 2995-3005.

35. Li, L.; Tang, S.; Wang, C.; Lv, X.; Jiang, M.; Wu, H.; Zhao, X., High Gas Storage Capacities and Stepwise Adsorption in a UiO Type Metal–Organic Framework Incorporating Lewis Basic Bipyridyl Sites. *Chemical Communications* **2014,** *50* (18), 2304-2307.

36. Gutov, O. V.; Hevia, M. G.; Escudero-Adán, E. C.; Shafir, A., Metal–Organic Framework (MOF) Defects under Control: Insights into the Missing Linker Sites and Their Implication in the Reactivity of Zirconium-Based Frameworks. *Inorganic Chemistry* **2015,** *54* (17), 8396-8400.

37. Sears, V. F., Neutron Scattering Lengths and Cross Sections. *Neutron News* **1992,** *3* (3), 26-37.

38. Young, R. A., *The Rietveld Method*. International Union of Crystallograhy: Chester, England, 1993.

39. Coelho, A., TOPAS and TOPAS-Academic: an Optimization Program Integrating Computer Algebra and Crystallographic Objects Written in C++. *Journal of Applied Crystallography* **2018,** *51* (1), 210-218.

40. Ko, N.; Hong, J.; Sung, S.; Cordova, K. E.; Park, H. J.; Yang, J. K.; Kim, J., A Significant Enhancement of Water Vapour Uptake at Low Pressure by Amine-Functionalization of UiO-67. *Dalton Transactions* **2015,** *44* (5), 2047-2051.

41. Trickett, C. A.; Gagnon, K. J.; Lee, S.; Gándara, F.; Bürgi, H.-B.; Yaghi, O. M., Definitive Molecular Level Characterization of Defects in UiO-66 Crystals. *Angewandte Chemie International Edition* **2015,** *54* (38), 11162-11167.

42. Øien-Ødegaard, S.; Shearer, G. C.; Wragg, D. S.; Lillerud, K. P., Pitfalls in Metal–Organic Framework Crystallography: towards More Accurate Crystal Structures. *Chemical Society Reviews* **2017,** *46* (16), 4867-4876.

43. Godfrey, H. G. W.; da Silva, I.; Briggs, L.; Carter, J. H.; Morris, C. G.; Savage, M.; Easun, T. L.; Manuel, P.; Murray, C. A.; Tang, C. C.; Frogley, M. D.; Cinque, G.; Yang, S.; Schröder, M., Ammonia Storage by Reversible Host–Guest Site Exchange

in a Robust Metal–Organic Framework. *Angewandte Chemie International Edition* **2018,** *57* (45), 14778-14781.

44. Hewat, A. W.; Riekel, C., The Crystal Structure of Deuteroammonia between 2 and 180 K by Neutron Powder Profile Refinement. *Acta Crystallographica Section A* **1979,** *35* (4), 569-571.

45. Matthias, T.; Katsumi, K.; Alexander, V. N.; James, P. O.; Francisco, R.-R.; Jean, R.; Kenneth, S. W. S., Physisorption of Gases, with Special Reference to the Evaluation of Surface Area and Pore Size Distribution (IUPAC Technical Report). *Pure and Applied Chemistry* **2015,** *87* (9-10), 1051-1069.

Chapter 4

Temperature-Dependent Responses of Defect-Rich Zr-Based Metal-Organic Frameworks via NH_3 Adsorption

To get a better understanding of the NH_3 adsorption behaviours and the role of functional linkers in defect-rich Zr-based MOFs including UiO-67 and UiO-bpydc, this Chapter presents the extended study of the responsive behaviours of these MOFs toward progressive adsorption of ND_3 under different temperatures by using high-resolution *in situ* neutron powder diffractions (NPD) combined with Rietveld refinement and density functional theory (DFT) calculations. While the NPD patterns of the ND_3-loaded UiO-67 alters under different measurement temperatures, those of the ND_3-loaded UiO-bpydc surprisingly remains unchanged. These observations indicate the remarkably higher rigidity (i.e. less flexibility) of the UiO-bpydc linkers induced by H-bond interactions with the adsorbed ND_3 molecules, consequently suppressing a linker flipping upon thermal motion. Rotational energy barriers of the simplified MOF-NH_3 models calculated by DFT further confirm the above hypothesis. These results highlight the importance of the flexibility of the MOF linkers induced by linker-NH_3 interaction(s), pore structures, and temperature on regulating the adsorption behaviours in these UiO-67 type MOFs. The collaborative DFT calculations were carried out by Dr. Xin-Ping Wu at Key Laboratory for Advanced Materials, Center for Computational Chemistry and Research Institute of Industrial Catalysis, East China University of Science and Technology, P.R. CHINA. The work in this Chapter has been published in Journal of the American Chemical Society (DOI: 10.1021/jacs.0c12483).

4.1) Introduction

Recalling the proposed NH_3 adsorption mechanism of the defective UiO-67 type MOFs by thorough analysis of the powder diffraction data at room temperature and DFT calculations (see Figure 3.14 in Chapter 3), it is exciting to see that the flexibility of the linkers and pore structures can be subtly altered through the specific linker host-guest NH_3 interaction(s) and hence result in the distinct NH_3 adsorption behaviours. Non-monodispersed pore windows created by missing linkers can introduce stepped and hysteresis NH_3 sorption in these studied MOFs. Substituting biphenyl linkers in UiO-67 by bipyridine analogues in UiO-bpydc induces the formation of H-bond network between the linkers and the adsorbed NH_3, hence causing the steric hindrance to block up the pore. Although the loading-dependent adsorption behaviours in the UiO-type MOFs has been comprehensively studied, a correlation of linker flexibility, host-guest interaction(s), and temperature is one of the most exciting topics to be further explored. This will certainly develop a better understanding of the stimuli-responsive properties in such NH_3-MOF system.

Temperature-dependent adsorption studies in flexible porous solids have been intensively explored since they play a key role in sorption-based applications. [1-5] For example, Kitagawa and co-workers reported that the adsorption behaviour and stepped isotherms in a porous coordination polymer (PCP) changed as a function of temperature due to the inhibition of the linker rotation providing kinetically-controlled functions for efficient gas separation and storage. [1] Dynamically-controlled alteration of pore accessibility and thus adsorption volume via a significant thermally-induced rotation of phenylene-incorporated PCPs has been also established. [6] These studies clearly emphasise the

importance of temperature effect on governing the structural responses of the adsorbate materials in addition to the guest inclusion.

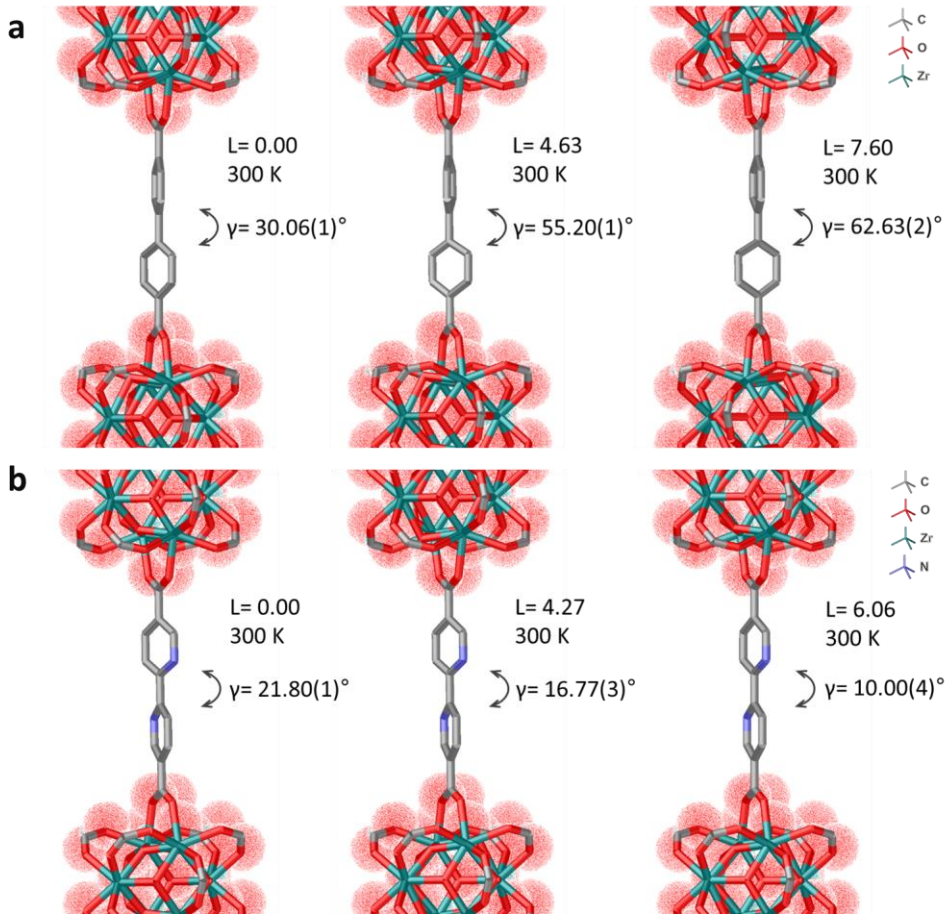

Figure 4.1 | Refined structures of UiO-67 (**a**) and UiO-bpydc (**b**) at different loadings of ND_3 at 300 K. The data were collected on the 58.3 ° detector bank of the WISH diffractometer. *L* and *γ* refer to the dosing amount of ND_3 in mmol/g and the dihedral angles between biphenyl rings, respectively. The host structures are illustrated by using a stick model; Zr: teal, O: red, C: grey, and N: blue. H atoms and loaded ND_3 molecules are omitted for clarity.

Considering the effect of temperature on the NH_3-adsorption behaviours of the UiO-type MOFs, the weak dipole-induced dipole interaction and strong H-bonding interaction as

compared to thermal motions may play a dramatic role on structural variations. This hypothesis is based on the fact that alteration of the dihedral angles of these MOFs derived from NPD data at 300 K are largely dependent on the ND_3 loading amount due to specific host-guest interactions (see Figure 4.1). This can open up the new way of controlling molecular rigidity of linkers using NH_3 and temperature as external triggers. As a result, I further investigates how the temperature influences structural change of the MOF-NH_3 system by means of *in situ* NPD in combination with Rietveld refinement and DFT calculations. As previously mentioned in Chapter 3, fully-deuterated ammonia (ND_3) was used in the NPD experiments to minimise the incoherent neutron scattering signal from hydrogen atoms causing a poor signal-to-noise ratio of the NPD patterns. The NPD experiments of the defective UiO-67, defective UiO-bpydc and their associated loaded samples were acquired at 300 K and 7 K by using WISH time-of-flight diffractometer, ISIS Neutron, and Muon Source, and Diamond of the UK STFC facilities. All the NPD patterns at 300 K are identical to those reported in Chapter 3. Details of the temperature-dependent NPD experiments and the DFT calculations of rotational energy barriers can be found in Section 2.2 of Chapter 2.

4.2) Results and Discussion

4.2.1) Structural Flexibility of Linker towards Temperature

NPD patterns of the ND_3-free and ND_3-loaded samples were measured at 300 K and/or 7 K and 150 K, respectively (Figures 4.2 and 4.3). Given the fact that the boiling and the melting points of ND_3 at 1 bar are 239.81 and 195.42 K, respectively, it is anticipated to

see different degrees of rotation of the linkers induced by the adsorbed ND_3 over these temperatures.

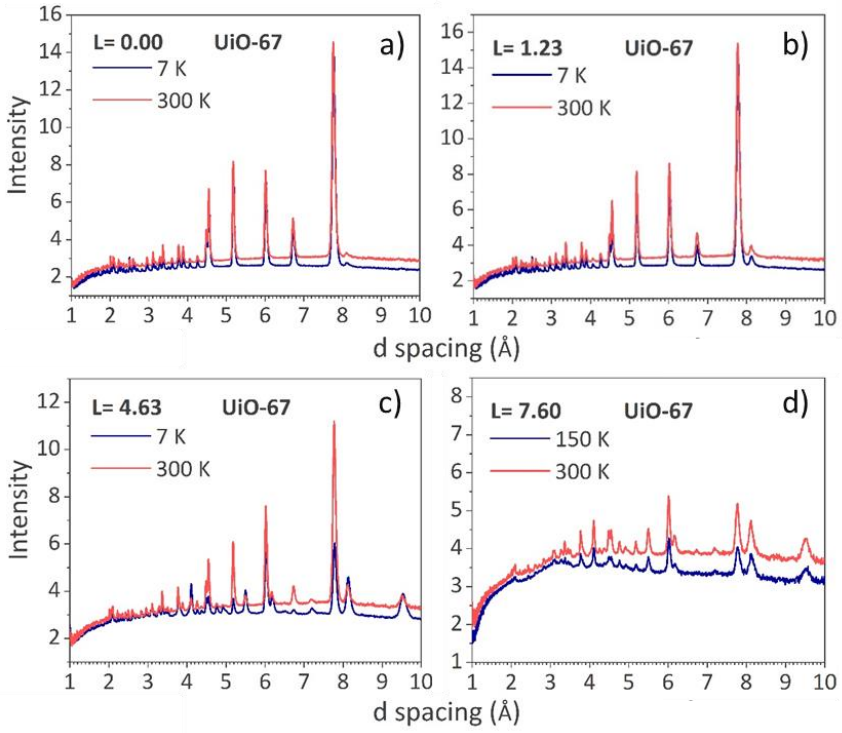

Figure 4.2 | *In situ* NPD patterns of UiO-67 at various loadings of ND_3 measured below 150 K and 300 K. The data were collected on the 58.3 ° detector bank of the WISH diffractometer. *L* refers to the dosing amount of ND_3 in mmol/g.

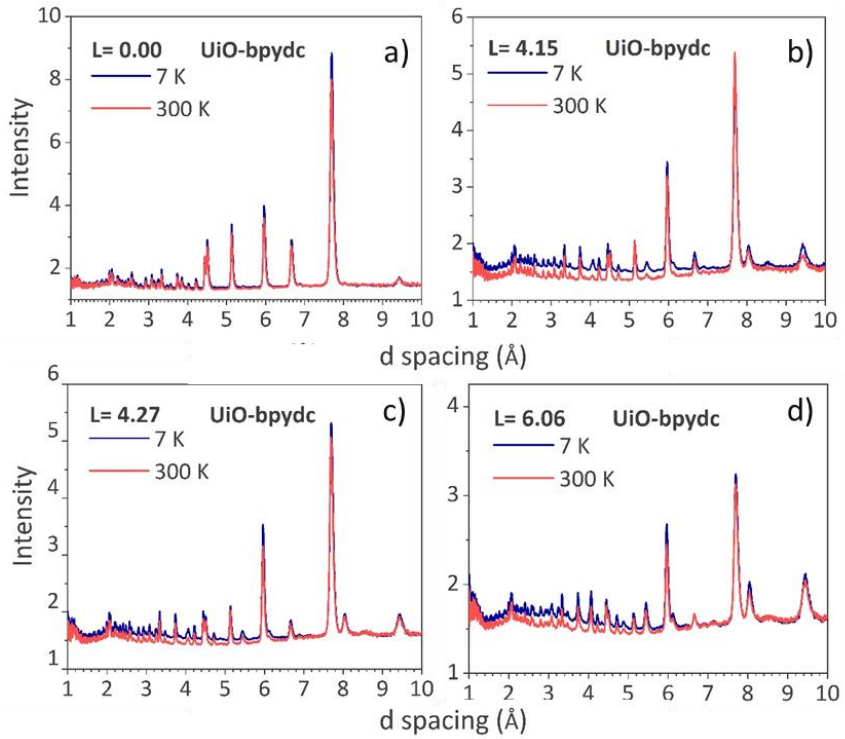

Figure 4.3 | *In situ* NPD patterns of UiO-bpydc at various loadings of ND_3 measured at 7 K and 300 K. The data were collected on the 58.3 ° detector bank of the WISH diffractometer. *L* refers to the dosing amount of ND_3 in mmol/g.

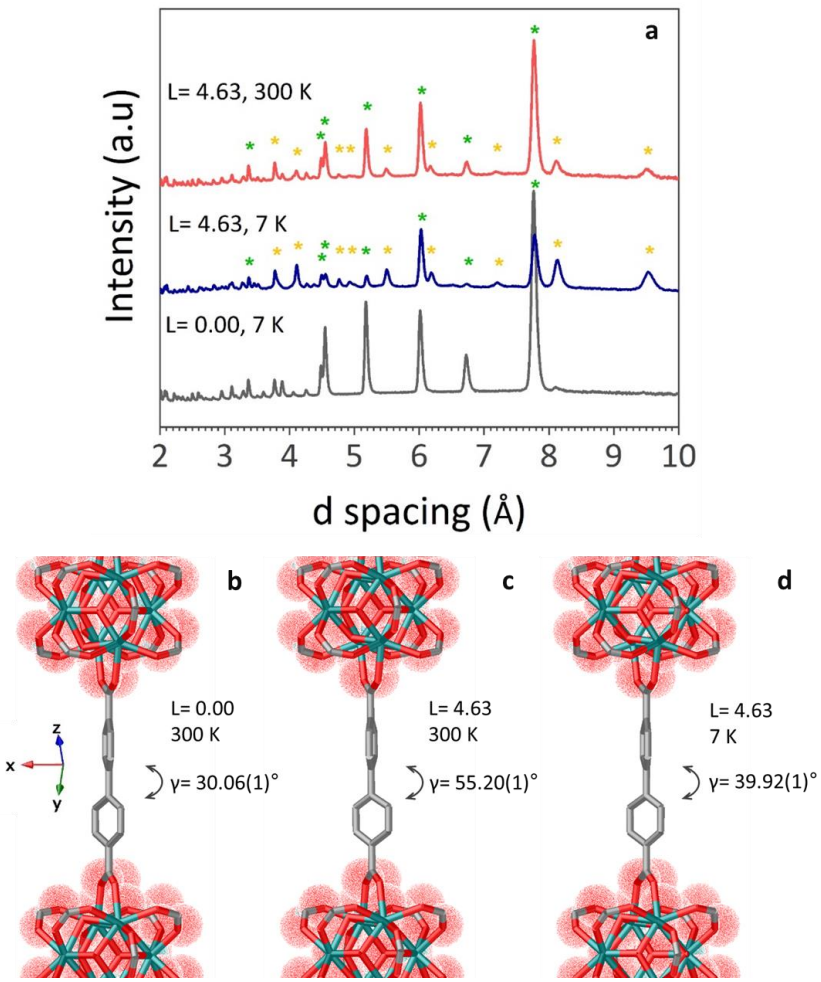

Figure 4.4 | Comparison of the NPD patterns of UiO-67 samples measured at different temperatures at L = 4.63 (36.3 ND_3 molecules/unit cell, **a**) and the refined structures at L= 0.00 mmol/g (**b**) and L= 4.63 (**c** and **d**), respectively. The data were collected on the 58.3 ° detector bank of the WISH diffractometer. L and γ refer to the dosing amount of ND_3 in mmol/g and the dihedral angles between biphenyl rings, respectively. Yellow asterisks indicate extra peaks (orderly packing of ND_3) after ND_3 dosing whereas green asterisks represent original peaks of the gas-free UiO-67. The host structures are illustrated by using a stick model; Zr: teal, O: red, and C: grey. H atoms and loaded ND_3 molecules are omitted for clarity.

Table 4.1 | Summary of the dihedral angles between two aromatic rings of the linkers in UiO-67 and UiO-bpydc derived from Rietveld refinement of the NPD data. The number in round brackets are referred to as an estimated standard deviation.

Sample	Measurement Temperature (K)	Dihedral angle (degree) at the ND_3 loading of		
		0.00 mmol/g	4.63 mmol/g	7.60 mmol/g
UiO-67	300	30.06(1)	55.20(1)	62.63(2)
	7	27.94(1)	39.92(1)	60.00(2)[a]
		0.00 mmol/g	4.27 mmol/g	6.06 mmol/g
UiO-bpydc	300	21.80(1)	16.77(3)	10.00(4)
	7	21.34(1)	16.04(2)	7.15(3)

[a] Determined at 150 K

To minimise the variance in ND_3 adsorption amount of each sample at different temperatures, the ND_3 gas uptake on the sample was first carried out and measured at room temperature (300 K), followed by isolation before cooling down to cryogenic temperature for further measurement. Thus, the NPD patterns were collected at 300 K for 20 minutes, and then at 7 K for 60 minutes (see detailed experimental procedure in Section 2.2 of Chapter 2). Due to constraints of allowed experimental time, the NPD data of UiO-67 at the highest ND_3 dosing was collected at 150 K instead of the base temperature of 7 K in liquid helium but with satisfying data quality. No significant change in the patterns was observed for both ND_3-free UiO-67 (Figures 4.2a and A4.1) and ND_3-free UiO-bpydc (Figures 4.3a and A4.5). Surprisingly, at the increasing ND_3 loading, dramatic changes of the peak intensities coupled with the formation of some small new Bragg peaks were found for the ND_3-loaded UiO-67

sample (Figures 4.2b-4.2d and Figures A4.2- A4.4). The new peaks (marked with yellow asterisks in Figure 4.4a) were due to the orderly packing of the ND_3 molecules in the MOF framework. [7] Notice that the diffraction peaks primarily derived from the gas-free UiO-67 structure with flexible linkers were pronouncedly broadened and attenuated in the intensity at increasing ND_3 loading. Whilst the change in the structure factors due to the extra nuclear density of the ND_3 molecules can cause the broadening and the attenuation, we anticipate that the degree of ND_3 adsorption on the linker molecules (dipole-induced dipole interaction) and filling to inner porous sites may also likely create a range of structural distortions or/and disorder states to the linker, leading to a spread of population in closely related diffractions. The peaks attenuation appear to be more prominent at 7 K than 300 K (Figures 4.2b-4.2d), which matches with the fact that the use of higher temperature with higher thermal energy can overcome the weak dipole-induced dipole interaction to set free the linkers from their distorted states. At higher loading (L= 4.63), the additional peaks were clearly visible with the ordered ND_3 (Figures 4.2c and 4.4a). Interestingly, at the highest ND_3 loading, the use of high temperatures including 150 K and 300 K seems unable to overcome the interlocking forces from the cumulative dipole interactions, which retain the peaks broadening and attenuation. Clearly, the flexibility of the linkers is tunable by ND_3 loading and temperature applied to this system. Similar behaviours of the linker dynamics in rigid MOFs towards guest molecules and temperature were also observed by using a solid state ^2H NMR technique. [4, 8] According to the refined structures of UiO-67 upon increasing ND_3 loading shown in Figure 4.1a and their summarised data in Table 4.1, the torsional distortion γ of the two biphenyl rings from 30.06 (1) ° is also varying due to the adsorbed ND_3 at different loading (for example, refined γ = 30.06 (1) ° at L= 0.00 can change to 55.20(1) ° and 63.62(2)

° at L= 4.63 and 7.60, respectively. This may be caused by the distortion to the hydrophobic linker with increasing amounts of hydrophilic guest molecules. [4, 9-10]

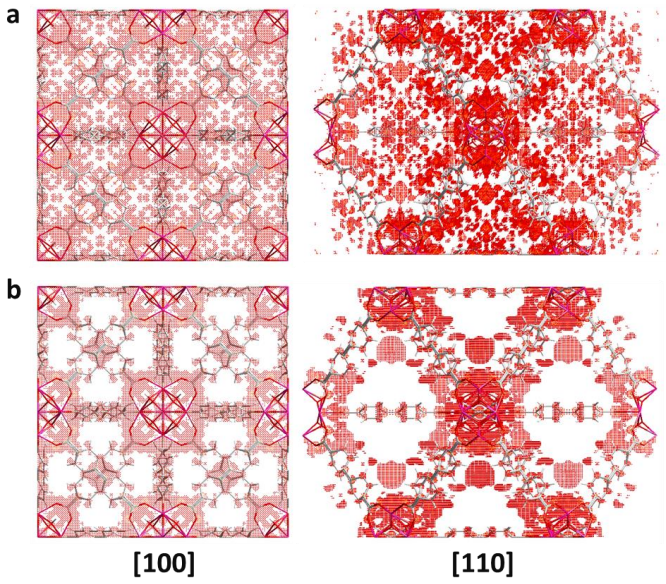

Figure 4.5 | Fourier maps of ND_3 molecules inside UiO-67 with a loading of 4.63 mmol/g, measured at 300 K (**a**) and 7 K (**b**).

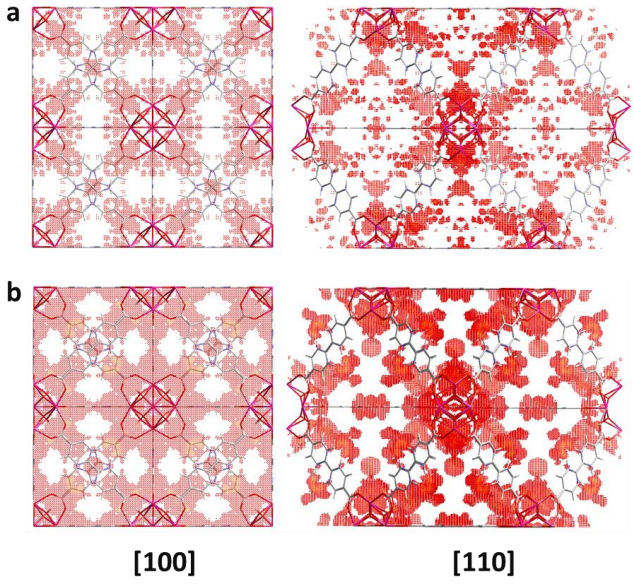

Figure 4.6 | Fourier maps of ND_3 molecules inside UiO-bpydc with a loading of 4.63 mmol/g, measured at 300 K (**a**) and 7 K (**b**).

Table 4.2 | Summary of the dihedral angles between two aromatic rings of the linkers of UiO-bpydc obtained from DFT calculations at 0 K.

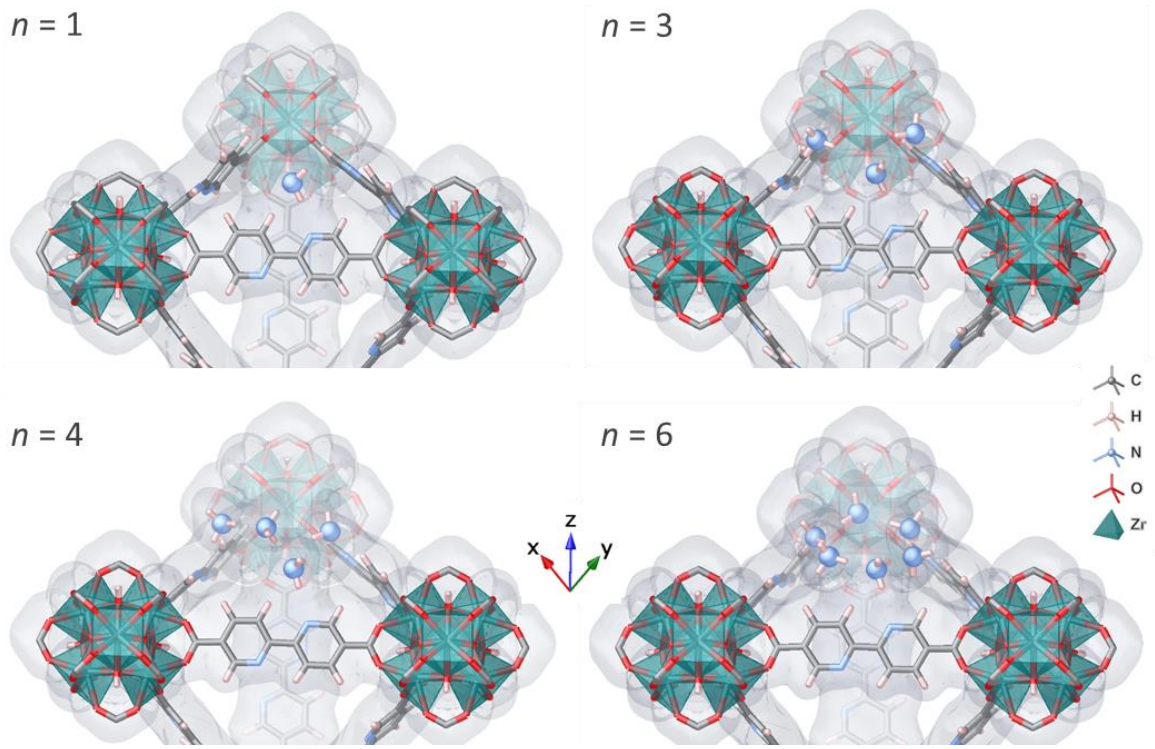

Sample	Dihedral angle (degree) with *n* NH_3 molecule(s) at the trigonal window				
	n= 0	*n*= 1	*n*= 3	n= 4	n= 6
UiO-bpydc	20.33	19.47	10.83	9.49	6.33

In contrast, these distinctive changes were totally prohibited in the presence of bipyridine linkers over the whole temperature regime in the case of UiO-bpydc (Figures 4.3b-4.3d and Figures A4.6-A4.8). As seen from the Table 4.1, at increasing ND_3 loading measured at 300 K, the dihedral angle of the two bipyridine rings this time became smaller (flattening) from 21.80(1) ° at *L*= 0.00 mmol/g to 16.77(3), and 10.00(4) ° at *L*= 4.27, and 6.60 mmol/g, respectively. Even at the measurement temperature of 7 K, the dihedral angles apparently converted to have nearly planar geometries as a function of ND_3 dosing: the

dihedral angles were reduced from 21.34(1) at *L*= 0.00 mmol/g to 16.04(2) and 7.15(3) ° at *L*= 4.27, and 6.60, respectively. The obtained results suggest the strong restriction in movement of the N-containing linker with ND_3 (H bonding) whereas no such motion restriction but a strong temperature effect with the nonpolar linker without N can be seen in the case of UiO-67. Clearly, the flexibility of the linkers is tunable by ND_3 loading and temperature applied to this system and the presence of bipyridine linkers suppress the flipping of the biphenyl angle over the whole temperature regime. These angle alterations in the both systems did not take place randomly as anticipated in the case of measurement errors/disorders. Analysis of nuclear density residues was also used to confirm the locations of the adsorbed ND_3 inside he MOF channels. For the ND_3-loaded UiO-67 samples, a dispersion of the nuclear density residues was observed when changing the measurement temperature from 300 K to 7 K (Figure 4.5). This finding was in sharp contrast to the UiO-bpydc at comparable ND_3 dosing where the pattern of the density residues clearly remained the same (Figure 4.6). Regarding the DFT calculations of the dihedral angles between two aromatic rings of the linker of UiO-bpydc upon addition of NH_3 molecules (Table 4.2), the strong H bonding indeed can flatten the dihedral angle and interlock with NH_3 molecules accordingly to render rigidity of this linker over the wide temperature range with the same trend as observed in the experiments.

4.2.2) Rotational energy barriers of the NH_3-free and NH_3-loaded MOFs

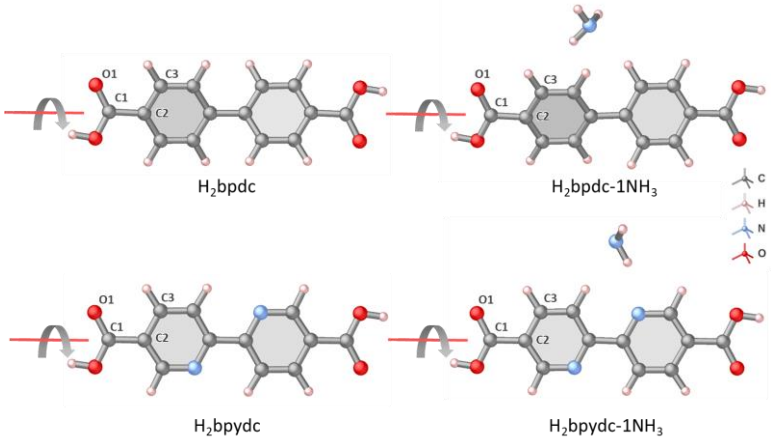

Figure 4.7 | Proton-capped linker models used for estimating the rotational energy barriers (E_{rb}) of the NH_3-free and NH_3-loaded MOF samples. Only the COO groups were fixed during the potential energy scans.

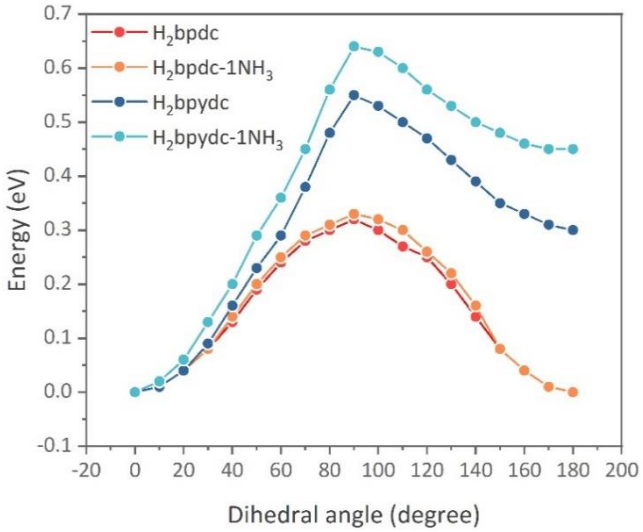

Figure 4.8 | Energy as a function of the dihedral angles of the NH_3-free and NH_3-loaded MOF samples estimated from H_2bpdc (red) , H_2bpdc-1NH_3 (orange), H_2bpydc (blue), and

H_2bpydc-1NH_3 (light blue) models. The dihedral angles were rotated around the rotational groups (O1-C1-C2-C3, see Figure 4.7) of the most stable configurations with 10° increments to scan the potential energy surfaces.

Table 4.3 | Rotational energy barriers (E_{rb}) of the NH_3-free and NH_3-loaded MOF samples estimated from H_2bpdc, H_2bpdc-1NH_3, H_2bpydc, and H_2bpydc-1NH_3 models.

	H_2bpdc	H_2bpdc-1NH_3	H_2bpydc	H_2bppdc-1NH_3
E_{rb} (eV)	0.32	0.33	0.55	0.64
E_{rb} (kJmol^{-1})	30.88	31.84	53.07	61.75

It is known that the modification of the organic linkers with substituent groups and incorporation of guest molecules can change not only the electrostatic effect and equilibrium structure but also the rotational energy barrier (E_{rb}) of the organic linkers in the MOFs. [6] The E_{rb} values can indicate the flexibility of the linkers in MOF materials: the higher value of E_{rb}, the less flexibility of the MOF linkers. As a result, the E_{rb} values of the model MOFs were also calculated by DFT. A potential energy scan was performed to explore the most stable and unstable positions of the organic linkers in the model MOFs during the rotation of the linkers with respect to the dihedral angle γ of O1-C1-C2-C3 (see Figure 4.7). The derived E_{rb} values were computed as the energy differences between the most unstable and the most stable configurations (see Section 2.3 of Chapter 2 for details of these calculations), and the results are shown in Figure 4.8 and Table 4.3. For the NH_3-free models, it is clearly found that the H_2bpydc linker of UiO-bpydc exhibits higher rotational barrier (0.55 eV) than the H_2bpdc of UiO-67 does (0.32 eV), revealing the less flexibility of the UiO-bpydc due to

the substitution effects. More interestingly, the adsorption of NH_3 in the UiO-bpydc dramatically increases the E_{rb} to 0.64 eV, almost twice higher than that in the UiO-67 analogue. These computational results emphasize the strong influence of NH_3-MOF interactions on controlling the E_{rb} of the MOFs as well as their flexibility towards guest molecules which are in excellent agreement with the corresponding NPD experiments. Although further improved models may also be necessary for in-depth study, these results support our initial hypothesis by which the effect of thermal motion at elevated temperature may set free the rotation of the biphenyl scaffold ND_3 molecules inside the UiO-67 pores. In contrast, the ND_3-loaded UiO-bpydc could greatly suppress this thermal linker flipping via a constraint of the stronger H-bonding network forming between the UiO-bpydc linkers and the adsorbed NH_3 molecules. This result strongly agrees with the previous report that steric hindrance on the MOF linkers, arising from strong interactions between the framework and the guest molecules in the pores can lead to an increase in rotational barriers. [6] Further thermodynamics and kinetic studies and computational modelling are required in order to get a full understanding of the temperature-dependent and loading effects. This will highlight the importance of the molecular bonding interaction to lock up or set free molecular motion of linkers for controlling the responsive behaviour of MOF materials with trapped guest molecules by external stimuli. At the uttermost exciting prospect, the ability to design and control the stimuli-responsive properties throughout linker motions might enable the development of artificial nanomachines for special usage.

4.3) Chapter summary

In summary, high-resolution *in situ* neutron diffraction along with Rietveld refinement and DFT calculations of rotational energy barriers have been used to elucidate

the effect of temperature on the structural responses of defective UiO-67 and UiO-bpydc with trapped ND_3. The results establish the importance of thermal linker flipping induced by the specific host-guest interactions on controlling the responsive adsorption behaviours in these MOFs. The steric hindrance of H-bond networks between the bipyridine linkers and the adsorbed ND_3 in UiO-bpydc makes the adsorption structures more rigid and hence inhibits the linker rotation over the studied temperature range. This finding can enable the development of stimuli-responsive materials for applications that heavily rely on the linker dynamics such as gas separation, molecular sieving, and molecular sensing. Further dynamic study of this NH_3-MOF system with a controllable host-guest interaction will be demonstrated in Chapter 5 by using advanced neutron scattering techniques and computational calculations.

The work in this section has been published in Journal of the American Chemical Society (DOI: 10.1021/jacs.0c12483).

4.4) References

1. Gu, C.; Hosono, N.; Zheng, J.-J.; Sato, Y.; Kusaka, S.; Sakaki, S.; Kitagawa, S., Design and Control of Gas Diffusion Process in a Nanoporous Soft Crystal. *Science* **2019,** *363* (6425), 387.
2. Dong, Q.; Zhang, X.; Liu, S.; Lin, R.-B.; Guo, Y.; Ma, Y.; Yonezu, A.; Krishna, R.; Liu, G.; Duan, J.; Matsuda, R.; Jin, W.; Chen, B., Tuning Gate-Opening of a Flexible Metal–Organic Framework for Ternary Gas Sieving Separation. *Angewandte Chemie International Edition* **2020,** *59* (50), 22756-22762.
3. Krause, S.; Evans, J. D.; Bon, V.; Senkovska, I.; Iacomi, P.; Kolbe, F.; Ehrling, S.; Troschke, E.; Getzschmann, J.; Többens, D. M.; Franz, A.; Wallacher, D.; Yot, P. G.; Maurin, G.; Brunner, E.; Llewellyn, P. L.; Coudert, F.-X.; Kaskel, S., Towards General Network Architecture Design Criteria for Negative Gas Adsorption Transitions in Ultraporous Frameworks. *Nature Communications* **2019,** *10* (1), 3632.
4. Inukai, M.; Tamura, M.; Horike, S.; Higuchi, M.; Kitagawa, S.; Nakamura, K., Storage of CO_2 into Porous Coordination Polymer Controlled by Molecular Rotor Dynamics. *Angewandte Chemie International Edition* **2018,** *57* (28), 8687-8690.

5. Krause, S.; Hosono, N.; Kitagawa, S., Chemistry of Soft Porous Crystals: Structural Dynamics and Gas Adsorption Properties. *Angewandte Chemie International Edition* **2020,** *59* (36), 15325-15341.

6. Gonzalez-Nelson, A.; Coudert, F.-X.; van der Veen, M. A., Rotational Dynamics of Linkers in Metal–Organic Frameworks. *Nanomaterials* **2019,** *9* (3).

7. Barter, M.; Hartley, J.; Yazigi, F.-J.; Marshall, R. J.; Forgan, R. S.; Porch, A.; Jones, M. O., Simultaneous Neutron Powder Diffraction and Microwave Dielectric Studies of Ammonia Absorption in Metal–Organic Framework Systems. *Physical Chemistry Chemical Physics* **2018,** *20* (15), 10460-10469.

8. Jiang, X.; Duan, H.-B.; Khan, S. I.; Garcia-Garibay, M. A., Diffusion-Controlled Rotation of Triptycene in a Metal–Organic Framework (MOF) Sheds Light on the Viscosity of MOF-Confined Solvent. *ACS Central Science* **2016,** *2* (9), 608-613.

9. Kanoo, P.; Matsuda, R.; Sato, H.; Li, L.; Hosono, N.; Kitagawa, S., Pseudo-Gated Adsorption with Negligible Volume Change Evoked by Halogen-Bond Interaction in the Nanospace of MOFs. *Chemistry – A European Journal* **2020,** *26* (10), 2148-2153.

10. Bärwinkel, K.; Herling, M. M.; Rieß, M.; Sato, H.; Li, L.; Avadhut, Y. S.; Kemnitzer, T. W.; Kalo, H.; Senker, J.; Matsuda, R.; Kitagawa, S.; Breu, J., Constant Volume Gate-Opening by Freezing Rotational Dynamics in Microporous Organically Pillared Layered Silicates. *Journal of the American Chemical Society* **2017,** *139* (2), 904-909.

Chapter 5

Dynamics and Kinetics of Ammonia Confined in Defective Zr-Based Metal-Organic Frameworks

This thesis chapter consists of two major studies: I) the investigation of the dynamics properties of the defective UiO-67 type MOFs with trapped NH_3 by using combined INS and lattice dynamics DFT calculations and II) the analysis of the diffusivity-loading relationship of the adsorbed NH_3 in the MOF channels by using QENS in conjunction with GCMC simulations. Identification of characteristic vibrational modes of both MOF linkers and adsorbed NH_3 molecules at various dosages will be discussed to link to the specific host-guest interactions that strongly govern the responsive adsorption properties of the studied system. The effects of pore surface functionality, linker flexibility, pore structure, and loading quantity on the nature of the NH_3 mobility in the MOF pores will be explored. The vibrational frequency calculations by DFT were carried out by our collaborator, Dr. Xin-Ping Wu at Key Laboratory for Advanced Materials, Centre for Computational Chemistry and Research Institute of Industrial Catalysis, East China University of Science and Technology, P.R. CHINA. The GCMC simulations were performed with assistance of Dr. Nakul Rampla, Dr. Rocio Bueno-Perez, and Prof. David Fairen-Jimenez at Adsorption & Advanced Materials Laboratory, Department of Chemical Engineering & Biotechnology, University of Cambridge, UK. Some parts of the dynamic study by INS have been published in Journal of the American Chemical Society (DOI: 10.1021/jacs.0c12483).

5.1) Introduction

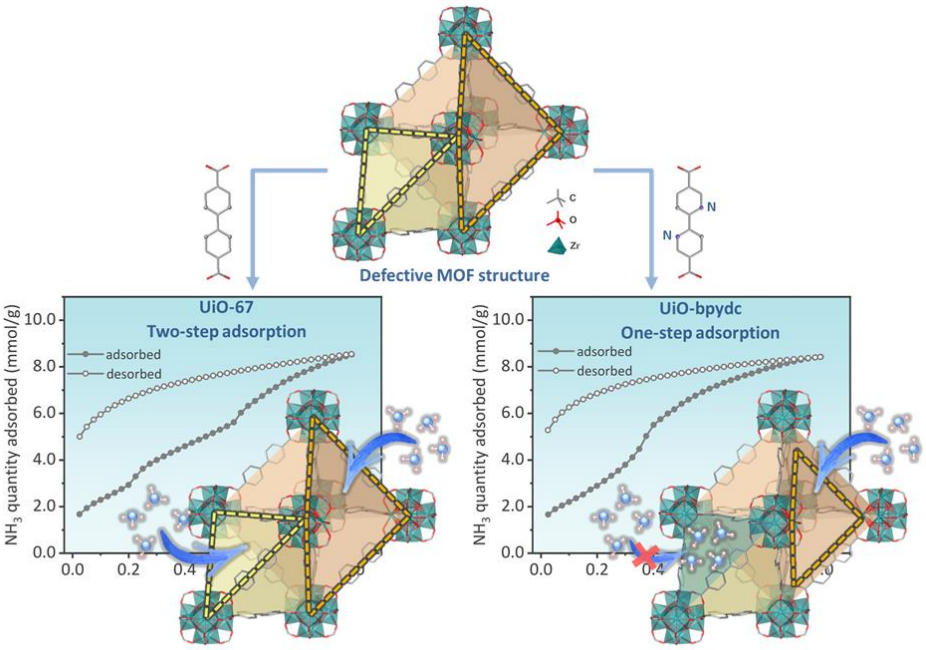

Figure 5.1 | Proposed NH_3 responsive behaviours responsible of the UiO-67-type MOFs containing missing linker defects. The NH_3 molecules enter the structures via different pore openings, leading to the stepwise adsorption isotherms.

Neutron powder diffraction (NPD), can provide the static crystallographic structures of materials upon guest inclusion, allowing the determination of the preferred binding sites in the MOF channels that strongly govern their adsorption mechanisms. [1] In Chapters 3 and 4, I have presented the use of NPD with the aid of density functional theory (DFT) calculations that can elucidate the time-averaged NH_3 adsorption sites in defective UiO-67 and UiO-bpydc containing flexible phenylene linkers over a range of NH_3 loadings and temperatures (Figure 5.1). Accordingly, the effects of the non-uniform pore windows created by missing linker defects, the surface pore functionality, and the linker flexibility can account for the stepped and hysteresis NH_3 sorption isotherms of the studied MOFs.

However, dynamical features of these NH_3-MOF systems are yet to be explored to get deeper insights into the specific host-guest interactions and the diffusion of NH_3 in the MOF cavities. Such dynamics information is of particular importance for controlling the gas-sorption-based processes in industry such as gas separation [2-4], drug delivery [5], and molecular sensing [6-7].

Neutron scattering, including inelastic neutron scattering (INS) and quasielastic neutron scattering (QENS), with high detection sensitivity to hydrogen combined with computational modelling has served as one of the most effective methods for analysis of the dynamical information of MOF materials toward external triggers at a molecular level, offering a profound understanding of the framework responsivity. [8-10] Specifically, the interactions between the guests and the framework can be thoroughly understood by studying both the local motions of the adsorbed species and the lattice vibrational modes of the host frameworks by INS accompanied by DFT calculations. [1, 9-12] For example, the binding dynamics of the trapped acetylene (C_2H_2), ethylene (C_2H_4), and ethane (C_2H_6) molecules in mesoporous MFM-300Al were studied by a combined use of INS and DFT. [10] The key findings revealed a new type of host-guest interactions via a cooperative hydrogen-bonding, $\pi \cdots \pi$ interactions, and intermolecular dipole interactions to account for superior selective binding to hydrocarbons. On the other hand, diffusion and kinetics of molecules confined in the MOF frameworks can be determined by QENS frequently joint with molecular dynamic (MD) simulations. [1, 9, 13] A pioneer work involving analysis of CO_2 mobility in a highly flexible MOF, named as MIL-53(Cr) by using this combined strategy was reported by Salles *et al*. [14] The authors were able to distinguish types and rates of transport diffusivity of the trapped CO_2 that link to the gas-induced phase transition in the MOF framework. Recently, by using QENS and GCMC simulations, CO_2 diffusion

in ZIF-7 with non-uniform porous structures has been proven to undergo a sequential pore filling, serving as an alternative mechanism for the observed stepwise gas sorption. [15] These discoveries clearly represent an importance of applying advanced neutron scattering techniques accompanied with theoretical calculations to unveil the dynamics and kinetics behaviours of MOFs with confined molecules, consequently allowing an interpretation of the adsorption mechanisms. However, such studies are commonly based on the perfect MOF frameworks despite that there have been several defective MOF structures reported to show defect-dependent adsorption properties. [16-18] To our knowledge, the use of these sophisticated methods in probing adsorption behaviours of MOFs containing missing linker defects is not yet established.

To this end, the combined experimental INS and theoretical DFT were employed to investigate both the lattice dynamics of the UiO-67-type MOFs having missing linker defects and the vibrational modes of adsorbed NH_3 inside the MOF pores as a function of NH_3 dosing, while QENS and GCMC simulations were used to study the diffusion and kinetics of the adsorbed NH_3. Details of experimental and computational procedures used in this study are presented in Chapter 2. Our analysis particularly highlights the role of defects, functionality, and linker flexibility of MOFs to control dynamic interactions and diffusion of polar NH_3 molecules within the MOF pores. The formation of H-bonding network between the trapped NH_3 and the host framework when replacing biphenyl to bipyridine linker is in excellent agreement with our recent study by using NPD technique, further indicating the gate-opening/blocking adsorption mechanism.

5.2) Results and Discussion

5.2.1) Analysis of NH_3-MOF binding interactions via inelastic neutron scattering

5.2.1.1) Analysis of the terminating species at defect sites of the hosts.

Defective UiO-67 and UiO-bpydc with reticular formula of $Zr_6O_4(OH)_4(bpdc)_{6-x}A_{2x}$ and $Zr_6O_4(OH)_4(bpydc)_{6-x}A_{2x}$ where x and A represent the number of the missing linkers per formula and the anionic capping species, respectively, was successfully synthesised by following the procedure given in Section 2.2 of Chapter 2. Full characterisation including X-ray powder diffraction (XRD), N_2 sorption analysis, Infrared (IR) spectroscopy, thermogravimetric (TG) analysis, inductively coupled plasma mass spectrometry (ICP-MS), and ^1H Nuclear magnetic resonance (NMR) are given in the Appendices. For clarity, UiO-67 and UiO-bpydc with defects will be referred to as "UiO-67" and "UiO-bpydc" throughout this study, respectively, unless otherwise specified.

Table 5.1 | Sample information used in the *in situ* INS experiments.

Sample	**UiO-67**				**UiO-bpydc**			
Reticular formula	$Zr_6O_4(OH)_4(bpdc)_{6-x}(acetate)_{2x}$				$Zr_6O_4(OH)_4(bpdc)_{6-x}(acetate)_{2x}$			
Actual reticular formula[a]	$Zr_6O_4(OH)_4(bpdc)_4(acetate)_4$				$Zr_6O_4(OH)_4(bpydc)_{4.5}(acetate)_3$			
Molar mass per unit cell (g/mol unit cell)	7749.7				7537.2			
Loading amount of NH_3 (mmol/g)	0.00	2.10	4.62	6.26	0.00	2.38	4.65	6.74
Loading amount of NH_3 (molecule/unit cell)	0.00	16.3	35.8	48.5	0.00	17.9	35.0	50.8
Loading temperature (K)	300							
Measurement temperature (K)	below 10 ± 0.1							

[a] Based on the ICP-MS data in the Appendices

For the first part of this study, *in situ* INS experiments and DFT calculations were combined to visualise the dynamic interactions between the defect-rich MOF hosts and the progressively adsorbed NH_3. Owing to the relatively large incoherent neutron scattering cross-section (σ_{inc}) of hydrogen atom (~80 barn) over other elements, the observed INS spectrum is thus dominated by any modes involved in hydrogen displacement. [8] All the INS measurements were recorded on TOSCA instrument at the ISIS Pulsed Neutron and Muon Source, Rutherford Appleton Laboratory, UK. The measurement temperature was kept under 10 ± 0.1 K to minimise the effects of Debye-Waller factor from the host and the adsorbed molecules and hence enhance the observed scattering intensities. Information on the properties of the studied samples along with their conditions for *in situ* INS experiments are shown in Table 5.1. The DFT calculations were performed to generate the simulated INS spectra and extract the vibrational modes. The calculated INS spectra and their corresponding vibrational modes were generated by OCLIMAX [19] and Jmol [20] software, respectively. The theoretical spectrum included overtones to the 10th order. The scaling factor of 0.985 was applied to all the calculated INS spectra for vibrational frequency correction. Details of the DFT calculations can be found in Section 2.3.1.3 of Chapter 2. The obtained experimental and simulated INS spectra of the unloaded UiO-67 and UiO-bpydc are shown in Figure 5.2 together with a summary of their vibrational modes with peak assignments in Tables 5.2 and 5.3.

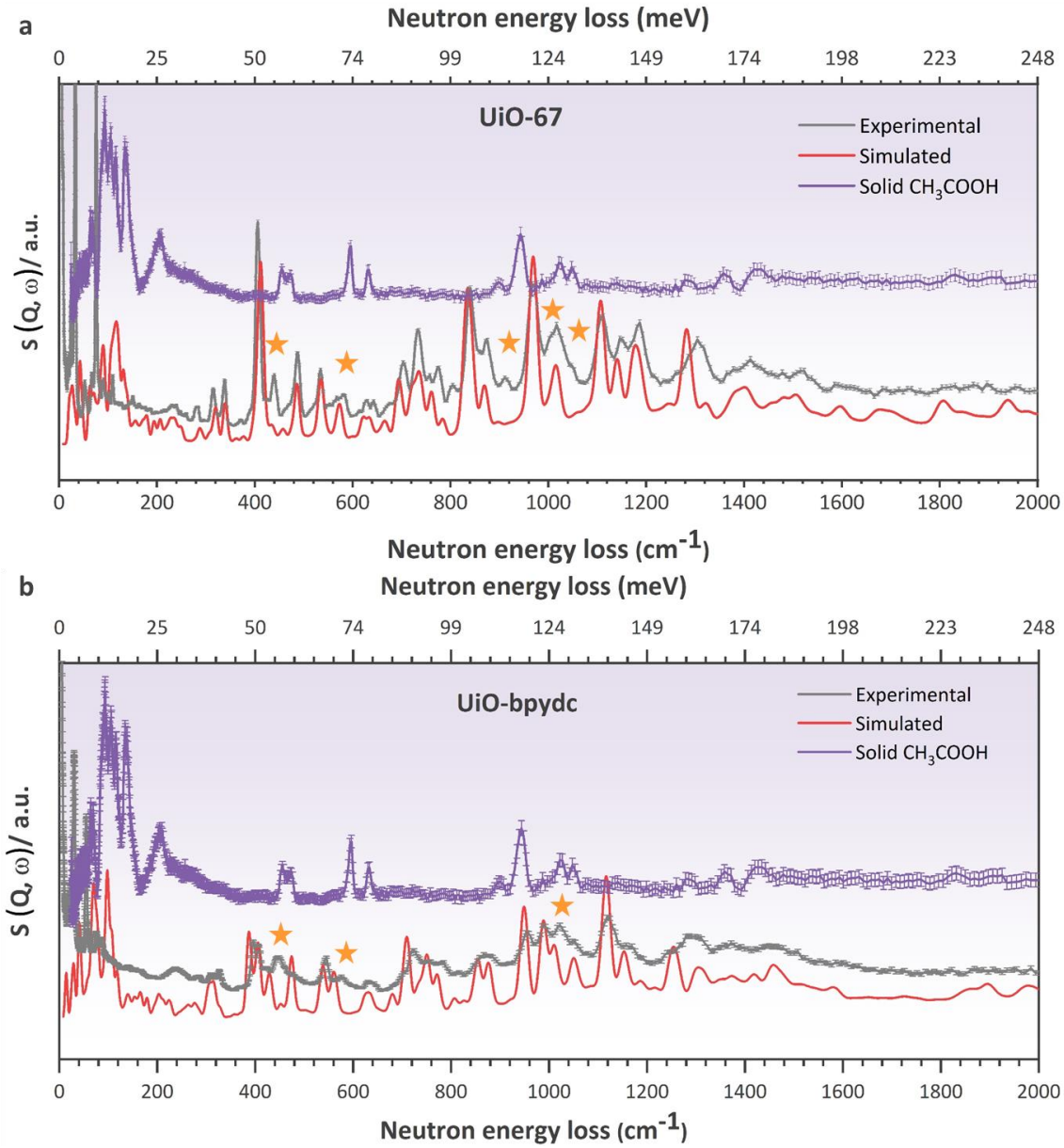

Figure 5.2 | Comparison of experimental and DFT-calculated INS spectra of UiO-67 (**a**), UiO-bpydc (**b**) against solid CH_3COOH (terminal species at the defective sites). The experimental spectra were collected below 10 K and displayed with errors. The INS spectrum of solid CH_3COOH measured at 20 K was reproduced from Ref [21] and scaled down the intensity by 0.8 for comparison. Yellow star symbols above the INS spectrum of UiO-67 mark the vibrations of CH_3COOH. Scaling factor of 0.985 was applied to the theoretical spectrum. Note that 1 meV ≈ 8.066 cm^{-1}.

Table 5.2 | Calculated and experimental vibrational modes of UiO-67. The experiment data were recorded by using an INS technique below 10 K.

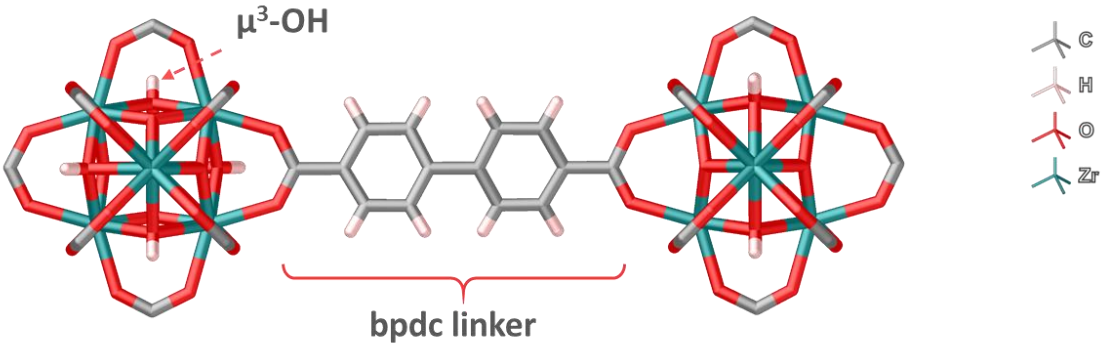

Frequency (cm^{-1})			Band assignment
Calculated		Experimental	
This work	Ref [22]*		
	26, 31	31	Linker libration
40	35, 37	43	Linker rotation
52	45, 47	53	PH libration+ Linker rocking+ Linker rotation
85	70	63, 73	Linker rocking+ PH deformation
115	80, 81	77	Linker rotation
	90, 92, 93	90	Linker wagging+ Linker rocking+ PH deformation
130-200	109	108	Linker wagging+ Linker twisting+ PH deformation
	124	117	Linker stretching+ Linker rocking, PH deformation
	174, 176	178	Linker wagging+ Linker rocking+ PH deformation
	190	194	Linker wagging+ PH deformation
	204, 210, 212	206	OCO twisting+ Linker rocking (non-rigid)+ PH deformation
221, 224	221, 224	228	OCO twisting+ Linker wagging+ Linker rocking+ PH deformation+ OH bending
235, 240	236, 241	235	OH bending+ Linker wagging+ PH deformation
248, 250	248, 250	247	Linker wagging+ OH stretching+ OCO twisting+ PH deformation
286, 290	287, 291	288	PH stretching (breathing)+ Linker stretching (rigid)+ Linker rocking (non-rigid)+ Linker wagging+ OCO bending
304	305	306	PH stretching (breathing)+ Linker stretching (rigid)

Frequency (cm^{-1})			Band assignment
Calculated		Experimental	
This work	Ref [22]*		
318, 323	318, 323	321	OCO bending+ PH deformation+ Linker rocking (non-rigid)+ Linker wagging
350	349	339	Linker wagging (non-rigid)+ PH deformation
375	375	376	Linker wagging (non-rigid)+ Linker rocking (non-rigid)
381	381	n.o.	Zr-OCO stretching+ PH deformation+ Linker stretching (rigid)
395	395, 402	397	Zr- μ_3-O and Zr-μ_3-OH stretching+ PH deformation
419-421	419-421	412	Zr- μ_3-O and Zr-μ_3-OH bending+ PH deformation+ Linker rocking (non-rigid)
433	435	435	CC_{ring} deformation (OP+IP)+ Zr-OCO deformation+ Zr- μ_3-O and Zr-μ_3-OH bending
455	457	458	Zr-μ_3-OH bending+ Zr- μ_3-O stretching+ OCO bending (IP)
484	486	486	Zr- μ_3-O stretching+ PH deformation
-	-	536	Zr-OCO stretching+ Zr- μ_3-O and Zr-μ_3-OH bending+ $CC_{backbone}$ stretching
551	552	n.o.	Zr-OCO stretching+ CC_{ring} deformation (OP)+ Zr-μ_3-OH bending
571, 574	570, 571, 574	575	Zr- μ_3-O and Zr-μ_3-OH deformation+ CC_{ring} and CH_{ring} deformation (IP)+ Zr-OCO stretching
	-	621	CC_{ring} deformation (IP)
642,643	642, 643	634	CC_{ring} and CH_{ring} deformation (IP)
657, 670	657, 670	665	Zr-O deformation+ CC_{ring} and CH_{ring} deformation (IP)
685, 693	686, 694	695	OH bending+ OCO bending+ CC_{ring} deformation (IP)
716	717, 720, 723	723	OH bending+ OCO bending+ CC_{ring} deformation
728	730	733	(OP, rigid)+ CH_{ring} wagging (rigid)
762	763	763	OH bending+ OCO bending+ CC_{ring} deformation (OP, rigid)+ CH_{ring} wagging (rigid)
776, 777	776, 777	784	OCO bending+ CC_{ring} bending and stretching (IP)
818	819	n.o.	OH bending+OCO bending+ CH_{ring} deformation (OP)
-	-	836	CH_{ring} wagging+ CC_{ring} deformation (OP)
868, 870	868, 870	871	CH_{ring} wagging
-	-	969	CH_{ring} wagging+ OCO bending+ OH bending
1021	1022	1020	CH_{ring} twisting
1051	1051	1047	CH_{ring} stretching+ CC_{ring} deformation (IP)
1116	-	1112	CH_{ring} rocking+ CC_{ring} deformation (IP)

Frequency (cm^{-1})			Band assignment
Calculated		Experimental	
This work	Ref [22]*		
1155	1140, 1141, 1145 1173,	1146	CH_{ring} scissoring+ CC_{ring} deformation (IP)
1165, 1170	1175, 1176	1180	CH_{ring} scissoring
1210	1210 1309		CH_{ring} close to Zr node bending+ CC_{ring} deformation (IP)
1309	1352	n.o.	Collective mode of the BPDC linker
1360	1422	1304	CH_{ring} rocking+ CC_{ring} deformation (IP)
1422	1538	n.o.	CH_{ring} rocking+ CC_{ring} deformation (IP)
1530-		n.o.	OCO sym. Stretching
1539	1630	n.o.	CH_{ring} rocking+ CC_{ring} deformation (IP)
1630- 1640	1667	n.o.	OCO asym. Stretching+ CC_{ring} deformation (IP)
1670- 1680		n.o.	CH_{ring} scissoring+ CC_{ring} deformation (IP)

n.o. = not observed; IP= in plane; OP= out of plane; PH= Zr-O polyhedral; sym= symmetric; asym.= asymmetric.

* The data were performed at hybrid B3LYP level of calculations and the obtained structure was optimised in *F*23 space group.

Table 5.3 | Calculated and experimental vibrational modes of UiO-bpydc. The experiment data were recorded by using an INS technique below 10 K.

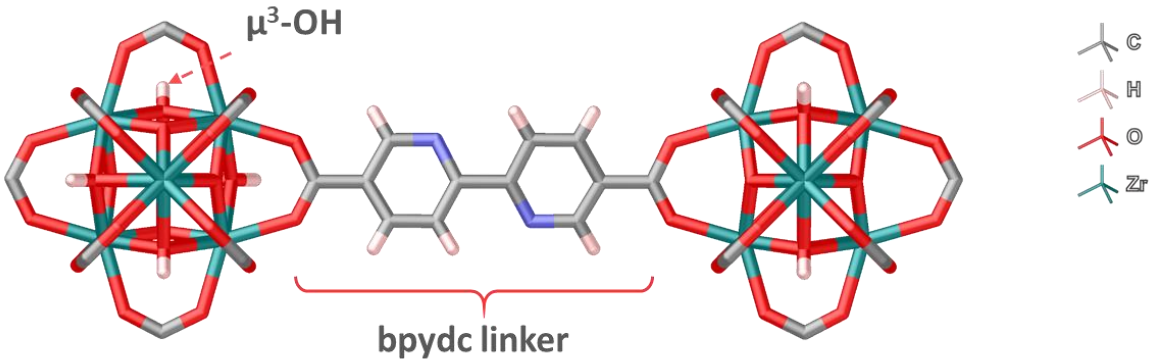

Frequency (cm^{-1})		Band assignment
Calculated	Experimental	
14	30, 55, 76, and 84	Whole framework translation
30		Linker wagging+ PH deformation
40, 41, 42		Linker wagging+ PH deformation
58		PH deformation+ Linker rocking
68, 70, 71		PH deformation+ Linker rotation (unchanged torsion angle)
74, 76, 77		PH deformation+ Linker rocking, Linker wagging, Zr-OCO deformation
99, 100		Linker wagging
107, 109	100-200 (Very broad and too low intensity to identify)	Linker rotation (changed torsion angle)+ PH deformation
118		PH deformation+ Zr-OCO stretching+ Linker shear motion+ Linker wagging
138, 140		Zr-OCO wagging+ PH deformation
153, 154		Zr-OCO wagging+ PH deformation
165, 166		Zr-O deformation (strong)+ PH deformation
179, 181		Zr-O deformation (strong)+ Linker deformation (IP, rigid)
194		Zr-O deformation (strong)+ rigid Linker deformation (IP)
202, 203	237 (very broad)	Zr-O deformation (strong)+rigid Linker wagging
213		Zr-O deformation (strong)+ rigid Linker deformation (IP+OP)
221, 223		Zr-OCO twisting and wagging (strong)+ Linker deformation (OP, non-rigid)
264		Zr-OCO wagging (strong)+ Linker deformation (OP, non-rigid)

Frequency (cm^{-1})		Band assignment
Calculated	Experimental	
276, 278, 279	285 (braod)	Zr-OCO rocking (strong)+ PH deformation+ Linker deformation (OP, non-rigid)
307		Zr-OCO libration (strong)
315, 316	310	Zr- μ_3-O and Zr-μ_3-OH deformation+ Linker deformation (OP, non-rigid)
328, 329	328	Zr-O deformation (strong)+ Zr-OCO stretching+ Linker deformation (IP, rigid)
385-391	396	Zr- μ_3-O and Zr-μ_3-OH sym. Stretching+ PH deformation (breathing)+ Zr-OCO deformation+ CC_{ring} deformation (OP, non-rigid)
404-412	406	CC_{ring} and CN_{ring} deformation (OP)+ PH deformation+ OH bending
428, 429, 430	422, 427	CC_{ring} and CN_{ring} deformation (OP+ IP)+ PH deformation (stretching)
452, 453	446	CC_{ring} and CN_{ring} deformation (IP)+ PH deformation (stretching) + Zr-OCO stretching
475, 476		CC_{ring} and CN_{ring} deformation (IP+ OP(weak))+ Zr-O and Zr-OH deformation+ Zr-OCO deformation
536-541	545	CC_{ring} and CN_{ring} deformation (OP)+ Zr-OCO stretching+ PH deformation
559, 562	576	Zr-O and Zr-OH deformation+ weak CC_{ring} and CN_{ring} deformation (IP+ OP)
626, 636	630-643	CC_{ring} and CN_{ring} deformation (IP)
678, 683	701	Linker deformation (IP, rigid)+ Zr-OCO libration, PH deformation+ OH bending
711, 712, 713	721	OH bending (strong)+ non-rigid Linker deformation (OP)
733, 740		OH bending+Zr-O deformation, PH deformation+ non-rigid Linker deformation (IP+OP)
750-755	753	OH bending (strong)+ non rigid Linker deformation (IP+OP)+ OCO libration+ PH deformation
771-774	781	OH bending (medium to strong)+non-rigid Linker deformation (OP)+ OCO bending (strong)
806-808	816	Non-rigid Linker deformation (OP+IP)(strong)
827, 828		Zr-OCO deformation (strong)+ Linker deformation (IP)
854-858		CH_{ring} wagging (strong)+ non-rigid CC_{ring} and CN_{ring} deformation (OP)(weak)
876-878	865-884	CH_{ring} wagging (strong)+ non-rigid CC_{ring} and CN_{ring} deformation (OP)(strong)
946-952	956	CH_{ring} and CC_{ring} close to N deformation (OP)(strong)
988-992	986	CH_{ring} twisting (strong)+ non-rigid CC_{ring} and CN_{ring} deformation (OP)(strong)
1007-1012	1022	CC_{ring} and CN_{ring} deformation (IP)(strong)

Frequency (cm^{-1})		Band assignment
Calculated	Experimental	
1048-1051	1048	CC_{ring} and CN_{ring} deformation (IP)(strong)+ CH_{ring} deformation (IP)(weak)
1114-1120	1118	CH_{ring} scissoring (strong)+ CC_{ring} deformation (IP)(strong)+ CN_{ring} deformation (IP)(weak)
1150-1157	1156-1169	OCO stretching (strong)+ CC_{ring} and CN_{ring} deformation (IP)(strong)+ $CC_{backbone}$ deformation (IP)(strong)
1261-1263	1276-1311 (broad)	$CC_{backbone}$ deformation (IP)(strong)+ CH_{ring} close to N deformation (IP)+ CH_{ring} rocking (strong)+ non-rigid CC_{ring} and CN_{ring} deformation (IP)(strong)
1298-1300		Non-rigid CC_{ring} and CN_{ring} deformation (IP)(strong)+ CH_{ring} close to N deformation (IP)(strong)
1352, 1353		CC_{ring} and CN_{ring} deformation (IP)(strong)+ CH_{ring} deformation (IP)+ OCO stretching (IP)
1369-1375	1374 (broad)	Non-rigid CC_{ring} and CN_{ring} deformation (IP)+ $CC_{backbone}$ deformation (IP)(strong)+ CH_{ring} close to N deformation (IP)+ CH_{ring} deformation (IP)(weak)+ OCO stretching
1413		OCO stretching (strong)
1453-1455	1456 (broad)	Non-rigid linker deformation (IP)(strong)+ CH_{ring} close to N deformation (IP)+ CH_{ring} rocking
1580, 1581		CC_{ring} and CN_{ring} stretching (strong)+ CH_{ring} deformation (IP)
1586-1589		CC_{ring} and CN_{ring} stretching (strong)+ CH_{ring} deformation (IP)
3135-3137		CH_{ring} sym. Stretching (excluding CH_{ring} close to N)
3786-3794		OH stretching

n.o. = not observed; IP= in plane; OP= out of plane; PH= Zr-O polyhedra; sym= symmetric; asym.= asymmetric.

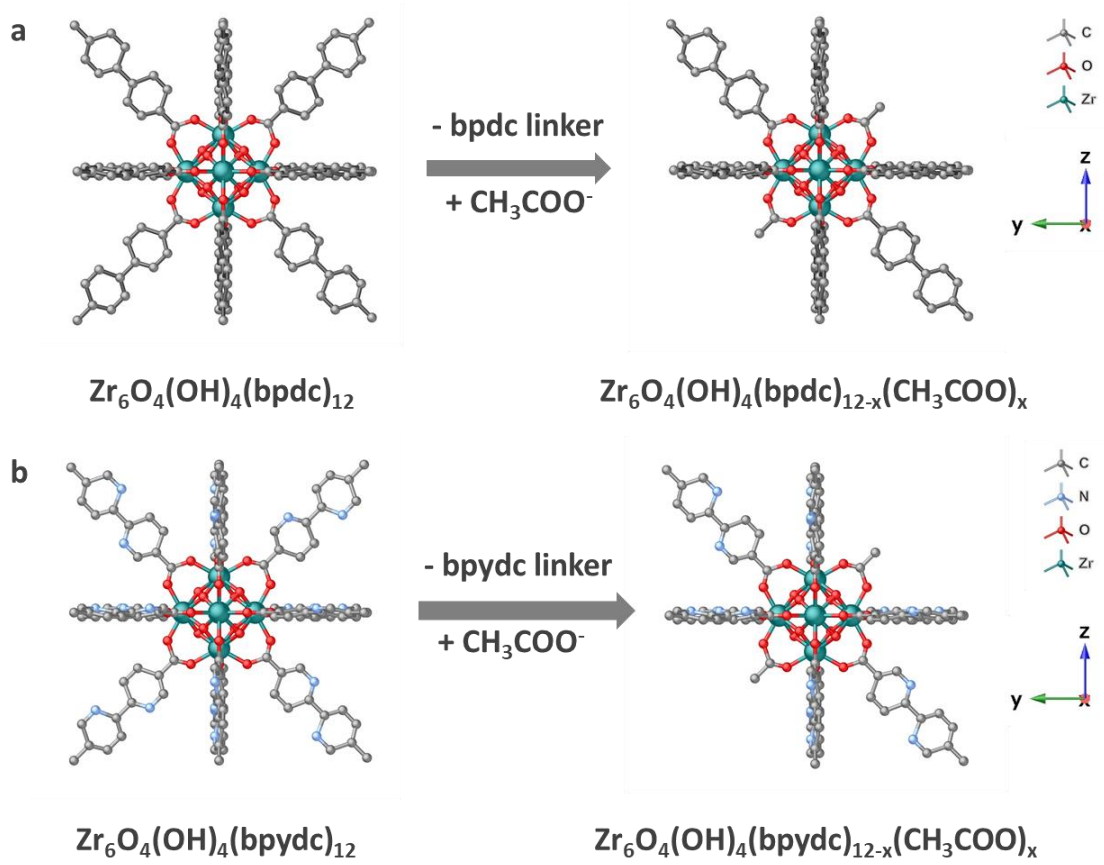

Figure 5.3 | Schematic representation of UiO-67 (**a**) and UiO-bpydc (**b**) structures with missing linker defects; bpdc and bpydc refer to biphenyl-*4,4′*-dicarboxylate and *2,2′*-bipyridine-*5,5′*-dicarboxylate, respectively. H atoms are omitted for clarity. The host structures are illustrated by using ball and stick models; Zr: teal, O: red, C: grey, N: blue, and H: pale pink.

The experimental and simulated INS spectra up to 2000 cm^{-1} (248 meV) of the NH_3-free UiO-67 sample are demonstrated in Figures 5.2a. The refined perfect (non-defective) structure of the UiO-67 obtained from the previous NPD study (see Chapter 3) was used as the model for DFT calculations. A good agreement between calculated and experimental determined spectra was mostly observed in a neutron energy loss between 200 and 1700 cm^{-1} with detailed peak assignments shown in Tables 5.2. There are significant

discrepancies between experimental and calculated data particularly for the low energy region (below 200 cm^{-1}) which are mainly associated to lattice vibrations or phonon modes (Figure 5.2). These spectral mismatches are potentially caused by the limitation of DFT calculations that do not take the dispersion correction factor into account. The dispersion force is one of the intermolecular interactions that strongly affects lattice modes in solid state materials. [9] For a better interpretation, the experimental vibrational modes in this region were compared to the reported data computed by using a dispersion-corrected DFT. [22] Considering the fact that there were some defects created by missing organic linkers and those sites should be terminated by either solvents or modulators used during the synthesis, we expected to see the scattering signals of these species. Interestingly, the additional peaks at ca. 420, 580, and 920 cm^{-1}, as well as overlapping peaks from 1010 to 1100 cm^{-1} (denoted as yellow stars) were clearly observed in the INS spectra of UiO-67. These peaks can be attributed to vibrational modes of acetate (CH_3COO) functional groups [21] (see Table A5.1 in the Appendices for the peak assignments). High intensity scattering peaks below 150 cm^{-1} also indicate the translations and rotations of the acetate methyl groups overlapping with lattice vibrations of the studied frameworks. [21] Moreover, the peaks corresponding to CH_3COO but slightly shifted to lower energy than those found in the solid acid, implying that the bond weakening of CH_3COO is due to the coordinative binding towards Zr metal nodes of UiO-67 (Figure 5.3). The overall observations are consistent with the fact that at least some of the CH_3COO groups terminate the defects sites of UiO-67, in agreement with the previous study on defective UiO-66 [16] and our recent work on defective UiO-67 type MOFs characterised by NPD (Chapter 3). For the experimental and simulated INS spectra of UiO-bpydc, a reasonably overall agreement of the spectra was also observed over the energy range of 200 and 1700 cm^{-1} (Figure 5.2b, and

see Table 5.3 for the detailed peak assignments). Extra vibrational peaks assigned to the characteristics of CH_3COO at 420, 580, and 1010 cm^{-1} were clearly found as similar to those found in the UiO-67. Although we cannot extract the actual concentration of CH_3COO from these INS data, these results highlight the use of neutron scattering for an indirect observation of terminal groups whose vibrational peaks severely overlap with other functional groups and difficult to be analysed by conventional techniques such as Infrared (IR) and Raman spectroscopy.

It is also notable that the calculated INS intensities of UiO-67 and UiO-bpydc from 800-1200 cm^{-1} are significantly higher than those of the observed ones, suggesting less vibrations of states possibly as a result of static disorders of the samples. This region can be associated with deformations of CH aromatic rings of the linkers. Therefore, such peak intensity decay indicates the occurrence of missing linker defects in these MOF structures in excellent agreement with the NPD results presented in Chapter 3.

5.2.1.2) Dynamics of the MOF hosts upon the adsorption of NH_3

Alterations in vibrational modes of UiO-67 and UiO-bpydc during NH_3 adsorption can provide a fundamental insight into the binding interactions of these host-guest systems that intensively govern their responsive behaviours. In this regard, the combined INS and DFT was applied to investigate the change in the dynamics of hydrogen atoms of the local MOF hosts including hydroxyl groups and aromatic linkers as well as those of the trapped NH_3 molecules. My recent study on the NPD technique in conjunction with DFT calculations revealed that the different pore openings (windows) induced by missing linkers and functionalized linkers can introduce stepped and hysteresis NH_3 sorption in UiO-type MOFs (Figure 5.1). The possible host-guest interactions between NH_3 and the host frameworks based on the NPD and DFT study are displayed in Figure 5.4. Thus, we will

discuss the INS results in comparison with these proposed binding configurations throughout this section.

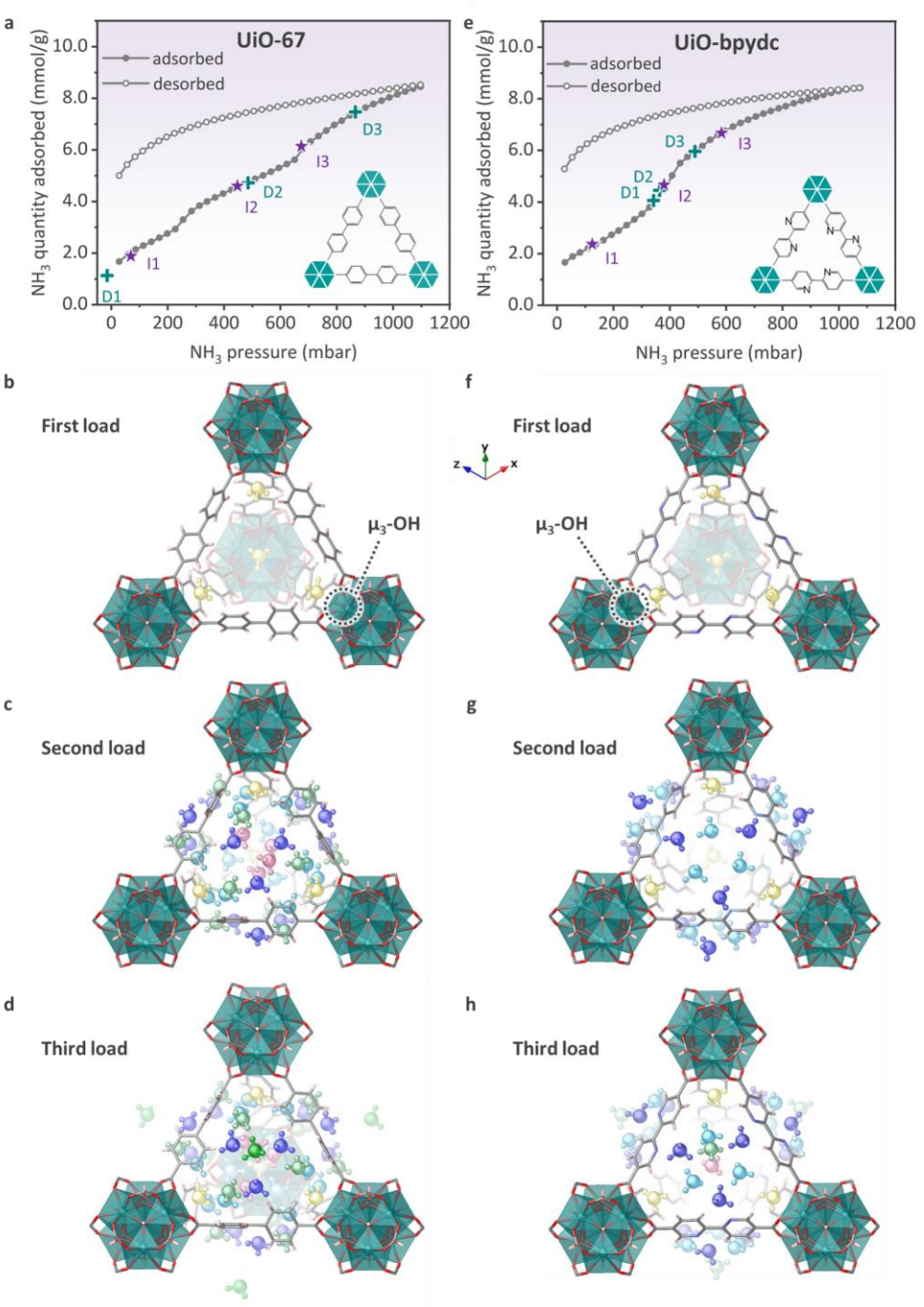

Figure 5.4 | NH_3 uptake of UiO-67 (**a**) and UiO-bpydc (**e**) in INS experiments compared with its NH_3 sorption isotherm measured at 298 K. Star and diamond symbols represent the NH_3 loading amount for INS (I1, I2, I3) in comparison to the previous NPD experiments

(cross symbol, D1, D2, D3). Proposed host-guest interactions at different NH_3 loadings are illustrated in (**b**), (**c**), (**d**) for NH_3-loaded UiO-67 and in (**f**), (**g**), (**h**) for NH_3-loaded UiO-bpydc, respectively. Only tetrahedral pores of the hosts are illustrated. Different colours of the NH_3 molecules represent the adsorbed NH_3 at crystallographically different binding sites inside the MOF hosts.

5.2.1.3) Overall INS spectra of defective UiO-67 as a function of NH_3 loadings

The INS spectra of defective UiO-67 at different NH_3 loadings were collected on TOSCA instrument below 10 K to minimise thermal motion of the host and the adsorbates. Three different NH_3 loadings of 2.10, 4.62, and 6.26 mmol/g (I1, I2, and I3 positions in Figure 5.4a) were assigned to cover the whole range of adsorption transitions. Thereafter, UiO-67_xNH_3 adducts referred to defective UiO-67 with NH_3 loading of x mmol/g.

For sake of simplicity, I will first interpret the vibrational motions of the host MOFs and the stored NH_3 separately before all data are accounted. Figure 5.5 displays the INS spectra up to 2000 cm^{-1} of UiO-67 during NH_3 adsorption measured below 10 K. Considerable changes in the vibrational modes of the UiO-67_xNH_3 adducts are clearly observed from 20 to 1500 cm^{-1}, suggesting the specific interactions between NH_3 and UiO-67 due to gas adsorption at different binding sites inside the host framework. The origin of the vibrational modes of the NH_3-free UiO-67 is analysed by comparing with the simulated spectrum of UiO-67 obtained from *ab initio* DFT calculations (see Table 5.2). This strategy allows a straightforward assignment of the main peaks observed in the INS data. To make a closer look at the details of the spectra, the vibrational modes are simply divided into three regions; I) below 200 cm^{-1}, II) 200-800 cm^{-1}, and III) 800-1500 cm^{-1}. Region I is associated to deformational and translational motions of Zr clusters and bpdc linkers (lattice vibrations). Region II is assigned to bending and stretching modes of CC aromatic, CH

aromatic, COC, Zr-O, and μ_3-OH. Region III corresponds to stretching modes of CC aromatic and COC, as well as collective motions of bpdc linker. Details of the peak assignment are given in Table 5.2.

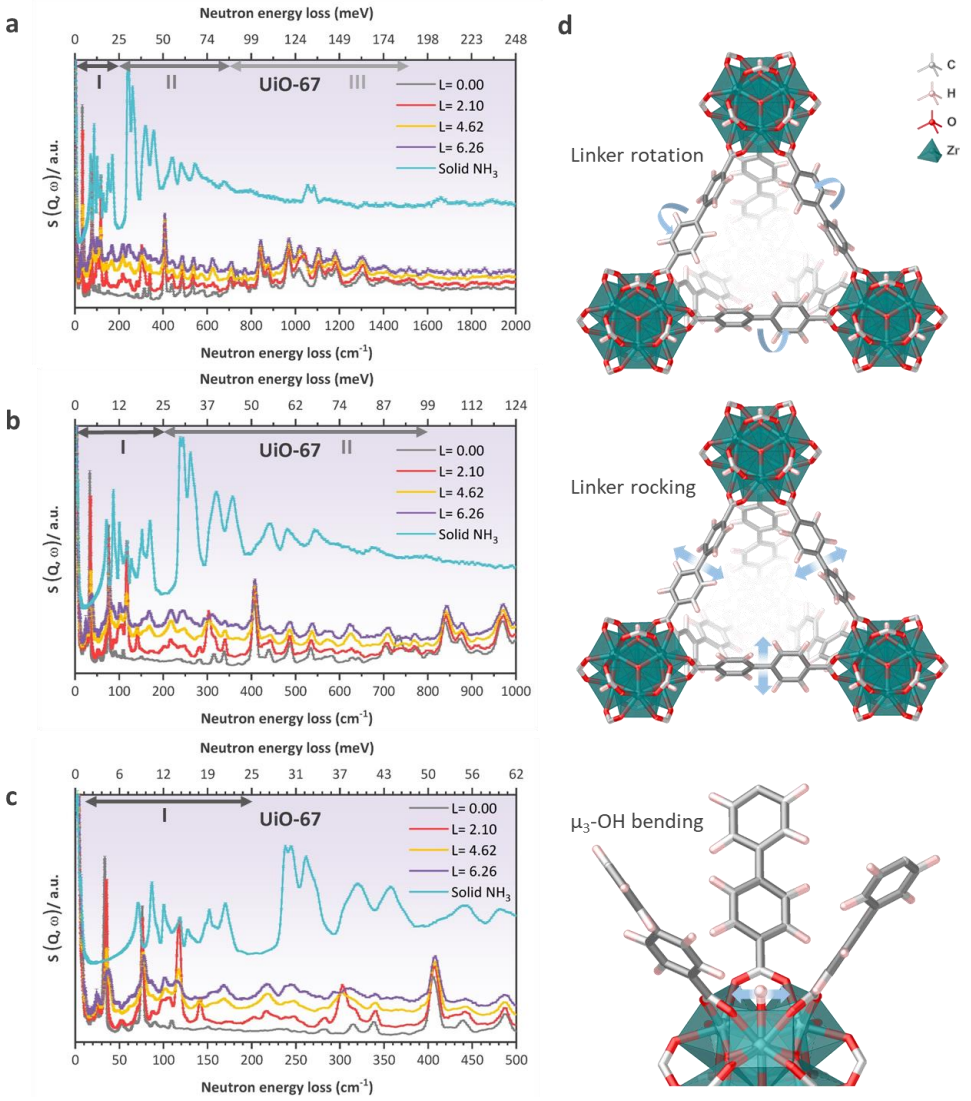

Figure 5.5 | INS spectra collected below 10 K for UiO-67 as a function of NH_3 loadings with the range of neutron energy loss up to 2000 cm^{-1} (248 meV, **a**), 1000 cm^{-1} (124 meV, **b**), and 500 cm^{-1} (62 meV, **c**) and examples of deformational modes of UiO-67 most affected by the loading of NH_3, **d**). Arrows indicate the directions of the deformations calculated by DFT. Colour scheme; Zr: teal, O: red, C: grey, and H: pale pink. *L* refers to loading amount

of NH_3 in mmol/g. The INS spectrum of solid NH_3 measured below 20 K was provided by the ISIS facility and its intensity was scaled down by 0.5 for a better comparison. Note that 1 meV ≈ 8.066 cm^{-1}.

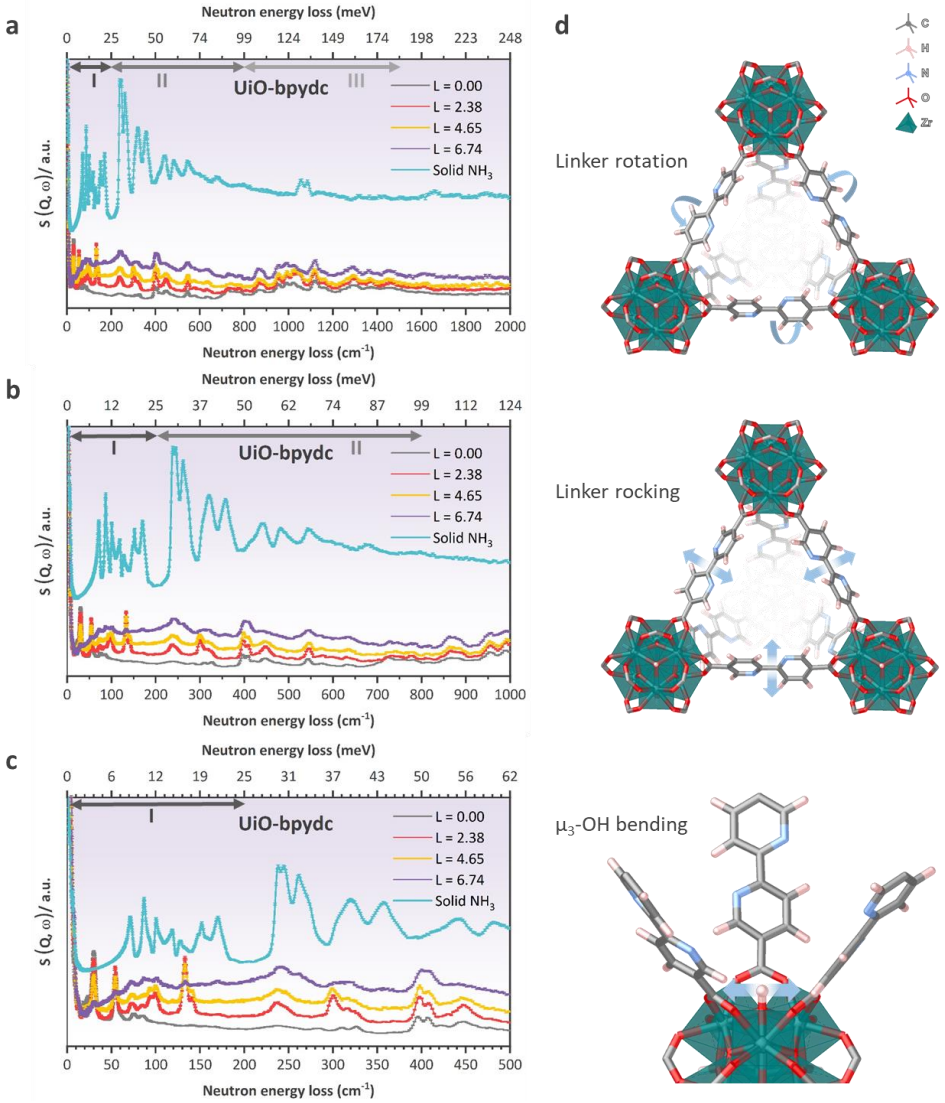

Figure 5.6 | INS spectra collected below 10 K for defective UiO-bpydc as a function of NH_3 loadings with the range of neutron energy loss up to 2000 cm^{-1} (248 meV, **a**), 1000 cm^{-1} (124 meV, **b**), and 500 cm^{-1} (62 meV, **c**) and examples of deformational modes of UiO-bpydc most affected by the loading of NH_3, **d**). Arrows indicate the directions of the deformations calculated by DFT. *L* refers to loading amount of NH_3 in mmol/g. The INS spectrum of solid

NH_3 was provided by the ISIS and its intensity was scaled down by 0.4 for a better comparison. Note that 1 meV ≈ 8.066 cm^{-1}.

Considering the skeletal peaks of UiO-67 in region I (Figure 5.5c), the peak intensities at ca. 31, 43, 53, and 77 cm^{-1} which correspond to libration of the bpdc linkers, deformation of Zr polyhedra, and rotation of the bpdc linkers that are sharply decreased together with peak broadening and a slight blue shift during the progressive NH_3 adsorption. This result is attributed to the suppression and stiffening of lattice motions such as linker rotation caused by either a strong host-guest interaction or guest-induced gate opening as previously reported in the literature. [23-24] In region II (200-800 cm^{-1}), substantial changes in peak positions to higher energy transfer are observed over the whole range, except a minor red shift at ca. 480 and 775 cm^{-1}. The most notable decrease in peak intensity was detected at ca. 740 cm^{-1}. This peak is assigned to the bending modes of μ_3-OH and CH aromatic, suggesting the hindrance of these motions when interacted with NH_3 molecules. At higher vibrational frequencies (region III, Figure 5.5a), a combination of blue shift (820-1000 cm^{-1}), associated with bending modes of μ_3-OH and CH aromatic and red shift (1050-1350 cm^{-1}), correlated to collective modes of bpdc and stretching modes of CC aromatic with increased NH_3 uptake are noted. These phenomena reflect the engagement of the host to form H-bonding and supramolecular interactions with the adsorbed NH_3, in well agreement with NPD and DFT study (see Chapter 3).

5.2.1.4) Overall INS spectra of defective UiO-bpydc as a function of NH_3 loadings

In addition to the defective UiO-67, the INS spectra of defective UiO-bpydc were also recorded on TOSCA equipment below 10 K at the NH_3 loadings of 2.38, 4.65, and 6.74 mmol/g (I1, I2, and I3 positions in Figure 5.4e), covering the entire range of the stepwise

adsorption transitions. UiO-bpydc_xNH_3 represented the defective UiO-bpydc with NH_3 loading of x mmol/g. The obtained INS spectra up to 2000 cm^{-1} of UiO-bpydc as a function of NH_3 dosing are shown in Figure 5.6. As expected, there were significant changes in the vibrational modes of the UiO-bpydc_xNH_3 adducts over the whole frequency range from 20 to 1500 cm^{-1}, reflecting the binding interactions between NH_3 and UiO-bpydc at different adsorption sites as previously discussed based on the NPD study (Chapter 3). Vibrational modes of the UiO-bpydc before NH_3 uptake was thoroughly identified by comparing with the simulated INS spectrum of the non-defective UiO-bpydc structure derived from DFT calculations (Table 5.3). To enable a detailed analysis, the vibrational modes are separated into three regions: I) below 200 cm^{-1}, II) 200-800 cm^{-1}, and III) 800-1500 cm^{-1}. Region I is associated to the lattice motions of Zr clusters and bpydc linkers such as deformational and translational modes. Region II is assigned to bending and stretching modes of CC aromatic, CN aromatic, CH aromatic, COC, Zr-O, and μ_3-OH. Region III corresponds to stretching modes of CC aromatic, CN aromatic, COC, as well as collective motions of the bpydc linker. Details of the peak assignment are given in Table 5.3.

According to the region I (Figure 5.6c), it is observed that the peak intensities at ca. 30 and 55 cm^{-1} which can be assigned to the rotational modes of the bpydc linkers drastically decrease in conjunction with peak broadening and slight blue shift upon NH_3 adsorption. Surprisingly, these peaks almost disappear at the highest loading of NH_3 (purple line). Such loading-dependent peak alterations are strongly related to the suppression and stiffening of lattice motions due to a steric hindrance caused by strong host-guest interactions, agreeable to the previous study from Kusaka *et al*. [23] It is also worth noting that the decline of peak intensities of the UiO-bpydc_xNH_3 adducts is more prominent than those of the UiO-67_xNH_3 analogues (Figure 5.5). This observation clearly reflects a stronger host-guest

interaction due to H-bonding between NH_3 and bipyridine linkers and thus making the framework more rigid. At a higher frequency (Region II, 200-800 cm^{-1}, Figure 5.6b), a little blue shift in peak position is detected over the whole range excluding a small red shift at ca. 450 and ca. 780 cm^{-1}. The most distinct increase and decrease in peak intensities appear at ca. 450 and ca. 720 cm^{-1}, respectively. The former is closely related to a combination of aromatic CC and CN deformations whereas the latter is attributed to a bending mode of μ_3-OH, indicating the presence of the host-guest interactions not only between the NH_3 and the μ_3-OH, but also the NH_3 and the bpydc linker. At the highest energy transfer range (region III, 800-1500 cm^{-1}, Figure 5.6a), minor changes in peak positions to higher energy associated to bending modes of μ_3-OH and CH and CN aromatic are observed from 800 to 1200 cm^{-1}, while those to lower energy correlated to deformational modes of the bpydc linker are found above 1200 cm^{-1}. The results indeed indicate the involvement of the μ_3-OH and the bpydc linkers as the specific binding sites for NH_3 adsorption in excellent agreement with the NPD data (see Chapter 3).

5.2.1.5) Comparison of INS difference spectra of defective UiO-67 and UiO-bpydc upon NH_3 adsorption

In previous sections, the dynamic behaviours of the host frameworks during NH_3 adsorption were discussed. Here, I will further analyse the dynamics of the trapped NH_3 molecules to get deeper insights into host-guest and guest-guest binding interactions of the studied system. To this end, difference spectra of both UiO-67 and UiO-bpydc upon addition of NH_3 were created by subtracting the spectrum of each NH_3-loaded sample with that of the unloaded sample (Figure 5.7). This strategy could eliminate scattering contributions from the host frameworks. The INS spectrum of solid NH_3 provided by the ISIS facility was also plotted against the difference spectra.

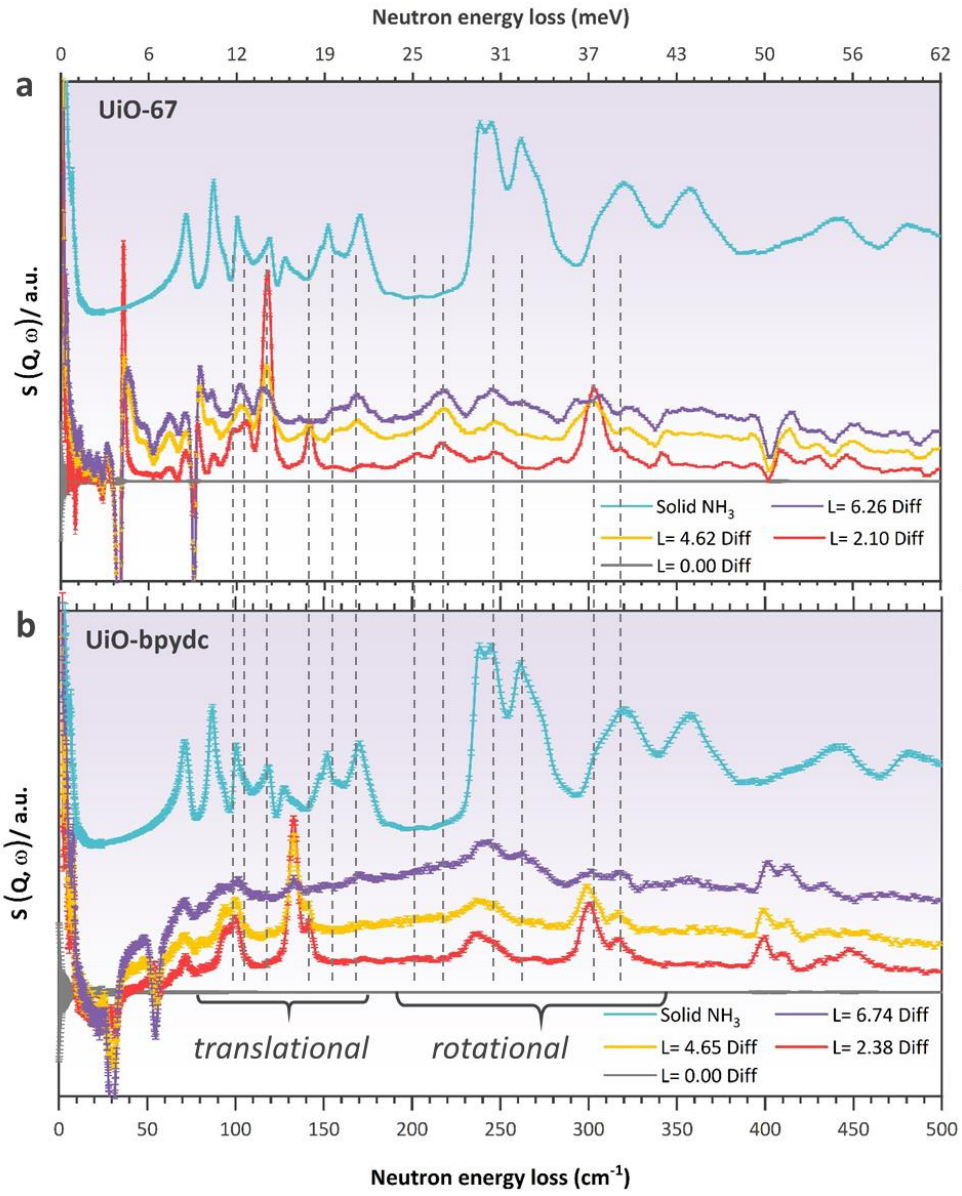

Figure 5.7 | Comparison of the difference plots between UiO-67 (**a**) and UiO-bpydc (**b**) with increased NH_3 adsorption. Dashed lines denote the vibrational modes of NH_3. The INS spectrum of solid NH_3 was provided by the ISIS and its intensity was scaled down by 0.5 and 0.3 in **a**) and **b**), respectively, for a better comparison. *L* refers to loading amount of NH_3 in mmol/g. Note that 1 meV ≈ 8.0655 cm^{-1}.

Additional well-defined peaks are clearly observed in the energy transfer range of 60 and 1100 cm^{-1} with increasing NH_3 (Figures 5.7a and A5.1). Such peaks show

characteristics similar to the vibrational spectrum of solid NH_3 but emerged at significantly lower frequencies. This result suggests that NH_3 molecules incorporated in the framework but their adsorption states explicitly differ from the bulk solid. The peaks appear at low energy transfer (60-150 cm^{-1}) could be ascribed to translational modes, whereas ones locate around 150-350 cm^{-1} could be attributed to librational motions of NH_3 (see Table A5.2 in the Appendices for details of peak assignment). [25] Upon NH_3 loading, distinct changes in peak intensities and positions associated to NH_3 are detected. These alterations implies that the NH_3 molecules experience different environments inside the pores of UiO-67, forming either NH_3-host or NH_3-NH_3 interactions. Relatively sharp peaks observed in the lowest NH_3 loading (2.10 mmol/g) implies ordered arrangement of the trapped NH_3 in the pores. These peaks become broader together with the emergence of extra vibrational bands in a range of 150-180 cm^{-1} and 260-280 cm^{-1} at higher loading (4.62 and 6.26 mmol/g) inferred that the increased disordering of the pore-confined NH_3 is due to the pore filling process. [26] The INS difference spectra of NH_3-loaded UiO-bpydc show peak positions and intensities in significant contrast to those of NH_3 loaded UiO-67, indicating different types and degrees of host-guest interactions between these two MOFs (Figure 5.7b and A5.2). In UiO-bpydc, well-defined vibrational modes of NH_3 at the first dosing can be ascribed to the isolated NH_3 molecules adsorbed at the μ_3-OH of the framework via H-bond interaction. Further adding NH_3 into the MOF structure at 4.65 mmol/g results in a slight peak broadening without significant additional peaks found, while at the highest loading, a drastic decrease in peak intensity and a presence of extra vibrational modes are visibly observed at 150-170 and 250-280 cm^{-1} regions. These results demonstrate that the dynamics of the NH_3 inside these defective MOF structures are intensely dependent on the types of pore functionality and the gas loading and hence affect the corresponding pore filling process.

For a deeper discussion on types of interactions, these INS spectra will be described in comparison with the data from DFT calculations in the following section.

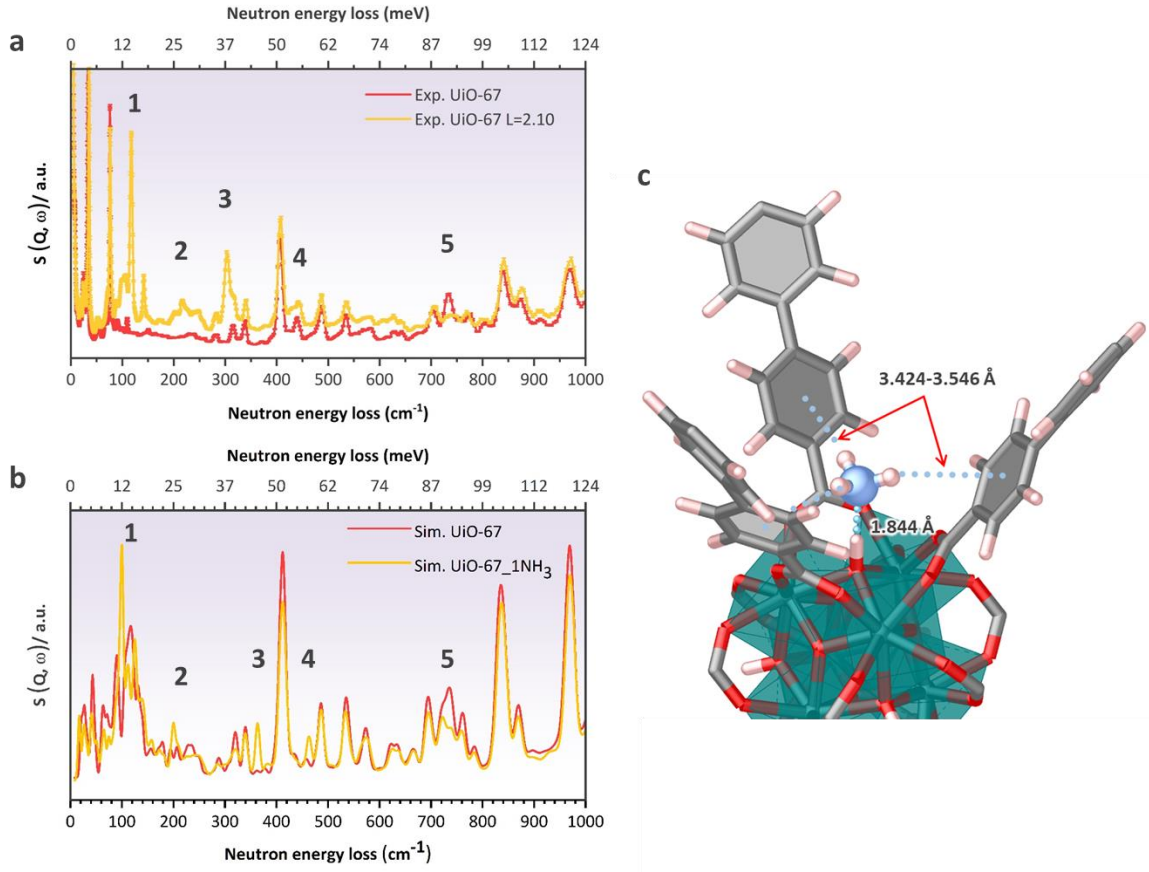

Figure 5.8 | Experimental (**a**) and simulated (**b**) INS spectra of UiO-67 and UiO-67_2.10NH_3 with the range of neutron energy loss up to 1000 cm^{-1} (124 meV). The optimised structure of UiO-67 with one NH_3 adsorbed at μ_3-OH obtained from DFT was shown in (**c**). **L** refers to loading amount of NH_3 in mmol/g. Arabic numbers mark the differences between the spectra of UiO-67 and UiO-67_2.10NH_3.

Prior to the first adsorption transition (position I1 in Figure 5.4a), we would like to probe the interactions between NH_3 and MOF that can correlate to primary binding site(s) responsible for an abrupt increase in NH_3 uptake of ca. 2.00 mmol/g. Figure 5.8 demonstrates the comparison of experimental and theoretical INS spectra for UiO-67 and

UiO-67_2.10NH_3 samples up to 1000 cm^{-1} (124 meV); the full spectra up to 2000 cm^{-1} are given in Figure A5.3. For the experimental INS spectra, six major changes in peak intensity were observed after the NH_3 dosing of 2.10 mmol/g (Figure 5.8a and Figure A5.3a). Peak 1, 2, and 3 occurred at the low energy transfer regime (<350 cm^{-1}), whereas peak 4, 5, and 6 emerge above 400 up to 1200 cm^{-1}. Sharp decrease in peak intensity at ca. 31 and 75 cm^{-1} together with a slight blue shift of the overall spectrum is found, reflecting the lattice stiffening as mentioned earlier.

To achieve a deeper understanding of these dynamic changes, DFT calculations were performed to optimise the structures and simulate the INS spectra for UiO-67 and its ammoniated structures. Based on the previous study, we used a structure of UiO-67 with 1 NH_3 bound to μ_3-OH as a starting model (1 NH_3 per Zr node, see Figure 5.4b). After convergence, the obtained theoretical INS spectra show good agreement with the experimental ones indicating that NH_3 molecules primarily interacted with μ_3-OH of the host framework at low surface coverage (Figure 5.8b). The optimised bond distance between N of NH_3 and H of hydroxyl is 1.844 Å and the ∠OHN bond angle is 179.05 ° (Figure 5.8c), corresponding to H-bond interaction. Moreover, the bond distances between H of NH_3 and the aromatic plane are in the range of 3.424-3.549 Å, implying that the adsorbed NH_3 could also form a weak dipole-induced dipole interaction with the surrounding electron-rich biphenyl rings of the bpdc linkers. As shown in Figure 5.8b, Peak 1, 2, and 3 are assigned to translational and rotational modes of the single NH_3 attaching to μ_3-OH via H-bonding. Peak 4 and 5 are attributed to μ_3-OH stretching (in-phase) and bending, respectively. Peak 6 (Figure A5.3) is ascribed to symmetric bending of the NH_3. Besides, noticeable increase in peak intensity from 800 to 1400 cm^{-1} could be associated to the biphenyl deformation, confirming weak supramolecular contacts between the NH_3 and the linkers.

From the overall INS and DFT data, it is confirmed that (i), the primary binding site for NH_3 in both defective UiO-67 and UiO-bpydc is μ_3-OH, forming a strong H-bond interaction, (ii) for the UiO-67, electron-rich biphenyl linkers can interact with the adsorbed NH_3 via dipole-induced dipole interactions and facilitate NH_3 clustering prior to filling up the pores. On the other hand, bipyridine linkers of UiO-bpydc can potentially contribute to the H-bonding network with NH_3 at the interconnected pore window leading to an obvious suppression of the linker rotation and hence further block up NH_3 to enter the pore interior at a certain partial pressure, (iii) adsorption states of NH_3 are greatly influenced by pore surface functionality and gas loading. At the lowest NH_3 uptake, the NH_3 molecules are primarily adsorbed at μ_3-OH of the host frameworks as isolated NH_3 molecules evidenced by the highly strong and sharp INS spectra associated to the NH_3 characteristics. At higher uptake, pre-adsorbed NH_3 molecules in UiO-67 (via dipole interactions) show higher tendency to propagate the binding contact with the incoming NH_3. This is reflected by the sudden broadening of the INS line shapes associated to the first-loaded NH_3. This observation strongly support our proposed adsorption mechanism that NH_3 molecules can enter the UiO-67 pores more easily since they do not suffer from the guest-induced pore blocking caused by H-bond network at the trigonal pore window found in the UiO-bpydc. To make a deeper interpretation, vibrational frequency calculations of the trapped NH_3 at elevated loadings are currently under investigation and will be included in the discussion in the near future.

5.2.2) Diffusion of adsorbed NH_3 inside the defective hosts

5.2.2.1) Analysis of NH_3 diffusion by QENS

QENS data analysis can be used to investigate the diffusive transportation of NH_3 inside the defective UiO-67 and UiO-bpydc at various NH_3 concentration gradients. Elucidating the dynamics of NH_3 molecules in such non-uniform porous materials generated by missing linker defects are key importance to gain an understanding of their distinctive stepped NH_3 sorption mechanism proposed in Chapter 3. Details of QENS experiments as a function of NH_3 dosing are presented in Figure 5.9 and Table 5.4. In the QENS experiments, the recorded total scattering function $S(\boldsymbol{Q}, \omega)$ consists of an elastic component occurring as a peak at energy transfer $\hbar\omega = 0$ and a quasielastic component appearing as a broadening of the elastic peak. The elastic component representing immobile scattering species that can be modelled by a delta function convoluted with an instrument resolution function. On the other hand, the quasielastic component reflecting the moving species can involve one or more Lorentzian functions. As the incoherent scattering cross-section of hydrogen (H) is extremely larger than all other elements, the observed broadening can be dominantly assigned to the uncorrelated motions of H atoms. In this study, one may consider that the mobile contribution of H atoms can come either from the adsorbed NH_3 or from MOF frameworks including aromatic linkers and μ_3-OH. The contribution of the latter can be omitted from the system by simply subtracting the QENS spectrum of the empty sample from that of the loaded sample.

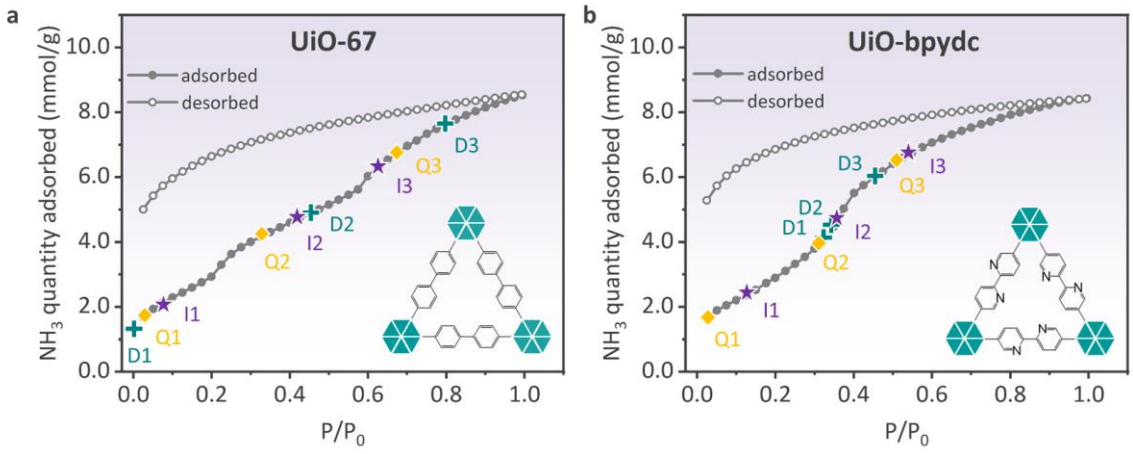

Figure 5.9 | NH_3 uptake of UiO-67 (**a**) and UiO-bpydc (**b**) in QENS experiments compared with its NH_3 sorption isotherm measured at 298 K. Diamond, star, and cross symbols represent the NH_3 loading amount for QENS (Q1, Q2, Q3) in comparison to the previous INS (I1, I2, I3) and NPD (D1, D2, D3) experiments.

Table 5.4 | Sample information used in the *in situ* QENS experiments.

Sample	**UiO-67**				**UiO-bpydc**			
Reticular formula	$Zr_6O_4(OH)_4(bpdc)_{6-x}(acetate)_{2x}$				$Zr_6O_4(OH)_4(bpdc)_{6-x}(acetate)_{2x}$			
Actual reticular formula[a]	$Zr_6O_4(OH)_4(bpdc)_4(acetate)_4$				$Zr_6O_4(OH)_4(bpydc)_{4.5}(acetate)_3$			
Molar mass per unit cell (g/mol unit cell)	7749.7				7537.2			
Loading amount of NH_3 (mmol/g)	0.00	1.89	4.11	6.72	0.00	1.86	4.04	6.55
Loading amount of NH_3 (molecule/unit cell)	0.00	14.6	31.8	52.0	0.00	14.0	30.4	49.4
Loading temperature (K)	298 ± 2							
Measurement temperature (K)	Below 10±2 and 298±2	298 ± 2			Below 10±2 and 298±2	298 ± 2		

[a] Based on the ICP-MS data in the Appendices.

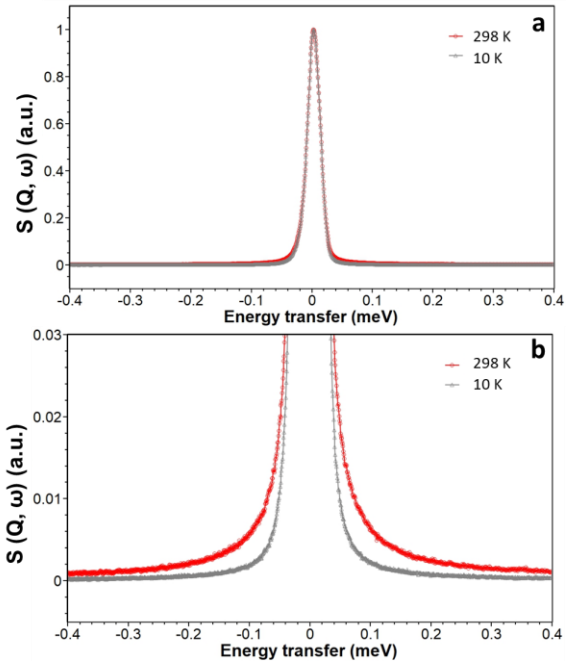

Figure 5.10 | Normalised QENS spectra measured for UiO-67 at 10 ± 2 K (grey triangle) and at 298 ± 2 K (red circle). (**a**) and **(b**) correspond to the same data, but with different intensity scales. The spectra were summed over a large number of detectors, to get good statistics.

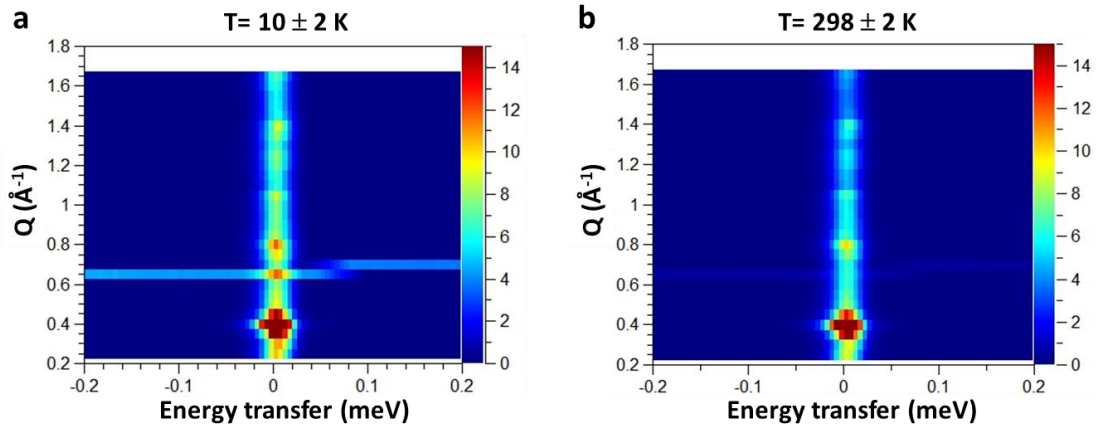

Figure 5.11 | Surface plot of energy transfer versus ***Q*** values for unloaded UiO-67 collected at 10 ± 2 K (**a**) and 298 ± 2 K (**b**). The ***Q*** and *d* ranges used were 0.225 – 1.675 $Å^{-1}$ and 3.8 – 27.9 Å, respectively. Faulty detector appeared at ***Q*** = 0.675 $Å^{-1}$.

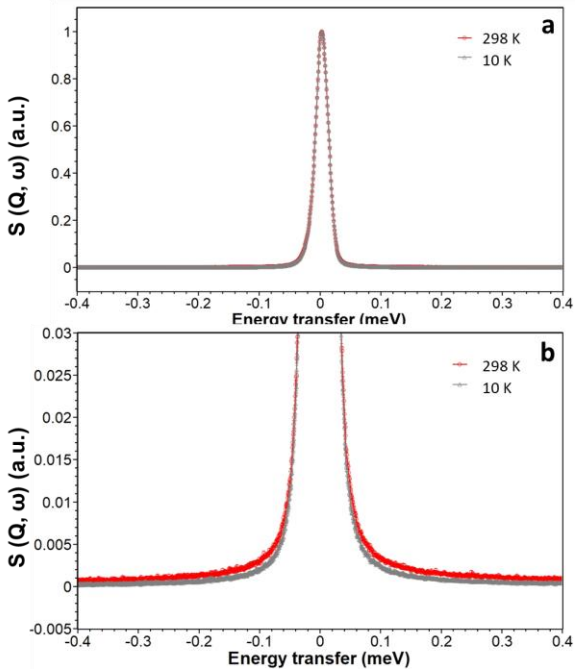

Figure 5.12 | Normalised QENS spectra measured for UiO-bpydc at 10 ± 2 K (grey triangle) and at 298 ± 2 K (red circle). (**a**) and (**b**) correspond to the same data, but with different intensity scales. The spectra were summed over a large number of detectors, to get good statistics.

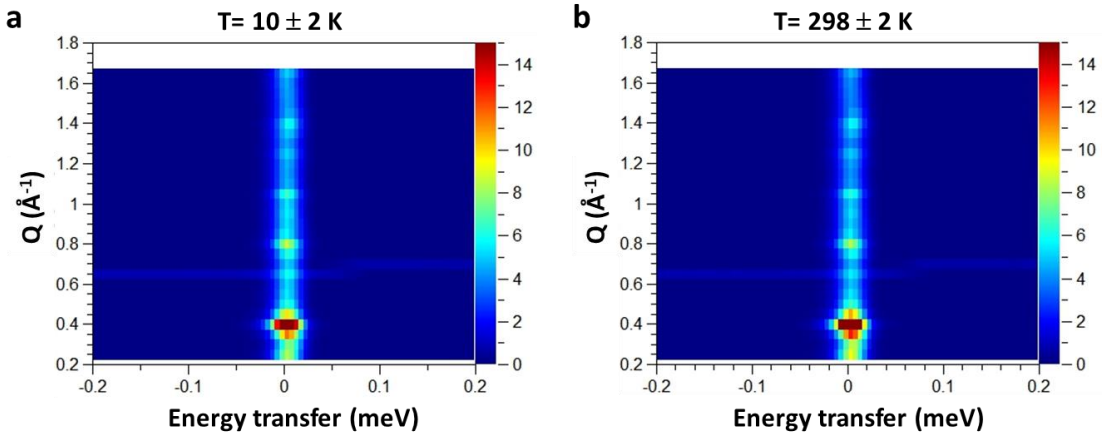

Figure 5.13 | Surface plot of energy transfer versus ***Q*** values for unloaded UiO-bpydc collected at 10 ± 2 K (a) and 298 ± 2 K (b). The ***Q*** and *d* ranges used were 0.225 – 1.675 $Å^{-1}$ and 3.8 – 27.9 Å, respectively. Faulty detector appeared at $\boldsymbol{Q} = 0.675$ $Å^{-1}$.

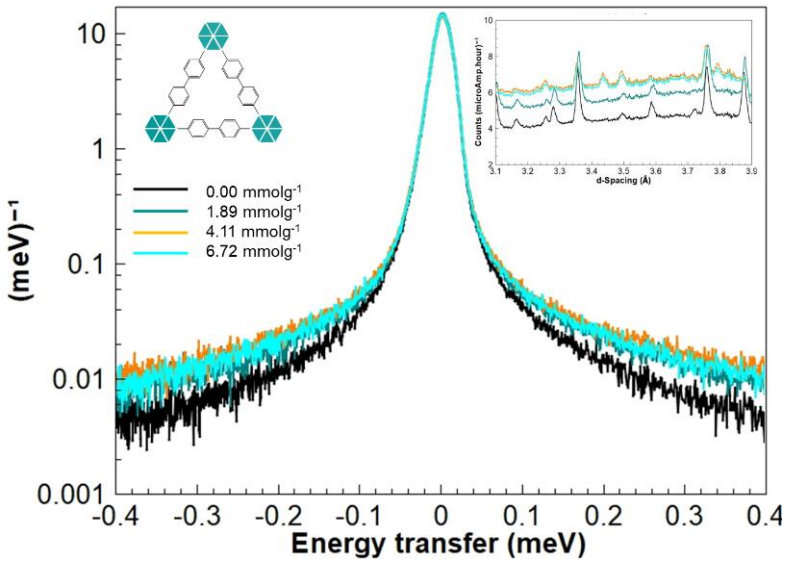

Figure 5.14 | QENS spectra of defective UiO-67 as a function of NH_3 loading at $\boldsymbol{Q}$ = 0.27 $Å^{-1}$. Inset represents their associated simultaneous diffraction patterns.

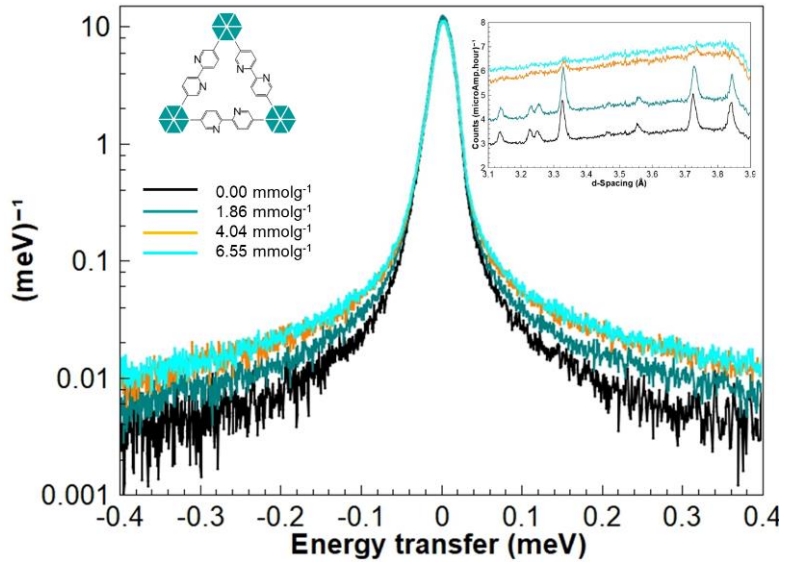

Figure 5.15 | QENS spectra of defective UiO-bpydc as a function of NH_3 loading at $\boldsymbol{Q}$ = 0.27 $Å^{-1}$. Inset represents their simultaneous diffraction patterns.

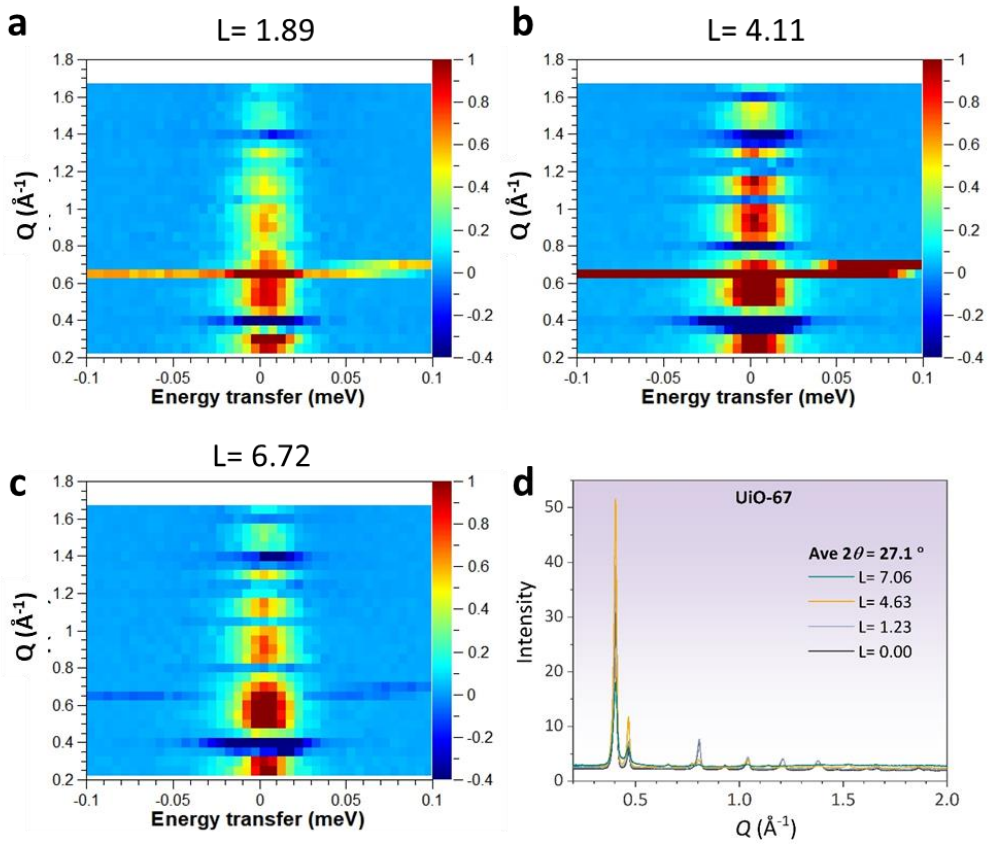

Figure 5.16 | Subtracted QENS data of NH_3-adsorbed UiO-67 measured at 298 ± 2 K (**a, b,** and **c**) and the loading-dependent neutron diffraction pattern of UiO-67 from Chapter 3 (**d**). The detectors covered measurements over a $\boldsymbol{Q}$ range of 0.225–1.675 $Å^{-1}$ (a d range of 3.8 – 27.9 Å) with a faulty detector at $\boldsymbol{Q}$ = 0.675 $Å^{-1}$. L refers to a loading quantity of NH_3 in mmol/g. The QENS signal of the empty UiO-67 was subtracted from that of the loaded UiO-67, so that only the signal from the NH_3 molecules could be extracted.

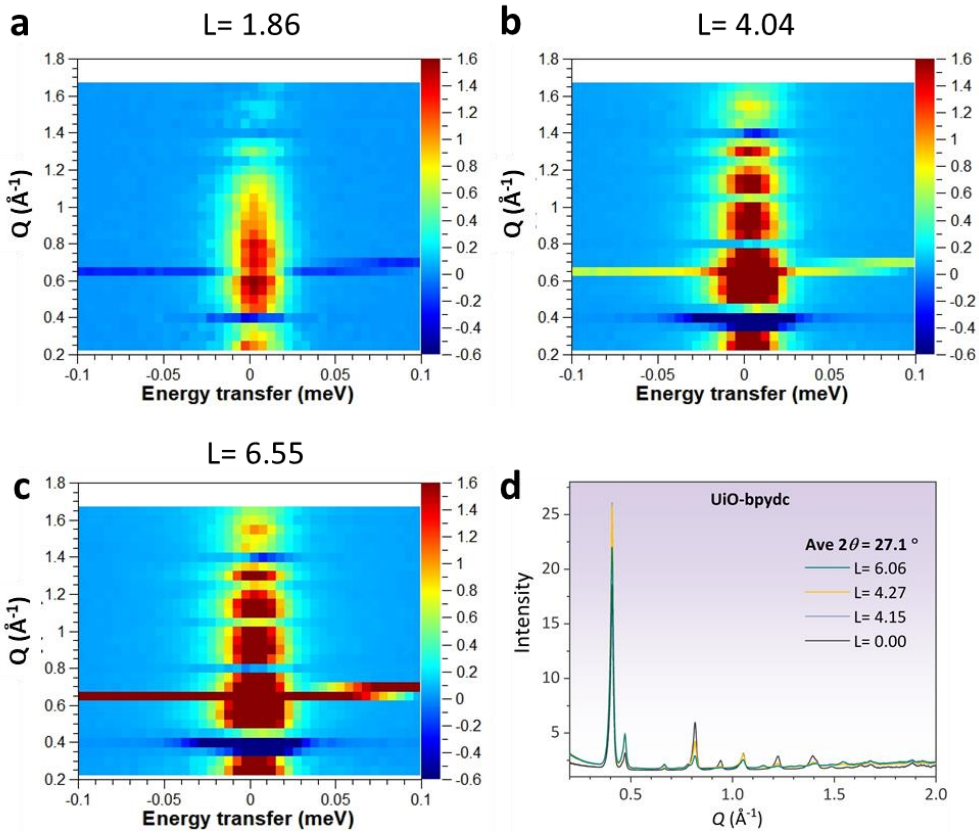

Figure 5.17 | Subtracted QENS data of NH_3-adsorbed UiO-bpydc measured at 298 ± 2 K (**a, b,** and **c**) and the loading-dependent neutron diffraction pattern of UiO-bpydc from Chapter 3 (**d**). The detectors covered measurements over a $\boldsymbol{Q}$ range of 0.225–1.675 $Å^{-1}$ (a d range of 3.8 – 27.9 Å) with a faulty detector at $\boldsymbol{Q}$ = 0.675 $Å^{-1}$. L refers to a loading quantity of NH_3 in mmol/g. The QENS signal of the empty UiO-bpydc was subtracted from that of the loaded UiO-bpydc, so that only the signal from the NH_3 molecules could be extracted.

The QENS spectra of unloaded MOF samples in Figures 5.10 and 5.12 were derived from a sum over a large $\boldsymbol{Q}$ range followed by normalisation of the maximum intensity. These QENS spectra reveal a small broadening of the elastic peaks when changing the measurement temperature from 7 K to 298 K. This observation indicates that any motions of the MOF frameworks existed inside the dynamic window of the spectrometer and hence the MOF frameworks cannot be treated as if they were purely static. The larger peak

broadening in UiO-67 also implies that the UiO-67 framework is more mobile than the UiO-bpydc counterpart. The QENS spectra of NH_3-loaded UiO-67 and NH_3-loaded UiO-bpydc measured at 298 K are displayed in Figures 5.14 and 5.15, respectively. They all exhibit a degree of quasielastic broadening compared to the corresponding NH_3-free samples. This indicates that motion is occurring on time scales visible to the OSIRIS spectrometer (~2−50 ps) [27]. The positioning of this accessible energy range is such that any motions observed are likely to be due to molecular rotation or confined diffusion of NH_3, with any translational movements of internally or externally physisorbed species being too slow to be resolved by this instrument.

Simultaneous diffraction data of UiO-67 and UiO-bpydc at different NH_3 loadings are shown in insets of Figures 5.14 and 5.15, respectively. The background increases with increasing NH_3 uptake due to incoherent scattering from the H atoms. The overall diffraction results indicate that the elastic scattering from adsorbed NH_3 is quite serious. This is reflected by the subtracted spectra: some of them are negative in certain $\boldsymbol{Q}$ ranges such as 0.4, 0.8, 1.1, and 1.4 $Å^{-1}$ (see Figures 5.16 and 5.17) which are equivalent to the d spacing values of 15.7, 7.8, 5.7, and 4.5 Å, respectively, where $\boldsymbol{Q} = 2\pi/d$. Noticeable changes in coherent Bragg scattering from both materials (Figures 5.14 and 5.15) are clearly observed upon NH_3 loading, in good agreement to the neutron diffraction data of the same samples at comparable ND_3 dosing (Figures 5.16d and 5.17d). For UiO-67, the presence of additional peaks at L= 4.11 and 6.72 mmol/g signifies either structural deformation of the MOF frameworks or periodic arrangement of the adsorbed NH_3 (Figure 5.14). On the other hand, slightly shifting of the peaks to larger d-spacing at the first NH_3 loading then back to lower d-spacing at the higher NH_3 uptake demonstrates that the UiO-67 is swelling and contracting induced by NH_3 concentration, showing flexibility of the framework. For UiO-bpydc, the

obtained diffraction patterns beyond the first NH_3 loading are severely broadened and cannot be analysed further (Figure 5.15). This observation might be due to either framework collapse or the effect of very large incoherent scattering of H atoms that increases the baseline component. Higher resolution diffraction data with a wider range of accessible *d*-spacing would be required to solve this hypothesis which is beyond the scope of this work.

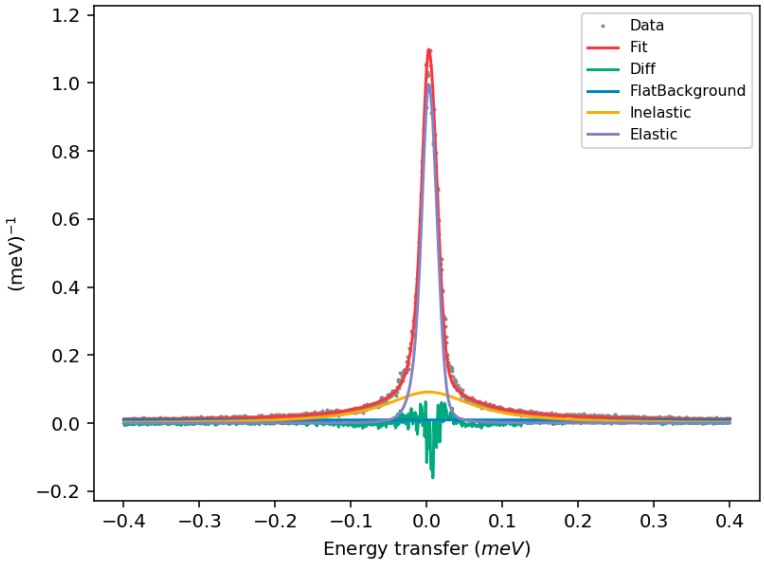

Figure 5.18 | The convolution fit of QENS spectrum of UiO-67 loaded with 4.11 mmol/g NH_3 at $\boldsymbol{Q}$= 0.27 $Å^{-1}$. The obtained χ^2 of the fit is 0.99.

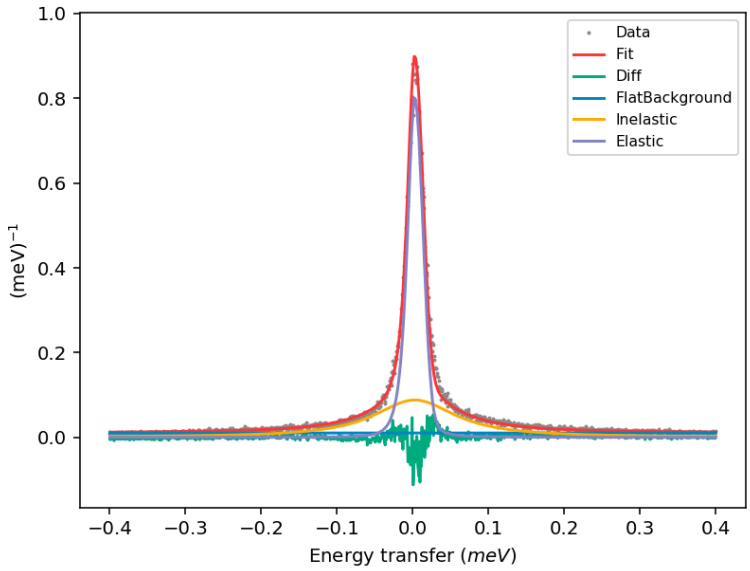

Figure 5.19 | The convolution fit of QENS spectrum of UiO-67 loaded with 6.72 mmol/g NH_3 at $\boldsymbol{Q}$= 0.27 Å^{-1}. The obtained χ^2 of the fit is 0.99.

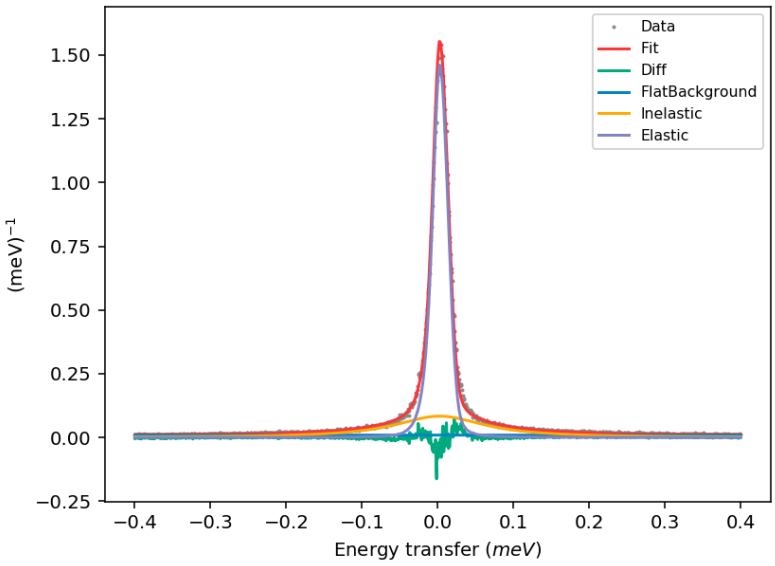

Figure 5.20 | The convolution fit of QENS spectrum of UiO-bpydc loaded with 4.04 mmol/g NH_3 at $\boldsymbol{Q}$= 0.27 Å^{-1}. The obtained χ^2 of the fit is 0.98.

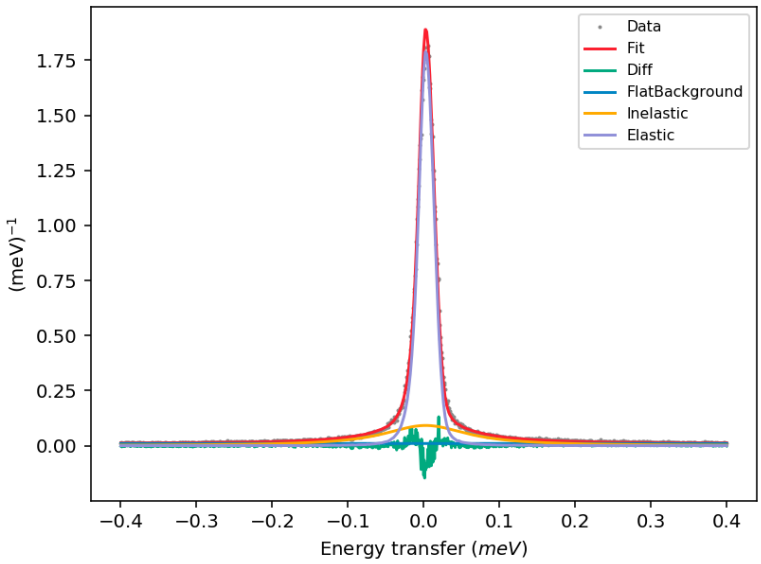

Figure 5.21 | The convolution fit of QENS spectrum of UiO-bpydc loaded with 6.55 mmol/g NH_3 at $\boldsymbol{Q}$= 0.27 Å^{-1}. The obtained χ^2 of the fit is 0.98.

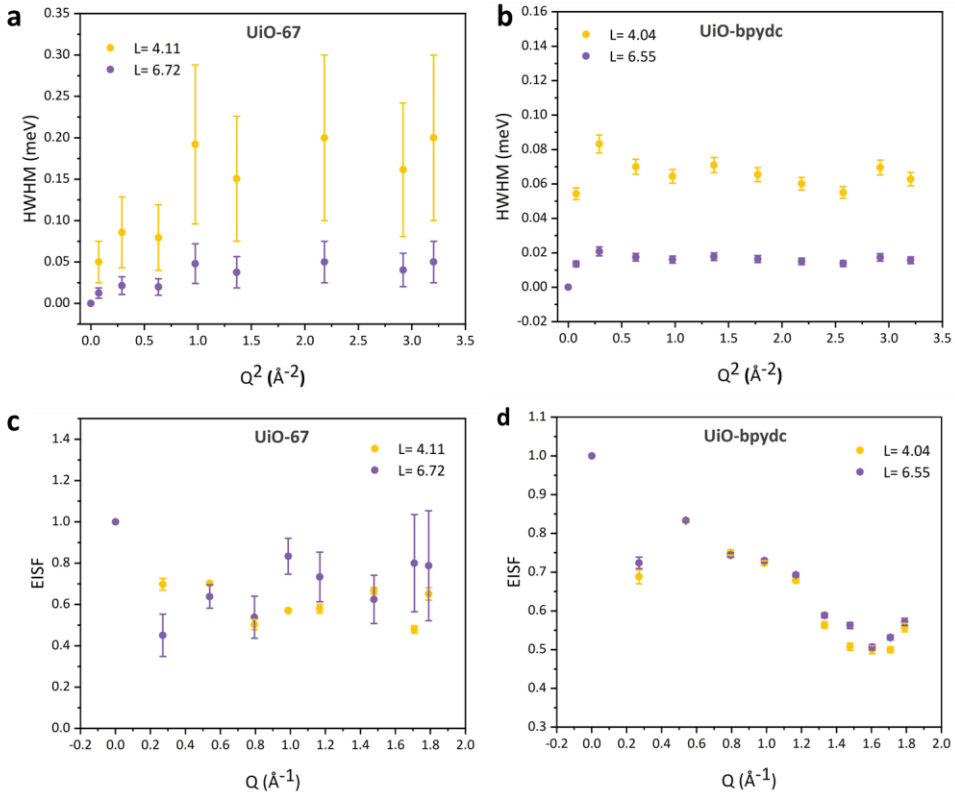

Figure 5.22 | Variations of the HWHM (**a, c**) and EISF (**b, d**) as a function of $\boldsymbol{Q}$ and NH_3 loading derived from QENS experiments at 298 ± 2 K.

As previously discussed, the variance of the spectra with respect to ***Q*** is complicated by contributions due to coherent Bragg scattering from the MOF frameworks and also sample environment. These contributions can be eliminated by subtracting the recorded spectra of unloaded samples from the spectra of the NH_3-loaded samples. This leaves just the neutron scattering contribution from the adsorbed NH_3. Then, fitting of the subtracted QENS spectra was performed by using the Mantid software package developed at the ISIS Pulsed Neutron and Muons Source. [28] The model contains a delta function convoluted with the experimentally measured resolution function, a single Lorentzian function, and a flat background function. The delta function convoluted with the resolution function represents the elastic scattering from static species, while the Lorentzian function reflects the quasielastic scattering from the mobile species in the dynamic window of the instrument. The flat background function defines any motions that are too fast for the OSIRIS time-window.

The subtracted QENS spectra of both MOF samples with the lowest NH_3 dosing show very small contribution of quasielastic scattering and become flattened at high ***Q*** values (Figures 5.16a and 5.17a). This observation can be described as the NH_3 motions being either too fast to detect on the spectrometer or virtually static due to strong host-guest interactions. [29] The latter is more convincing as the loaded NH_3 molecules at this stage are proven to form a H-bonding with μ_3-OH of the frameworks, evidenced by the previous NPD and INS studies. Unfortunately, these QENS spectra cannot be analysed further since their subtracted signals are too low to achieve a good quality of fitting. Thus, the following discussion will solely focus on the NH_3 mobility in defective frameworks at higher NH_3 uptake.

Examples of fits at the second and the third NH_3 loadings at certain $\boldsymbol{Q}$ values are presented in Figures 5.18 and 5.19 for defective UiO-67 and Figures 5.20 and 5.21 for defective UiO-bpydc, respectively. The goodness of fit is determined by a chi-squared (χ^2) test with each fit having a value close to 1. The single Lorentzian function indicates that the one dominant motion of mobile hydrogens in the adsorbed NH_3 is presented. The existence of a flat background implies an additional motion which falls outside the time scale samples by the OSIRIS. The diffusive behaviours of NH_3 can be derived from the broadenings of the fitted Lorentzian function. The variations in the half width at half maximum (HWHM) of the fitted Lorentzians against $\boldsymbol{Q}^2$ at different NH_3 loadings are shown in Figure 5.22. The $\boldsymbol{Q}$ values associated with the Bragg peak positions were omitted from the fitting to minimise the elastic scattering deviation. For NH_3 confined in UiO-67, $\boldsymbol{Q}$ dependencies of HWHM are observed for both loading quantities with similar characteristic shapes indicating the same mode of NH_3 motion inside the framework (Figure 5.22a). The shapes of these fits are possibly associated to a Singwi-Sjölander [30] jump diffusion within a confined volume [31], where the discontinuities agree to the *d* spacings of ca. 6.6 and 8.9 Å for the NH_3 loadings of 4.11 and 6.72 mmol/g, respectively (using $\boldsymbol{Q}= 2\pi/d$). Although this is a tentative data analysis, the obtained results reveal that NH_3 molecules can transport inside the UiO-67 cavity at diffusion length scales depending on the gas loading. The decay of the broadening slopes with increasing NH_3 dosing can reflect slower mobility of NH_3 caused by steric hindrance as more NH_3 fill into the pores and hence reducing free space for the NH_3 to diffuse through. [29] In contrast to UiO-67, HWHM of NH_3 adsorbed in UiO-bpydc is independent of $\boldsymbol{Q}^2$ at the values higher than ca. 0.5 $Å^{-2}$ which is equivalent to $d= 8.9$ Å, while the broadening becomes $\boldsymbol{Q}$-dependent below this point (Figure 5.22b). This observation indicates that NH_3 molecules undergo localised and spatially confined motion within a 8.9

Å diameter cage whilst they have a long-range diffusive translational motion beyond this confined sphere. This significantly represent the involvement of H-bond network between the NH_3 molecules and the bipyridine linker around the trigonal window of UiO-bpydc, thus inhibiting translational diffusion of the NH_3 within this framework. Moreover, the elastic incoherent scattering factor (EISF), defined as the ratio of the intensities of the elastic peak and the sum of QENS and elastic peaks, provides geometric information about the localised motions of NH_3 molecules. Non-zero EISF patterns over the whole $\boldsymbol{Q}$ range are observed for both MOF materials (Figures 5.22c and 5.22d), implying significant elastic contribution arising from either localised motions or static components on the instrument time window. [32] However, the motions of NH_3 in these frameworks are different as reflected by an obvious change in the EISF patterns when replacing UiO-67 by UiO-bpydc. To further assess the nature of NH_3 motions, various plausible models are required to get the best fit for the experimental data, for example, jump rotation around 3 equivalent sites on a circle with a radius comparable to the N−H bond (1 Å) [33], isotropic rotation around a sphere [33], diffusion confined to a spherical volume [34], or a combination of these motions. The NH_3 molecules in defective MOF structures may undergo complex diffusional processes due to multiple host-guest interactions and non-uniform porosity. Thus, special data treatment is crucial to obtain the best fit that represents the actual diffusive behaviours. This data fitting process is still on-going and will be discussed elsewhere in future.

5.2.2.2) Analysis of stepwise adsorption in defective hosts by grand canonical Monte Carlo (GCMC) simulations

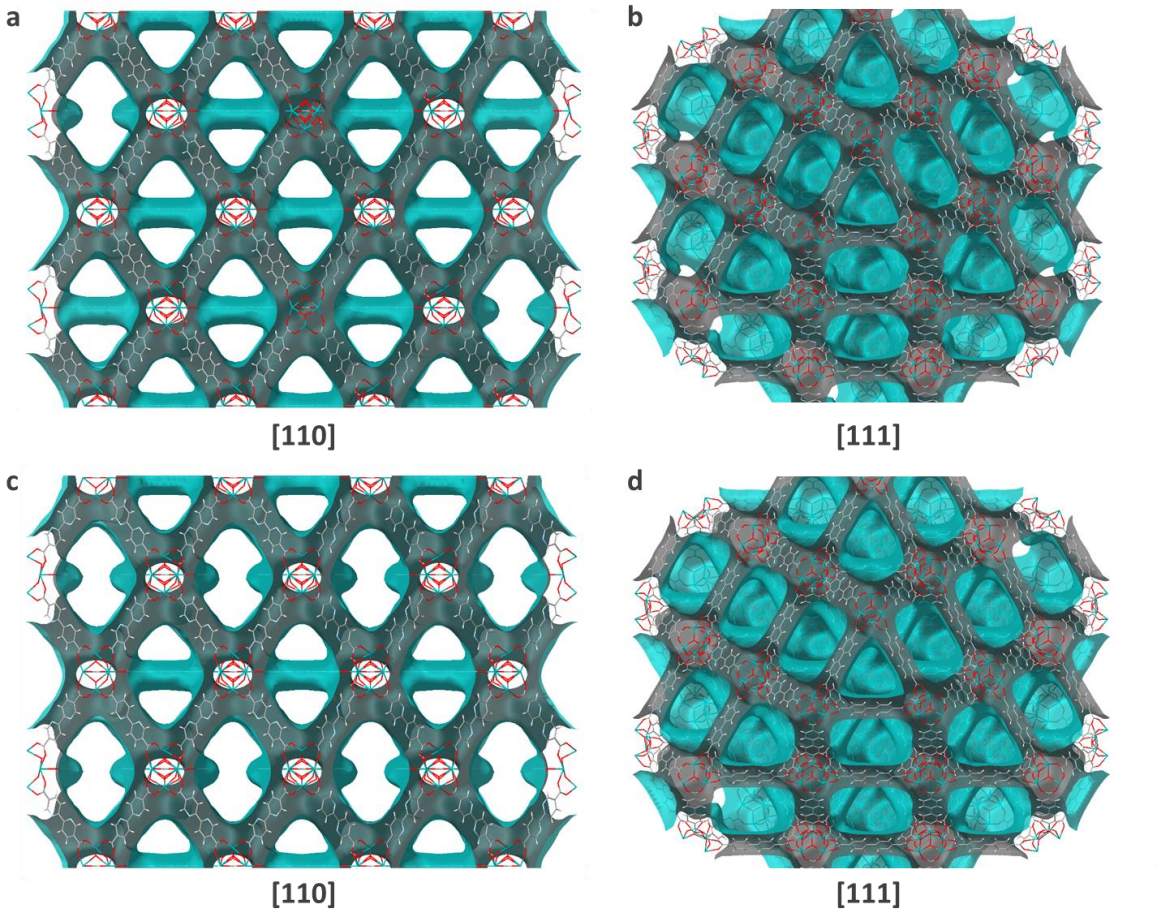

Figure 5.23 | Solvent-excluded surface maps of defective MOF Models with 2x2x2 supercells used in the GCMC simulations: UiO-67 with 1.5 missing linkers per reticular formula (**a** and **b**) and UiO-bpydc with 2.0 missing linkers per reticular formula (**c** and **d**), viewed in different directions. The radius of the probe sphere is 1.826 Å equivalent to the approximate van der Waals radius of an NH_3 molecule. The pore window diameters of the primitive trigonal and the lozenge windows created by missing linker defects are ca. 11 Å and larger than 14 Å, respectively. For the UiO-67 model, to arrange the missing linker vacancies with the lowest energy configuration, its 2x2x2 supercell contains 4 primitive unit

cells with 1 missing linkers per reticular formula and the other 4 with 2 missing linkers per reticular formula. On average, the structure can be crystallographically described as a model with 1.5 missing linkers per reticular formula.

The adsorption isotherms of N_2 at 77 K and NH_3 at 298 K in defective UiO-67 type MOFs were simulated using the GCMC method as implemented in the RASPA simulation package. [35] Models of UiO-67 and UiO-bpydc with missing linker defects were built based on the crystal structures from neutron diffraction data reported in Chapter 3. A 2x2x2 supercell was constructed to represent each of the MOF models as displayed in Figure 5. 23. Prior to the GCMC simulations, geometrical properties of the MOF models such as specific surface area (SSA) and pore volume were computed by using Poreblazer [36] and the results are shown in Table 5.5. Framework atoms were kept fixed at the crystallographic positions thereby ignoring the skeleton stretching and bending vibrations as these materials did not show significant volume change. Table 5.6 demonstrates the numbers of adsorbed NH_3 molecules used in the simulations at various loadings estimated based on the respective experimental NH_3 adsorption isotherm at 298 K. Tables 5.7 and 5.8 show the Lennard-Jones (LJ) parameters and the relevant charges used for the adsorbates and the atoms in the framework, respectively. Details of these GCMC simulations can be found in Section 2.3.2 of Chapter 2.

Table 5.5 | Comparison of the experimental and simulated geometric properties of UiO-67-type MOFs with missing linker defects using He as a probe molecule.

UiO-67 (bpdc linker)		
	Experimental	**Simulated**
Surface area (m^2/g)	1916	2914.59
Pore volume (cm^3/g)	0.75	1.173
Scaling factor	0.6394	
UiO-bpydc (bpydc linker)		
Surface area (m^2/g)	1953	2826.40
Pore volume (cm^3/g)	0.76	1.089
Scaling factor	0.6979	

All the properties were calculated using Poreblazer. [36]

Table 5.6 | Details of the MOF-NH_3 models used in the GCMC simulations.

	Number of NH_3 molecules					
	UiO-67 $Zr_6O_4(OH)_4(bpdc)_{4.5}(acetate)_3$			UiO-bpydc $Zr_6O_4(OH)_4(bpydc)_4(acetate)_4$		
	2.0 mmol/g	4.5 mmol/g	7.0 mmol/g	2.0 mmol/g	4.5 mmol/g	7.0 mmol/g
Per unit cell	13.9	31.3	48.7	13.5	30.4	47.4
Per 2x2x2 supercell	111.3	250.4	389.4	108.2	243.6	379.0

Table 5.7 | Lennard Jones (LJ) parameters and charges for N_2 and NH_3. Column 1 lists the name of the adsorbate; column 2 lists the corresponding atom types of N_2 and NH_3, where M is the dummy atom; columns 3, 4 and 5 list their corresponding LJ parameters and charges, σ in Å, ε/k_B in K, and q in e, taken from the TraPPE force field. [37]

Adsorbate	Atom	LJ Parameters		q (e)
		σ (Å)	ε/k_B (K)	
N_2	N	3.31	36	-0.482
	M	0	0	0.964
	N	3.31	36	-0.482
NH_3	N	3.42	185	0
	H	0	0	0.410
	H	0	0	0.410
	H	0	0	0.410
	M	0	0	-1.230

Table 5.8 | Lennard Jones (LJ) parameters, charges and polarizabilities for the atoms in the framework. Column 1 lists the atom type; columns 2 and 3 list the LJ parameters for the corresponding atom types, σ in Å and ε/k_B in K, taken from the DREIDING force field [38], and for metals not present in the DREIDING force field, from the UFF force field [39] (marked with an asterisk).

Atom	LJ Parameters	
	σ (Å)	ε/k_B (K)
C	3.47	47.854
H	2.844	7.65
N	3.26	38.948
O	3.03	48.156
Zr*	2.783	34.75

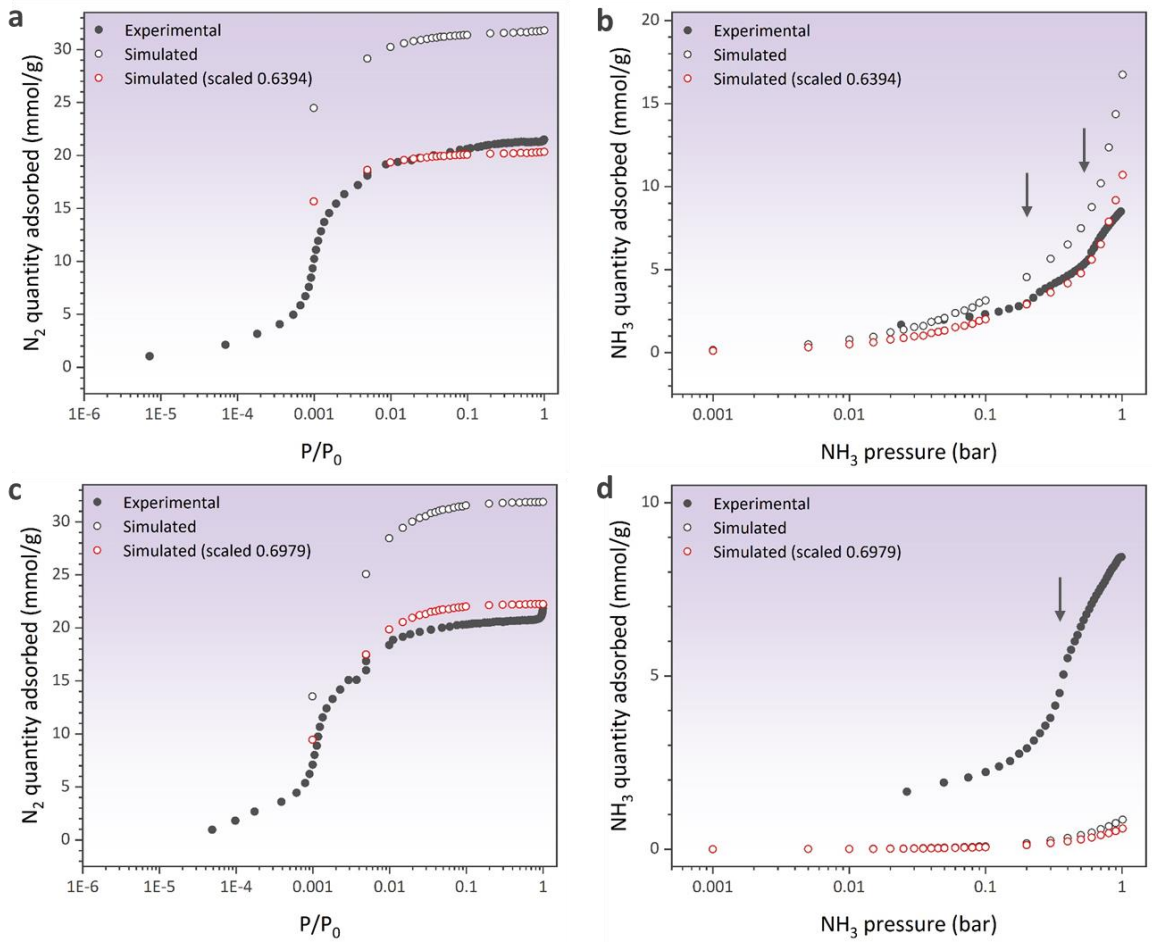

Figure 5.24 | Comparison of experimental and simulated adsorption isotherms computed by GCMC: adsorption isotherms of defective UiO-67 for N_2 up to P/P_0= 1 at 77 K (**a**) and NH_3 at 298 K **(b**) and those of defective UiO-bpydc for N_2 up to P/P_0= 1 at 77 K (**c**) and NH_3 at 298 K (**d**). Filled and Open circles refer to the experimental and the simulated data, respectively. Red circles represent the simulated isotherms with particular scaling factors. Arrows denote the stepped adsorption pressures.

According to Figures 5.24a and 5.24b, when applying a scaling factor of 0.6394, the simulated adsorption isotherms of defective UiO-67 up to P/P_0= 1 for N_2 at 77 K and for NH_3 at 298 K match well with the experimental data with a slight under-prediction below 0.1 bar. Two distinct stepped NH_3 adsorption transitions at the pressures of ca. 0.2 and 0.65

bar strongly support the sequential pore fillings of NH_3 into the non-monodispersed pore windows created by missing linker defects as discussed in Chapter 3. However, the current GCMC simulations for the adsorption of N_2 and NH_3 in UiO-bpydc are unable to show a good agreement with the observed adsorption isotherms (Figures 5.24c and 5.24d). I speculate that the influence of H-bond interactions between the NH_3 and the bpydc linker at the interconnected trigonal pore window leading to modification of the pore structure might be the case and should be taken into consideration. Applying multiple models with different pore accessibility [15, 40-41] may be worth trying to improve the simulations.

Despite the preliminary data analysis, we can conclude from the above results that the difference between responsive behaviours of UiO-67 and UiO-bpydc induced by NH_3 adsorption stems not only from non-uniform pore openings created by missing linkers, but also the binding interactions between the NH_3 and the host structures that can strongly affect the linker dynamics of the MOF framework. Future study may involve the improvement of GCMC simulations as well as application of MD simulations to get the computed results comparable to the experimental data. Determination of self-diffusion coefficient (D_s) of NH_3 derived from mean-squared displacement (MSD) plots would be useful to explore the loading-dependence of D_s of NH_3 due to preferred host-guest interactions, especially the H-bonding network formed at the pore openings of the host structures. Change in molecular diffusion as a result of NH_3 agglomeration in the pore (e.g. pore filling by NH_3) could be larger in the UiO-67 framework as a result of weaker host-guest interactions, but less significant in the N-containing UiO-bpydc framework where H-bonding network could suppress the self-diffusion of NH_3. MD trajectories of NH_3 distribution at particular time scale upon progressive loadings in the defective frameworks would generate useful information. In particular, I would like to further verify whether NH_3 molecules preferably

localise at the trigonal window, at the lozenge window created by missing linker defects, or inside the trigonal window before and after the stepped adsorption transition.

5.3) Chapter summary

In summary, by using advanced inelastic and quasi-elastic neutron scattering techniques in conjunction with computational calculations, the dynamics and kinetics of NH_3 confined in defect-rich UiO-67-type MOFs as a fundamental linkage to stepwise adsorption have been comprehensively investigated. INS study reveals that the lattice dynamics of the host framework especially the linker rotation are clearly suppressed by NH_3 adsorption. This guest-induced linker stiffening is more prominent in UiO-bpydc, indicating stronger host-guest interaction due to evolution of H bonding network between the NH_3 and the bpydc linker as previously evidenced by NPD data. Moreover, analysis of INS difference spectra can remarkably establish the heterogeneous dynamical features of the trapped NH_3 depending on MOF functionality and gas loading. For UiO-67, the well-ordered NH_3 molecules first adsorbed at μ_3-OH is much readily to undergo progressive interactions with the incoming NH_3 molecules. This is reflected by the broadening of the INS spectra associated to such primarily adsorbed NH_3 with increasing NH_3 uptake. This result further confirms that, unlike UiO-bpydc, UiO-67 exhibits greater pore accessibility for NH_3 inclusion largely due to the lack of H-bond network at the trigonal window that could impede NH_3 entering into the inner pores. Considering the QENS data analysis, negligible mobility of NH_3 in both MOFs at the lowest dosage has been observed reflecting the localised diffusion of initial NH_3 sites strongly bound to μ_3-OH of the frameworks. Excitingly, distinct diffusive behaviours of the confined NH_3 occur when increasing the NH_3 adsorption implying that NH_3 molecules experience different pore environments. Although further

interpretation is required, this initial observation provides importance evidence for future computational studies to get deeper insight into a correlation between the NH_3 diffusivity in confined space and the corresponding guest-induced stepwise adsorption behaviours. Overall, this mechanistic study advances the understanding of not only the dynamic interactions between the defect-rich MOF hosts and the progressively adsorbed NH_3, but the NH_3 mobility inside these non-uniform porous structures which can contribute to the rational design of next-generation stimuli-responsive materials.

5.4) References

1. Easun, T. L.; Moreau, F.; Yan, Y.; Yang, S.; Schröder, M., Structural and Dynamic Studies of Substrate Binding in Porous Metal–Organic Frameworks. *Chemical Society Reviews* **2017,** *46* (1), 239-274.
2. Sato, H.; Kosaka, W.; Matsuda, R.; Hori, A.; Hijikata, Y.; Belosludov, R. V.; Sakaki, S.; Takata, M.; Kitagawa, S., Self-Accelerating CO Sorption in a Soft Nanoporous Crystal. *Science* **2014,** *343* (6167), 167.
3. Krause, S.; Bon, V.; Senkovska, I.; Stoeck, U.; Wallacher, D.; Többens, D. M.; Zander, S.; Pillai, R. S.; Maurin, G.; Coudert, F.-X.; Kaskel, S., A Pressure-Amplifying Framework Material with Negative Gas Adsorption Transitions. *Nature* **2016,** *532*, 348.
4. Gu, C.; Hosono, N.; Zheng, J.-J.; Sato, Y.; Kusaka, S.; Sakaki, S.; Kitagawa, S., Design and Control of Gas Diffusion Process in a Nanoporous Soft Crystal. *Science* **2019,** *363* (6425), 387.
5. Horcajada, P.; Serre, C.; Maurin, G.; Ramsahye, N. A.; Balas, F.; Vallet-Regí, M.; Sebban, M.; Taulelle, F.; Férey, G., Flexible Porous Metal-Organic Frameworks for a Controlled Drug Delivery. *Journal of the American Chemical Society* **2008,** *130* (21), 6774-6780.
6. Chen, Q.; Chang, Z.; Song, W.-C.; Song, H.; Song, H.-B.; Hu, T.-L.; Bu, X.-H., A Controllable Gate Effect in Cobalt(II) Organic Frameworks by Reversible Structure Transformations. *Angewandte Chemie International Edition* **2013,** *52* (44), 11550-11553.
7. Yanai, N.; Kitayama, K.; Hijikata, Y.; Sato, H.; Matsuda, R.; Kubota, Y.; Takata, M.; Mizuno, M.; Uemura, T.; Kitagawa, S., Gas Detection by Structural Variations of Fluorescent Guest Molecules in a Flexible Porous Coordination Polymer. *Nature Materials* **2011,** *10* (10), 787-793.
8. Mitchell, P. C. H., *Vibrational Spectroscopy with Neutrons : with Applications in Chemistry, Biology, Materials Science and Catalysis*. World Scientific: New Jersey

London, 2005.

9. Armstrong, J.; O'Malley, A. J.; Ryder, M. R.; Butler, K. T., Understanding Dynamic Properties of Materials Using Neutron Spectroscopy and Atomistic Simulation. *Journal of Physics Communications* **2020,** *4* (7), 072001.

10. Yang, S.; Ramirez-Cuesta, A. J.; Newby, R.; Garcia-Sakai, V.; Manuel, P.; Callear, S. K.; Campbell, S. I.; Tang, C. C.; Schröder, M., Supramolecular Binding and Separation of Hydrocarbons within a Functionalized Porous Metal–Organic Framework. *Nature Chemistry* **2015,** *7* (2), 121-129.

11. Yang, S.; Sun, J.; Ramirez-Cuesta, A. J.; Callear, S. K.; David, W. I. F.; Anderson, D. P.; Newby, R.; Blake, A. J.; Parker, J. E.; Tang, C. C.; Schröder, M., Selectivity and Direct Visualization of Carbon Dioxide and Sulfur Dioxide in a Decorated Porous Host. *Nature Chemistry* **2012,** *4*, 887.

12. Han, X.; Godfrey, H. G. W.; Briggs, L.; Davies, A. J.; Cheng, Y.; Daemen, L. L.; Sheveleva, A. M.; Tuna, F.; McInnes, E. J. L.; Sun, J.; Drathen, C.; George, M. W.; Ramirez-Cuesta, A. J.; Thomas, K. M.; Yang, S.; Schröder, M., Reversible Adsorption of Nitrogen Dioxide within a Robust Porous Metal–Organic Framework. *Nature Materials* **2018,** *17* (8), 691-696.

13. Jan Peter Embs, F. J., Rolf Hempelmann, Introduction to Quasielastic Neutron Scattering. *Zeitschrift für Physikalische Chemie* **2010,** *224*, 28.

14. Salles, F.; Jobic, H.; Ghoufi, A.; Llewellyn, P. L.; Serre, C.; Bourrelly, S.; Férey, G.; Maurin, G., Transport Diffusivity of CO_2 in the Highly Flexible Metal–Organic Framework MIL-53(Cr). *Angewandte Chemie International Edition* **2009,** *48* (44), 8335-8339.

15. Zhao, P.; Fang, H.; Mukhopadhyay, S.; Li, A.; Rudić, S.; McPherson, I. J.; Tang, C. C.; Fairen-Jimenez, D.; Tsang, S. C. E.; Redfern, S. A. T., Structural Dynamics of a Metal–Organic Framework Induced by CO_2 Migration in Its Non-Uniform Porous Structure. *Nature Communications* **2019,** *10* (1), 999.

16. Wu, H.; Chua, Y. S.; Krungleviciute, V.; Tyagi, M.; Chen, P.; Yildirim, T.; Zhou, W., Unusual and Highly Tunable Missing-Linker Defects in Zirconium Metal–Organic Framework UiO-66 and Their Important Effects on Gas Adsorption. *Journal of the American Chemical Society* **2013,** *135* (28), 10525-10532.

17. Gutov, O. V.; Hevia, M. G.; Escudero-Adán, E. C.; Shafir, A., Metal–Organic Framework (MOF) Defects under Control: Insights into the Missing Linker Sites and Their Implication in the Reactivity of Zirconium-Based Frameworks. *Inorganic Chemistry* **2015,** *54* (17), 8396-8400.

18. Fang, Z.; Bueken, B.; De Vos, D. E.; Fischer, R. A., Defect-Engineered Metal–Organic Frameworks. *Angewandte Chemie International Edition* **2015,** *54* (25), 7234-7254.

19. Cheng, Y. Q.; Daemen, L. L.; Kolesnikov, A. I.; Ramirez-Cuesta, A. J., Simulation of Inelastic Neutron Scattering Spectra Using OCLIMAX. *Journal of Chemical Theory and Computation* **2019,** *15* (3), 1974-1982.

20. Jmol: an Open-Source Java Viewer for Chemical Structures in 3D. http://www.jmol.org/.

21. Johnson, M. R.; Trommsdorff, H. P., Vibrational Spectra of Crystalline Formic and Acetic Acid Isotopologues by Inelastic Neutron Scattering and Numerical Simulations. *Chemical Physics* **2009,** *355* (2), 118-122.

22. Chavan, S.; Vitillo, J. G.; Gianolio, D.; Zavorotynska, O.; Civalleri, B.; Jakobsen, S.; Nilsen, M. H.; Valenzano, L.; Lamberti, C.; Lillerud, K. P.; Bordiga, S., H_2 Storage in Isostructural UiO-67 and UiO-66 MOFs. *Physical Chemistry Chemical Physics* **2012,** *14* (5), 1614-1626.

23. Kusaka, S.; Nakajima, Y.; Hori, A.; Yonezu, A.; Kikushima, K.; Kosaka, W.; Ma, Y.; Matsuda, R., Molecular Motion in the Nanospace of MOFs uponG Adsorption Investigated by *in situ* Raman Spectroscopy. *Faraday Discussions* **2021**.

24. Lu, Z.; Godfrey, H. G. W.; da Silva, I.; Cheng, Y.; Savage, M.; Tuna, F.; McInnes, E. J. L.; Teat, S. J.; Gagnon, K. J.; Frogley, M. D.; Manuel, P.; Rudić, S.; Ramirez-Cuesta, A. J.; Easun, T. L.; Yang, S.; Schröder, M., Modulating Supramolecular Binding of Carbon Dioxide in a Redox-Active Porous Metal-Organic Framework. *Nature Communications* **2017,** *8* (1), 14212.

25. Binbrek, O. S.; Anderson, A., Raman Spectra of Molecular cCrystals. Ammonia and 3-Deutero-Ammonia. *Chemical Physics Letters* **1972,** *15* (3), 421-427.

26. Rieth, A. J.; Hunter, K. M.; Dincă, M.; Paesani, F., Hydrogen Bonding Structure of Confined Water Templated by a Metal-Organic Framework with Open Metal Sites. *Nature Communications* **2019,** *10* (1), 4771.

27. Telling, M. T. F.; Andersen, K. H., Spectroscopic Characteristics of the OSIRIS Near-Backscattering Crystal Analyser Spectrometer on the ISIS Pulsed Neutron Source. *Physical Chemistry Chemical Physics* **2005,** *7* (6), 1255-1261.

28. Mukhopadhyay, S.; Hewer, B.; Howells, S.; Markvardsen, A., A modern Approach to QENS Data Analysis in Mantid. *Physica B: Condensed Matter* **2019,** *563*, 41-49.

29. Silverwood, I. P., SAPO-34 Framework Contraction on Adsorption of Ammonia: A Neutron Scattering Study. *ChemPhysChem* **2019,** *20* (13), 1747-1751.

30. Singwi, K. S.; Sjölander, A., Diffusive Motions in Water and Cold Neutron Scattering. *Physical Review* **1960,** *119* (3), 863-871.

31. Volino, F.; Perrin, J.-C.; Lyonnard, S., Gaussian Model for Localized Translational Motion: Application to Incoherent Neutron Scattering. *The Journal of Physical Chemistry B* **2006,** *110* (23), 11217-11223.

32. O'Malley, A. J.; Sarwar, M.; Armstrong, J.; Catlow, C. R. A.; Silverwood, I. P.; York, A. P. E.; Hitchcock, I., Comparing Ammonia Diffusion in NH_3-SCR Zeolite Catalysts: a Quasielastic Neutron Scattering and Molecular Dynamics Simulation Study. *Physical Chemistry Chemical Physics* **2018,** *20* (17), 11976-11986.

33. Bée, M., *Quasielastic Neutron Scattering : Principles and Applications in Solid State Chemistry, Biology, and Materials Science*. Adam Hilger: Bristol, 1988.

34. Volino, F.; Dianoux, A. J., Neutron Incoherent Scattering Law for Diffusion in a Potential of Spherical Symmetry: General Formalism and Application to Diffusion inside a Sphere. *Molecular Physics* **1980,** *41* (2), 271-279.

35. Dubbeldam, D.; Calero, S.; Ellis, D. E.; Snurr, R. Q., RASPA: Molecular Simulation Software for Adsorption and Diffusion in Flexible Nanoporous Materials. *Mol Simulat* **2016,** *42* (2), 81-101.

36. Sarkisov, L.; Harrison, A., Computational Structure Characterisation Tools in Application to Ordered and Disordered Porous Materials. *Molecular Simulation* **2011,** *37* (15), 1248-1257.

37. Potoff, J. J.; Siepmann, J. I., Vapor–Liquid Equilibria of Mixtures Containing Alkanes, Carbon Dioxide, and Nitrogen. *Aiche J* **2001,** *47* (7), 1676-1682.

38. Mayo, S. L.; Olafson, B. D.; Goddard, W. A., DREIDING: a Generic Force Field for Molecular Simulations. *Journal of Physical chemistry* **1990,** *94* (26), 8897-8909.

39. Rappé, A. K.; Casewit, C. J.; Colwell, K.; Goddard Iii, W.; Skiff, W., UFF, a Full Periodic Table Force Field for Molecular Mechanics and Molecular Dynamics Simulations. *Journal of the American chemical society* **1992,** *114* (25), 10024-10035.

40. Du, Y.; Wooler, B.; Nines, M.; Kortunov, P.; Paur, C. S.; Zengel, J.; Weston, S. C.; Ravikovitch, P. I., New High- and Low-Temperature Phase Changes of ZIF-7: Elucidation and Prediction of the Thermodynamics of Transitions. *Journal of the American Chemical Society* **2015,** *137* (42), 13603-13611.

41. Fairen-Jimenez, D.; Moggach, S. A.; Wharmby, M. T.; Wright, P. A.; Parsons, S.; Düren, T., Opening the Gate: Framework Flexibility in ZIF-8 Explored by Experiments and Simulations. *Journal of the American Chemical Society* **2011,** *133* (23), 8900-8902.

Chapter 6

Conclusion and Future Perspectives

6.1) Conclusion

This thesis presents detailed investigation of stimuli-responsive behaviours to account for stepwise NH_3 adsorption in the defect-rich Zr-based metal-organic frameworks (MOFs), namely UiO-67 and its isostructural UiO-bpydc, by using the combined experimental and theoretical approaches. Structural and dynamics features of the NH_3-MOF systems induced by the intrinsic factors including surface pore functionality, linker flexibility, and non-uniform porosity created by missing linker defects and the extrinsic stimuli such as gas dosage and temperature have been comprehensively explored.

Chapter 3 first describes the structural responses of UiO-67 and UiO-bpydc containing missing linker defects toward NH_3 adsorption based on their *in situ* crystallographic data measured by high-resolution NPD and Rietveld refinement in conjunction with theoretical studies by DFT calculations. ND_3 was used in the NPD experiments to minimise the incoherent scattering from H atoms. It is demonstrated that the different pore openings (windows) induced by missing linkers can introduce stepped and hysteresis NH_3 sorption in UiO-type MOFs. Despite their structural similarities, the distinctive alteration of stepwise adsorption profiles is clearly observed when biphenyl dicarboxylate linkers in UiO-67 are replaced by the bipyridine dicarboxylate analogues. Based on the refined crystal structures, a H-bonding network of six ND_3 molecules (two crystallographically independent sites) with the three bipyridine linkers around the trigonal window of UiO-bpydc can be formed. This host-guest configuration attains the highest

binding energy against other configurations at the trigonal window, as shown by DFT. The adsorption transition thus stems from the steric hindrance of H-bond networks between the bipyridine scaffold and the adsorbed NH_3 molecules, forcing the linkers to adopt a planar geometry to block up the pore and hence making the NH_3-loaded structure rigid without major change in pore volume and unit cell parameters.

Inspired by the unusual NH_3-responsive behaviours in the defective UiO-67- type MOFs, their temperature-dependent study has been further investigated and presented in Chapter 4. The same methodology including *in situ* NPD and Rietveld refinement supported by DFT calculations has been used to gain deeper insights into the adsorption mechanism of these NH_3-loaded frameworks. It is exciting to see that while the NPD patterns of the ND_3-loaded UiO-67 dramatically alter under different measurement temperatures (298 and 7 K), those of the ND_3-loaded UiO-bpydc surprisingly remains constant. This observation suggests the higher rigidity (i.e. less flexibility) of the UiO-bpydc linkers induced by H-bond interactions with the trapped ND_3 molecules, hence inhibiting a linker flipping upon thermal motion. This hypothesis is supported by the refined torsional angles of the MOF linkers derived from the NPD data. Specifically, the dihedral angle between two aromatic rings of the UiO-bpydc linker becomes flattened as a function of ND_3 loading in order to maximise the H bonding interaction with the adsorbed ND_3 and hence hindering the pore accessibility under the designated temperature range. Further DFT study of the rotational energy barriers of the simplified MOF-NH_3 models also reveals the NH_3-induced rigidity in the UiO-bpydc linker, in excellent agreement with the NPD results. Clearly, the flexibility of the linkers is tunable by NH_3 loading and temperature applied to this system and the presence of bipyridine linkers suppresses the flipping of the biphenyl dihedral angle over the whole temperature regime.

Finally, Chapter 5 studies the host-guest interactions between NH_3 molecules and defective UiO-67 and UiO-bpydc as a function of NH_3 loading by using high-resolution INS and QENS joint with computational calculations. The results reveal that the lattice vibrational modes of the host frameworks associated to the linker rotations are drastically hindered upon NH_3 dosing. This guest-induced linker stiffening is more prominent in the UiO-bpydc, suggesting the stronger host-guest interactions as a result of H bond network between the NH_3 and the bpydc linker. Moreover, heterogeneity in vibrational modes of the trapped NH_3 is clearly observed, which shows a strong dependency toward MOF functionality and gas loading. Despite that the first NH_3 molecule is found to primarily adsorb at the μ_3-OH sites in both MOFs, the one within the UiO-67 framework shows more propensity to undergo progressive interactions with the incoming NH_3 molecules. This is evidenced by the broadening of the INS spectra associated to the pre-adsorbed NH_3 with increasing NH_3 uptake. This result indicates that UiO-67 exhibits greater pore accessibility for NH_3 adsorption due to no steric hindrance caused by H-bond network as contrarily observed in UiO-bpydc. QENS data analysis demonstrates negligible mobility of NH_3 in both MOFs at the lowest dosage, pointing out to the restricted diffusion of strongly adsorbed NH_3 close to μ_3-OH of the frameworks. At elevated NH_3 dosing, where step-like adsorption transitions occur, distinctive diffusive behaviours of the trapped NH_3 are clearly detected. This evidence suggests that the NH_3 molecules experience different pore environments with different host-guest interactions. Further kinetic studies and molecular dynamic simulations are required in order to get a full understanding of the loading-dependent diffusivity that links to the stepwise adsorption phenomena.

Overall, this thesis has elucidated the relationship between structural and dynamics of the defective UiO-67-type MOFs towards external triggers including NH_3 and

temperature. The combined use of advanced diffraction, spectroscopy, and theoretical calculations has yielded important information on preferred binding sites and host-guest interactions at a molecular level which are responsible for the distinctive stepped NH_3 adsorption. This study has also highlighted the impact of molecular bonding interactions induced by external stimuli to lock up or set free motions of the linkers for controlling the responsive behaviours of MOF materials. At the uttermost exciting prospect, the ability to design and optimise the stimuli-responsive properties throughout linker motions enable the development of next generation smart materials for sorption-related applications such as gas separation, controlled drug delivery, and molecular sensing.

6.2) Future Perspectives

Based on the findings presented in this thesis, future research may provide a complement and extension to the current work.

According to the study of diffusive behaviours of confined NH_3 in MOFs by using the combined QENS technique and GCMC simulations, so far I am not yet able to interpret the data in more detail due to the complexity of the studied system where multiple dynamic processes are coupled. Specifically, the diffusion phenomena of molecules within non-uniform pore openings with different binding interactions have not been modelled. In this case, introduction of modern GCMC and MD simulations can substantially support the QENS data analysis. It enables not only qualitative verification of the diffusion derived from the QENS experiments, but also quantitative correlation to the QENS data. [1]Future work may involve improving the current GCMC simulations to get the computed results well matched with the experimental data, then further applying MD simulations. Determination of self-diffusion coefficient (D_s) of NH_3 derived from mean-squared displacement (MSD)

plots would be useful to explore the loading-dependence of D_s of NH_3 due to preferred host-guest interactions, especially the H-bond network forming at the pore openings of the host structures. Alteration in molecular diffusion as a result of NH_3 filling in the pore could be larger in the UiO-67 framework as a result of weaker host-guest interactions, but less significant in the N-containing UiO-bpydc framework where H-bond network could impede the self-diffusion of NH_3. MD trajectories of NH_3 distribution at particular time scales upon progressive loadings in the defective frameworks are worthwhile to collect. In particular, information on preferred locations of NH_3 inside the MOF frameworks before and after the stepped adsorption transitions would be essential to further appreciate the adsorption mechanism.

6.3) Reference

1. Armstrong, J.; O'Malley, A. J.; Ryder, M. R.; Butler, K. T., Understanding Dynamic Properties of Materials Using Neutron Spectroscopy and Atomistic Simulation. *Journal of Physics Communications* **2020,** *4* (7), 072001.

Appendices

A) Appendices for Chapter 3

CCDC 2047200, 2047201, 2047202, 2047203, 2047204, and 2047205 contain the supplementary crystallographic data for this paper. The data can be obtained free of charge from The Cambridge Crystallographic Data Centre via www.ccdc.cam.ac.uk/structures. A list of the crystal structures obtained from the Rietveld refinements of the NPD data at 300 K and their corresponding CCDC Deposition numbers is given below;

CCDC 2047200: UiO-67 with the first ND_3 loading

CCDC 2047201: UiO-67 with the third ND_3 loading

CCDC 2047202: UiO-bpydc with the first ND_3 loading

CCDC 2047203: UiO-bpydc with the second ND_3 loading

CCDC 2047204: UiO-bpydc with the third ND_3 loading

CCDC 2047205: UiO-67 with the second ND_3 loading

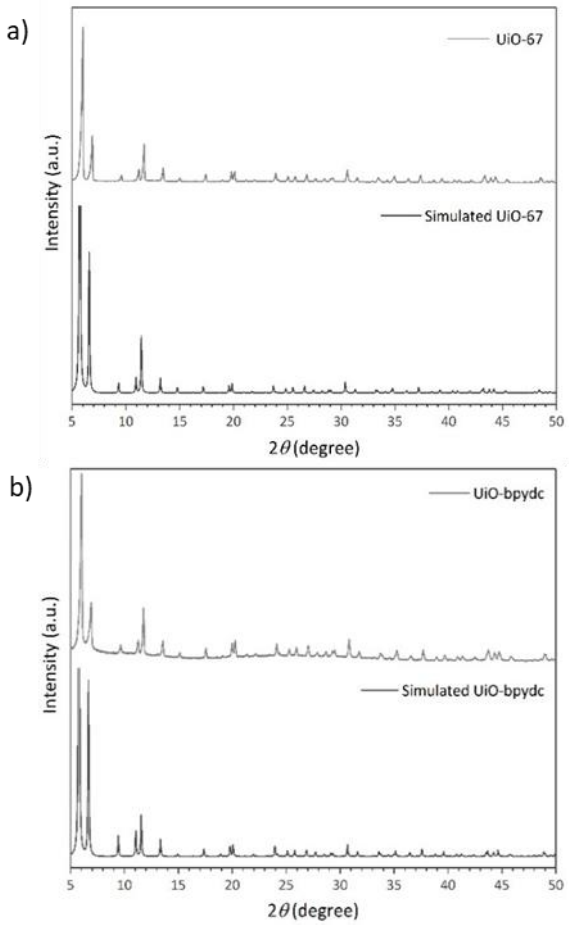

Figure A3.1 | Powder XRD patterns of UiO-67 (a) and UiO-bpydc (b) along with their corresponding diffraction patterns obtained from the literature.[1-2] Note that the simulated patterns are derived from single-crystal diffraction data of the solvated samples. Thus, inclusion of the disordered solvent molecules such as water or *N,N*-dimethylformamide in the crystals as well as structural defects in powdered samples could cause the differences in peak intensities compared to the observed diffraction patterns.

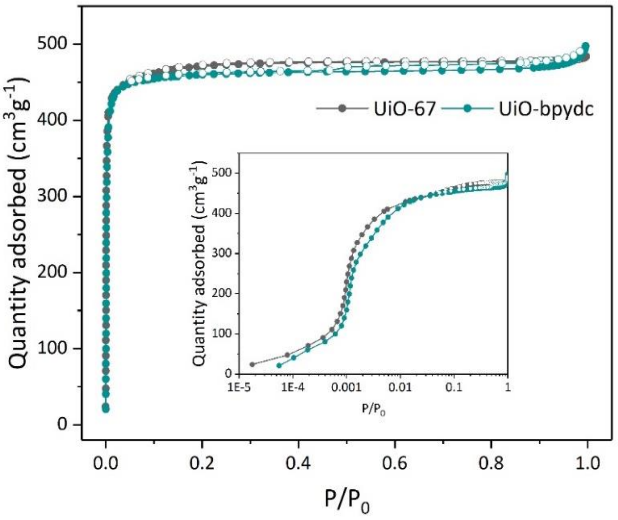

Figure A3.2 | N_2 physisorption isotherms of activated samples at 77 K. The isotherms indicate the typical microporous structures. Inset is the isotherms plotted in semi-log scale at low relative pressure. The isotherms of UiO-67 and UiO-bpydc show a slight step at ca. 0.1 P/P_o due to the presence of two types of pore windows. BET specific surface area and pore volume of UiO-67 and UiO-bpydc are 1916 m^2/g, 0.75 cm^3/g and 1953 m^2/g, 0.76 cm^3/g, respectively.

Table A3.1 | Corresponding missing linkers of the MOF samples derived from the elemental analyses and ICP-MS techniques.

Sample	**Numbers of missing linker (x) per formula unit**	**Actual formula $Zr_6O_4(OH)_4(bpdc)_{6-x}(acetate)_{2x}$**
UiO-67	2.0 ± 0.5	$Zr_6O_4(OH)_4(bpdc)_4(acetate)_4$
UiO-67-healed	0.0± 0.5	$Zr_6O_4(OH)_4(bpdc)_6$
UiO-bpydc	1.5 ± 0.5	$Zr_6O_4(OH)_4(bpydc)_{4.5}(acetate)_3$

Sample	Numbers of missing linker (x) per formula unit	Actual formula $Zr_6O_4(OH)_4(bpdc)_{6-x}(acetate)_{2x}$
UiO-bpydc-healed	0.8 ± 0.5	$Zr_6O_4(OH)_4(bpydc)_{5.2}(acetate)_{1.6}$

Note: Six linkers per formula unit is equivalent to twelve linkers coordinated to each metal node. The analysed samples were from different batches with respect to those used in the TGA experiments.

Table A3.2 | Corresponding missing linkers of the MOF samples obtained from the TGA results.

Sample	Weight loss (%) between 350 and 600 °C	Numbers of missing linker (x) per formula unit	Actual formula $Zr_6O_4(OH)_4(bpdc)_{6-x}(acetate)_{2x}$
UiO-bpydc	61.2	1.8 ± 0.3	$Zr_6O_4(OH)_4(bpydc)_{4.2}(acetate)_{3.6}$
UiO-bpydc-healed	63.3	1.4 ± 0.3	$Zr_6O_4(OH)_4(bpydc)_{4.6}(acetate)_{2.8}$

Note: Six linkers per formula unit is equivalent to twelve linkers coordinated to each metal node.

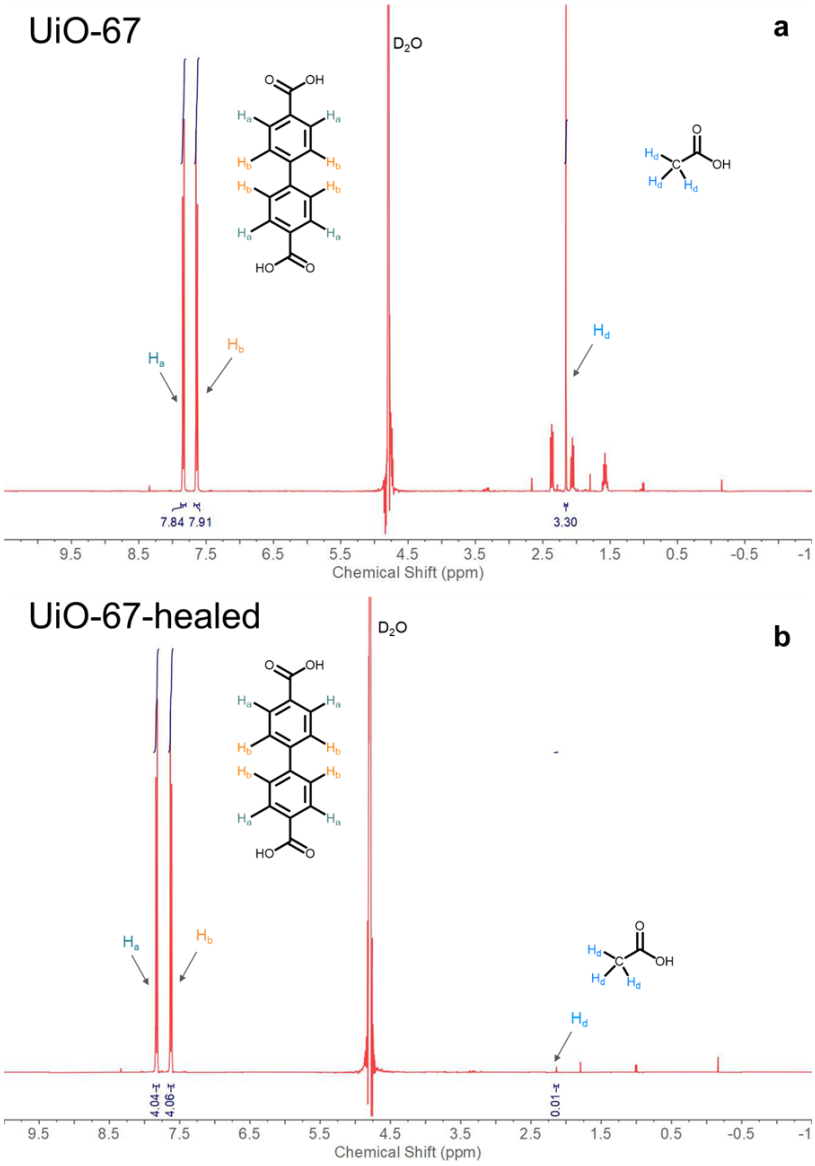

Figure A3.3 | ^{1}H NMR spectra of aliquots from the UiO-67 (**a**) and UiO-67-healed (**b**) in 0.1 M NaOH in D_2O at 298 K. The chemical shift of H_2bpdc linker: δ 7.88 – 7.79 (m, 4H), 7.66 – 7.58 (m, 4H) and acetic acid: δ 2.16 (s, 3H).

The above ^{1}H NMR results reveal the presence of acetic acid in the unhealed sample (**a**) indicating that missing linker defects are feasibly terminated by acetates. After the healing process (**b**), the signal from acetic acid almost disappears implying the completion of linker exchange with H_2bpdc.

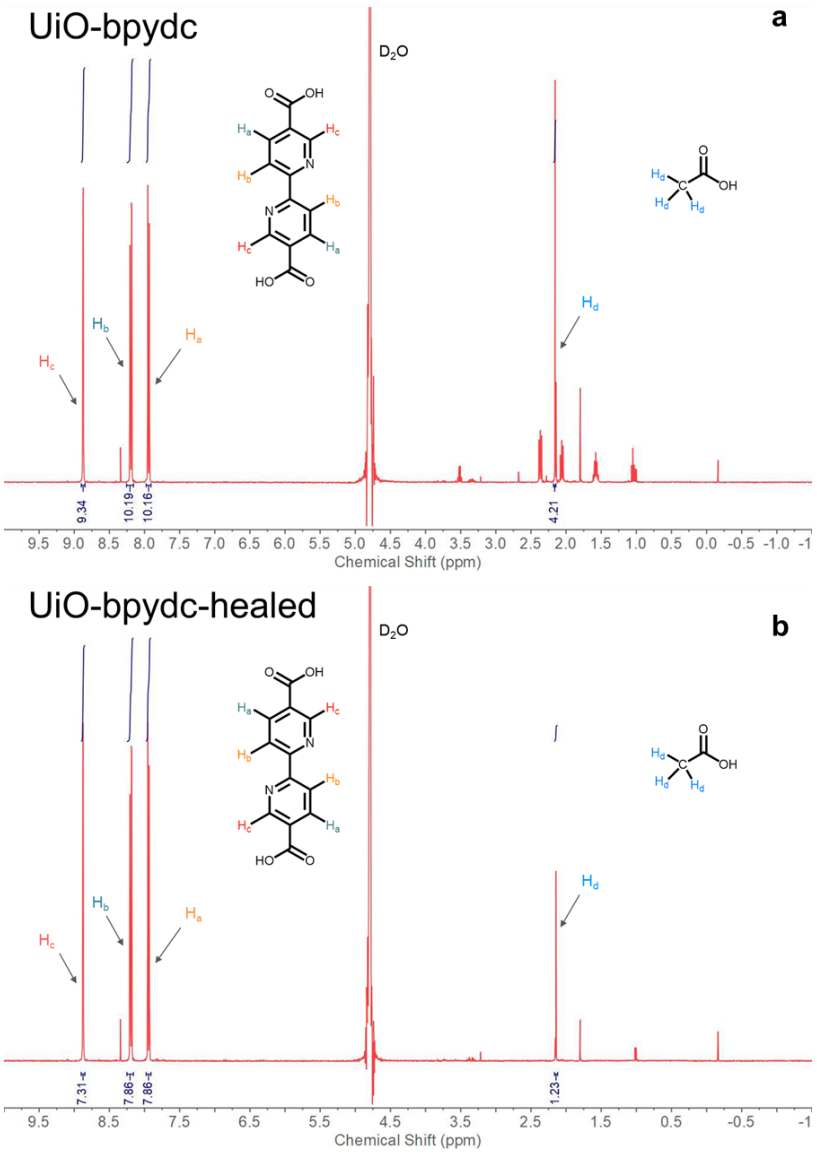

Figure A3.4 | ^{1}H NMR spectra of aliquots from the UiO-bpydc (**a**) and UiO-bpydc-healed (**b**) in 0.1 M NaOH in D_2O at 298 K. The chemical shift of H_2bpydc linker: δ 8.87 (dd, 2H), 8.20 (dd, 2H), 7.94 (dd, 2H) and acetic acid: δ 2.16 (s, 3H).

The above ^{1}H NMR results show the presence of acetic acid in the unhealed sample (**a**) indicating that missing linker defects are feasibly terminated by acetates. After the healing treatment (**b**), a drastic decrease of the signal from acetic acid is observed suggesting that most of the defect capping acetates are substituted by H_2bpydc linkers.

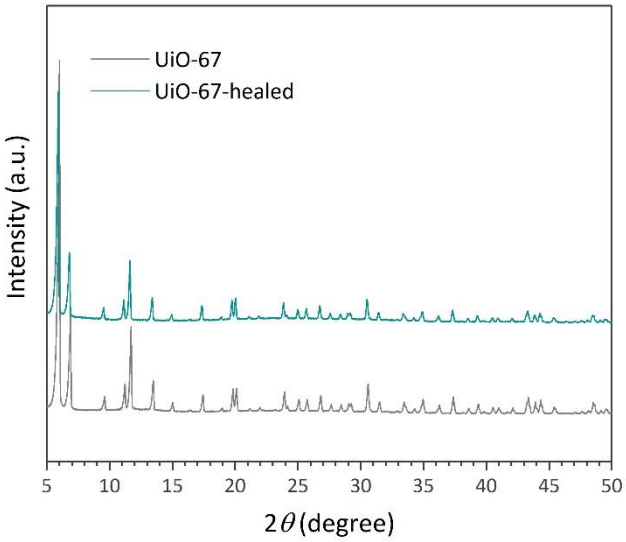

Figure A3.5 | Powder XRD patterns of UiO-67 samples before and after the healing process.

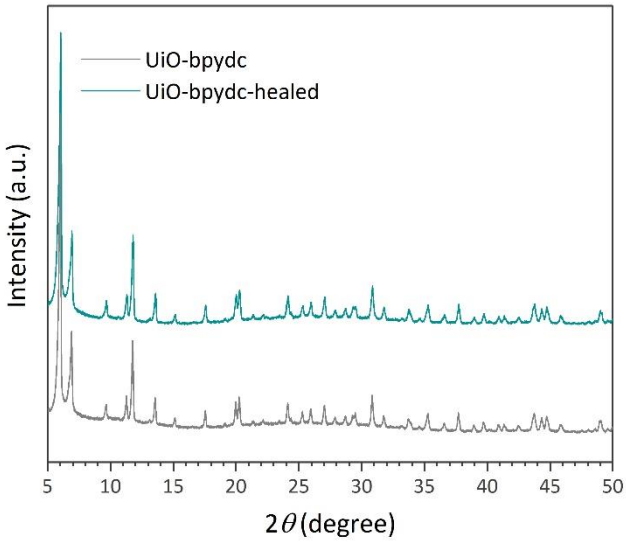

Figure A3.6 | Powder XRD patterns of UiO-bpydc samples before and after the healing process.

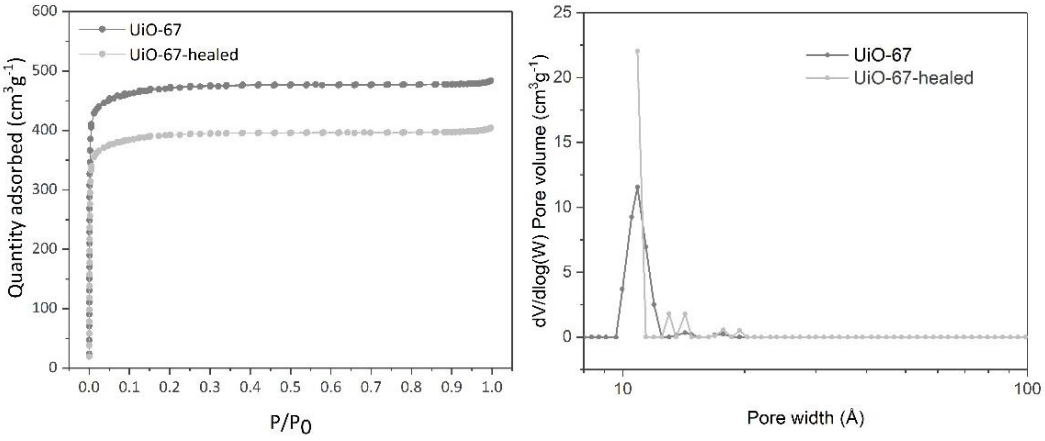

Figure A3.7 | N_2 sorption profiles and pore size distribution of UiO-67 samples before and after the healing process. The BET specific surface area and pore volume are changed from 1916 m^2/g, 0.75 cm^3/g to 1961 m^2/g, 0.72 cm^3/g, respectively. Pore size distribution (PSD) was examined by DFT embedded in a Micromeritics software. A model used in the PSD analysis is based on a slit-type pore structure with carbon surface.

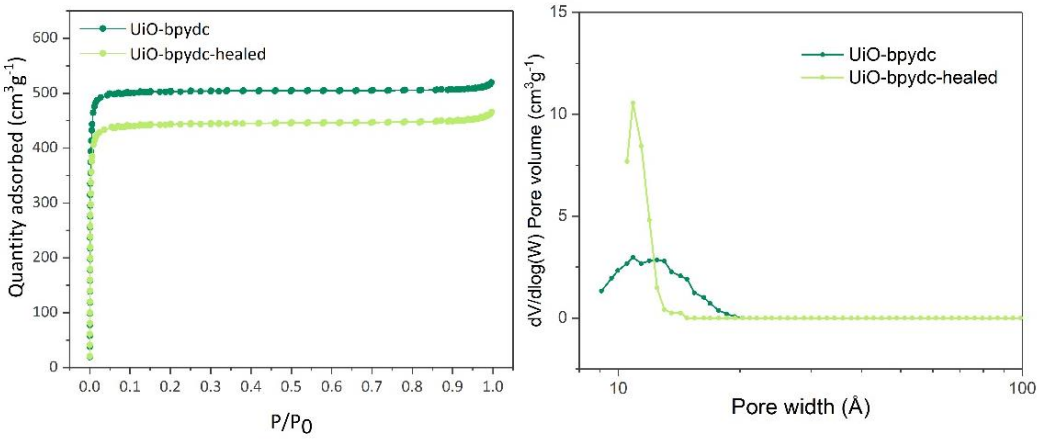

Figure A3.8 | N_2 sorption profiles and pore size distribution of UiO-bpydc samples before and after the healing process. The BET specific surface area and pore volume are changed from 1953 m^2/g, 0.76 cm^3/g to 1948 m^2/g, 0.72 cm^3/g, respectively. Pore size distribution (PSD) was examined by DFT method embedded in a Micromeritics software. A model used in the PSD analysis is based on a slit-type pore structure with carbon surface.

The non-uniform porous structure is due to the non-monodisperse pore structure created by missing linker defects as indicated by pore size distribution (PSD) analyses (see Figures A3.7 and A3.8). The defective MOF samples show broad PSD whereas their corresponding samples after the healing process (ligand exchange) have much smaller PSD centred at 11 Å. This result imply that the non-monodisperse pore structures of the defect-rich UiO-67 type MOFs in this work is caused by the missing linker defects. Similar PSD analyses of UiO-67 can be also found in Ref [3].

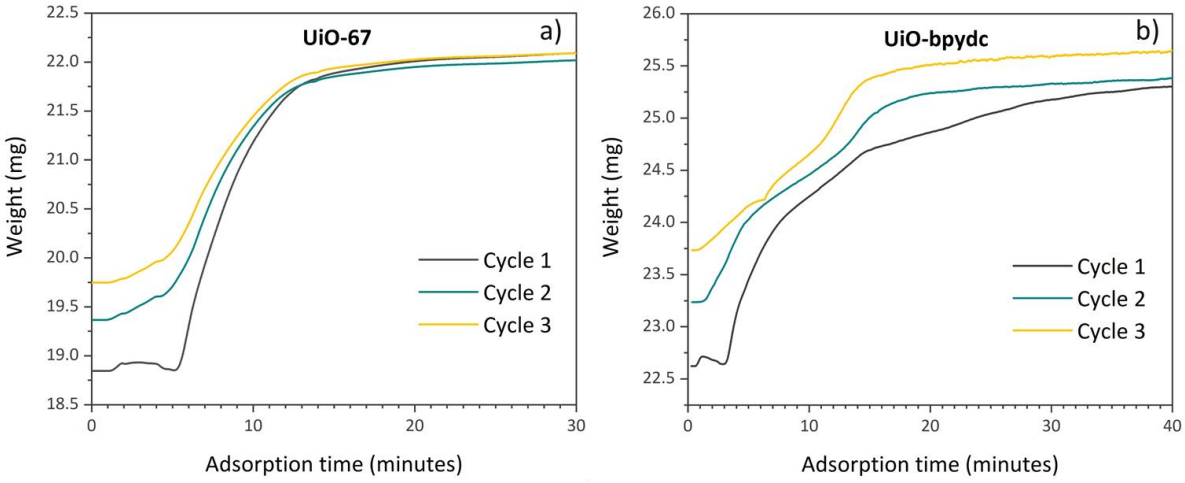

Figure A3.9 | Stability tests of UiO-67 (a) and UiO-bpydc (b) for NH_3 uptake, measured by repeated gravimetric analysis. The adsorption temperature and the maximum NH_3 pressure used were 298 K and 600 mbar, respectively.

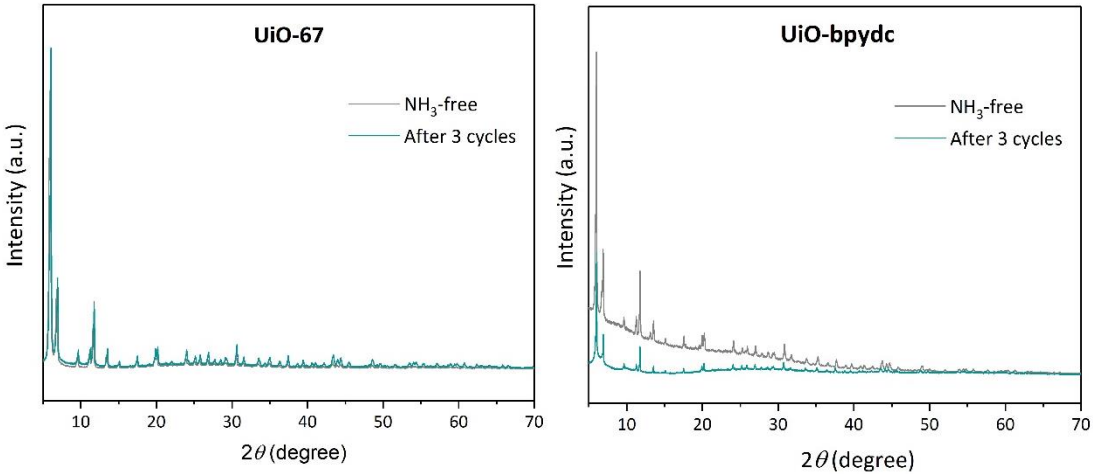

Figure A3.10 | Powder XRD patterns of defective Zr-based MOFs before and after three cycles of NH_3 adsorption at 298 K and up to 600 mbar of NH_3 pressure, measured by gravimetric analysis

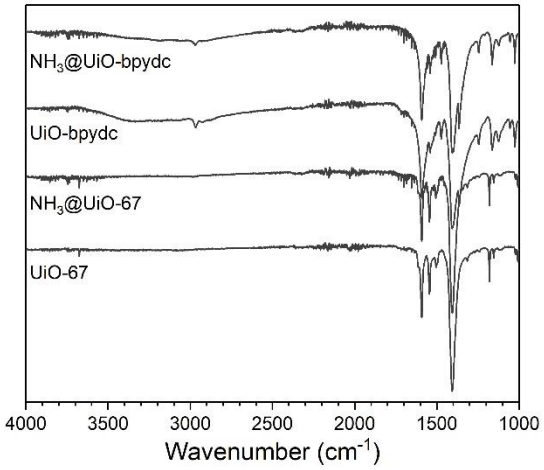

Figure A3.11 | FT-IR spectra of the samples before and after NH_3 adsorption at room temperature. Before the NH_3 adsorption each sample was placed in a bottom flask and activated at 423 K for 24 hrs under vacuum by using a Schlenk line. After being cooled to room temperature, the sample was exposed to NH_3 vapor for 30 mins, sealed tightly and kept in a dry place for one week.

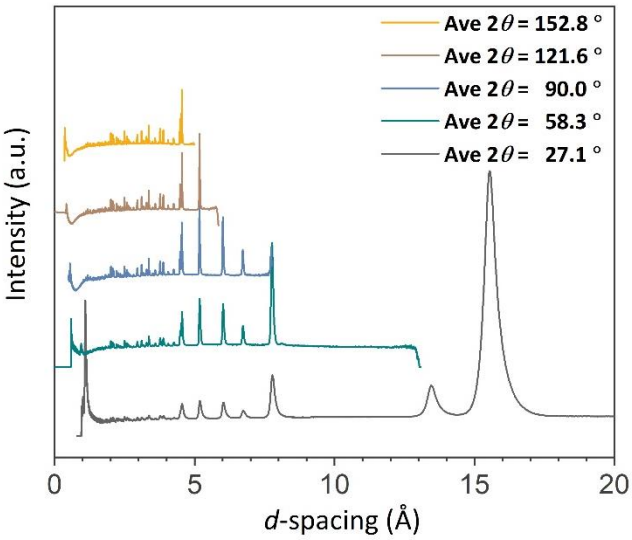

Figure A3.12 | ND patterns of ND_3-free UiO-67 recorded at 300 K by using different detector banks. Ave 2θ refers to the average 2θ of the detector banks.

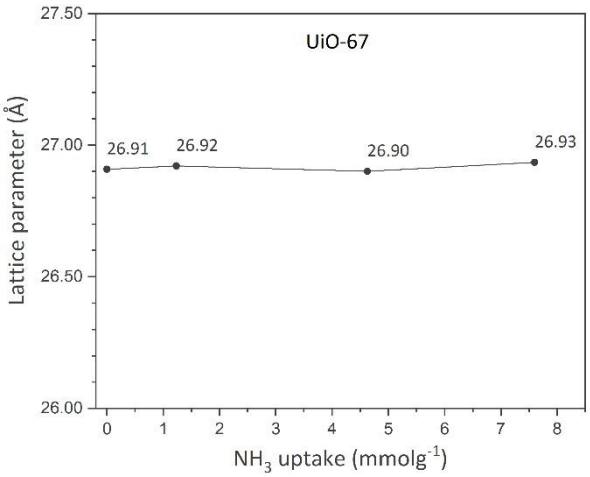

Figure A3.13 | Refined lattice parameters of the NPD data of defective UiO-67 at different ND_3 loadings. The maximum standard deviation value of the refined lattice parameters is ± 7.0 x 10^{-4}

Table A3.3 | *R*-factors and *GOF* values of UiO-67 as a function of ND_3 loading obtained from Rietveld refinement of the associated NPD data recorded at 300 K. UiO-67·*n*ND_3 represents the UiO-67 structure with addition of *n* ND_3 molecule(s) per asymmetric unit. The underlined structures provide the best fit of the refinement

Entry	R_{wp} (%)	R_p (%)	R_{exp} (%)	*GOF*
L= 0.00 at 300 K				
UiO-67	1.77	1.32	0.47	3.79
L= 1.23 at 300 K				
UiO-67	3.14	2.45	0.38	8.26
UiO-67·1ND_3	2.49	1.98	0.38	6.55
UiO-67·2ND_3	2.18	1.84	0.38	5.68
UiO-67·3ND_3	2.47	1.95	0.38	6.50
L= 4.63 at 300 K Mixed phases between *Fm*-3*m* (78.16%) and *Pa*-3 (21.84%)				
UiO-67	5.59	3.56	0.50	11.18
UiO-67·1ND_3	4.42	2.65	0.50	8.84
UiO-67·2ND_3	4.10	2.47	0.50	8.20
UiO-67·3ND_3	3.94	2.34	0.50	7.88
UiO-67·4ND_3	3.43	2.12	0.50	6.86
UiO-67·5ND_3 (*Fm*-3*m*) and UiO-67·1ND_3 (*Pa*-3)	1.81	1.46	0.50	3.63
UiO-67·6ND_3	2.24	1.60	0.50	4.08
L= 7.60 at 300 K Mixed phases between *Fm*-3*m* (78.16%) and *Pa*-3 (21.84%)				
UiO-67	2.91	1.96	0.49	5.96
UiO-67·1ND_3	2.46	1.59	0.49	5.04

Entry	R_{wp} (%)	R_p (%)	R_{exp} (%)	*GOF*
UiO-67·2ND_3	2.14	1.59	0.49	4.39
UiO-67·3ND_3	1.96	1.50	0.49	4.00
UiO-67·4ND_3	1.91	1.51	0.49	3.91
UiO-67·5ND_3 (*Fm*-3*m*) and UiO-67·1ND_3 (*Pa*-3)	1.39	1.09	0.49	2.85
UiO-67·6ND_3	1.50	1.11	0.49	3.06

Table A3.4 | Summary of Rietveld refinement results of ND_3@UiO-67.

	Loading amount of ND_3 (mmol/g)			
	0.00	**1.23**	**4.63**	**7.60**
Site occupancy factor (per asymmetric unit) of ND_3 at				
Site I	-	0.02	0.04	0.15
Site II	-	0.01	0.01	0.19
Site III	-	-	0.01	0.18
Site IV	-	-	0.02	0.04
Site V	-	-	0.02	0.04
Site I-d[a]	-	-	0.01	0.01
Dihedral angle between two aromatic rings (°)	30.60(1)	32.42(1)	55.20(1)	62.63(2)

[a] This site is created by using a distorted phase (i.e. a lower symmetry phase with a *Pa*-3 space group) which indicates the adsorption of ND_3 at the non-uniform binding sites of UiO-67 caused by missing linker defects.

Table A3.5 | Structural data from the Rietveld refinement of UiO-67 sample loaded with 1.23 mmol/g ND_3 (9.65 ND_3 molecules per unit cell).

Species	**Atom**	**x**	**y**	**z**	**SOF**[a]	***B*eq**[b] **(Å²)**	**Wyckoff**
UiO-67	C4	0.3775(1)	0.0000(1)	0.1168(1)	0.5395(1)	5.3657(7)	96j
	C5	0.3382(1)	0.0000(1)	0.1561(1)	0.5395(1)	5.3657(7)	96j
	C10	0.2902(1)	-0.0121(1)	0.1448(1)	0.4826(1)	4.1290(4)	192l
	H10	0.2818(1)	-0.0206(1)	0.1115(1)	0.4826(1)	4.9548(5)	192l
	C9	0.2541(1)	-0.0122(1)	0.1804(1)	0.4826(1)	4.1290(4)	192l
	H9	0.2206(1)	-0.0207(1)	0.1724(1)	0.4826(1)	4.9548(5)	192l
	C8	0.2672(1)	0.0000(1)	0.2271(1)	0.4826(1)	4.1290(4)	96j
	Zr1	0.5000	0.0000	0.0932	1	3.5338(7)	24e
	O2A	0.4465	-0.0535	0.0535	0.5	0.0100(7)	32f
	O2B	0.4594	-0.0406	0.0406	0.5	0.0100(7)	32f
	H1	0.4284	-0.0716	0.0716	0.5	0.0120(8)	32f
	O1	0.4269	0.0000	0.1336	1	5.4939(6)	96j
Ammonia I	N1rg	-0.1114(2)	0.3889(2)	0.1112(2)	0.0153(2)	5.0000(2)	192l
	H1rg	-0.1312(2)	0.4023(2)	0.0816(2)	0.0153(2)	6.0000(3)	192l
	H2rg	-0.1256(2)	0.4057(2)	0.1423(2)	0.0153(2)	6.0000(3)	192l
	H3rg	-0.1230(2)	0.3530(2)	0.1168(2)	0.0153(2)	6.0000(3)	192l
Ammonia II	N2rg	0.3503(1)	-0.0218(1)	0.3766(1)	0.0098(1)	5.0000(2)	192l
	H4rg	0.3572(1)	-0.0328(1)	0.3408(1)	0.0098(1)	6.0000(3)	192l
	H5rg	0.3130(1)	-0.0144(1)	0.3787(1)	0.0098(1)	6.0000(3)	192l
	H6rg	0.3532(1)	-0.0530(1)	0.3983(1)	0.0098(1)	6.0000(3)	192l

[a] B_{eq} refers to the isotropic displacement factor or the thermal parameter.

[b] SOF represents the site occupancy factor per asymmetric unit.

Table A3.6 | Structural data from the Rietveld refinement of UiO-67 sample loaded with 4.63 mmol/g ND_3 (36.3 ND_3 molecules per unit cell). Only the structural data obtained from using the cubic *Fm*-3*m* MOF model (major phase) are presented here.

Species	Atom	x	y	z	SOF[a]	*B*eq[b] (Å^2)	Wyckoff
UiO-67	C4	0.3774(1)	0.0000(1)	0.1168(1)	0.5395(1)	15.000(13)	96j
	C5	0.3381(1)	0.0000(1)	0.1560(1)	0.5395(1)	15.000(13)	96j
	C10	0.2936(1)	-0.0228(1)	0.1482(1)	0.4826(1)	4.2455(7)	192l
	H10	0.2875(1)	-0.0390(1)	0.1172(1)	0.4826(1)	5.0946(9)	192l
	C9	0.2574(1)	-0.0231(1)	0.1837(1)	0.4826(1)	4.2455(7)	192l
	H9	0.2264(1)	-0.0391(1)	0.1781(1)	0.4826(1)	5.0946(9)	192l
	C8	0.2671(1)	0.0000(1)	0.2270(1)	0.4826(1)	4.2455(7)	96j
	Zr1	0.5000	0.0000	0.0932	1	7.8860(13)	24e
	O2A	0.4465	-0.0535	0.0535	0.5	12.151(18)	32f
	O2B	0.4594	-0.0406	0.0406	0.5	12.15118)	32f
	H1	0.4284	-0.0716	0.0716	0.5	14.581(2)	32f
	O1	0.4269	0.0000	0.1336	1	1.3847(7)	96j
Ammonia I	N1rg	-0.1134(2)	0.3864(2)	0.1142(2)	0.0361(2)	3.6561(13)	192l
	H1rg	-0.1377(2)	0.3985(2)	0.0874(2)	0.0361(2)	4.3873(15)	192l
	H2rg	-0.1257(2)	0.4008(2)	0.1473(2)	0.0361(2)	4.3873(15)	192l
	H3rg	-0.1206(2)	0.3494(2)	0.1197(2)	0.0361(2)	4.3873(15)	192l
Ammonia II	N2rg	0.3638(1)	-0.0279(1)	0.3871(1)	0.0071(1)	3.6561(13)	192l
	H4rg	0.3646(1)	-0.0546(1)	0.3510(1)	0.0071(1)	4.3873(15)	192l
	H5rg	0.3278(1)	-0.0258(1)	0.3994(1)	0.0071(1)	4.3873(15)	192l
	H6rg	0.3814(1)	-0.0428(1)	0.4175(1)	0.0071(1)	4.3873(15)	192l
Ammonia III	N3rg	0.9445(2)	1.0300(2)	1.0549(2)	0.0238(2)	3.6561(13)	192l
	H7rg	0.9203(2)	1.0049(2)	1.0702(2)	0.0238(2)	4.3873(15)	192l
	H8rg	0.9659(2)	1.0434(2)	1.0835(2)	0.0238(2)	4.3873(15)	192l
	H9rg	0.9705(2)	1.0099(2)	1.0357(2)	0.0238(2)	4.3873(15)	192l

Species	Atom	x	y	z	SOF[a]	*B*eq[b] (Å^2)	Wyckoff
Ammonia	N4rg	0.1935(2)	0.1984(2)	0.2050(2)	0.0122(2)	3.6561(13)	192l
IV	H10rg	0.2204(2)	0.2191(2)	0.2223(2)	0.0122(2)	4.3873(15)	192l
	H11rg	0.1767(2)	0.2214(2)	0.1797(2)	0.0122(2)	4.3873(15)	192l
	H12rg	0.2116(2)	0.1745(2)	0.1815(2)	0.0122(2)	4.3873(15)	192l
Ammonia	N5rg	2.8167(1)	-0.5892(1)	2.5731(1)	0.0186(1)	3.6561(13)	192l
V	H13rg	2.7941(1)	-0.5962(1)	2.5433(1)	0.0186(1)	4.3873(15)	192l
	H14rg	2.8334(1)	-0.5556(1)	2.5666(1)	0.0186(1)	4.3873(15)	192l
	H15rg	2.7939(1)	-0.5801(1)	2.6022(1)	0.0186(1)	4.3873(15)	192l

[a] B_{eq} refers to the isotropic displacement factor or the thermal parameter.

[b] SOF represents the site occupancy factor per asymmetric unit.

Table A3.7 | Structural data from the Rietveld refinement of UiO-67 sample loaded with 7.60 mmol/g ND_3 (59.6 ND_3 molecules per unit cell). Only the structural data obtained from using the cubic *Fm*-3*m* MOF model (major phase) are presented here.

Species	Atom	x	y	z	SOF[a]	B_{eq}[b] (Å^2)	Wyckoff
UiO-67	C4	0.3775(2)	0.0000(2)	0.1168(2)	0.5416(2)	8.0000(17)	96j
	C5	0.3382(2)	0.0000(2)	0.1561(2)	0.5416(2)	8.0000(17)	96j
	C10	0.2926(2)	-0.0202(2)	0.1472(2)	0.4838(2)	7.3467(1)	192l
	H10	0.2858(2)	-0.0344(2)	0.1154(2)	0.4838(2)	8.8160(1)	192l
	C9	0.2564(2)	-0.0204(2)	0.1827(2)	0.4838(2)	7.3467(1)	192l
	H9	0.2246(2)	-0.0345(2)	0.1764(2)	0.4838(2)	8.8160(1)	192l
	C8	0.2672(2)	0.0000(2)	0.2271(2)	0.4838(2)	7.3467(1)	96j
	Zr1	0.5000	0.0000	0.0932	1	0.0100(3)	24e
	O2A	0.4465	-0.0535	0.0535	0.5	0.0100(3)	32f
	O2B	0.4594	-0.0406	0.0406	0.5	0.0100(3)	32f
	H1	0.4284	-0.0716	0.0716	0.5	0.0120(4)	32f
	O1	0.4269	0.0000	0.1336	1	8.0000(2)	96j

Species	Atom	x	y	z	SOF[a]	B_{eq}[b] (Å^2)	Wyckoff
Ammonia I	N1rg	-0.1288(2)	0.3875(2)	0.1093(2)	0.1488(2)	5.0000(14)	192l
	H1rg	-0.1526(2)	0.4006(2)	0.0826(2)	0.1488(2)	6.0000(17)	192l
	H2rg	-0.1414(2)	0.4008(2)	0.1426(2)	0.1488(2)	6.0000(17)	192l
	H3rg	-0.1363(2)	0.3504(2)	0.1134(2)	0.1488(2)	6.0000(17)	192l
Ammonia II	N2rg	0.3436(2)	-0.0281(2)	0.3905(2)	0.1944(1)	5.0000(14)	192l
	H4rg	0.3386(2)	-0.0544(2)	0.3633(2)	0.1944(1)	6.0000(17)	192l
	H5rg	0.3089(2)	-0.0158(2)	0.4002(2)	0.1944(1)	6.0000(17)	192l
	H6rg	0.3543(2)	-0.0468(2)	0.4219(2)	0.1944(1)	6.0000(17)	192l
Ammonia III	N3rg	0.9046(1)	1.0418(1)	0.7737(1)	0.1790(1)	5.0000(14)	192l
	H7rg	0.8917(1)	1.0413(1)	0.8096(1)	0.1790(1)	6.0000(17)	192l
	H8rg	0.9346(1)	1.0184(1)	0.7726(1)	0.1790(1)	6.0000(17)	192l
	H9rg	0.8796(1)	1.0220(1)	0.7528(1)	0.1790(1)	6.0000(17)	192l
Ammonia IV	N4rg	0.1879(1)	0.2043(1)	0.2143(1)	0.0359(1)	5.0000(14)	192l
	H10rg	0.1807(1)	0.1784(1)	0.2413(1)	0.0359(1)	6.0000(17)	192l
	H11rg	0.2226(1)	0.2182(1)	0.2214(1)	0.0359(1)	6.0000(17)	192l
	H12rg	0.1947(1)	0.1850(1)	0.1821(1)	0.0359(1)	6.0000(17)	192l
Ammonia V	N5rg	0.9686(1)	0.9833(1)	1.0445(1)	0.0400(1)	5.0000(14)	192l
	H13rg	0.9424(1)	1.0089(1)	1.0550(1)	0.0400(1)	6.0000(17)	192l
	H14rg	0.9498(1)	0.9511(1)	1.0363(1)	0.0400(1)	6.0000(17)	192l
	H15rg	0.9804(1)	0.9934(1)	1.0097(1)	0.0400(1)	6.0000(17)	192l

[a] B_{eq} refers to the isotropic displacement factor or the thermal parameter.

[b] SOF represents the site occupancy factor per asymmetric unit.

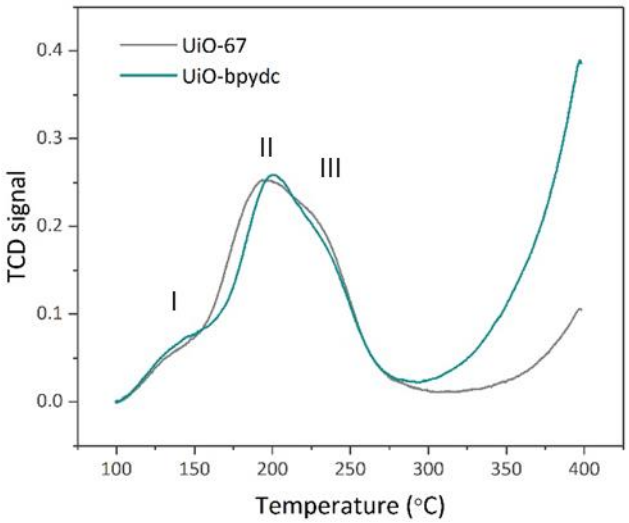

Figure A3.14 | Normalised NH_3-TPD curves of defective MOF samples, measured with a heating rate of 10 °C/min.

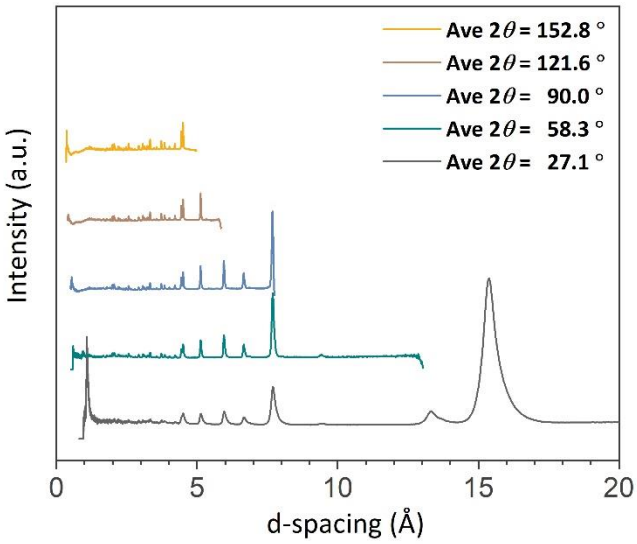

Figure A3.15 | ND patterns of ND_3-free UiO-bpydc recorded at 300 K by using different detector banks. Ave 2θ refers to the average 2θ of the detector banks.

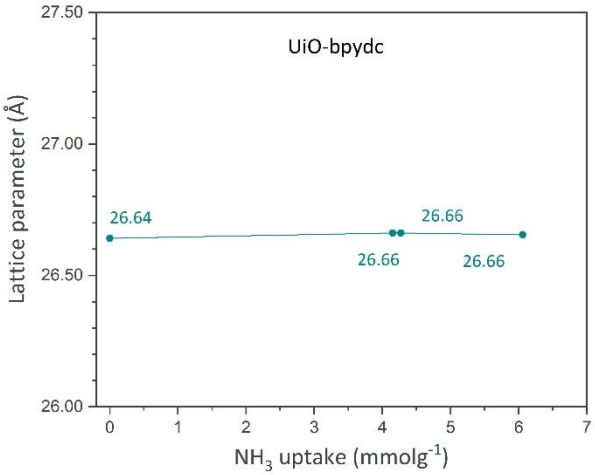

Figure A3.16 | Refined lattice parameters of the NPD data of defective UiO-bpydc at different ND_3 loadings. The maximum standard deviation value of the refined lattice parameters is ± 7.0 x 10^{-4}.

Table A3.8 | *R*-factors and *GOF* values of UiO-bpydc as a function of ND_3 loading obtained from Rietveld refinement of the associated NPD data recorded at 300 K. UiO-bpydc·*n*ND_3 represents the UiO-bpydc structure with addition of *n* ND_3 molecule(s) per asymmetric unit. The underlined structures provide the best fit of the refinement.

Entry	R_{wp} (%)	R_p (%)	R_{exp} (%)	*GOF*
L= 0.00 at 300 K				
UiO-bpydc	2.56	1.82	0.77	2.80
L= 4.15 at 300K				
UiO-bpydc	6.90	2.55	0.75	9.20
UiO-bpydc·1ND_3	6.13	2.46	0.75	8.17
UiO-bpydc·2ND_3	4.78	1.93	0.75	5.97
UiO-bpydc·3ND_3	1.99	1.66	0.75	2.66
UiO-bpydc·4ND_3	3.68	1.66	0.75	4.90

Entry	R_{wp} (%)	R_p (%)	R_{exp} (%)	*GOF*
L= 4.27 at 300 K				
UiO-bpydc	5.72	2.59	0.61	9.38
UiO-bpydc·1ND_3	5.45	2.36	0.61	8.93
UiO-bpydc·2ND_3	5.42	2.45	0.61	8.88
UiO-bpydc·3ND_3	5.31	2.85	0.61	8.70
UiO-bpydc·4ND_3	1.66	1.41	0.61	2.74
UiO-bpydc·5ND_3	4.06	1.97	0.61	6.66
L= 6.06 at 300 K				
UiO-bpydc	3.55	2.42	0.53	6.70
UiO-bpydc·1ND_3	3.49	2.17	0.53	6.58
UiO-bpydc·2ND_3	3.27	2.07	0.53	6.17
UiO-bpydc·3ND_3	2.50	1.95	0.53	4.72
UiO-bpydc·4ND_3	2.15	1.64	0.53	4.06
UiO-bpydc·5ND_3	1.55	1.31	0.53	2.94
UiO-bpydc·6ND_3 too close to the N3 site	2.02	1.59	0.53	3.81

Table A3.9 | Summary of the Rietveld refinement results of ND_3@UiO-bpydc samples.

	Loading amount of ND_3 (mmol/g)			
	0.00	**4.15**	**4.27**	**6.06**
Site occupancy factor per asymmetric unit of ND_3 at				
Site I'	-	0.08	0.07	0.10
Site II'	-	0.02	0.03	0.08
Site III'	-	0.01	0.01	0.01
Site IV'	-	-	0.01	0.03
Site V'	-	-	-	0.04
Dihedral angle between two aromatic rings (°)	21.80(1) 20.33 (DFT)	19.95(1)	16.77(3)	10.00(4)

Table A3.10 | Structural data from the Rietveld refinement of UiO-bpydc sample loaded with 4.15 mmol/g ND_3 (32.6 ND_3 molecules per unit cell).

Species	Atom	x	y	z	SOF[a]	B_{eq}[b] (Å^2)	Wyckoff
UiO-bpydc	C4	0.3811(2)	0.0000(2)	0.1179(2)	0.6667(2)	8.0000(12)	96j
	C5	0.3411(2)	0.0000(2)	0.1576(2)	0.6667(2)	8.0000(12)	96j
	C10	0.2919(2)	-0.0042(2)	0.1451(2)	0.4855(2)	0.0100(6)	192l
	H10	0.2826(2)	-0.0071(2)	0.1107(2)	0.4855(2)	0.0120(8)	192l
	N9	0.2554(2)	-0.0042(2)	0.1810(2)	0.2428(2)	0.0100(6)	192l
	C9	0.2554(2)	-0.0042(2)	0.1810(2)	0.2428(2)	0.0100(6)	192l
	H9	0.2209(2)	-0.0071(2)	0.1722(2)	0.2428(2)	0.0120(8)	192l
	C8	0.2697(2)	0.0000(2)	0.2292(2)	0.4855(2)	0.0100(6)	96j
	Zr1	0.5000	0.0000	0.0932	1	0.0100(11)	24e
	O2A	0.4465	-0.0535	0.0535	0.5	0.0100(13)	32f
	O2B	0.4594	-0.0406	0.0406	0.5	0.0100(143	32f
	H1	0.4284	-0.0716	0.0716	0.5	0.0100(16)	32f
	O1	0.4269	0.0000	0.1336	1	0.0100(10)	96j

Species	Atom	x	y	z	SOF[a]	B_{eq}[b] (Å^2)	Wyckoff
Ammonia I’	N1rg	0.1180(1)	0.3831(1)	0.1168(1)	0.0751(1)	0.0100(9)	192l
	H1rg	0.1550(1)	0.3831(1)	0.1063(1)	0.0751(1)	0.0120(11)	192l
	H2rg	0.1070(1)	0.3462(1)	0.1183(1)	0.0751(1)	0.0120(11)	192l
	H3rg	0.1170(1)	0.3921(1)	0.1542(1)	0.0751(1)	0.0120(11)	192l
Ammonia II’	N2rg	0.3723(1)	-0.0457(1)	0.3413(1)	0.0219(1)	0.0100(9)	192l
	H4rg	0.3901(1)	-0.0159(1)	0.3579(1)	0.0219(1)	0.0120(11)	192l
	H5rg	0.3604(1)	-0.0336(1)	0.3068(1)	0.0219(1)	0.0120(11)	192l
	H6rg	0.3996(1)	-0.0709(1)	0.3316(1)	0.0219(1)	0.0120(11)	192l
Ammonia III’	N3rg	0.4549(1)	-0.0740(1)	0.3333(2)	0.0098(3)	0.0100(9)	192l
	H7rg	0.4843(1)	-0.0557(1)	0.3501(2)	0.0098(3)	0.0120(11)	192l
	H8rg	0.4502(1)	-0.0579(1)	0.2987(2)	0.0098(3)	0.0120(11)	192l
	H9rg	0.4680(1)	-0.1088(1)	0.3232(2)	0.0098(3)	0.0120(11)	192l

[a] B_{eq} refers to the isotropic displacement factor or the thermal parameter.

[b] SOF represents the site occupancy factor per asymmetric unit.

Table A3.11 | Structural data from the Rietveld refinement of UiO-bpydc sample loaded with 4.27 mmol/g ND_3 (33.6 ND_3 molecules per unit cell).

Species	**Atom**	**x**	**y**	**z**	**SOF[a]**	***B*eq[b] (Å^2)**	**Wyckoff**
UiO-bpydc	C4	0.3811(1)	0.0000(1)	0.1179(1)	0.6667(1)	8.0000(11)	96j
	C5	0.3414(1)	0.0000(1)	0.1575(1)	0.6667(1)	8.0000(11)	96j
	C10	0.2921(1)	-0.0066(1)	0.1454(1)	0.4855(1)	0.0100(5)	192l
	H10	0.2830(1)	-0.0113(1)	0.1111(1)	0.4855(1)	0.0120(6)	192l
	N9	0.2556(1)	-0.0067(1)	0.1812(1)	0.2428(1)	0.0100(5)	192l
	C9	0.2556(1)	-0.0067(1)	0.1812(1)	0.2428(1)	0.0100(5)	192l
	H9	0.2212(1)	-0.0114(1)	0.1726(1)	0.2428(1)	0.0120(6)	192l
	C8	0.2697(1)	0.0000(1)	0.2292(1)	0.4855(1)	0.0100(5)	96j

Species	Atom	x	y	z	SOF[a]	*B*eq[b] (Å^2)	Wyckoff
	Zr1	0.5000	0.0000	0.0932	1	0.0100(9)	24e
	O2A	0.4465	-0.0535	0.0535	0.5	0.0100(11)	32f
	O2B	0.4594	-0.0406	0.0406	0.5	0.0100(11)	32f
	H1	0.4284	-0.0716	0.0716	0.5	0.0100(13)	32f
	O1	0.42693	0.0000	0.13363	1	0.0100(8)	96j
Ammonia I’	N1rg	-0.1129(1)	0.3809(1)	0.1199(1)	0.0736(1)	0.0100(1)	192l
	H1rg	-0.1123(1)	0.3418(1)	0.1201(1)	0.0736(1)	0.0120(1)	192l
	H2rg	-0.0801(1)	0.3930(1)	0.1374(1)	0.0736(1)	0.0120(1)	192l
	H3rg	-0.1059(1)	0.3922(1)	0.0831(1)	0.0736(1)	0.0120(1)	192l
Ammonia II’	N2rg	0.3605(2)	0.0010(2)	0.3377(2)	0.0308(3)	0.0100(1)	192l
	H4rg	0.3711(2)	-0.0191(2)	0.3138(2)	0.0308(3)	0.0120(1)	192l
	H5rg	0.3615(2)	0.0426(2)	0.3162(2)	0.0308(3)	0.0120(1)	192l
	H6rg	0.3222(2)	0.0054(2)	0.3439(2)	0.0308(3)	0.0120(1)	192l
Ammonia III’	N3rg	0.4609(2)	0.0754(2)	0.3354(2)	0.0134(1)	0.0100(1)	192l
	H7rg	0.4320(2)	0.0491(2)	0.3353(2)	0.0134(1)	0.0120(1)	192l
	H8rg	0.4611(2)	0.0924(2)	0.3002(2)	0.0134(1)	0.0120(1)	192l
	H9rg	0.4494(2)	0.1050(2)	0.3583(2)	0.0134(1)	0.0120(1)	192l
Ammonia IV’	N4rg	0.4702(2)	0.0655(2)	0.4865(2)	0.0090(1)	0.0100(1)	192l
	H10rg	0.4535(2)	0.0691(2)	0.4513(2)	0.0090(1)	0.0120(1)	192l
	H11rg	0.4910(2)	0.0325(2)	0.4859(2)	0.0090(1)	0.0120(1)	192l
	H12rg	0.4988(2)	0.0920(2)	0.4883(2)	0.0090(1)	0.0120(1)	192l

[a] B_{eq} refers to the isotropic displacement factor or the thermal parameter.

[b] SOF represents the site occupancy factor per asymmetric unit.

Table A3.12 | Structural data from the Rietveld refinement of UiO-bpydc sample loaded with 6.06 mmol/g ND_3 (47.6 ND_3 molecules per unit cell).

Species	Atom	x	y	z	SOF[a]	B_{eq}[b] (Å^2)	Wyckoff
UiO-bpydc	C4	0.3810(2)	-0.0000(2)	0.1178(2)	0.6667(2)	8.0000(13)	96j
	C5	0.3413(2)	-0.0000(2)	0.1575(2)	0.6667(2)	8.0000(13)	96j
	C10	0.3536(2)	-0.0056(2)	0.2068(2)	0.4855(2)	0.0100(11)	192l
	H10	0.3879(2)	-0.0096(2)	0.2160(2)	0.4855(2)	0.0120(14)	192l
	N9	0.3178(2)	-0.0057(2)	0.2434(2)	0.2428(2)	0.0100(11)	192l
	C9	0.3178(2)	-0.0057(2)	0.2434(2)	0.2428(2)	0.0100(11)	192l
	H9	0.3265(2)	-0.0096(2)	0.2778(2)	0.2428(2)	0.0120(14)	192l
	C8	0.2696(2)	0.0000(2)	0.2292(2)	0.4855(2)	0.0100(11)	96j
	Zr1	0.5000	0.0000	0.0932	1	0.0100(11)	24e
	O2A	0.4465	-0.0535	0.0535	0.5	0.0100(13)	32f
	O2B	0.4594	-0.0406	0.0406	0.5	0.0100(13)	32f
	H1	0.4234	-0.0766	0.0766	0.5	0.0100(16)	32f
	O1	0.4269	0.0000	0.1336	1	0.0100(10)	96j
Ammonia I’	N1rg	-0.1129(2)	0.3809(2)	0.1199(2)	0.0975(1)	0.0100(10)	192l
	H1rg	-0.1032(2)	0.3774(2)	0.1560(2)	0.0975(1)	0.0120(12)	192l
	H2rg	-0.0931(2)	0.3554(2)	0.1006(2)	0.0975(1)	0.0120(12)	192l
	H3rg	-0.1476(2)	0.3666(2)	0.1164(2)	0.0975(1)	0.0120(12)	192l
Ammonia II’	N2rg	0.3605(3)	0.0010(3)	0.3377(3)	0.0771(2)	0.0100(10)	192l
	H4rg	0.3771(3)	0.0268(3)	0.3066(3)	0.0771(2)	0.0120(12)	192l
	H5rg	0.3744(3)	-0.0266(3)	0.3390(3)	0.0771(2)	0.0120(12)	192l
	H6rg	0.3774(3)	0.0262(3)	0.3691(3)	0.0771(2)	0.0120(12)	192l
Ammonia III’	N3rg	0.4488(3)	0.0738(3)	0.3331(3)	0.0134(2)	0.0100(10)	192l
	H7rg	0.4193(3)	0.0508(3)	0.3291(3)	0.0134(2)	0.0120(12)	192l
	H8rg	0.4710(3)	0.0685(3)	0.3032(3)	0.0134(2)	0.0120(12)	192l
	H9rg	0.4364(3)	0.1088(3)	0.3272(3)	0.0134(2)	0.0120(12)	192l
	N4rg	0.4728(2)	-0.0138(2)	0.4222(2)	0.0304(4)	0.0100(10)	192l

Species	Atom	x	y	z	SOF[a]	B_{eq}[b] (Å^2)	Wyckoff
Ammonia	H10rg	0.4660(2)	-0.0512(2)	0.4132(2)	0.0304(4)	0.0120(12)	192l
IV’	H11rg	0.4402(2)	0.0065(2)	0.4150(2)	0.0304(4)	0.0120(12)	192l
	H12rg	0.4747(2)	-0.0109(2)	0.4612(2)	0.0304(4)	0.0120(12)	192l
	N5rg	0.2465(3)	0.2536(3)	0.2561(3)	0.0397(3)	0.0100(10)	192l
Ammonia	H13rg	0.2409(3)	0.2227(3)	0.2354(3)	0.0397(3)	0.0120(12)	192l
V’	H14rg	0.2531(3)	0.2818(3)	0.2321(3)	0.0397(3)	0.0120(12)	192l
	H15rg	0.2131(3)	0.2639(3)	0.2698(3)	0.0397(3)	0.0120(12)	192l

[a] B_{eq} refers to the isotropic displacement factor or the thermal parameter.

[b] SOF represents the site occupancy factor per asymmetric unit.

Table A3.13 | The guiding values of “strong”, “moderate” and “weak” hydrogen bonds.[4]

	Strong	Moderate	Weak
Interaction type	Strongly covalent	Mostly electrostatic	Electrostatic/ dispersion
Bond lengths B—H (Å)	1.2- 1.5	ca. 1.0	ca. 1.0
Bond lengths H---A (Å)	1.2- 1.5	1.5- 2.2	> 2.2
Bond lengths B---A (Å)	2.2- 2.5	2.5- 3.2	3.2- 4.0
Bond energy (kJmol^{-1})	63- 167	16- 63	< 16
Bond angles (°)	170- 180	> 130	> 90

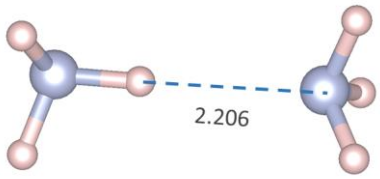

Figure A3.17 | DFT Optimised structure of NH_3 dimer. The binding energy is 0.13 eV. The unit of the H bond length is in angstrom (Å).

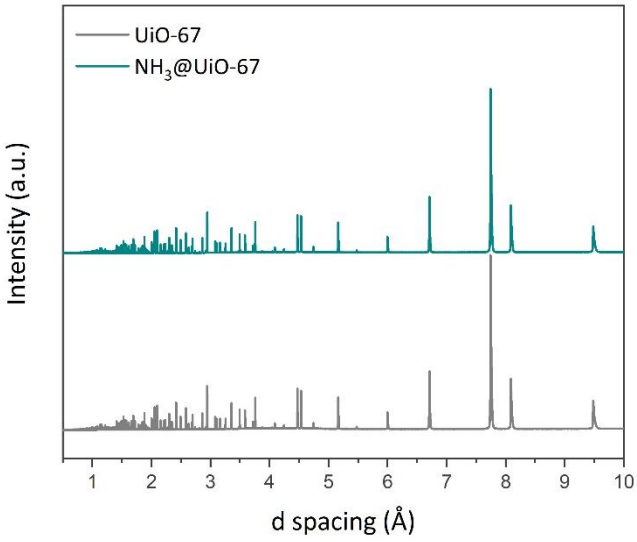

Figure A3.18 | Synchrotron PXRD patterns of UiO-67 before and after NH_3 adsorption, measured at 298 K.

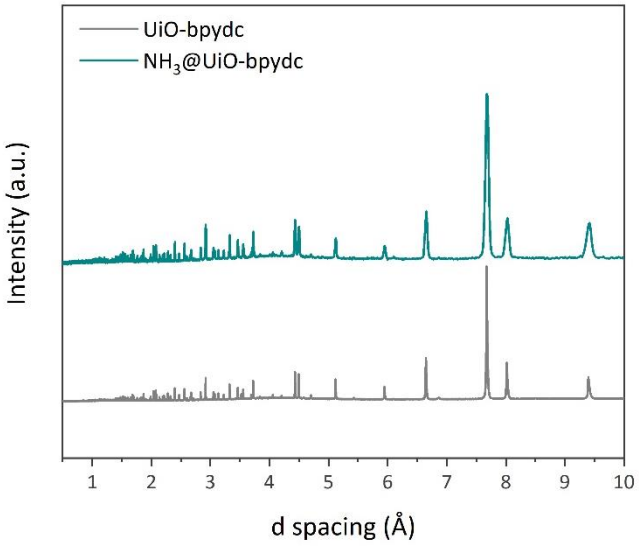

Figure A3.19 | Synchrotron PXRD patterns of UiO-bpydc before and after NH_3 adsorption, measured at 298 K.

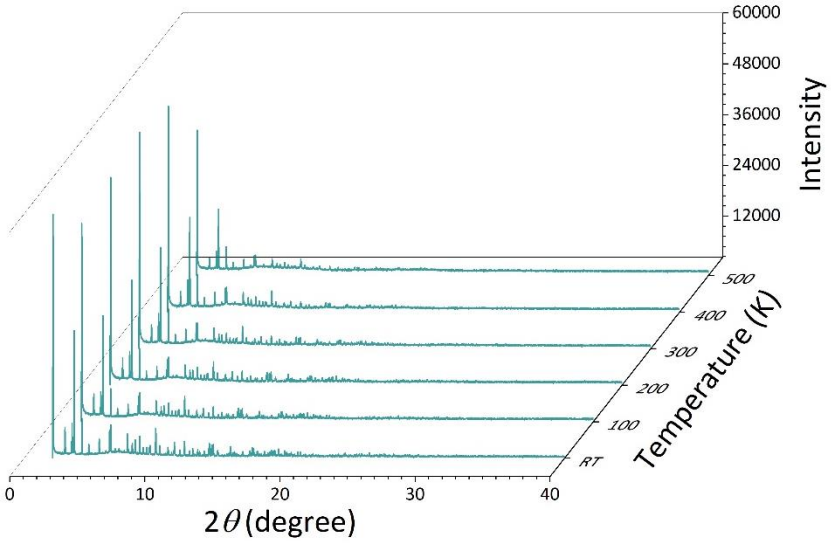

Figure A3.20 | Synchrotron XRD patterns of the NH_3-loaded UiO-bpydc sample measured at different temperatures from 298 K to 773 K.

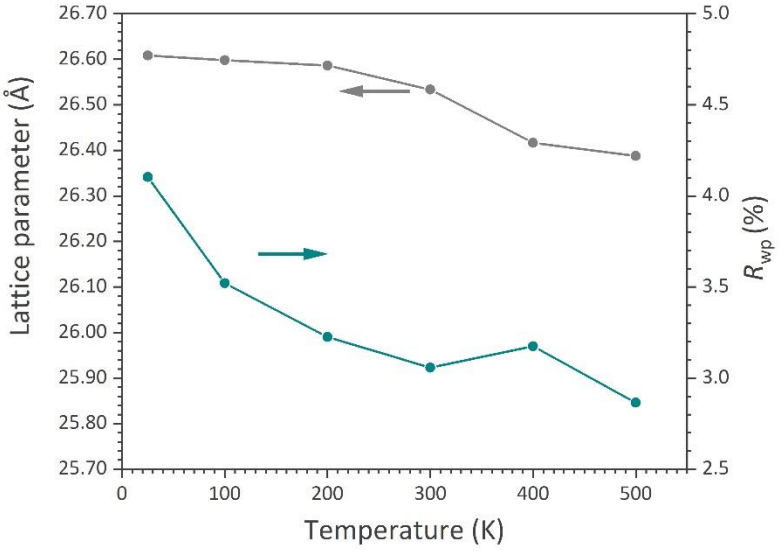

Figure A3.21 | Refined lattice parameters and their corresponding R_{wp} values of the NH_3-loaded UiO-bpydc sample obtained from the synchrotron XRD results. The maximum standard deviation value of the refined lattice parameters is ± 8.42x10^{-4}.

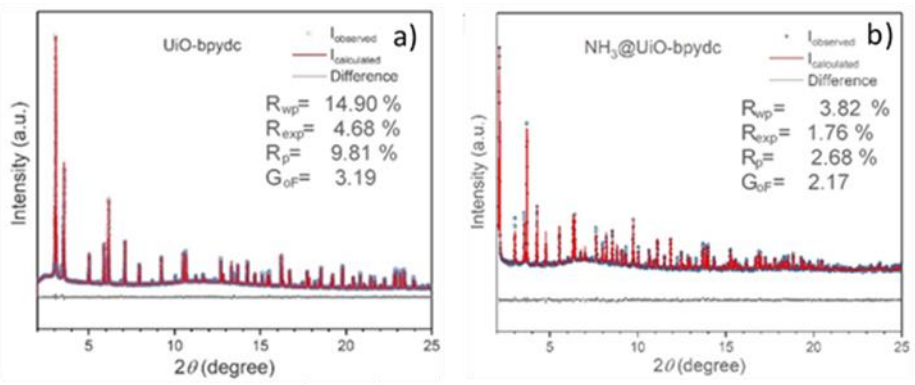

Figure A3.22 | Synchrotron PXRD patterns and refined NH_3 positions in the channel of the UiO-bpydc structure. (**a**) Diffraction patterns before and (**b**) after NH_3 adsorption in UiO-bpydc at 298 K. The ratio of peak intensities alters upon adsorption of NH_3 with a slight peak broadening. The refinement results with acceptable *R*-factors clearly demonstrate the remaining of *Fm*-3*m* space group after NH_3 uptake. The refinement results indicate four

possible binding sites of NH_3 in the UiO-bpydc channel. The synchrotron XRD data shows the adsorbed NH_3 are possibly located above the μ_3-O/ or μ_3-OH group (site I, occupancy 0.176 ± 0.007), close to the basal planes of bipyridine linkers (site II, occupancy 0.286 ± 0.014), above the trigonal window with a proximity to site II (site III, occupancy 0.255 ± 0.007) and inside the MOF cavities (site IV, occupancy 0.162 ± 0.005). Note that the NH_3-loaded sample used in the synchrotron PXRD measurement was under saturation. Thus, the quantity of adsorbed NH_3 of this sample is different from that of the sample used in the NPD experiment.

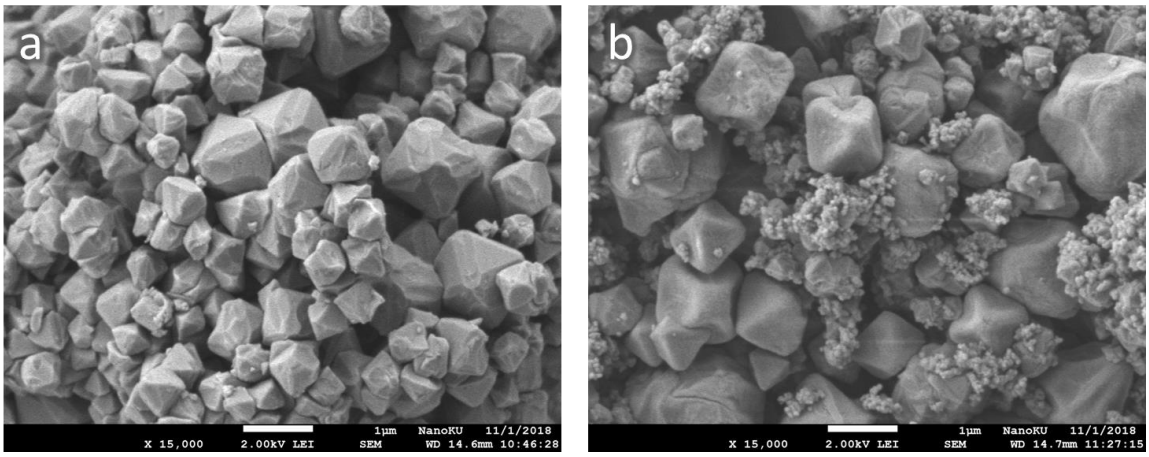

Figure A3.23 | Scanning electron microscope (SEM) images of defective UiO-67 (**a**) and UiO-bpydc (**b**). Scale bar: 1 µm. The images were acquired at Center of Nanotechnology, Kasetsart University, Thailand.

B) Appendices for Chapter 4

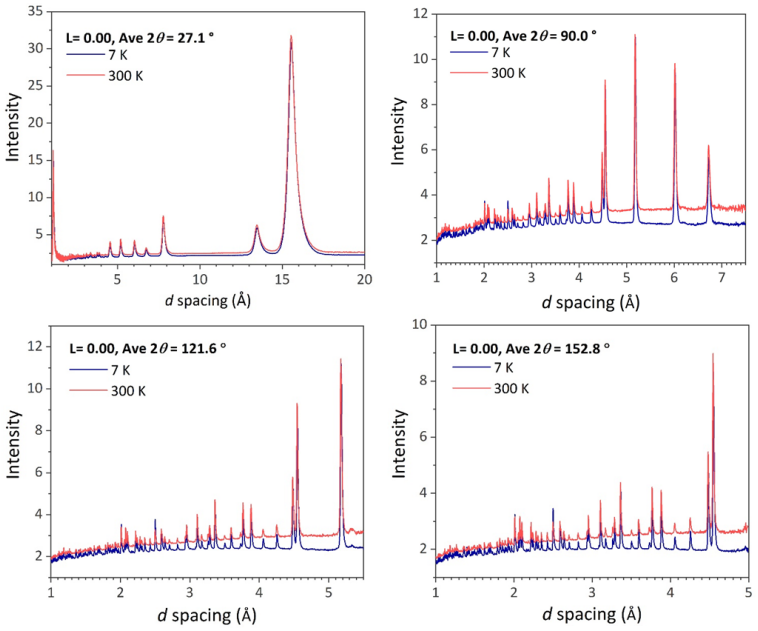

Figure A4.1 | *In situ* NPD patterns of UiO-67 before ND_3 loading measured at 7 K (blue line) and 300 K (red line). The data were collected from different detector banks.

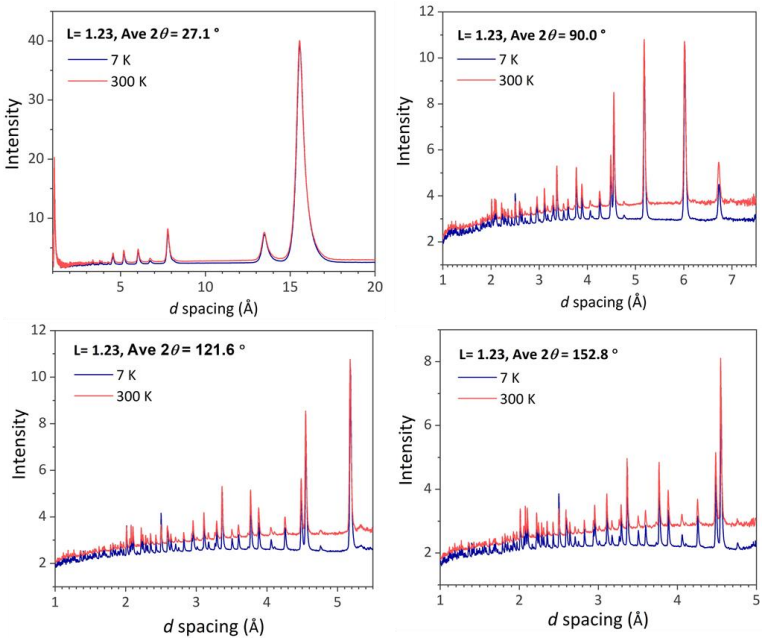

Figure A4.2 | *In situ* NPD patterns of UiO-67 at ND_3 loading (L) of 1.23 mmol/g measured at 7 K (blue line) and 300 K (red line). The data were collected from different detector banks.

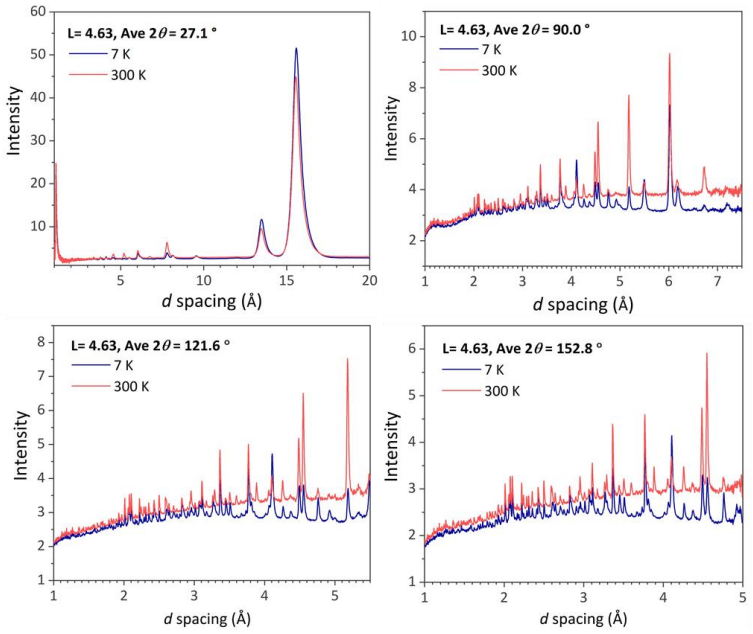

Figure A4.3 | *In situ* NPD patterns of UiO-67 at ND_3 loading (L) of 4.63 mmol/g measured at 7 K (blue line) and 300 K (red line). The data were collected from different detector banks.

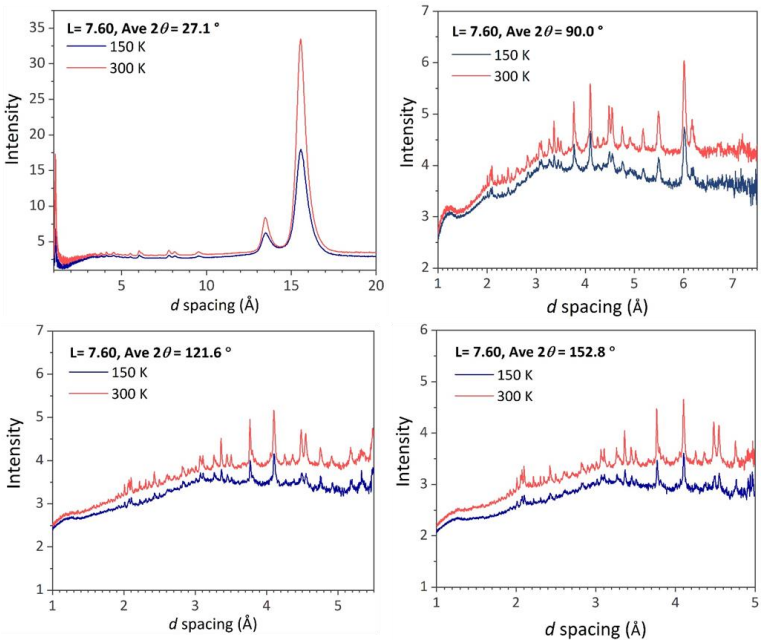

Figure A4.4 | *In situ* NPD patterns of UiO-67 at ND_3 loading (L) of 7.60 mmol/g measured at 150 K (blue line) and 300 K (red line). The data were collected from different detector banks.

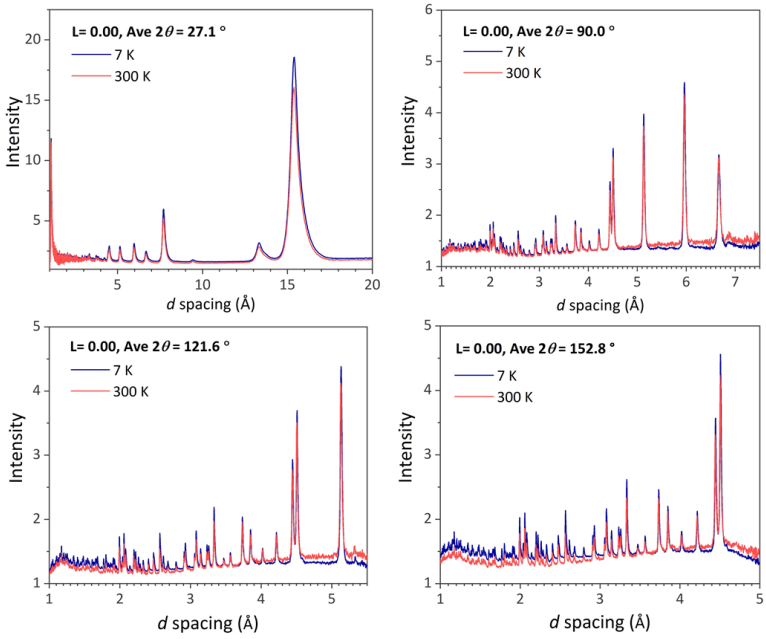

Figure A4.5 | *In situ* NPD patterns of UiO-bpydc before ND_3 loading measured at 7 K (blue line) and 300 K (red line). The data were collected from different detector banks.

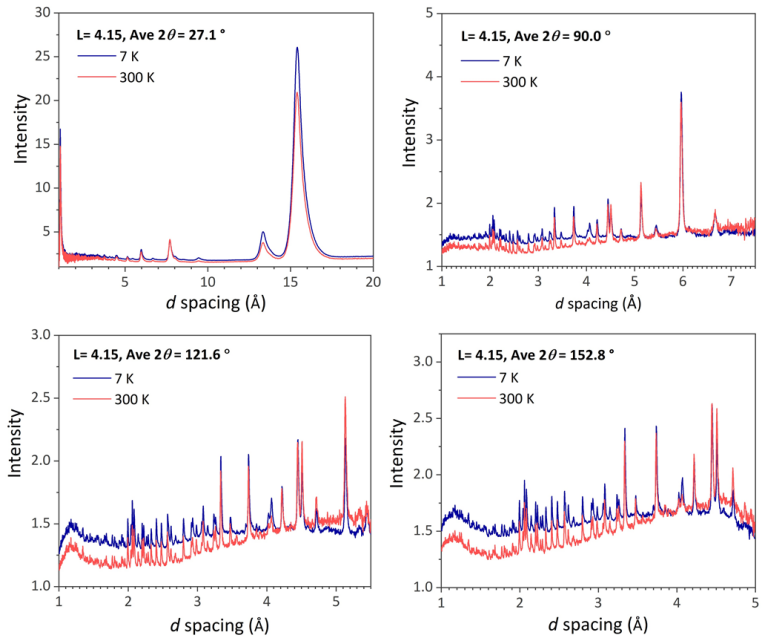

Figure A4.6 | *In situ* NPD patterns of UiO-bpydc at ND_3 loading (L) of 4.15 mmol/g measured at 7 K (blue line) and 300 K (red line). The data were collected from different detector banks.

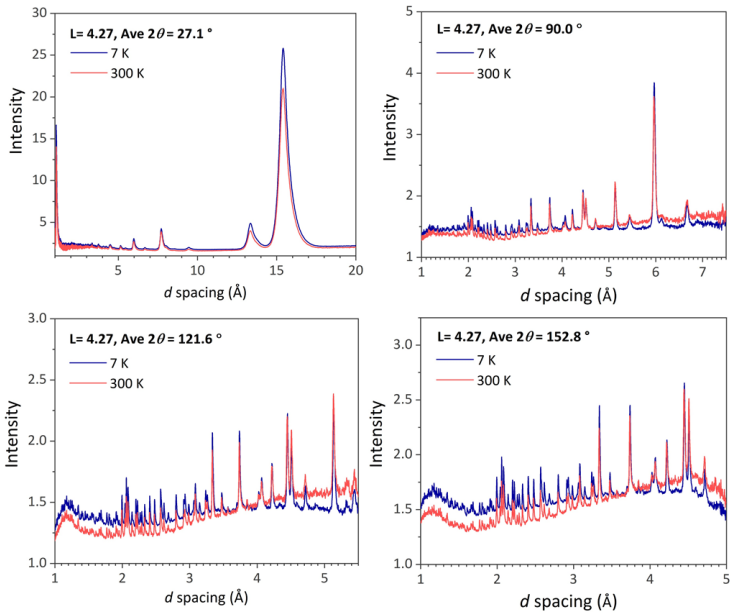

Figure A4.7 | *In situ* NPD patterns of UiO-bpydc at ND_3 loading (L) of 4.27 mmol/g measured at 7 K (blue line) and 300 K (red line). The data were collected from different detector banks.

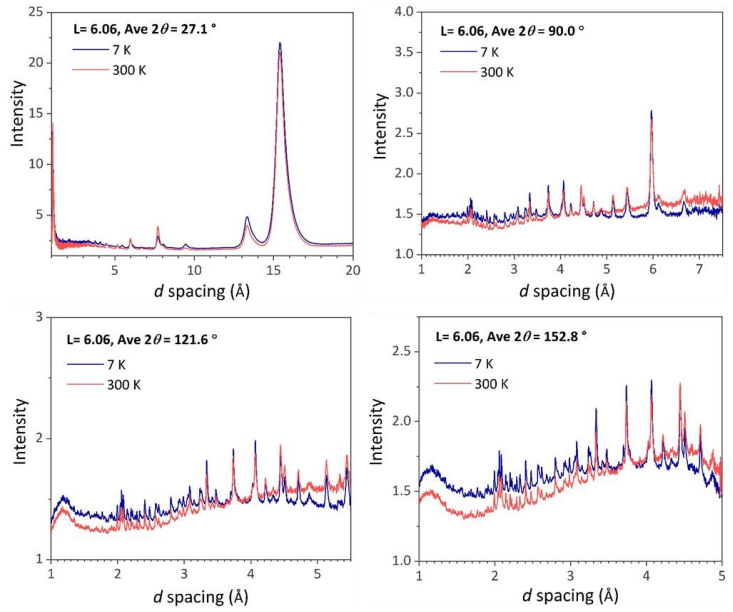

Figure A4.8 | *In situ* NPD patterns of UiO-bpydc at ND_3 loading (L) of 6.06 mmol/g measured at 7 K (blue line) and 300 K (red line). The data were collected from different detector banks.

It is noted that the change in frameworks structure may occur through linker rotation (like local flexibility in rigid frameworks) which causes the change in peak intensity. Thus, the variation of peak intensities and positions in this study can cause by both orderly adsorbed NH_3 molecules and the linker rotation. One possible way that would help to clarify this observation is to perform the NPD measurement of the ND_3-desorbed samples and see how the diffraction patterns change. As shown by our study, the peak intensities of the extra peaks decreased during ND_3 desorption, we can therefore ensure such additional peaks at high ND_3 loading originated from ND_3 orderly confined in the MOF pores, not from the framework deformation.

C) Appendices for Chapter 5

Table A5.1 | Calculated and experimental vibrational modes of solid acetic acid (CH_3COOH). The experiment data were recorded by using an INS technique at 20 K. [5]

Frequency (cm^{-1})			Band assignment
Calculated [5]	Experimental		
	Ref [5]	This work	
60- 100	200	Below 300	CH_3 torsion, CH_3 rotation
162	Below 300	Below 300	entire CH_3 group rotation
430, 450	440, 460	450, 460	CH_3 bending (OP)
580	600	600	CH_3 bending (IP)
620	620	640	OCO bending
900	900	900	CC bending (OP)
920	940	940	OH bending (OP)
1020-1100	1010, 1020	1010, 1020	CH_3 rocking
1280	1300	n.o.	OH bending (IP)
1420	1410	n.o.	C=O stretching

n.o. = not observed; IP= in plane; OP= out of plane.

Table A5.2 | Calculated and experimental vibrational modes of crystalline ammonia (NH_3) phase I from experimental data measured at 20 K.

Frequency (cm^{-1})			Suggested assignment	Band assignment
Calculated [6]	Experimental			
	Ref [6]*	This work		
111.4	108	120	A	translation
174.1	141	130	E	translation
160.1	141	152	F	translation
187.1	184	170	F	translation
259.8	261.5	240	F; R_z	libration
	n.o.	245	unknown	unknown

Frequency (cm^{-1})			Suggested assignment	Band assignment
Calculated [6]	Experimental			
	Ref [6]*	This work		
328.0	299.5	260	A; R_z	libration
325.0	313	321	E: R_{xy}	libration
351.5	360.5	360	F; R_{xy}	libration
	366.5	n.o.	F; R_{xy}	libration
	431	440	νR_{xy} F(LO)	combination (two librations)
	n.o.	470	unknown	unknown
526.5	533	545	L_X	combination
1019.6	1057	1056	F (TO)	sym. bending
1098.0	1072.5	1083	A	sym. bending
1640.7	1636	n.o.	F	asym. bending
1657.4	1650	n.o.	F	asym. bending
1641.7	1678	n.o.	E	asym. bending
3231.3	3203.5	n.o.	A	sym. stretching
3229.9	3210	n.o.	F	sym. stretching
3324.1	3370	n.o.	F, E	asym. stretching
3335.5	3378	n.o.	F (TO)	asym. stretching
	3383.5	n.o.	F (LO)	asym. stretching

n.o.= not observed; sym.= symmetric; asym.= asymmetric

* The data were analysed by using Raman spectroscopy at 18 K and Infrared spectroscopy at 61 K.

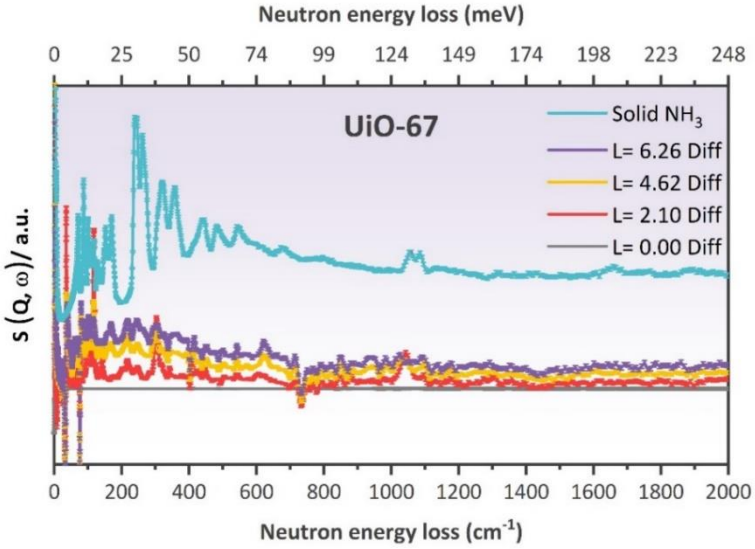

Figure A5.1 | INS difference plots of UiO-67 with increased NH_3 adsorption. The INS spectrum of solid NH_3 was provided by the ISIS. *L* refers to loading amount of NH_3 in mmol/g. Note that 1 meV ≈ 8.0655 cm^{-1}.

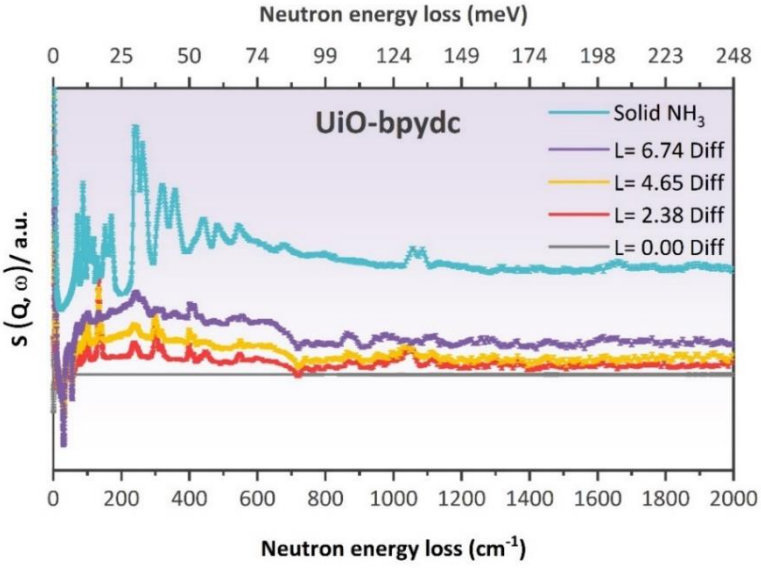

Figure A5.2 | INS difference plots of UiO-bpydc with increased NH_3 adsorption. The INS spectrum of solid NH_3 was provided by the ISIS. *L* refers to loading amount of NH_3 in mmol/g. Note that 1 meV ≈ 8.0655 cm^{-1}.

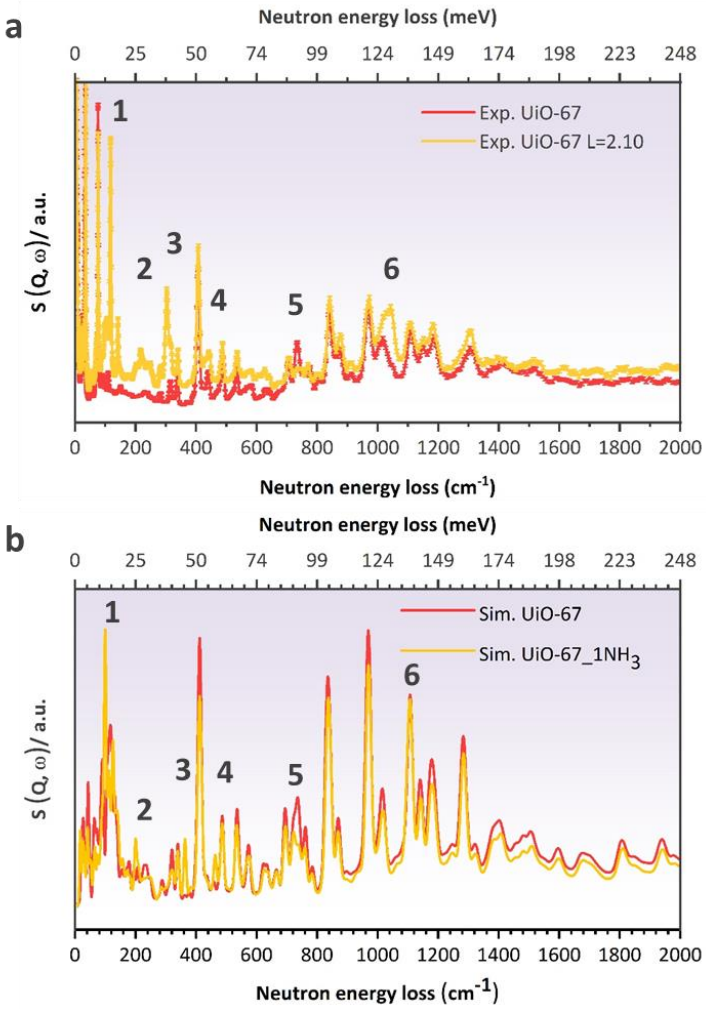

Figure A5.3 | Experimental (**a**) and simulated (**b**) INS spectra of UiO-67 and UiO-67_2.10NH_3 with the range of neutron energy loss up to 2000 cm^{-1} (248 meV). L refers to loading amount of NH_3 in mmol/g. Arabic numbers mark the differences between the spectra of UiO-67 and UiO-67_2.10NH_3.

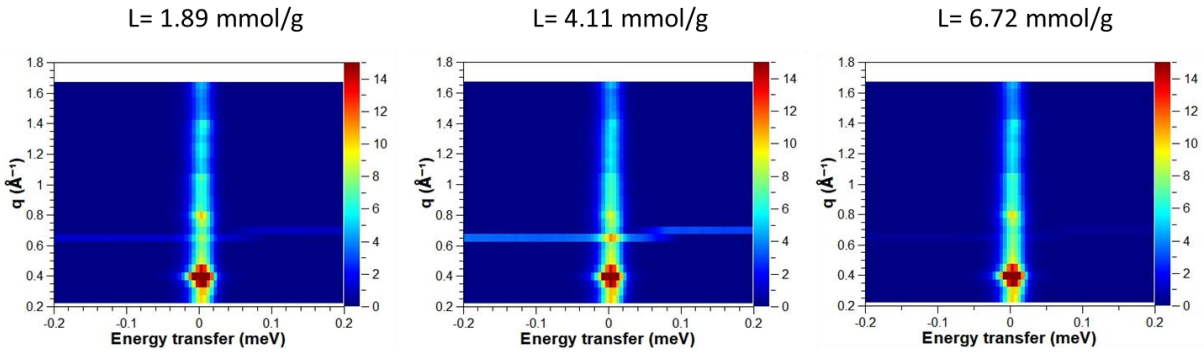

Figure A5.4 | QENS data of NH_3-adsorbed UiO-67 measured at 298 ± 2 K. The detectors covered measurements over a ***Q*** range of 0.225–1.675 $Å^{-1}$ (a *d* range of 3.8 – 27.9 Å) with a faulty detector at ***Q*** = 0.675 $Å^{-1}$. *L* refers to a loading quantity of NH_3 in mmol/g.

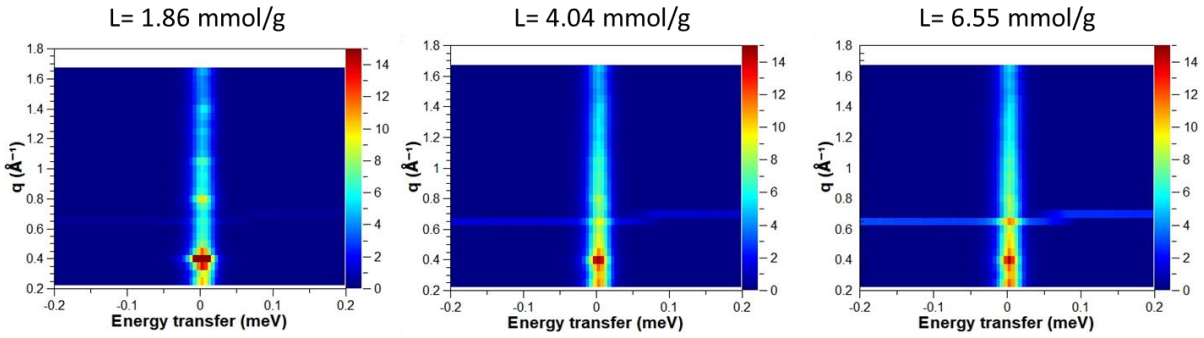

Figure A5.5 | QENS data of NH_3-adsorbed UiO-bpydc measured at 298 ± 2 K. The detectors covered measurements over a ***Q*** range of 0.225–1.675 $Å^{-1}$ (a *d* range of 3.8 – 27.9 Å) with a faulty detector at ***Q*** = 0.675 $Å^{-1}$. *L* refers to a loading quantity of NH_3 in mmol/g.

D) References

1. Cavka, J. H.; Jakobsen, S.; Olsbye, U.; Guillou, N.; Lamberti, C.; Bordiga, S.; Lillerud, K. P., A New Zirconium Inorganic Building Brick Forming Metal Organic Frameworks with Exceptional Stability. *Journal of the American Chemical Society* **2008,** *130* (42), 13850-13851.
2. Ko, N.; Hong, J.; Sung, S.; Cordova, K. E.; Park, H. J.; Yang, J. K.; Kim, J., A Significant Enhancement of Water Vapour Uptake at Low Pressure by Amine-Functionalization of UiO-67. *Dalton Transactions* **2015,** *44* (5), 2047-2051.
3. Ayoub, G.; Islamoglu, T.; Goswami, S.; Friščić, T.; Farha, O. K., Torsion Angle Effect on the Activation of UiO Metal–Organic Frameworks. *ACS Applied Materials & Interfaces* **2019,** *11* (17), 15788-15794.
4. Steiner, T., The Hydrogen Bond in the Solid State. *Angewandte Chemie International Edition* **2002,** *41* (1), 48-76.
5. Johnson, M. R.; Trommsdorff, H. P., Vibrational Spectra of Crystalline Formic and Acetic Acid Isotopologues by Inelastic Neutron Scattering and Numerical Simulations. *Chemical Physics* **2009,** *355* (2), 118-122.
6. Binbrek, O. S.; Anderson, A., Raman Spectra of Molecular Crystals. Ammonia and 3-Deutero-Ammonia. *Chemical Physics Letters* **1972,** *15* (3), 421-427.